
Crystallization via Amorphous Intermediates

Dissertation

zur Erlangung des Grades

„Doktor der Naturwissenschaften“

im Promotionsfach Chemie

am Fachbereich Chemie, Pharmazie und Geowissenschaften der
Johannes Gutenberg-Universität Mainz



Sebastian Leukel

geboren in Hachenburg

Mainz, 2018

Dekan: [REDACTED]

Erster Berichterstatter: [REDACTED]

Zweite Berichterstatterin: [REDACTED]

Tag der mündlichen Prüfung: 14.11.2018

ERKLÄRUNG

Hiermit erkläre ich, dass die vorliegende Arbeit in der Zeit von Februar 2015 bis Juli 2018 unter der Leitung von Univ.-Prof. Dr. Wolfgang Tremel am Institut für Anorganische Chemie und Analytische Chemie der Johannes Gutenberg-Universität Mainz angefertigt wurde. Ich versichere, die vorliegende Arbeit selbstständig und ohne fremde Hilfe verfasst zu haben. Alle verwendeten Quellen und Hilfsmittel sind vollständig angegeben.

Mainz, den 27.07.2018

Für meine Familie

ABSTRACT

This dissertation studies the role of amorphous intermediates during crystallization, specifically in carbonate systems. The stabilization and isolation of these transient species represent a unique challenge in regard to chemical synthesis. Structural characterization and crystallization experiments were performed to investigate these intermediates in detail. Thereby, this work contributes to a deeper understanding of the fundamental processes occurring during crystallization. Additionally, two sub-projects were addressed. Crystalline calcium carbonate was amorphosized mechanochemically in a planetary ball mill, and the properties of the new material were investigated. Also, a synthesis of partially amorphous calcium sulfate nanoparticles was devised. These particles exhibit unusual dispersibility properties in organic media and promise interesting applications as “nano-gypsum”.

The main part of this thesis deals with the role of amorphous intermediate species of carbonates; it is divided into three separate projects as discussed below.

In the first project, a new two-phase reaction system was developed that enables the stabilization of amorphous carbonates of various metals (calcium, strontium, barium, manganese, and cadmium). Droplet-shaped nanoparticles of the amorphous carbonates were coated with an oleate layer immediately after their formation. These nanoparticles exhibited unusual long-term stability for several days to weeks, despite normally being an extremely short-lived species. The only exception was amorphous barium carbonate, which was stabilized only for a few hours. Heteronuclear correlation spectroscopy (HETCOR) indicated that the oleate ligand was solely found on the surface of the particles; no mixed carbonate/oleate phase was detected. Therefore, the samples were regarded as actual intermediates during the crystallization process, which were stabilized by an oleate capping *ex post*. Through thermogravimetric analysis (TGA), the amount of structural water in the hydrated amorphous carbonates was determined to be less than 1 mol H₂O per formula unit. Simultaneously, the thermally induced crystallization was monitored by differential thermal analysis (DTA). In order to characterize the local structure of the amorphous carbonates, total scattering experiments utilizing high-energy synchrotron radiation were performed that allowed

the derivation of the respective pair distribution function (PDF). On basis of the PDF, a structural model for amorphous calcium carbonate was developed.

The approach above describes a stabilization of amorphous carbonates, but it does not allow the study of the crystallization mechanism. Therefore, a synthesis for non-stabilized amorphous carbonates was devised in a second project. By precipitation in an organic solvent and using solid cesium carbonate as a precursor, dispersions of non-stabilized amorphous calcium, strontium, and manganese carbonate were obtained. With these samples, the crystallization mechanism and the influence of water were probed. For all carbonates, the crystallization speed increased with increasing water concentration, which implies a dissolution-recrystallization mechanism for the phase transformation of the amorphous intermediates. This was further supported by potentiometric experiments and electron microscopy.

In the carbonate system, the hydration of the amorphous intermediate species represents a profound difference from the anhydrous crystalline modifications. Therefore, in the third project, the local water environment and the strength of the hydrogen bonding network in the amorphous carbonates were investigated in detail by various nuclear magnetic resonance techniques (NMR) and Fourier transform infrared spectroscopy (FTIR). To this end, the synthesis of non-stabilized amorphous carbonates was modified and relatively stable powders of the amorphous carbonates of magnesium, calcium, strontium, and barium were prepared. The strength of the internal hydrogen bonding network is predominantly determined by the Pearson hardness of the respective cation. Yet, in amorphous magnesium carbonate, hydroxide ions were identified that additionally strengthen the hydrogen bonding network by acting as strong hydrogen bond acceptors. The detailed examination of the structural water in amorphous carbonates represents a key aspect of completely characterizing these transient intermediate species.

In the first sub-project, the mechanochemical amorphization of crystalline calcium carbonate was studied. High-energy ball milling of calcite with a certain amount of sodium carbonate yielded a new form of amorphous calcium carbonate, which was referred to as BM-ACC (ball milled amorphous calcium carbonate). The formation process was monitored by using sodium ions as a probe for changes in their local environment *via* ^{23}Na NMR. Total scattering experiments were performed to illuminate the structure of BM-ACC. The coordination number of calcium was decreased in this compound, compared to crystalline calcium

carbonate. Finally, the crystallization kinetics and mechanism were studied of both thermally induced and water-induced crystallization. In both cases, BM-ACC exhibited a distinctively different crystallization behavior from amorphous calcium carbonate prepared by wet-chemical methods.

Inspired by the precipitation of amorphous carbonates in organic solvents, in the second sub-project, calcium sulfate nanoparticles were synthesized. These droplet-shaped particles (~30 nm) were predominantly amorphous with small crystalline areas of γ -anhydrite. The most prominent feature of the nanoparticles was their highly unusual dispersibility in acetone, which allowed the fabrication of transparent calcium sulfate films. By ^1H NMR and FTIR, 2-propanol molecules were identified as surface-attached species, which induced the dispersibility in organic media. Finally, the transformation of the particles to gypsum on contact with water was monitored with electron microscopy. The crystallization proceeded *via* bassanite as an intermediate phase that formed by oriented attachment of the calcium sulfate nanoparticles.

KURZZUSAMMENFASSUNG

Die vorliegende Dissertation untersucht die Rolle amorpher Intermediate bei der Kristallisation, insbesondere von Carbonaten. Die Stabilisierung und Isolierung dieser kurzlebigen Spezies stellt die besondere Herausforderung in Bezug auf die chemische Synthese dar. Zur genauen Untersuchung der Intermediate wurden diese strukturell charakterisiert und Kristallisationsexperimente wurden durchgeführt. Damit trägt diese Arbeit zu einem tieferen Verständnis der fundamentalen Mechanismen während des Kristallisationsprozesses bei. Darüber hinaus wurden zwei Nebenprojekte bearbeitet. Kristallines Calciumcarbonat wurde in einer Planetenkugelmühle mechanochemisch amorphisiert und die Eigenschaften dieser neuartigen Verbindung wurden untersucht. Zusätzlich wurde eine Synthese für teilamorphe Calciumsulfat-Nanopartikel entwickelt. Diese Partikel weisen eine ungewöhnliche Dispergierbarkeit in organischen Lösungsmitteln auf und versprechen somit interessante Anwendungen als „Nano-Gips“.

Der Hauptteil dieser Arbeit beschäftigt sich mit der Rolle amorpher Carbonatspezies; er ist in drei separate Projekte aufgeteilt.

Im ersten Projekt wurde ein Zwei-Phasen-Reaktionssystem entwickelt, das die Stabilisierung amorpher Carbonate verschiedenster Metalle (Calcium, Strontium, Barium, Mangan und Cadmium) ermöglicht. Tropfenförmige Nanopartikel der amorphen Carbonate wurden sofort nach ihrer Bildung mit einer Oleat-Schicht umschlossen. Diese Nanopartikel wiesen eine ungewöhnliche Langzeitstabilität von mehreren Tagen bis Wochen auf, obwohl es sich dabei normalerweise um extrem kurzlebige Spezies handelt. Amorphes Bariumcarbonat bildete die einzige Ausnahme, es konnte nur für wenige Stunden stabilisiert werden. Heteronukleare Korrelationsspektroskopie (HETCOR) zeigte, dass sich die Oleat-Liganden nur auf der Oberfläche der Partikel befanden; keine gemischte Carbonat/Oleat-Phase wurde detektiert. Daher wurden die Proben als tatsächliche Kristallisationsintermediate betrachtet, die nachträglich mit einer Oleat-Hülle stabilisiert wurden. Mittels thermogravimetrischer Analyse (TGA) wurde der Wassergehalt der hydratisierten amorphen Carbonate auf unter 1 mol H₂O pro Formeleinheit bestimmt. Gleichzeitig wurde die thermisch induzierte Kristallisation durch differentielle Thermoanalyse (DTA) verfolgt. Zur Aufklärung der

lokalen Struktur der amorphen Carbonate wurden Streuexperimente mit hochenergetischer Synchrotronstrahlung durchgeführt, welche die Berechnung der jeweiligen Paarverteilungsfunktion (PDF) ermöglichten. Auf Grundlage der PDF wurde ein Strukturmodell für amorphes Calciumcarbonat entwickelt.

Der oben beschriebene Ansatz ermöglicht die Stabilisierung amorpher Carbonate, erlaubt jedoch nicht die Untersuchung des Kristallisationsmechanismus. Daher wurde in einem zweiten Projekt eine Synthese für nicht-stabilisierte amorphe Carbonate ausgearbeitet. Durch die Fällung in einem organischen Lösungsmittel und die Verwendung von Cäsiumcarbonat als Präkursor wurden Dispersionen nicht-stabilisierten amorphen Calcium-, Strontium- und Mangancarbonats erhalten. Mit diesen Proben wurden der Kristallisationsmechanismus und der Einfluss von Wasser untersucht. Alle Carbonate zeigen einen Anstieg der Kristallisationsgeschwindigkeit mit steigender Wasserkonzentration, was auf einen Auflösungs-Rekristallisationsmechanismus für die Phasenumwandlung der amorphen Carbonate hindeutet. Dies wurde zudem durch potentiometrische Messungen und Elektronenmikroskopie bestätigt.

Die Hydratisierung der amorphen Intermediate stellt einen grundlegenden Unterschied zu den wasserfreien kristallinen Modifikationen im Carbonat-System dar. Daher wurde in einem dritten Projekt die lokale Wasserumgebung und die Stärke des Wasserstoffbrückennetzwerks mit verschiedenen Kernspinresonanz-Techniken (NMR) und Fourier-Transformations-Infrarotspektroskopie (FTIR) untersucht. Zu diesem Zweck wurde die Synthese für nicht-stabilisierte amorphe Carbonate modifiziert und relativ stabile Pulver amorphen Magnesium-, Calcium-, Strontium- und Bariumcarbonats erhalten. Die Stärke des internen Wasserstoffbrückennetzwerks wird hauptsächlich von der Pearson-Härte des jeweiligen Kations bestimmt. In amorphem Magnesiumcarbonat wurden Hydroxidionen identifiziert, die das Wasserstoffbrückennetzwerk durch ihre ausgeprägte Akzeptorwirkung zusätzlich stärken. Die genaue Untersuchung des strukturellen Wassers in amorphen Carbonate repräsentiert einen Schlüsselaspekt in Bezug auf die vollständige Charakterisierung dieser kurzlebigen Intermediate.

In dem ersten Nebenprojekt wurde die mechanochemische Amorphisierung kristallinen Calciumcarbonats untersucht. Mechanische Behandlung von Calcit in einer Planetenkugelmühle führte bei der Zugabe einer geringen Menge Natriumcarbonat zu einer neuen Form

amorphen Calciumcarbonats, welches als BM-ACC (ball milled amorphous calcium carbonate) bezeichnet wurde. Der Bildungsprozess wurde untersucht, indem Natriumionen mittels ^{23}Na NMR als Sonde für Veränderungen in der lokalen Struktur verwendet wurden. Zur Strukturaufklärung von BM-ACC wurden Streuexperimente durchgeführt. Es zeigte sich, dass die Koordinationszahl des Calciums in dieser Verbindung, verglichen mit kristallinem Calciumcarbonat, erniedrigt ist. Abschließend wurden die Kinetik und der Mechanismus sowohl der thermisch induzierten als auch der wasserinduzierten Kristallisation untersucht. BM-ACC zeigte in beiden Fällen ein Kristallisationsverhalten, welches deutlich von nass-chemisch hergestelltem amorphem Calciumcarbonat abwich.

Inspiziert durch die Fällung amorpher Carbonate in organischen Lösungsmitteln, wurde in einem weiteren Nebenprojekt eine Synthese für Calciumsulfat-Nanopartikel entwickelt. Die tropfenförmigen Partikel (~ 30 nm) waren überwiegend amorph mit kleinen kristallinen Bereichen aus γ -Anhydrit. Die herausragende Eigenschaft dieser Partikel war ihre ungewöhnlich gute Dispergierbarkeit in Aceton, was die Herstellung transparenter Calciumsulfat-Filme ermöglichte. Mittels ^1H NMR und FTIR wurde 2-Propanol auf der Oberfläche der Partikel identifiziert, welches die Dispergierbarkeit in organischen Lösungsmitteln induzierte. Schließlich konnte die Umwandlung der Partikel zu Gips durch Wasserkontakt elektronenmikroskopisch verfolgt werden. Die Kristallisation verlief dabei über Bassanit als Intermediat, welcher sich durch orientierte Anlagerung aus Calciumsulfat-Nanopartikeln bildete.

LIST OF PUBLICATIONS

S. Leukel, M. Panthöfer, M. Mondeshki, W. Schärtl, S. Plana Ruiz, and W. Tremel. Calcium Sulfate Nanoparticles with Unusual Dispersibility in Organic Solvents for Transparent Film Processing. *Langmuir* **2018**, 34, 7096–7105.

S. Leukel and W. Tremel. Water-Controlled Crystallization of CaCO_3 , SrCO_3 , and MnCO_3 from Amorphous Precursors. *Crystal Growth & Design* **2018**, DOI: 10.1021/acs.cgd.8b00627.

S. Leukel, M. Panthöfer, M. Mondeshki, G. Kieslich, Y. Wu, N. Krautwurst, and W. Tremel. Mechanochemical Access to Defect-Stabilized Amorphous Calcium Carbonate. *submitted*

S. Leukel, M. Panthöfer, M. Mondeshki, G. Kieslich, Y. Wu, N. Krautwurst, and W. Tremel. Trapping Amorphous Intermediates of Carbonates – A Combined Total Scattering and NMR Study. *submitted*

S. Leukel, M. Mondeshki, and W. Tremel. Amorphous Alkaline Earth Carbonates are Stabilized by Hydrogen Bonding. *submitted*

M. Dietzsch, **S. Leukel**, G. Kieslich, D. Daisenberger, Y. Wu, M. J. Cliffe, M. Panthöfer, and W. Tremel. High-Magnesian Calcite $\text{Ca}_{1-x}\text{Mg}_x\text{CO}_3$ ($0 \leq x \leq 1$) from Ionic Liquids. *in preparation*

M. Dietzsch, R. Siegel, **S. Leukel**, P. Leidich, K. Fischer, M. Mondeshki, J. Senker, and W. Tremel. Ligand-Protected Amorphous Calcium Carbonate Nanoparticles. *in preparation*

N. Krautwurst, L. Nicoleau, M. Dietzsch, I. Lieberwirth, C. Labbez, A. Fernandez-Martinez, A. van Driessche, B. Barton, **S. Leukel**, and W. Tremel. Two-Step Nucleation Process of Calcium Silicate Hydrate, the Nano-Brick of Cement. *Chemistry of Materials* **2018**, 30, 2895–2904.

ACKNOWLEDGMENTS

First of all, I sincerely thank my supervisor [REDACTED] for giving me the opportunity to work on this interesting project, for his support and input, as well as for many inspiring discussions. Especially, I thank him for granting me the possibility to work freely and self-responsibly.

My sincere thanks goes to my co-supervisor [REDACTED] for the helpful conversations and the great input.

I express my gratitude to the “**Carl Zeiss Foundation**” for the financial support of my doctoral thesis. Furthermore, I thank the **MAINZ Graduate School of Excellence** for enabling me to attend conferences, summer schools, and training courses. Also, my thank goes to the **Gutenberg Academy** for the highly interesting interdisciplinary exchange and for the financial support to cover the printing costs of my thesis.

Throughout my doctoral studies, I had the opportunity to collaborate with several great partners. Many experiments and results would not have been attainable without their help and expertise:

I thank [REDACTED] for countless hours of NMR experiments and the fruitful discussion of the results. My sincere thank goes to [REDACTED] for the refinement of powder X-ray diffractograms, but especially for the complex analysis of the PDF data. I also thank him for proofreading my thesis. The organization and realization of the total scattering experiments was only possible by the generous help of [REDACTED], whom I thank profoundly. I express my gratitude to [REDACTED] for performing light scattering experiments. Also, I thank [REDACTED] for performing and evaluating electron diffraction measurements.

Additionally, I thank [REDACTED] for recording dozens of PXRDs and our TEM crew, especially [REDACTED], who provided many fantastic images for this work. I am grateful to [REDACTED] for access to the FTIR spectrometer and to [REDACTED] for access to the TGA-DTA. In particular, I thank her co-workers [REDACTED] for performing the measurements.

A special thank goes to [REDACTED] for managing all bureaucratic issues. I am grateful for having been part of the biomineralization sub-working group and for all the helpful discussions we had over the last years (in alphabetical order): [REDACTED]
[REDACTED]. Furthermore, I thank the whole [REDACTED] for the friendly working atmosphere and the many times we laughed together. I enjoyed being part of this wonderful group. Moreover, I want to express my gratitude to both my mentors, [REDACTED]
[REDACTED] for the great discussions and counseling. Finally, I am most grateful to my parents [REDACTED], my brother [REDACTED], and my girlfriend [REDACTED] for always being there for me and supporting me. Thank you!

LIST OF CONTENT

ABSTRACT	vii
KURZZUSAMMENFASSUNG	xi
LIST OF PUBLICATIONS	xv
ACKNOWLEDGEMENTS	xvii
LIST OF CONTENT	xix
LIST OF FIGURES	xxi
LIST OF TABLES	xxv
LIST OF ABBREVIATIONS	xxvii
1. THEORETICAL BACKGROUND	1
1.1 LaMer Model	1
1.2 Nucleation	2
1.3 Crystal Growth.....	14
1.4 Mechanochemistry	18
1.5 Calcium Carbonate.....	21
1.6 Calcium Sulfate.....	28
1.7 References.....	31
2. TRAPPING AMORPHOUS CARBONATES	39
2.1 Introduction.....	41
2.2 Results and Discussion	43
2.3 Experimental Section	53
2.4 References.....	55
3. CRYSTALLIZATION MECHANISM OF AMORPHOUS CARBONATES	61
3.1 Introduction.....	63
3.2 Results and Discussion	64
3.3 Experimental Section	74
3.4 References.....	76

4. HYDROGEN BONDING IN AMORPHOUS CARBONATES	81
4.1 Introduction.....	83
4.2 Results and Discussion	85
4.3 Experimental Section.....	96
4.4 References.....	99
5. MECHANOCHEMICAL ACCESS TO AMORPHOUS CALCIUM CARBONATE ..	105
5.1 Introduction.....	107
5.2 Results and Discussion	108
5.3 Experimental Section.....	124
5.4 References.....	127
6. CALCIUM SULFATE NANOPARTICLES WITH UNUSUAL DISPERSIBILITY ..	133
6.1 Introduction.....	135
6.2 Results and Discussion	137
6.3 Experimental Section.....	147
6.4 References.....	150
7. CONCLUSION	155
APPENDIX	I
Supporting Information	I
Curriculum Vitae	XIX

LIST OF FIGURES

Figure 1.1 LaMer Model.....	1
Figure 1.2 Spinodal decomposition.	3
Figure 1.3 Homogeneous nucleation according to the classical nucleation theory.....	5
Figure 1.4 Heterogeneous nucleation.	8
Figure 1.5 Polymorphism of calcium carbonate.....	10
Figure 1.6 Two-step nucleation <i>via</i> a dense liquid.....	11
Figure 1.7 Free enthalpy of two-step nucleation <i>via</i> a dense liquid.	12
Figure 1.8 Crystallization <i>via</i> an amorphous intermediate.....	13
Figure 1.9 Crystal shape through thermodynamic and kinetic control.....	15
Figure 1.10 Crystal growth by the attachment of single building blocks.....	16
Figure 1.11 Non-classical crystal growth.	17
Figure 1.12 High-energy ball milling.	18
Figure 1.13 Defects in crystalline materials.	19
Figure 1.14 Mechanochemical reactions.	20
Figure 1.15 Coordination sphere and unit cell of ikaite.	22
Figure 1.16 Coordination sphere and unit cell of monohydrocalcite.	23
Figure 1.17 Coordination spheres and unit cell of vaterite.....	24
Figure 1.18 Coordination sphere and unit cell of aragonite.	26
Figure 1.19 Coordination sphere and unit cell of calcite.....	27
Figure 1.20 Coordination sphere and unit cell of anhydrite.	29
Figure 1.21 Coordination sphere and unit cell of bassanite.	30
Figure 1.22 Coordination sphere and unit cell of gypsum.	31
Figure 2.1 Reaction scheme of the stabilization of ACC.	43
Figure 2.2 TEM images of amorphous carbonates.....	44
Figure 2.3 TGA-DTA of ACC with oleate.....	45
Figure 2.4 $^{13}\text{C}\{^1\text{H}\}$ CP MAS-NMR and HETCOR of ^{13}C -enriched ACC with oleate.....	47
Figure 2.5 FTIR spectrum of ACC and trends of the vibrational modes	49
Figure 2.6 Structure of amorphous carbonates.....	51
Figure 3.1 PXRD and FTIR spectra of amorphous ASC, ACC, and AMnC.	65
Figure 3.2 Crystallization kinetics of ASC, ACC, and AMnC.....	67

Figure 3.3	TEM snapshots during the crystallization of amorphous carbonates.	68
Figure 3.4	Carbonate concentration with time during crystallization.	70
Figure 4.1	PXRD and TGA of ASC, ACC, and AMC.....	86
Figure 4.2	FTIR spectra and O-H band analysis of amorphous carbonates.....	87
Figure 4.3	$^{13}\text{C}\{^1\text{H}\}$ CP MAS-NMR of amorphous carbonates and build-up curve.....	89
Figure 4.4	^1H NMR and HETCOR spectra of amorphous carbonates.	91
Figure 4.5	^1H chemical shift and T1 relaxation time at different temperatures.	93
Figure 5.1	PXRDs of calcite/ Na_2CO_3 mixtures after ball milling and reaction scheme. ..	109
Figure 5.2	Vibrational spectroscopy of BM-ACC and reactants	110
Figure 5.3	^{13}C and ^{23}Na NMR spectra of BM-ACC and reactants.....	112
Figure 5.4	Formation of BM-ACC.....	114
Figure 5.5	Structure of BM-ACC.....	116
Figure 5.6	Water-induced crystallization of BM-ACC.	118
Figure 5.7	Thermally induced crystallization of BM-ACC.	120
Figure 6.1	TEM and DLS of calcium sulfate nanoparticles.....	137
Figure 6.2	Composition and structure of calcium sulfate nanoparticles.	139
Figure 6.3	Solvent surface binding on calcium sulfate nanoparticles.	141
Figure 6.4	Behavior of the nanoparticles on water contact and film fabrication.	143
Figure 6.5	FTIR study of the crystallization kinetics of calcium sulfate nanoparticles....	144
Figure 6.6	TEM study of the crystallization of calcium sulfate nanoparticles.....	146
Figure S1.	PXRD of amorphous BaCO_3 with oleate.....	II
Figure S2.	Thermal analysis of amorphous carbonates.....	III
Figure S3.	^1H NMR spectrum of ACC with oleate capping.	III
Figure S4.	$^{13}\text{C}\{^1\text{H}\}$ CP MAS-NMR and HETCOR spectra of amorphous carbonates.....	IV
Figure S5.	FTIR spectra of crystalline carbonates.	V
Figure S6.	FTIR spectra of amorphous carbonates.	V
Figure S7.	ACC dispersion in acetonitrile.....	VI
Figure S8.	Exemplary calibration curve of the carbonate concentration.	VI
Figure S9.	Stability of amorphous carbonates with regard to crystallization.	X
Figure S10.	FTIR spectra of hydrated and dried ACC.....	XI
Figure S11.	PXRD and FTIR spectrum of amorphous barium carbonate.....	XI
Figure S12.	FTIR spectra of earth alkali hydroxides.	XII

Figure S13. Characterization of monohydrocalcite.	XII
Figure S14. Determination of the T1 relaxation time by inversion recovery method.	XIII
Figure S15. ¹ H and ¹³ C NMR spectra of BM-ACC.	XIII
Figure S16. Crystallization of BM-ACC in air.	XIV
Figure S17. Three possible sodium coordinations in Na ₂ CO ₃	XIV
Figure S18. Partial PDFs in the structural model of BM-ACC.	XV
Figure S19. Crystallization of BM-ACC in 10 vol% water in acetonitrile.	XV
Figure S20. TEM image of BM-ACC heated to 300 °C for 8 h.	XVI
Figure S21. PXRD with Rietveld refinement of BM-ACC heated to 550 °C for 1h.	XVI
Figure S22. Apparent diffusion coefficient of the calcium sulfate nanoparticles.	XVII
Figure S23. ¹ H NMR spectrum of liquid 2-propanol.	XVII
Figure S24. PXRD of calcium sulfate nanoparticles after water contact.	XVIII

LIST OF TABLES

Table 1.1 Crystallographic data of ikaite.	22
Table 1.2 Crystallographic data of monohydrocalcite.	24
Table 1.3 Crystallographic data of vaterite.	25
Table 1.4 Crystallographic data of aragonite.	26
Table 1.5 Crystallographic data of calcite.	27
Table 1.6 Crystallographic data of anhydrite.	29
Table 1.7 Crystallographic data of bassanite.	30
Table 1.8 Crystallographic data of gypsum.	31
Table 2.1 ¹³ C chemical shift and linewidth of amorphous and crystalline carbonates.	48
Table 2.2 Vibrational modes of amorphous and crystalline carbonates.	50
Table 4.1 Hydrogen bonding in amorphous earth alkali carbonates.	95

LIST OF ABBREVIATIONS

Abbreviation or Symbol	Meaning
a	activity
a_e	equilibrium activity
A	Arrhenius factor
ABC	amorphous barium carbonate
ACC	amorphous calcium carbonate
ACdC	amorphous cadmium carbonate
AMC	amorphous magnesium carbonate
AMnC	amorphous manganese carbonate
ASC	amorphous strontium carbonate
a.u.	arbitrary units
ATR	attenuated total reflectance
BM-ACC	ball milled amorphous calcium carbonate
c	concentration
$c_{crit.}$	critical concentration
c_s	saturation concentration
CN	coordination number
CNT	classical nucleation theory
CP	cross polarization
DLS	dynamic light scattering
DOSY	Diffusion-ordered NMR spectroscopy
DTA	differential thermal analysis
D_s	self-diffusion coefficient
E_a	activation energy
FTIR	Fourier transform infrared spectroscopy
FWHM	full width at half-maximum

g_1	amplitude correlation function
G_2	intensity correlation function
HETCOR	heteronuclear correlation spectroscopy
I	intensity
J	nucleation rate
k	rate constant
k_B	Boltzmann constant
k_{cyrs}	crystallization rate constant
k_{dis}	dissolution rate constant
K	equilibrium constant
K_{sp}	solubility product
MAS	magic angle spinning
NMR	nuclear magnetic resonance
p	pressure
PDF	pair distribution function
PXRD	powder X-ray diffraction
Q	scattering vector
r	radius
$r_{\text{crit.}}$	critical radius
R_H	hydrodynamic radius
rpm	rotations per minute
R_{wp}	weighted-profile R-factor
S	supersaturation
SP	single pulse
SAED	selected area electron diffraction
T	temperature
T1	spin-lattice relaxation time
t_{cp}	cross polarization time
T_{IS}	cross polarization time constant

TEM	transmission electron microscopy
TGA	thermogravimetric analysis
v	volume of a single building block in a crystal
VT	variable temperature
α_{XY}	surface free enthalpy between X and Y
γ	surface tension
ΔG	free enthalpy
$\Delta G_{\text{crit.}}$	nucleation barrier
ΔG_s	surface free enthalpy
ΔG_v	volume free enthalpy
ΔG_v	volume free enthalpy per building block
ΔH	reaction enthalpy
ΔS	reaction entropy
μ	chemical potential
δ	chemical shift
σ	logarithmic supersaturation
ρ	density
τ	correlation time
χ	molar fraction
ω	Larmor frequency

THEORETICAL BACKGROUND

1.1 LAMER MODEL

Crystallization describes the formation of a new solid phase with highly ordered structure from a supersaturated solution, a melt, or a gaseous phase. Classically, this process is divided into two sub-processes: (i) The nucleation of the second phase in the former one-phase system by the generation of a new phase boundary and (ii) the subsequent growth of the second phase to the final crystal.

A general approach, including both nucleation and crystal growth, was developed by V.K. LaMer in 1950 (Figure 1.1).¹ This model describes the concentration of the building blocks of the crystal (atoms, ions, monomers) with time at a constant addition/generation rate. In the original work, this model is based on the disproportionation of $\text{Na}_2\text{S}_2\text{O}_3$ in the presence of HCl to S_8 and HSO_3^- , which results in a constant increase of the sulfur concentration in water, until nucleation and growth of bulk sulfur occur.

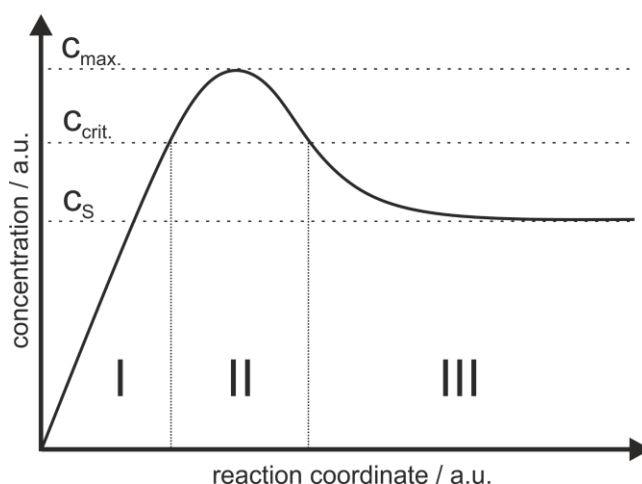


Figure 1.1 LaMer Model. Building block concentration at a constant addition rate over the course of the crystallization. (I) Linear increase of the concentration. (II) The incipient nucleation on reaching $C_{crit.}$ consumes the building blocks. (III) Diffusion-controlled crystal growth. Based on [1].

This model is applicable to a wide variety of systems. In stage I, the monomer concentration increases linearly with constant rate. Even after the saturation concentration c_s is reached, no measurable nucleation occurs and the system becomes supersaturated. In stage II, the critical concentration $c_{crit.}$ for homogeneous nucleation is reached and nucleation occurs. Afterwards, the concentration increases with a lower rate due to the consumption of the building blocks for the generation of nuclei. With stable nuclei present, also crystal growth starts, which consumes further building blocks. At the maximum of the curve, the nucleation and growth rate compensate for the generation of new building blocks. The increasing number of nuclei leads to a faster consumption of the building blocks and the concentration drops under the critical concentration again; the generation of new nuclei stops. The final stage III is dominated by diffusion-controlled growth of the nuclei to larger crystals. As every newly generated building block is consumed by the growing crystals, the concentration approaches the saturation concentration c_s .

1.2 NUCLEATION

Nucleation describes the formation of a new phase boundary in a parent phase. This process is classified as a first order transition according to Ehrenfest,² as it exhibits a discontinuity in the first derivative of the free energy at the transition. In a one-component system, the nucleation event generates a phase boundary, resulting in a heterogeneous system with two separate phases. Thermodynamically, nucleation can only occur, if the free enthalpy of the resulting two-phase system ΔG_2 is lower than the one of the one-phase system ΔG_1 .

$$\Delta G_2 < \Delta G_1 \quad (1.1)$$

Different theories and models were established to describe the nucleation process, which will be discussed in the following sections.

Spinodal Decomposition

Spinodal decomposition is a nucleation pathway that is accessible especially at high supersaturation. Emerging from a homogeneous solution, a barrier-free demixing process into two phases takes place.³ Thereby, one phase, rich in the formerly dissolved component, and a depleted second phase form.⁴ The transition exhibits no distinct nucleation event, but

is a global process in the whole reaction volume.⁵ Such a pathway was proposed for the nucleation of calcium carbonate by Faatz et al.⁶ In 2013, Wallace et al. predicted a possible liquid-liquid phase separation in the $\text{CaCO}_3\text{-H}_2\text{O}$ system by molecular dynamics simulations.⁷

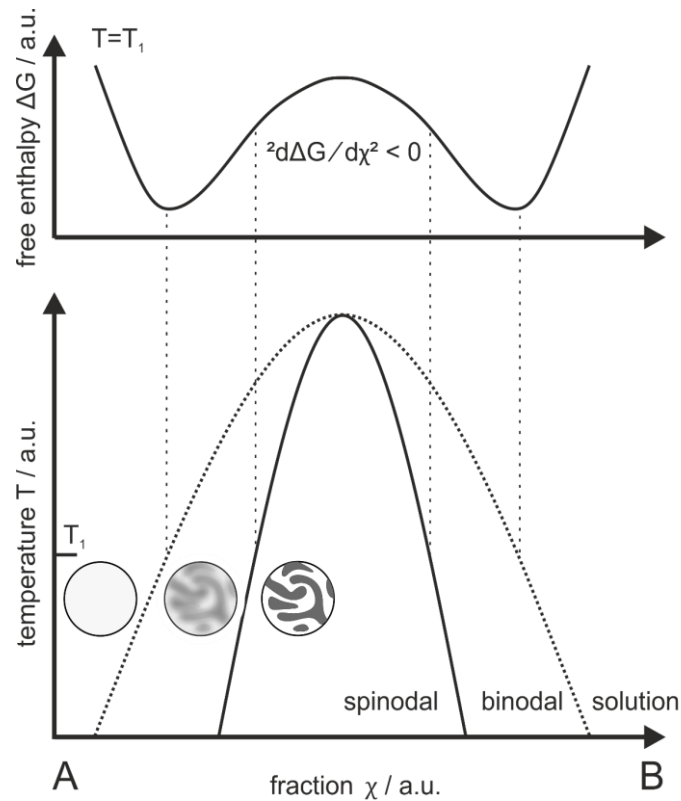


Figure 1.2 Spinodal decomposition. Bottom image: Phase diagram of two partly miscible components, A and B. Outside the binodal, A and B form a stable homogeneous solution. Within the binodal, the system is meta-stable with respect to small fluctuations. Within the spinodal, the system is unstable and spontaneous demixing occurs. Top image: Free enthalpy ΔG of the system at given temperature T . Minima determine the position of the binodal, turning points determine the position of the spinodal. Based on [4].

Figure 1.2 displays the phase diagram of a system with two components, A and B. They exhibit a miscibility gap, confined by the binodal (dotted line). As mixing is favorable from an entropic point of view, the miscibility gap gets smaller with rising temperature due to $\Delta G_{\text{mix}} = \Delta H_{\text{mix}} - T \cdot \Delta S_{\text{mix}}$. Outside the miscibility gap, a homogeneous stable mixture exists. The binodal is calculated by the minima of the free enthalpy ΔG at every temperature T (Figure 1.2, top image).

$$\left(\frac{\delta\Delta G}{\delta\chi}\right) = 0 \quad (1.2)$$

Within in the binodal regime, demixing is thermodynamically favored. The system is meta-stable with regard to small fluctuations though. By random collision of many molecules, a local phase separation can take place in the solution, comparable to a classical nucleation event (*vide infra*). The diffusion in the solution is defined by Fick's law:

$$J = -D \left(\frac{\delta c}{\delta x}\right)_{p,T} \quad (1.3)$$

The particle flux J per area and time is associated with the concentration gradient over the diffusion constant D of the respective species. The flux is directed downhill the gradient of c (minus), which results in a homogeneous distribution of the molecules in solution. Thermodynamically, the flux within the solution is driven by a gradient in the chemical potential μ . A modified Fick's law is formulated, which depends *via* the constant K on μ and the molar fraction χ .

$$J = -K \left(\frac{\delta\mu}{\delta\chi}\right)_{p,T} \quad (1.4)$$

Comparing eq. 1.3 with eq. 1.4 gives a relation between the gradients in concentration and the chemical potential:

$$\left(\frac{\delta\mu}{\delta\chi}\right)_{p,T} \propto \left(\frac{\delta c}{\delta x}\right)_{p,T} \quad (1.5)$$

Within the binodal and the miscible regime, the free enthalpy curve ΔG is concave (Figure 1.2, top image) and $\left(\frac{\delta\mu}{\delta\chi}\right)_{p,T}$ is positive.

$$\left(\frac{\delta^2\Delta G}{\delta\chi^2}\right)_{p,T} = \left(\frac{\delta\mu}{\delta\chi}\right)_{p,T} > 0 \quad (1.6)$$

Due to eq. 1.5, the diffusion is directed downhill the concentration gradient and a homogeneous solution is favored, even in the binodal regime. However, in the spinodal regime, the free enthalpy curve ΔG is convex and $\left(\frac{\delta\mu}{\delta\chi}\right)_{p,T}$ becomes negative (Figure 1.2, top image).

$$\left(\frac{\delta^2\Delta G}{\delta\chi^2}\right)_{p,T} = \left(\frac{\delta\mu}{\delta\chi}\right)_{p,T} < 0 \quad (1.7)$$

According to eq. 1.5, this leads to an inversion of the diffusion direction and molecules flow to regions of already high concentration. So, in the spinodal regime, microscopic fluctuations of the concentration cause a flux along the concentration gradient and result finally in the phase separation of the solution.

Classical Nucleation Theory

The classical nucleation theory (CNT) describes the homogeneous nucleation of a spherical particle based on thermodynamic considerations. The energetics of the nucleation are primarily dominated by two terms, the surface free enthalpy ΔG_s and the volume free enthalpy ΔG_v . The surface term ΔG_s increases the free enthalpy of the system, as a new surface has to be generated between the nucleus and the liquid. The surface free enthalpy is proportional to r^2 of the spherical nucleus. The overall attractive interaction of the building blocks within the nucleus releases energy, which is proportional to the volume ($\propto r^3$).

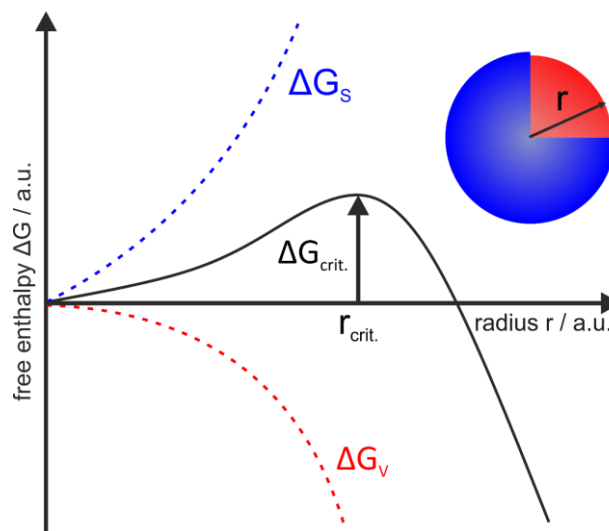


Figure 1.3 Homogeneous nucleation according to the classical nucleation theory. Free enthalpy of the nucleus is defined by the surface enthalpy ΔG_s ($\propto r^2$) and the volume enthalpy ΔG_v ($\propto r^3$). At the critical radius r_{crit} , the nucleus becomes stable, as every further addition of a building block – increasing r – leads to a decrease of ΔG .

$$\Delta G = \Delta G_S + \Delta G_V \quad (1.8)$$

$$\Delta G = 4\pi r^2 \cdot \gamma + \frac{4\pi r^3}{3 \cdot v} \cdot \Delta G_V \quad (1.9)$$

The surface tension between the nucleus and the liquid is given by γ . The free enthalpy for the incorporation of one building block with the volume v in the nucleus is represented by ΔG_V ; it is negative by definition. Therefore, the stability of the nucleus is defined by its ratio of surface to volume, *ergo* its size. The surface tension represents an energy barrier that hinders small nuclei to form. It can only be overcome by the collision of enough building blocks to form a nucleus, whose volume free enthalpy exceeds the surface term. The critical radius $r_{\text{crit.}}$ of such a nucleus can be determined by deviation of eq. 1.9.

$$\frac{\partial \Delta G}{\partial r} = 8\pi r \cdot \gamma + \frac{4\pi r^2}{v} \cdot \Delta G_V = 0 \quad (1.10)$$

$$r_{\text{crit.}} = \frac{-2\gamma \cdot v}{\Delta G_V} \quad (1.11)$$

Substituting $r_{\text{crit.}}$ in eq. 1.9 gives an expression for the nucleation barrier $\Delta G_{\text{crit.}}$:

$$\Delta G_{\text{crit.}} = \frac{16\mu \cdot \gamma^3 \cdot v^2}{3 \cdot \Delta G_V^2} = \frac{4}{3} \pi \cdot \gamma \cdot r_{\text{crit.}}^2 \quad (1.12)$$

A characteristic parameter to describe crystallization processes is the supersaturation S . It is defined as the ratio between the activity a of building blocks in the liquid and the activity in equilibrium a_e . Often, the natural logarithm σ of the supersaturation is deployed.

$$S = \frac{a}{a_e} \quad (1.13)$$

$$\sigma = \ln(S) \quad (1.14)$$

The supersaturation S can be linked to the chemical potential μ . Therefore, the chemical potentials of the solution in equilibrium with the solid after nucleation and at a different activity prior to nucleation are calculated. The chemical potential and the activity of an arbitrary reference state are marked with an asterisk; T is the temperature and k_B is the Boltzmann constant.

$$\mu = \mu^* + k_B T \cdot \ln\left(\frac{a}{a^*}\right) \quad (1.15)$$

$$\mu_e = \mu^* + k_B T \cdot \ln\left(\frac{a_e}{a^*}\right) \quad (1.16)$$

$$\Delta\mu = \mu_e - \mu = k_B T \cdot \ln\left(\frac{a_e}{a}\right) = -k_B T \cdot \ln(S) = -k_B T \cdot \sigma \quad (1.17)$$

If the supersaturation S is higher than 1, $\ln(S)$ becomes positive and the difference in the chemical potentials between building blocks in the solid and the solution is negative. So, the supersaturation is the thermodynamic driving force for the transition of the building blocks from the solution into the crystal. At a supersaturation of $S = 1$, the system is in equilibrium and $\Delta\mu = 0$. As $\Delta\mu$ for this process is equal to the free enthalpy change for the inclusion of a building block in the solid, which was defined prior as ΔG_v , the combination of eq. 1.11 and eq. 1.17 gives an expression for the critical radius, which depends on the logarithmic supersaturation σ .

$$r_{\text{crit.}} = \frac{2\gamma \cdot v}{k_B T \cdot \sigma} \quad (1.18)$$

Substituting eq. 1.18 in eq. 1.12 yields the following expression for the nucleation barrier:

$$\Delta G_{\text{crit.}} = \frac{16\pi \cdot \gamma^3 \cdot v^2}{3 \cdot (k_B T \cdot \sigma)^2} \quad (1.19)$$

The nucleation barrier depends on the cube of the surface tension γ and reciprocally on the square of the temperature and the square of the logarithmic supersaturation. Hence, higher temperatures and supersaturations are an effective way to induce nucleation. The kinetics of the nucleation can be approximated with an Arrhenius approach.⁸

$$J = A \cdot \exp\left(\frac{-\Delta G_{\text{crit.}}}{k_B T}\right) \quad (1.20)$$

The experimental nucleation rates often deviate by magnitudes from the predicted values.^{9,10} The CNT gives a relatively simple image for the nucleation, only considering surface and volume energy of the nucleus and assuming continuous thermodynamics in nano-sized systems. A lot of assumptions and simplifications cause the inability of the CNT to predict nucleation quantitatively in most cases. The values of the surface tension are assumed to be constant, whereas on a microscopic scale, the curvature of the surface depends strongly on the size of the particle. Even if a spherical nucleus is a reasonable approach due to the favorable volume surface ratio, different shaped nuclei have been observed.¹¹ Finally, the influence of the solvent is completely neglected. However, the gain in entropy by the release of solvent molecules on the incorporation of the building blocks in the solid is an important driving force for crystallization.^{12,13}

Heterogeneous Nucleation

Heterogeneous nucleation takes place on surfaces and interfaces, e.g. templates, vessel walls, solution air interface, or impurities.

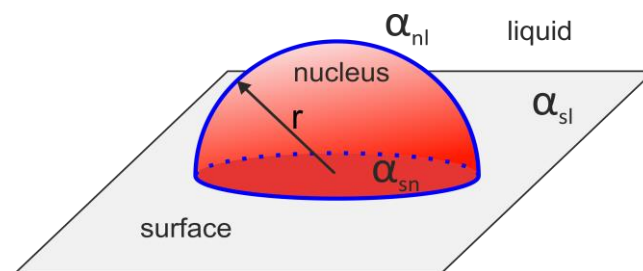


Figure 1.4 Heterogeneous nucleation. The total surface enthalpy of the system is decreased due to a favorable interaction between the nucleus and a surface. The respective surface enthalpies between surface (s), nucleus (n), and liquid (l) are referred to as α .

For heterogeneous nucleation, the same approach is possible as for the CNT.¹⁴ But, all the different surface interactions α in the system are taken into account (Figure 1.4). For a hemisphere on a flat surface, the change in the free enthalpy can be written as:

$$\Delta G_H = \frac{1}{2} \left(\frac{4\pi r^3}{3 \cdot v} \cdot \Delta G_v \right) + \frac{1}{2} (4\pi r^2 \cdot \alpha_{nl}) + \pi r^2 \cdot \alpha_{sn} - \pi r^2 \cdot \alpha_{sl} \quad (1.21)$$

The volume term is bisected, compared to homogeneous case of the CNT, as only a hemisphere is considered. For the same reason, the surface term between nucleus and liquid (α_{nl}) is multiplied by the factor $\frac{1}{2}$. Additionally, the new interface between surface and nucleus (α_{sn}) has to be taken into account, as well as the loss of the liquid surface interaction (α_{sl}) in that specific area. As α_{nl} is identical with the surface tension γ in the case of homogeneous nucleation, equation 1.21 is transformed to:

$$\Delta G_H = \frac{2\pi r^3}{3 \cdot v} \cdot \Delta G_v + \pi r^2 \cdot (2\gamma + \alpha_{sn} - \alpha_{sl}) \quad (1.22)$$

Analogously to the homogeneous case, the critical radius can be calculated for the heterogeneous nucleation.

$$r_{\text{crit,H}} = \frac{-2\gamma \cdot v}{\Delta G_v} \cdot \left(1 - \frac{\alpha_{sl} - \alpha_{sn}}{2\gamma} \right) \quad (1.23)$$

So, the critical radius – and consequently the nucleation barrier – is reduced in the heterogeneous case, if the interaction of the surface with the nucleus is energetically favored over the one with the liquid ($\alpha_{sl} > \alpha_{sn}$). Hence, to promote heterogeneous nucleation, a favorable interaction of the surface with the nucleus is necessary. This can be achieved by attraction through opposing surface charges,¹⁵ a lattice match, e.g. for heterodimer nanoparticle synthesis,¹⁶ or complexation of ions *via* functional groups, e.g. in biominerals.¹⁷ Consequently, the heterogeneous nucleation can also be suppressed by increasing the interfacial energy, e.g. silylation of glassware on nucleation from aqueous media. In an experimental setup, usually both homogeneous and heterogeneous nucleation take place. The separation of both processes is hardly possible. However, a specific nucleation pathway can be promoted by the choice the experimental conditions. As the nucleation barrier is usually lower for heterogeneous nucleation, this pathway is preferred at low supersaturations, where the homogeneous nucleation rate is slow. At high supersaturation, the nucleation barrier for homogeneous nucleation can be overcome easily. Due to the finite number of heterogeneous nucleation sites, homogeneous nucleation becomes the preferred pathway then.

Ostwald-Volmer Rule of Stages

Solid compounds of the same composition can appear in different crystal structures; this phenomenon is known as polymorphism. Only one modification represents the thermodynamic stable phase of the system at a given state, while the other modifications are metastable and transform on varying timescales to the thermodynamic end product. Usually, the thermodynamic stable modification exhibits the highest density, as it realizes the most attractive interactions and the closest packing. The metastable modifications are less dense; they can also be amorphous. The solubility of the respective modifications decreases with increasing stability. Hence, the thermodynamic stable phase is the least soluble one (compare eq. 1.15). In Figure 1.5, the polymorphism of the calcium carbonate system is displayed.

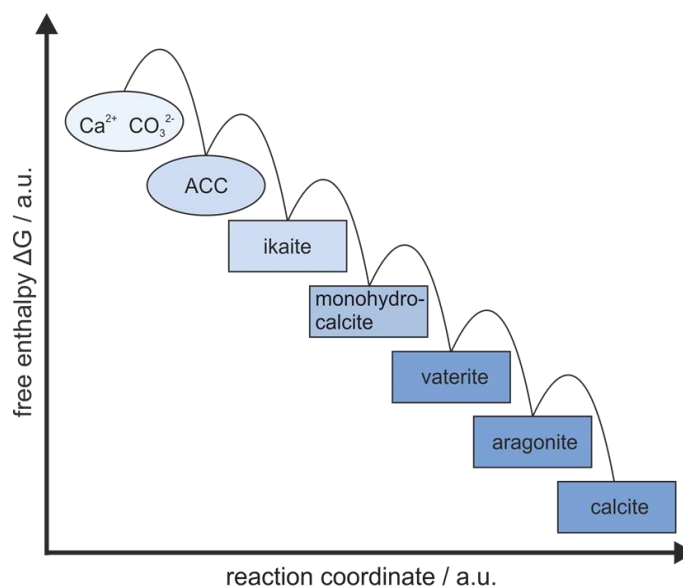


Figure 1.5 Polymorphism of calcium carbonate. The modifications are sorted with regard to the decreasing free enthalpy. Amorphous calcium carbonate (ACC) is the least stable modification. Ikaite and monohydrocalcite are metastable crystalline hydrates. Vaterite is an anhydrous metastable modification. Aragonite represents the high-pressure phase of calcium carbonate. Calcite is the thermodynamically stable phase at ambient conditions.

The Ostwald-Volmer rule claims that the least dense and most soluble phase nucleates first at sufficient supersaturation and cascades successively through the metastable phases to the thermodynamic product.¹⁸ In the calcium carbonate system, usually ACC forms immediately and transforms to vaterite and finally to aragonite and calcite.¹⁹ Ikaite and monohydrocalcite are not observed. This example illustrates that the Ostwald-Volmer rule is a good concept to understand complex crystallization processes, but no strict law. The faster formation of the metastable intermediates can be explained by the CNT. According to eq. 1.20, the nucleation

rate depends on the ratio of surface tension to supersaturation (γ^3/σ^2). The nucleation rate increases with a decreasing value for this ratio. As the thermodynamic stable modification generally exhibits the highest density, the amount of unsaturated bonds on the surface should be increased accordingly. This results in a higher surface enthalpy and consequently a higher nucleation barrier. Since the supersaturation σ is lower for all metastable phases, their lower surface tension has to overcompensate this effect to reach a higher nucleation rate.

Two-step Nucleation

In a two-step nucleation pathway, the nucleation event is divided into two separate processes: (i) the concentration of the building blocks in dense liquid droplets and (ii) the subsequent formation of a crystalline phase in this dense liquid (Figure 1.6, top image).²⁰ CNT suffers from the assumption that solute building blocks exchange directly with an ordered nucleus. This implies that two parameters change abruptly on the face boundary of the nucleus: the concentration of the building blocks, which is significantly higher in the nucleus, and the order parameter, as the nucleus has an ordered crystal structure, whereas the solvated building blocks are randomly distributed.

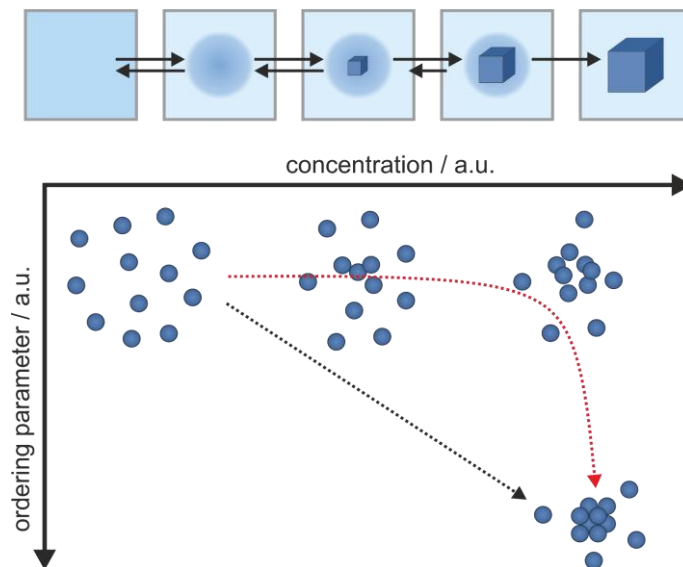


Figure 1.6 Two-step nucleation via a dense liquid. Top image: Dense liquid droplets form from solution. Within the droplets, the crystal nucleates. Bottom image: Phase transition from solution to a crystal is a propagation along the concentration and an ordering parameter. In the case of two-step nucleation, first, the concentration of the building blocks is increased in a dense droplet and, subsequently, it orders to a crystal (red line). In the CNT, concentration and ordering parameter change simultaneously (black line). Based on [21].

So, the nucleation is to be seen as progression along the concentration and the order parameter. It is argued that the simultaneous change of both parameters is unlikely and that a local densification of the solvated building blocks and a subsequent ordering is a more favorable pathway (Figure 1.6, bottom image). The ordering process is assumed to proceed by small fluctuations in the dense liquid, where pairs of the building blocks are formed with the identical orientation as in the crystal. These pre-oriented pairs agglomerate to form the nucleus.

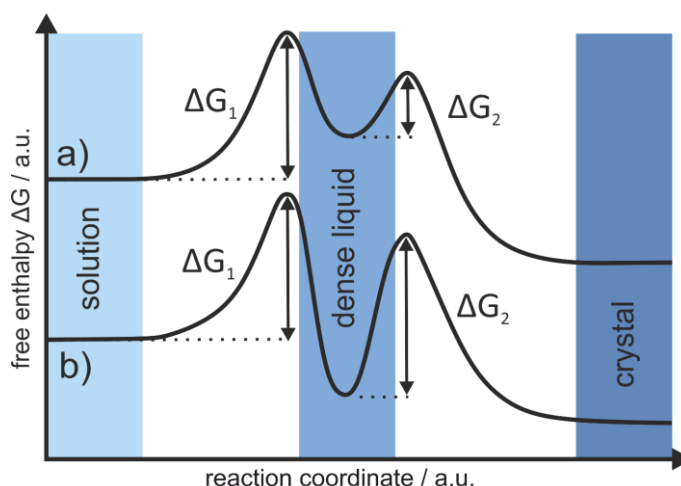


Figure 1.7 Free enthalpy of two-step nucleation *via* a dense liquid. Two nucleation barriers occur respectively for formation of the dense liquid droplet and for its crystallization. The dense liquid can be metastable (a) or stable (b) with regard to the solution. Based on [21].

As a result, two energy barriers have to be overcome stepwise, which each should be lower than the single one in the CNT though. The intermediate dense liquid phase can be stable or metastable with regard to the building blocks in solution. For proteins, e.g. lysozymes, the formation of macroscopic droplets with subsequent crystallization is a common mechanism.^{22,23} But, also small organic molecules form liquid-like clusters as intermediary phase.²⁴ For biominerals, like calcium carbonate, many examples are known, where proteins²⁵ or polymers^{26,27} can stabilize dense liquid phases. These so-called PILPs (Polymer Induced Liquid Precursors) present highly interesting systems to study the complex morphology design in biominerals.

Amorphous Intermediates

The formation of amorphous intermediates prior to the final crystal is observed in various systems, like calcium phosphate,²⁸ iron oxide,²⁹ or clathrates.³⁰ Especially amorphous calcium carbonate (ACC) is of high interest, as it seems to play a key role in the formation of biominerals.³¹ Even though the nucleus is usually considered crystalline, the occurrence of an amorphous phase is not excluded by the CNT. The Ostwald-Volmer rule allows the precipitation of metastable amorphous phases at a sufficient supersaturation. For the nucleation rate of an amorphous phase to be dominant, the surface tension of this phase has to be small according to the CNT. In the case of ACC, this is a reasonable assumption, as the amorphous phase is less dense and hydrated, which should cause a favorable interaction with the surrounding solvent phase and therefore a lower nucleation barrier. The energetics of this pathway are comparable to the two-step nucleation with a dense liquid as intermediate. The morphology and the internal structure of the amorphous phase resembles a liquid. It is reasonable to assume a lower mobility in the amorphous structure than in the liquid, which hinders a direct rearrangement of the ions to a crystalline structure at ambient conditions.

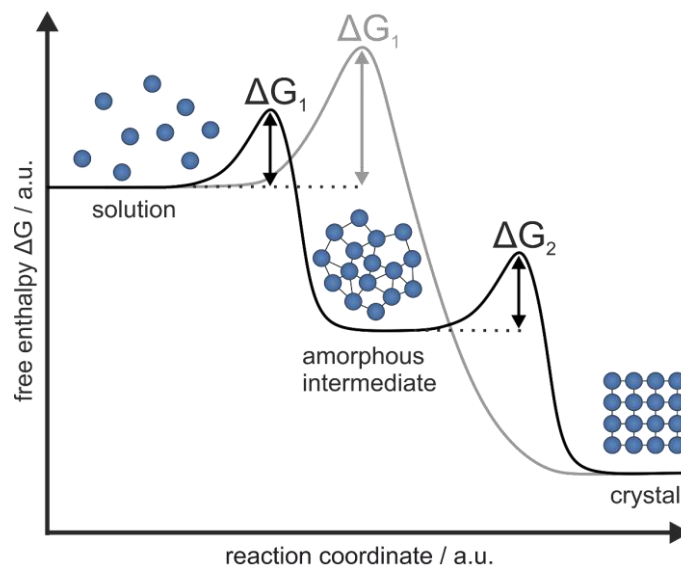


Figure 1.8 Crystallization *via* an amorphous intermediate. From the supersaturated solution, a metastable amorphous phase nucleates, which subsequently transforms to the thermodynamic stable crystal. This pathway exhibits two smaller barriers, in contrast to one high barrier in the CNT (gray line).

A more plausible mechanism is the dissolution of the amorphous phase followed by the recrystallization to crystalline modifications. This is also in accordance with the CNT and Ostwald-Volmer rule: As the supersaturation is drastically decreased by the precipitation of

the amorphous phase, the system is closer to an equilibrium state and the thermodynamic product forms now due to the lower concentration of building blocks in solution. As solvated building blocks are consumed for the formation of the crystalline phase, the amorphous phase dissolves with time.

By the formation of an amorphous intermediate, the high nucleation barrier for the direct formation of a crystalline phase is split up into two smaller barriers for the formation of the amorphous phase and its subsequent crystallization. In general, a high supersaturation is an effective way to promote the formation of an amorphous intermediate, as it is kinetically favored over the thermodynamic crystalline product.

1.3 CRYSTAL GROWTH

After the nucleus has formed, the crystal starts growing until the concentration of the building blocks in solution drops under the critical concentration, which is given by the solubility product of the crystalline phase.

Classical Crystal Growth

In the classical image, the crystal grows layer-wise by the attachment of single building blocks from solution. Analogously to the nucleation event, supersaturation is essential for this process. At low supersaturation, the growth is mainly thermodynamically controlled, whereas kinetics play the dominant role at high supersaturation.

When the growth is thermodynamically controlled, the system strives for a minimization of the surface energy. The morphology with the lowest surface energy is exhibited by the crystal. If the surface energy for every possible surface is known, the thermodynamic equilibrium shape can be derived by the Wulff construction (Figure 1.9), which gives the crystal shape with the minimum surface energy.³² Usually, crystal planes with zero net charge are expressed.

Often, the actual morphology of a crystal strongly deviates from the equilibrium morphology, predicted by the Wulff construction. Due to a high supersaturation, the crystal growth is controlled mainly by kinetics. Thus, the growth rates of the respective crystal facets determine the morphology rather than their surface energy. The slowest growing crystal facets will mainly terminate the crystal. This growth mechanism provides a way to influence

the final morphology of a crystal. As additives bind to the specific facets with deviating binding constants, these facets can be blocked and the growth rate decreases in this direction. Consequently, the final crystal will mainly exhibit the facets blocked by the additive. For this reason, small impurities or the change of the solvent can have severe influence on the crystal morphology.

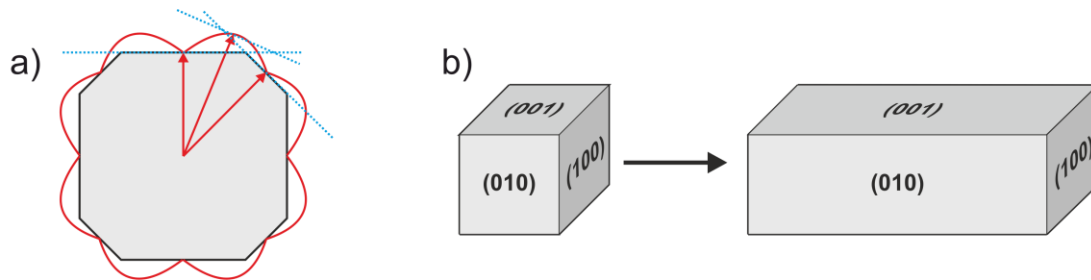


Figure 1.9 Crystal shape. a) The Wulff construction gives the thermodynamic equilibrium shape of a crystal by minimization of the surface enthalpy. The red line is the orientation-dependent surface enthalpy. In every direction, the intersection of a line emerging from the center of the crystal with the surface energy is determined (red arrow). The perpendicular blue line at the intersection is the respective lattice plane. The inner lattice planes are lowest in energy and define the final crystal morphology. b) A crystal that grows kinetically controlled will be terminated mainly by the slowest growing facets (001) and (010), while the fast growing facet (100) outgrows.

The classical crystal growth proceeds by the attachment of single building blocks to the crystal. As the surface of the growing crystal is not completely flat and uniform, preferred positions for the attachment of the next building block exist (Figure 1.10). The adhesion of a single building block on a flat surface is a kinetically favored process, as this area is large and easily accessible. However, the flat surface position is energetically unfavored, as a bond can only be formed in one direction. Therefore, the building block will diffuse on the surface until it reaches a step or kink, where more bonds can be formed to neighboring building blocks. Then, it is integrated into the crystal lattice. This leads to the formation of terraces; their growth front proceeds over the crystal surface to form a new layer. At higher supersaturation, islands can form on the crystal surface, which is also referred to as 2D nucleation. The critical size for such an island can be calculated analogously to the CNT for heterogeneous nucleation.³³

On a microscopic scale, the growth of a crystal can be divided into several steps. First, the building block has to diffuse to a surface on the crystal, where it attaches to. To minimize the surface energy and to form more bonds, it diffuses on the surface to a kink or step. In order to form a bond to the crystal, the building block has to lose its solvation layer. Finally,

it is incorporated into the crystal. Since the desolvation is the only process which requires the splitting of bonds, it is presumably the rate-determining step. Therefore, changes in the pH, ionic strength, or even a complete exchange of the solvent can have drastic effects on the growth kinetics.

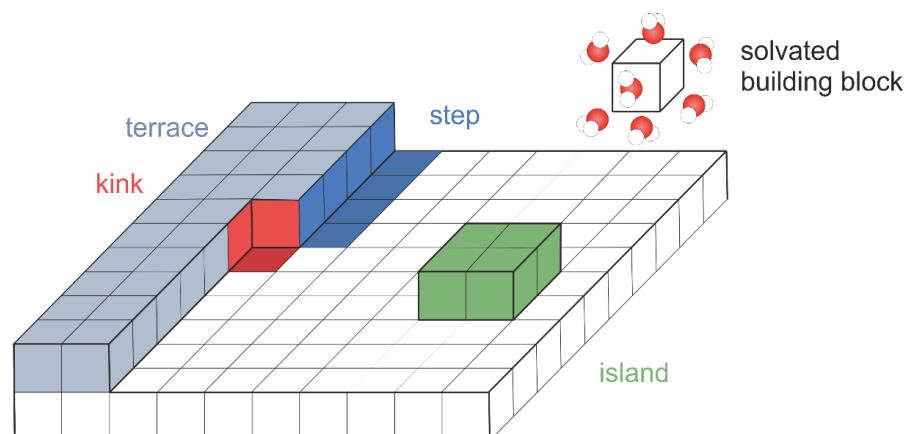


Figure 1.10 Crystal growth by the attachment of single building blocks. After adsorption on the surface, the building block diffuses to a step edge or a kink, where it is incorporated into the crystal. These positions are energetically favored, as the relative increase in surface energy is minimized and a greater number of bonds to neighboring building blocks is exhibited. This leads to the formation of terraces and a layer-wise growth of the crystal. At high supersaturations, also island growth on flat surfaces is observed.

Even if the concentration of the building blocks drops under the supersaturation and the actual crystal growth has stopped, another process can still change the size of the crystals. Larger crystals grow further on the expense of smaller crystals, which dissolve over time. This phenomenon is referred to as Ostwald ripening.¹⁸ Due to the higher surface enthalpy and the energetically unfavorable ratio of surface atoms to bulk atoms, small crystals dissolve and the building blocks are attached to larger, more stable particles. Ostwald ripening usually occurs, if the crystals have a sufficiently high solubility.

Non-classical Crystal Growth

While classical crystal growth proceeds by the attachment of single ions/atoms/molecules to the growing crystal, in the case of non-classical growth, primary nanoparticles are formed from these building blocks, which subsequently arrange themselves.^{34,35} This mechanism is preferred at high supersaturation, where many nanoparticulate seeds form, and in the presence of additives, which stabilize these primary nanoparticles. The crystal grows by the oriented attachment of the nanoparticles to minimize the surface energy. This presents an alternative

process to the Oswald ripening in order to decrease the total energy of the system. The attachment of the nanoparticles is favored, if their solubility is comparably low. If the nanoparticles are crystalline and align along a certain crystallographic axis, the formed superstructure is referred to as mesocrystal. Due to the alignment of the subunits, the mesocrystal shows a diffraction pattern comparable to a single crystal and can only be identified by electron microscopy. Still, the numerous interfaces of the nanoparticles in a mesocrystal cause a high surface energy, which makes the mesocrystals metastable with regard to fusion.

Non-classical growth allows potentially a wide series of non-equilibrium morphologies that cannot be explained by classical layer-by-layer growth. Therefore, this process is believed to be crucial in the formation of biominerals, where mesocrystalline structure with organic or amorphous matrices are found.^{36,37}

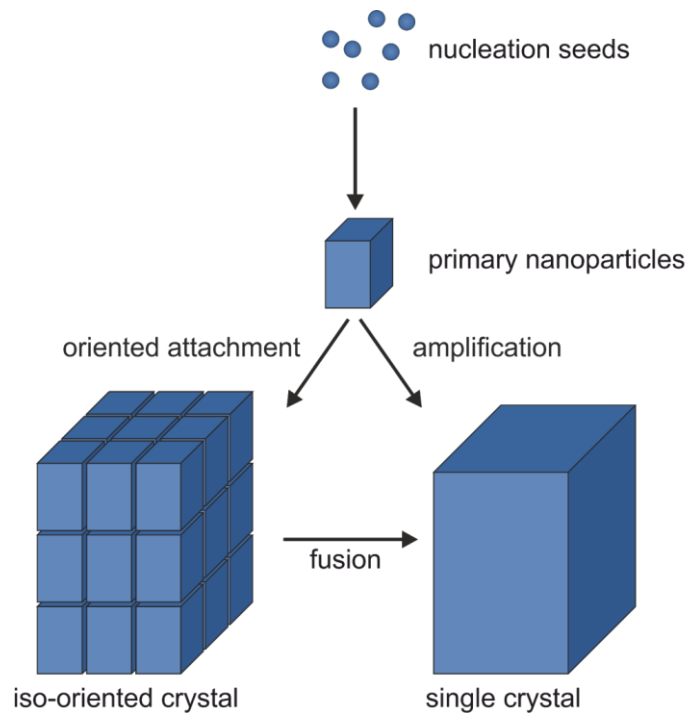


Figure 1.11 Non-classical crystal growth. Nuclei form primary nanoparticles that agglomerate along a special crystallographic axis to form an iso-oriented crystal (mesocrystal). By fusion of the respective building blocks, a single crystal forms. Based on [35].

1.4 MECHANOCHEMISTRY

Since the amorphous state of a system has a higher free enthalpy than the crystalline one, the amorphization of a crystalline material can only proceed by the external supply of energy. The amorphization requires the breaking of bonds and the dislocation of atoms in the crystal lattice until the long-range order breaks down. This degradation of the crystalline material can be achieved in a planetary ball mill (Figure 1.12a). Initially, the material is placed in a jar – eventually, a dispersion medium is needed – and grinding balls are added. Usually, these balls consist of a material with great hardness, like zirconium oxide or tungsten carbide. The jar rotates on a plate and additionally around its own axis at high speed and the material is ground by the collision with the grinding balls and the wall. In industrial processes, ball mills are used in larger scales to grind materials to fine powders. With laboratory ball mills, which operate with high rotational speed of several 100 rpm, the production of nanoparticles,³⁸ alloying of metals³⁹ and amorphization is feasible.^{40,41}

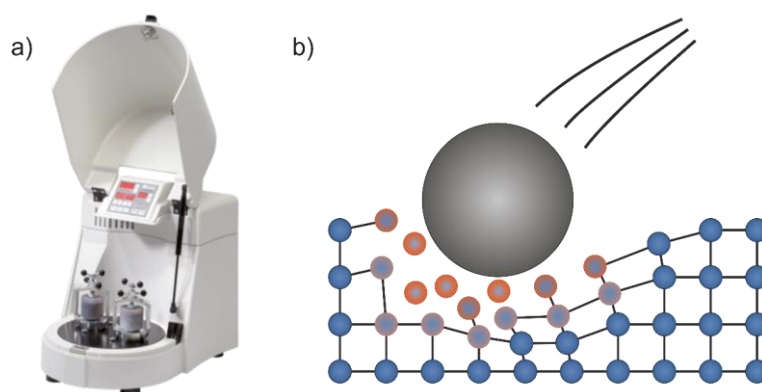


Figure 1.12 High-energy ball milling. a) Planetary ball mill deployed in this work (Pulverisette 7, Fritsch).⁴² b) Magma plasma model: By the impact of the grinding balls on the material, high-energy plasma-like states are generated in a locally confined area. The sudden increase in pressure and temperature enables mechanochemical reactions.⁴³

The mechanical energy is transferred to the material by the impact of the grinding balls (Figure 1.12b) and by the collision with the jar walls and other grains. A qualitative model for this process was developed by Thiessen et al. in 1967, the so-called magma plasma model.⁴³ The impact on the particle creates a highly excited plasma-like state with a lifetime of less than 10^{-7} s. In a small locally confined area, pressure and temperature increase by magnitudes. Simulations predict temperatures of 10000 K and pressure of several GPa.⁴⁴ This highly excited state relaxes *via* different channels, which include the emission of

photons, the dispersion of heat, and the plastic deformation of the material. Some of these plastic deformations are metastable over a longer time. So, the impact energy is stored in the material in form of defects; this phenomenon is referred to as mechanical activation. The mechanochemical treatment of a material brings a material in a high-energy non-equilibrium state by the induction of defects and strain.⁴⁵

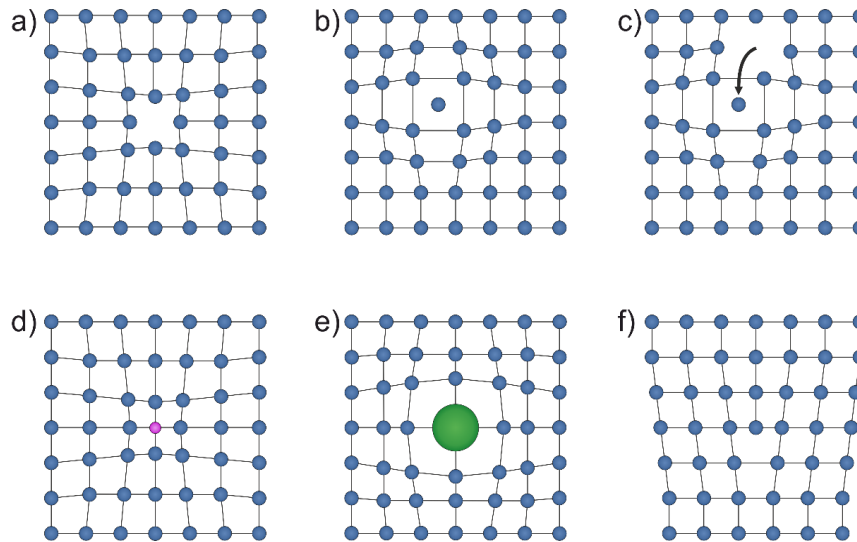


Figure 1.13 Defects in crystalline materials: a) vacancy, b) interstitial atom, c) Frenkel defect, d) small substitutional atom, e) large substitutional atom, and f) edge dislocation.

Figure 1.13 displays different kinds of defects that can be found in a crystalline system: An unoccupied lattice position is referred to as vacancy (a). Surplus atoms can be found in voids as interstitial atoms (b). Often, the combination of the two former defects occurs, where an atom leaves its position in the lattice for an interstitial spot. This so-called Frenkel defect usually is found in Pearson soft systems with small cations (c). In addition, atoms can be replaced by foreign atoms, which induces strain due to the deviating radii (d,e). As these defects only occur on one distinct position in the lattice, they are referred to as point defects. Moreover, defects also exist in higher dimensions, like screw dislocations, stacking faults, and edge dislocation (f). Already in thermodynamic equilibrium, defects exist in every crystalline material above 0 K due to the gain in entropy. The mechanochemical treatment of a material increases the number of defects significantly and prepares the system in a metastable non-equilibrium state. After sufficient milling time, when the particle size cannot decrease anymore and further energy is supplied still, the accumulation of defects and the deformation of the crystal lead to the collapse of long-range order; the materials gets

amorphous. This behavior is found in broad variety of substances ranging from pure elements, like silicon⁴⁶ and germanium,⁴⁷ over inorganic⁴⁸ and organic materials⁴⁹ to organometallic compounds.^{50,51}

Mechanochemical reactions often follow specific kinetics that is divided into three regimes (Figure 1.14a):⁵² Initially, the material is broken down to smaller particles. The so-called Rittinger law is valid:⁵³ The generated surface area increases linearly with the imparted energy, which is mainly transformed to surface energy of the material. In the second regime, new surface area is produced at a lower rate, as structural changes inside the material start to appear, e.g. the defect concentration rises. In the final regime, the surface area decreases, as the particles agglomerate to minimize their surface energy. This phenomenon is considered the equilibrium state of milling.⁴¹ In this state, the amorphization of the material occurs.

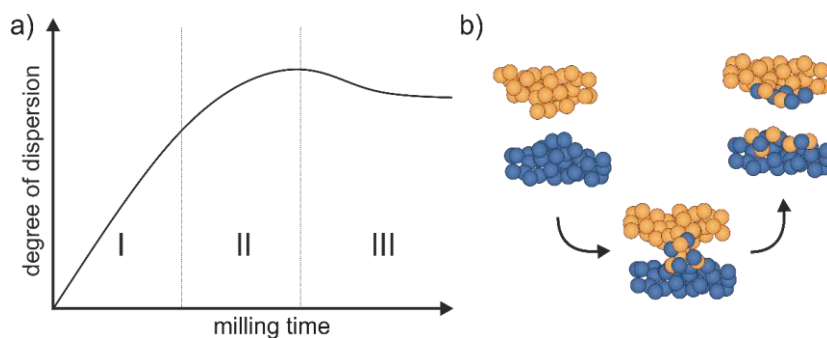


Figure 1.14 Mechanochemical reactions: a) Kinetics of mechanochemical treatment is defined by three regimes. Whereas, in regime I, the particles are crushed and the surface increases linearly, the material starts to deform plastically in II. Finally, the surface decreases due to the agglomeration of the particles, which minimizes the surface energy of the system. Based on [52]. b) The local high-energy states during the collision of particles allow for material transfer on their surface. Based on [54].

When two different compounds are processed together in a ball mill, material is transferred between the particles (Figure 1.14b).^{54,55} On collision of the particles, the kinetic energy is deposited on the rough surfaces, causing a sudden increase in temperature and excitation of several hundred/thousand atoms.⁵⁶ Under these conditions, alloying processes are possible and material is transferred. Moreover, the defects on the surface decrease the melting temperature, which further supports atom mobility and material transport. The mechanochemical alloying of metals is based on this mechanism.⁵⁷ For the system germanium-niobium, Koch et al. showed by electron microscopy that the homogeneity increased with milling time.⁵⁸ The efficiency of this process depends significantly on the hardness of the materials,⁵⁷ their asperities,⁵⁹ and the work of adhesion.⁶⁰

1.5 CALCIUM CARBONATE

Calcium carbonate represents one of the most common materials on earth, it is found in huge deposits, in form of chalk, marble, and limestone.⁶¹ Moreover, a large number of different organisms use calcium carbonate as biomineral to form hard, structure-giving frameworks, i.e. eggshells, corals, clams, and the exoskeletons of various animals.^{62–65} In all these examples, calcium carbonate crystallites exhibit unique shapes and morphologies, which deviate from the equilibrium structures due to the influence of proteins and the organic matrices. The widespread use of calcium carbonate originates from the large abundance of both components, calcium salts and carbon dioxide, as well as from its large structural diversity. The wide solubility range of the different modifications, the reversible hydration of the calcium ion, and the pH dependence of the system open a multitude of ways to influence the crystallization process. Calcium carbonate exhibits a rich polymorphism with one – or several⁶⁶ – amorphous species and five crystalline modifications (Figure 1.5).

ACC

Despite being the least stable modification, amorphous calcium carbonate attracted a lot of attention over the past decades, as its importance in biological crystallization processes became evident. Many examples were found in which ACC was deployed as structure-giving biomineral itself⁶⁷ or served as calcium reservoir to precipitate other crystalline modifications.^{68,69} Living organisms have developed different strategies to stabilize this metastable species. The incorporation of foreign ions, especially Mg^{2+} , enhances the stability of ACC significantly.^{70,71} The higher hydration energy of magnesium, in contrast to calcium, is assumed to pose a high barrier for the transformation of the magnesium bearing amorphous phase to an anhydrous crystalline modification. Also, the interaction with proteins or other biological macromolecules,⁷² as well as the local confinement of ACC in vesicles^{73–75} exhibit a stabilizing effect.

In accordance with the Ostwald-Volmer rule, ACC forms directly at higher supersaturation during the precipitation of calcium carbonate. The low interfacial energy between ACC and the solution kinetically favors its formation. ACC exhibits the highest solubility of all calcium carbonate modifications (Ikaite solubility cannot be determined at ambient temperature), it was determined by Brečević and Nielsen as $4.0 \times 10^{-7} \text{ mol}^2/\text{L}^2$.⁷⁶

ACC readily transforms to the crystalline modifications, usually to calcite *via* vaterite as intermediate. In aqueous solution, the transformation of ACC occurs within seconds to minutes.¹⁹ By rapid quenching of the reaction solution and drying of ACC, it can be stabilized for several months.⁷⁷ This presents strong evidence that the transformation of ACC proceeds *via* a dissolution-recrystallization process, and not *via* a solid state reaction.

Ikaite

Ikaite is the least stable crystalline modification of calcium carbonate. It is strongly hydrated with six molecules of water per formula unit. Natural deposits are found at elevated hydrostatic pressure and temperatures around the freezing point in marine environments.^{78,79} At ambient temperatures, ikaite readily dehydrates and transforms to calcite.⁸⁰ Therefore, it is not observed as intermediate during the transformation of ACC to calcite.

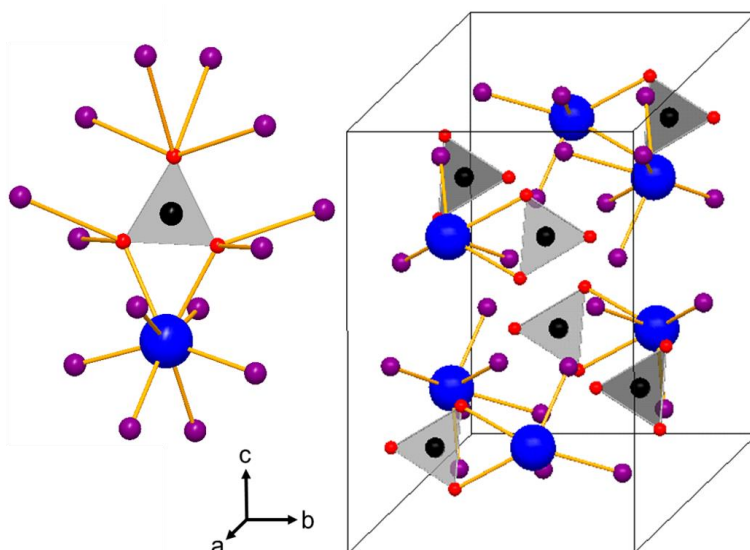


Figure 1.15 Coordination sphere and unit cell of ikaite.⁸² Ca = blue, C = black, O = red, H₂O = purple.

Table 1.1 Crystallographic data of ikaite. Data from reference [82].

composition	$\text{CaCO}_3 \times 6 \text{H}_2\text{O}$
space group	C2/c (15) – monoclinic, Z = 4
lattice parameters	$a = 8.7920 \text{ \AA}$, $b = 8.3100 \text{ \AA}$, $c = 11.0210 \text{ \AA}$, $\beta = 110.5300^\circ$
density ρ	1.83 g/cm ³
solubility K_{sp} (-1.1 °C) ⁸³	$4.35 \times 10^{-6} \text{ mol}^2/\text{L}^2$

The structure of ikaite consists of lone CaCO_3 pairs, lying on twofold axis. These pairs are isolated by 18 enveloping water molecules. Eight of these molecules form hydrogen bonds with the carbonate ion, while six are coordinated to the calcium ion. Four additional water molecules are not bonded directly to the ion pair, but to adjacent water molecules.^{81,82} The carbonate ions binds bidentately to the calcium ion, which gives, together with the water molecules, a total coordination number of eight for the calcium.

Monohydrocalcite

Monohydrocalcite is a hydrated crystalline modification of calcium carbonate with one water molecule per formula unit CaCO_3 . As it is metastable with regard to the anhydrous crystalline modifications of calcium carbonate, natural deposits are rarely found. Usually, monohydrocalcite is associated with other magnesium and calcium carbonate bearing minerals⁸⁴ Also, monohydrocalcite is reported to act as biomineral in specific organism, e.g. in the otoliths of tiger sharks⁸⁵ and the calcareous corpuscles of a cestode parasite.⁸⁶ Monohydrocalcite can be synthesized in the presence of magnesium, whose partial incorporation apparently stabilizes this modification.⁸⁷ When monohydrocalcite is stored in dry air, it is stable for several months. In water, crystallization occurs to aragonite and calcite. Monohydrocalcite crystallizes with a trigonal unit cell. The calcium ion exhibits an eightfold coordination by two water molecules and four carbonate ions, of which two are bound bidentately.

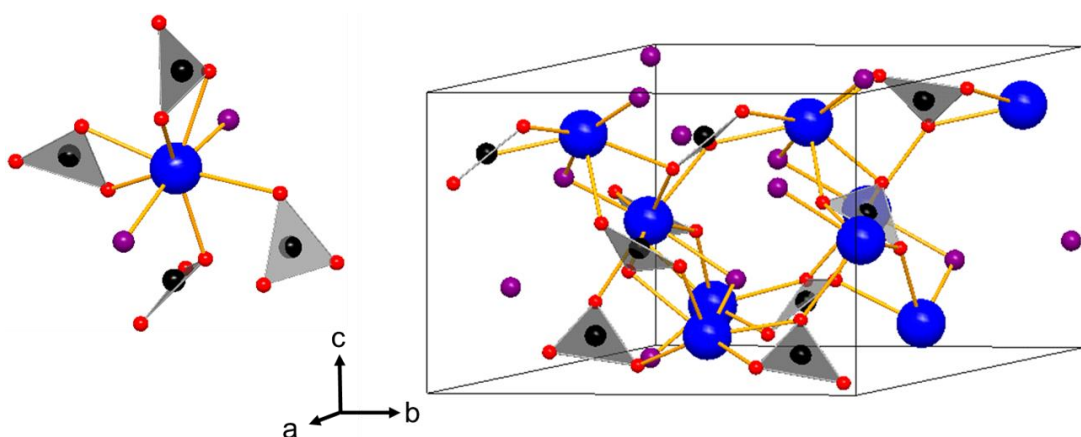


Figure 1.16 Coordination sphere and unit cell of monohydrocalcite.⁸⁸ Ca = blue, C = black, O = red, H_2O = purple.

Table 1.2 Crystallographic data of monohydrocalcite. Data from reference [88].

composition	$\text{CaCO}_3 \times 1 \text{H}_2\text{O}$
space group	$P3_1(144)$ – trigonal, $Z = 9$
lattice parameters	$a = 10.5536 \text{ \AA}$, $c = 7.5446 \text{ \AA}$
density ρ	$2,43 \text{ g/cm}^3$
solubility $K_{\text{sp}}(25 \text{ }^\circ\text{C})^{89}$	$6.14 \times 10^{-8} \text{ mol}^2/\text{L}^2$

Vaterite

Vaterite represents the least stable anhydrous crystalline modification in the calcium carbonate system. It is by far the least abundant anhydrous modification of calcium carbonate on earth, only few natural deposits exist.^{90,91} Also, vaterite is of minor relevance in biomineralization and only few examples are known.^{92,93} Even though, vaterite seems to play a role in healing and regeneration processes of biominerals,⁹⁴ e.g. it is found in deformed shells of *Corbicula fluminea*.⁹⁵ In a similar way, vaterite nanoparticles can be employed in bone replacement materials, as they exhibit a relatively high solubility and can act therefore as calcium reservoir.⁹⁶ Even after decades of research, the structure of vaterite is still debated heavily and a multitude of structure solutions was proposed over the years.⁹⁷

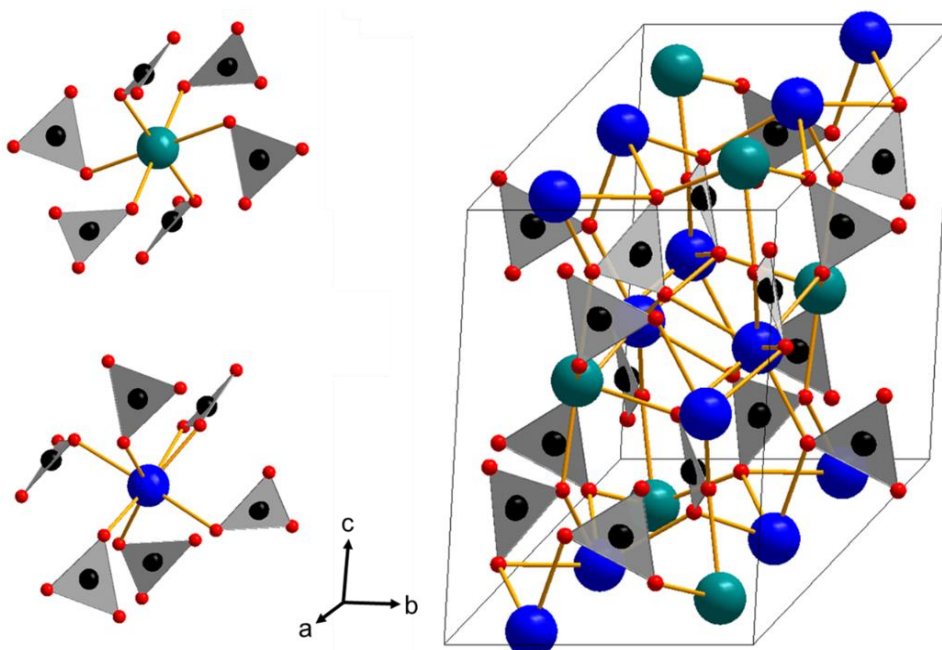


Figure 1.17 Coordination spheres and unit cell of vaterite.⁹⁸ Ca₁ = green, Ca₂ = blue, C = black, O = red.

Table 1.3 Crystallographic data of vaterite. Data from reference [98].

composition	CaCO ₃
space group	C2/c (15) – monoclinic, Z = 12
lattice parameters	a = 12.1700 Å, b = 7.1200 Å, c = 9.4700 Å β = 118.3700°
density ρ	2,65 g/cm ³
solubility K _{sp} (25 °C) ¹⁰⁰	1.22 × 10 ⁻⁸ mol ² /L ²

Vaterite does not form macroscopic single crystals, but is a polycrystalline material, which is built up from nano-sized domains. This impedes an accurate structural characterization by scattering methods, as only powder techniques can be employed. Recent studies try to circumvent this problem by using electron diffraction on nano-sized vaterite crystals.^{98,99} The structural model proposed by Mugnaioli et al. has a monoclinic unit cell and exhibits two distinct sites for the calcium ion. In both cases, it is coordinated by six carbonate ions. This leads to an oxygen coordination number of six for the first position. In the second calcium site though, one carbonate ion binds bidentately and the coordination number is increased to seven.

Aragonite

Aragonite has the highest density of all calcium carbonate modifications and it represents the high-pressure phase in this system. It is the second most abundant calcium carbonate mineral and it is found in sedimentary deposits, especially in hydrothermal and marine environments.¹⁰¹ The most prominent example for aragonite as biomineral is the nacre in clams. This material consists of 500 nm thick platelets of aragonite embedded in an organic matrix.¹⁰² The periodicity is on the length scale of the visible light, which causes the interference colors of nacre. Moreover, the composite-like construction enhances the mechanical properties of the shell. Aragonite can be synthesized easily by precipitating calcium carbonate at elevated temperatures above 50 °C.¹⁰³ Also, the presence of certain foreign ions, especially strontium and magnesium, favor the formation of aragonite. Strontium carbonate itself exhibits aragonite structure because of the larger size of the cation. If calcium carbonate is precipitated in the presence of strontium, its incorporation will promote the formation of aragonite.

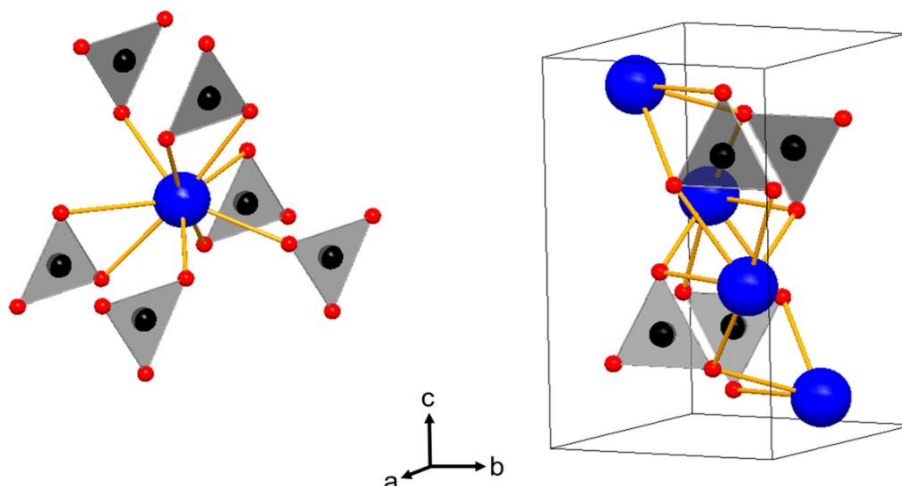


Figure 1.18 Coordination sphere and unit cell of aragonite.¹⁰⁶ Ca = blue, C = black, O = red.

Table 1.4 Crystallographic data of aragonite. Data from reference [106].

composition	CaCO ₃
space group	Pnma (62) – orthorhombic, Z = 4
lattice parameters	a = 5.7952 Å, b = 5.0192 Å, c = 8.0393 Å
density ρ	2,84 g/cm ³
solubility K _{sp} (25 °C) ¹⁰⁰	4.61 × 10 ⁻⁹ mol ² /L ²

The aragonite-inducing effect of magnesium works presumably by the destabilization of the calcite phase. Whereas the small magnesium ion can be incorporated into the calcite structure, it is not tolerated by aragonite. Due to lattice strain, the solubility of the formed magnesian calcite rises above the one of aragonite, which makes it the thermodynamic stable modification under these conditions.¹⁰⁴ Although aragonite is metastable at ambient conditions, its transformation can take millions of years.¹⁰⁵

Aragonite has an orthorhombic unit cell and it exhibits the highest coordination number for Ca²⁺ of all calcium carbonate modifications. The calcium ion is enclosed by six carbonate ions. Three are bound bidentately, which results in a coordination number of nine. This high coordination number is favorable for bigger cations. Therefore, strontium carbonate and barium carbonate crystallize in the aragonite type, while carbonates with smaller divalent cations, i.e. magnesium, manganese, or iron, exhibit calcite structure.

Calcite

Calcite is the thermodynamic stable modification of calcium carbonate. Thus, huge deposits of chalk and limestone mainly consist of calcite.⁶¹ Calcite crystals usually exhibit a typical rhombohedral shape and are terminated by (104) lattice planes. Due to the equal number of calcium and carbonate ions in this plane, resulting in a zero net charge, the surface energy is minimized. Calcite occurs as biomineral in various organisms, e.g. mussels,¹⁰⁷ eggshells,¹⁰⁸ algae,¹⁰⁹ and corals;¹¹⁰ even lenses in the eyes of trilobites are made of calcite.¹¹¹

As it represents the thermodynamic minimum of the calcium carbonate system at ambient conditions, all modifications transform with time to calcite, especially when exposed to moisture and/or heat.

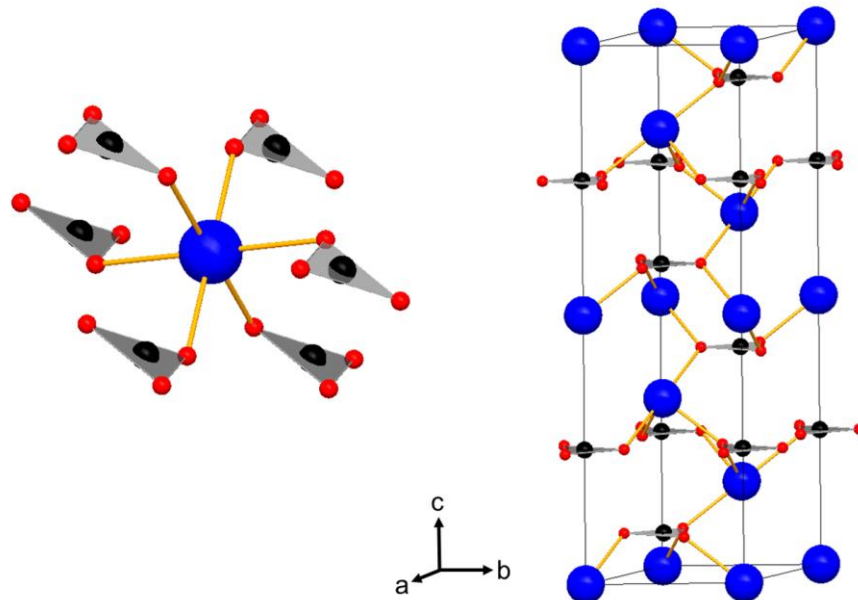


Figure 1.19 Coordination sphere and unit cell of calcite.¹¹² Ca = blue, C = black, O = red.

Table 1.5 Crystallographic data of calcite. Data from reference [112].

composition	CaCO_3
space group	$R\bar{3}c$ (167) – trigonal, $Z = 6$
lattice parameters	$a = 4.9920 \text{ \AA}$, $c = 17.0690 \text{ \AA}$
density ρ	$2,70 \text{ g/cm}^3$
solubility K_{sp} (25 °C) ¹⁰⁰	$3.31 \times 10^{-9} \text{ mol}^2/\text{L}^2$

Calcite consists of alternating layers of calcium ions and carbonate ions. The calcium ions are enclosed in a distorted octahedron of carbonate ions, which results in a coordination number of six. The lower coordination number enables substitution of the calcium by small cations, e.g. magnesium. Statistical substitution of the calcium ions (magnesian calcite) is equally possible as alternating substitution of complete calcium layers (dolomite).

1.6 CALCIUM SULFATE

Calcium sulfate occurs in nature in three different modifications, which can be distinguished by their degree of hydration: anhydrite (CaSO_4), bassanite ($\text{CaSO}_4 \times 0.5 \text{H}_2\text{O}$), and gypsum ($\text{CaSO}_4 \times 2 \text{H}_2\text{O}$). Moreover, calcium sulfate is one of the most important construction materials for thousands of years.^{113,114} The transformation of anhydrite to gypsum and the simultaneous uptake of structural water represent the molecular mechanism for the hardening of plaster. Calcium sulfate is found in huge quantities in evaporitic mineral deposits,¹¹⁵ especially gypsum¹¹⁶ and anhydrite.¹¹⁷ Bassanite is less common.¹¹⁸ Even on Mars, evidence of calcium sulfate materials were observed.¹¹⁹

Due to its relatively high solubility, calcium sulfate is rarely employed as biomineral. Even though, it was found in the stems of *Salvadora persica*, a plant known as natural tooth-brush.¹²⁰ The gravity sensing organs, so-called statoliths, of *Scyphomedusae* contain small bassanite crystals.¹²¹ These findings underline the importance of an organic matrix in the formation of biominerals, as bassanite is metastable at all temperatures. Gypsum is the thermodynamically stable modification at ambient temperature, whereas it dehydrates *via* bassanite to anhydrite upon heating. At elevated temperatures, anhydrite becomes the stable modification. The exact value of the gypsum-anhydrite transition temperature was heavily discussed in the last century though. The difficulty of an exact determination arises from the fact that the crystallization of anhydrite in solution is kinetically hindered at temperatures below 70 °C.¹²² The reports range from 25 °C up to 60 °C.^{123,124}

Anhydrite

Anhydrite is the anhydrous crystalline modification in the calcium sulfate system and represents the thermodynamically stable phase at temperatures above 60 °C. The structure is characterized by chains of calcium ions alternating with sulfate tetrahedrons. The calcium ion has six neighboring sulfate groups, of which two are bound bidentately, resulting in a coordination number of eight.

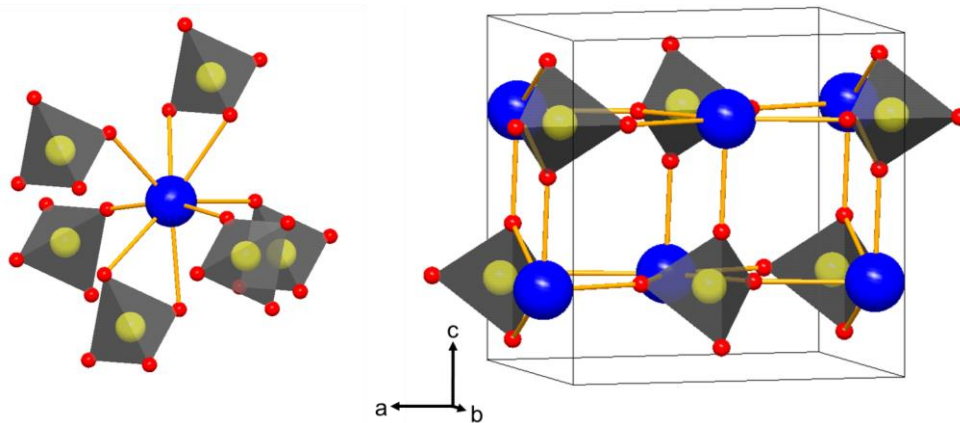


Figure 1.20 Coordination sphere and unit cell of anhydrite.¹²⁵ Ca = blue, S= yellow, O = red.

Table 1.6 Crystallographic data of anhydrite. Data from reference [125].

composition	CaSO ₄
space group	Cmcm (63) – orthorhombic, Z = 4
lattice parameters	a = 6.9980 Å, b = 6.2450 Å, c = 7.0060 Å
density ρ	2,95 g/cm ³
solubility K _{sp} (25 °C) ¹²⁶	4.08 × 10 ⁻⁴ mol ² /L ²

Bassanite

Bassanite is a metastable crystalline modification of calcium sulfate, containing half a formula unit of water. Bassanite crystals show a typical rod-shaped morphology.¹²⁷ It appears as intermediate product during the thermal transformation of gypsum to anhydrite. Also, bassanite plays a key role in crystallizing calcium sulfate from solution.¹²⁸ Nano-sized bassanite rods were found as precursor phase of gypsum.¹²⁹ Like anhydrite, bassanite consists of alternating calcium sulfate chains. These chains form pores along the c-axis with a diameter of 4 Å, in which the water molecules are situated. Figure 1.21 displays all possible

water positions in the channel structure, which would correspond to one formula unit water per CaSO_4 . Actually, only half of these positions are occupied; the ordering of the water molecules results in an orthogonal superstructure cell of the symmetry $I2$.¹³⁰ This open framework structure facilitates hydration/dehydration processes and the incorporation foreign ions.¹²² With four mono- and two bidentate sulfate ions, the calcium coordination in bassanite is similar to anhydrite. The additional water molecule increases the coordination number to nine.

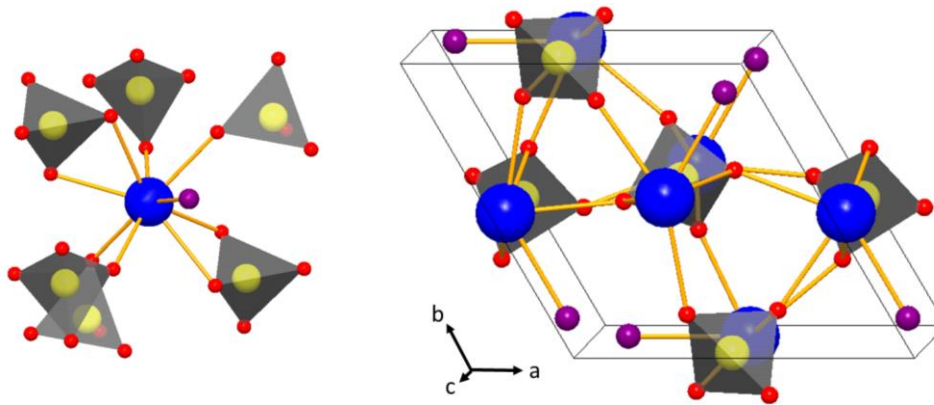


Figure 1.21 Coordination sphere and unit cell of bassanite.¹³⁰ Ca = blue, S = yellow, O = red, H₂O = purple.

Table 1.7 Crystallographic data of bassanite. Data from reference [130].

composition	$\text{CaSO}_4 \times 0.5 \text{H}_2\text{O}$
space group	$P3_121$ (152) – trigonal, $Z = 3$
lattice parameters	$a = 6.9370 \text{ \AA}$, $c = 6.3450 \text{ \AA}$
density ρ	2.74 g/cm^3
solubility K_{sp} (25 °C) ¹³¹	$2.14 \times 10^{-3} \text{ mol}^2/\text{L}^2$

Gypsum

Gypsum is the thermodynamically stable modification at ambient conditions and has the highest degree of hydration in the calcium sulfate system. Gypsum crystals show a characteristic needle-like morphology. The entanglement of these needles influences the mechanical properties of plaster as construction material.^{132,133} Gypsum exhibits a layered structure perpendicular to the b-axis. Between double layers of calcium and sulfate ions, the water

molecules are situated. The calcium ion is enclosed by four sulfate groups in the layer, of which two are bound bidentately. The coordination of two additional water molecules results in a total coordination number of eight.

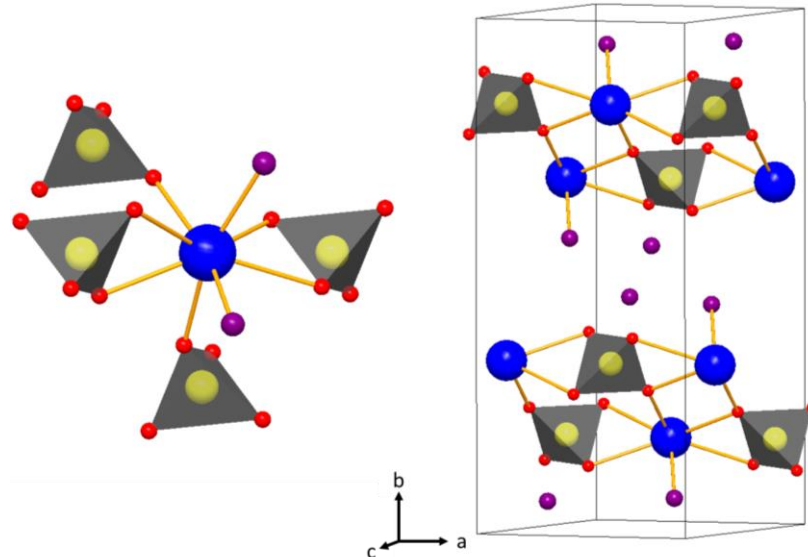


Figure 1.22 Coordination sphere and unit cell of gypsum.¹³⁴ Ca = blue, S = yellow, O = red, H₂O = purple.

Table 1.8 Crystallographic data of gypsum. Data from reference [134].

composition	CaSO ₄ × 2 H ₂ O
space group	C2/c (15) – monoclinic, Z = 4
lattice parameters	a = 6.2910 Å, b = 15.2180 Å, c = 5.6810 Å β = 114.1430°
density ρ	2.31 g/cm ³
solubility K _{sp} (25 °C) ¹²⁶	1.45 × 10 ⁻⁴ mol ² /L ²

1.7 REFERENCES

- (1) LaMer, V. K., R. H. Dinegar. *J. Am. Chem. Soc.* **1950**, 72, 4847–4855.
- (2) Ehrenfest, P. *Proc. R. Neth. Acad. Arts Sci.* **1933**, 36, 153–157.
- (3) García-Ojalvo, J., Lacasta, A. M., Sancho J. M., Toral, R. *Europhys. Lett.* **1998**, 42, 125–130.
- (4) Favvas, E. P., Mitropoulos, A. C. *J. Eng. Sci. Technol. Rev.* **2008**, 1, 25–27.

- (5) Smith, J., Hamilton, R., McCulloch, I., Stingelin-Stutzmann, N., Heeney, M., Bradley, D. D. C., Anthopoulos, T. D. *J. Mater. Chem.* **2010**, *20*, 2562–2574.
- (6) Faatz, M., Gröhn, F., Wegner, G. *Adv. Mater.* **2004**, *16*, 996–1000.
- (7) Wallace, A. F., Hedges, L. O., Fernandez-Martinez, A., Raiteri, P., Gale, J. D., Waychunas, G. A., Whitelam, S., Banfield, J. F., J. De Yoreo, J. J. *Science* **2013**, *341*, 885–889.
- (8) Volmer, M., Weber, A. *Z. Phys. Chem.* **1925**, *119*, 277–301.
- (9) Heady, R. B., Cahn, J. W. *J. Chem. Phys.* **1973**, *58*, 896–910.
- (10) Neilson, G. F., Weinberg, M. C. *J. Non-Cryst. Solids* **1979**, *34*, 137–147.
- (11) Yau, S. T., Vekilov, P. G. *J. Am. Chem. Soc.* **2001**, *123*, 1080–1089.
- (12) Lekkerkerker, H. N. W., Stroobants, A. *Nature* **1998**, *393*, 305–307.
- (13) Karayiannis, N. C., Foteinopoulou, K., Laso, M. *Phys. Rev. Lett.* **2009**, *103*, 45703.
- (14) Yoreo, J. J. de, Vekilov, P. G. *Rev. Mineral. Geochem.* **2003**, *54*, 57–93.
- (15) Zhu, P., Masuda, Y., Koumoto, K. *Biomaterials* **2004**, *25*, 3915–3921.
- (16) Tahir, M. N., Natalio, F., Cambaz, M. A., Panthöfer, M., Branscheid, R., Kolb, U., Tremel, W. *Nanoscale* **2013**, *5*, 9944–9949.
- (17) Cölfen, H. *Nat. Mater.* **2010**, *9*, 960–961.
- (18) Ostwald, W. *Z. Phys. Chem.* **1897**, *22U*, 289–330.
- (19) Rodriguez-Blanco, J. D., Shaw, S., Benning, L. G. *Nanoscale* **2011**, *3*, 265–271.
- (20) Vekilov, P. G. *Cryst. Growth Des.* **2004**, *4*, 671–685.
- (21) Vekilov, P. G. *Nanoscale* **2010**, *2*, 2346–2357.
- (22) Maes, D., Vorontsova, M. A., Potenza, M. A. C., Sanvito, T., Sleutel, M., Giglio, M., Vekilov, P. G. *Acta Crystallogr., Sect. F: Struct. Biol. Commun.* **2015**, *71*, 815–822.
- (23) Shah, M., Galkin, O., Vekilov, P. G. *J. Chem. Phys.* **2004**, *121*, 7505–7512.
- (24) Garetz, B. A., Matic, J., Myerson, A. S. *Phys. Rev. Lett.* **2002**, *89*, 175501.
- (25) Wolf, S. E., Leiterer, J., Pipich, V., Barrea, R., Emmerling, F., Tremel, W. *J. Am. Chem. Soc.* **2011**, *133*, 12642–12649.
- (26) Wolf, S. E., Müller, L., Barrea, R., Kampf, C. J., Leiterer, J., Panne, U., Hoffmann, T., Emmerling, F., Tremel, W. *Nanoscale* **2011**, *3*, 1158–1165.
- (27) Bewernitz, M. A., Gebauer, D., Long, J., Cölfen, H., Gower, L. B. *Faraday Discuss.* **2012**, *159*, 291–312.
- (28) Posner, A. S., Betts, F. *Acc. Chem. Res.* **2002**, *8*, 273–281.

- (29) Liang, X., Wang, X., Zhuang, J., Chen, Y., Wang, D., Li, Y. *Adv. Funct. Mater.* **2006**, *16*, 1805–1813.
- (30) Jacobson, L. C., Hujo, W., Molinero, V. *J. Am. Chem. Soc.* **2010**, *132*, 11806–11811.
- (31) Addadi, L., Raz, S., Weiner, S. *Adv. Mater.* **2003**, *15*, 959–970.
- (32) Wulff, G. Z. *Kristallogr. Cryst. Mater.* **1901**, *34*, 449–530.
- (33) Krug, J., Politi, P., Michely, T. *Phys. Rev. B* **2000**, *61*, 14037–14047.
- (34) Niederberger, M., Cölfen, H. *Phys. Chem. Chem. Phys.* **2006**, *8*, 3271–3287.
- (35) Cölfen, H., Mann, S. *Angew. Chem. Int. Ed.* **2003**, *42*, 2350–2365.
- (36) Bergström, L., Sturm née Rosseeva, E. V., Salazar-Alvarez, G., Cölfen, H. *Acc. Chem. Res.* **2015**, *48*, 1391–1402.
- (37) Yang, L., Killian, C. E., Kunz, M., Tamura, N., Gilbert, P. U. P. A. *Nanoscale* **2011**, *3*, 603–609.
- (38) Chakka, V. M., Altunçevahir, B., Jin, Z. Q., Li, Y., Liu, J. P. *J. Appl. Phys.* **2006**, *99*, 08E912.
- (39) Koch, C. C., Whittenberger, J. D. *Intermetallics* **1996**, *4*, 339–355.
- (40) Koch, C. C., Cavin, O. B., McKamey, C. G., Scarbrough, J. O. *Appl. Phys. Lett.* **1983**, *43*, 1017–1019.
- (41) Baláž, P., Achimovičová, M., Baláž, M., Billik, P., Cherkezova-Zheleva, Z., Manuel Criado, J., Delogu, F., Dutková, E., Gaffet, E., Gotor, F. J., Kumar, R., Mitov, I., Rojac, T., Senna, M., Streletskiikl, A., Wiczorek-Ciurowam, K. *Chem. Soc. Rev.* **2008**, *42*, 7571–7637.
- (42) FRITSCH GmbH. Planeten-Mikromühle PULVERISETTE 7 classic line.
<https://www.fritsch.de/probenaufbereitung/ueberblick/details/produkt/pulverisette-7-classic-line/> Accessed: June 27, 2018.
- (43) Thiessen P. A., Meyer K., Heinicke G. *Grundlagen der Tribochemie*, 1st ed.; Akademie Verlag: Berlin, 1967.
- (44) Delogu, F. *Phys. Rev. B* **2010**, *82*, 205415.
- (45) Boldyrev, V. V., Tkáčová, K. *J. Mater. Synth. Process.* **2000**, *8*, 121–132.
- (46) Shen, T. D., Koch, C. C., McCormick, T. L., Nemanich, R. J., Huang, J. Y., Huang, J. *G. J. Mater. Res.* **1995**, *10*, 139–148.
- (47) Gaffet, E. *Mater. Sci. Eng., A* **1991**, *136*, 161–169.
- (48) Rojac, T., Benčan, A., Kosec, M. *J. Am. Ceram. Soc.* **2010**, *93*, 1619–1625.

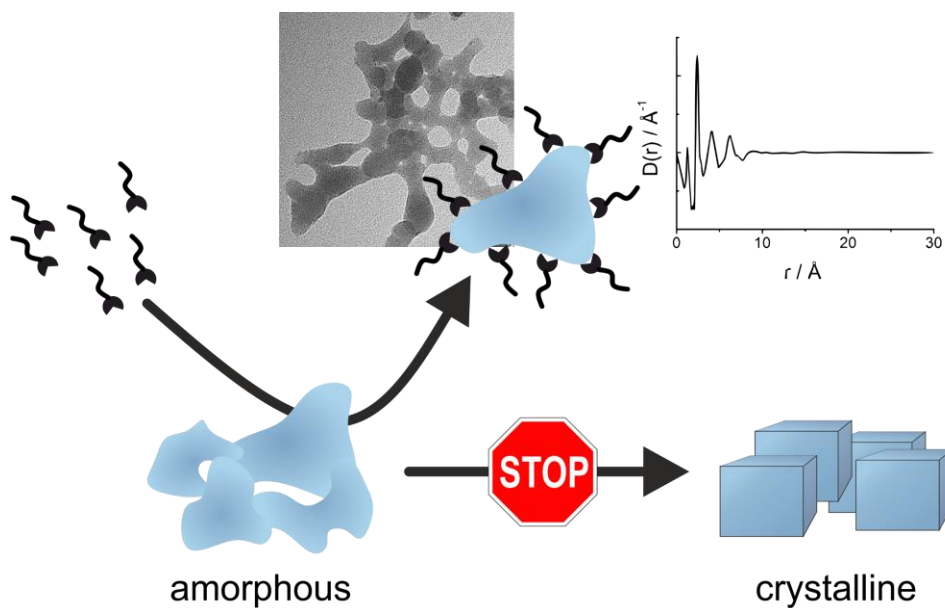
- (49) Machon, D., Meersman, F., Wilding, M. C., Wilson, M., McMillan, P. F. *Prog. Mater. Sci.* **2014**, *61*, 216–282.
- (50) Bennett, T. D., Saines, P. J., Keen, D. A., Tan, J.-C., Cheetham, A. K. *Chemistry (Weinheim an der Bergstrasse, Germany)* **2013**, *19*, 7049–7055.
- (51) Cao, S., Bennett, T. D., Keen, D. A., Goodwin, A. L., Cheetham, A. K. *Chem. Commun.* **2012**, *48*, 7805–7807.
- (52) Opoczky, L. *Powder Technol.* **1977**, *17*, 1–7.
- (53) Rittinger P. von. *Lehrbuch der Aufbereitungskunde in ihrer neuesten Entwicklung und Ausbindung systematisch dargestellt*; Ernst & Korn: Berlin, 1867.
- (54) Delogu, F., Cocco, G. *Phys. Rev. B* **2006**, *74*, 35406.
- (55) Rigney, D.A. *Wear* **2000**, *245*, 1–9.
- (56) Delogu, F. *Phys. Rev. B* **2009**, *80*, 14115.
- (57) Delogu, F. *Chem. Phys. Lett.* **2012**, *521*, 125–129.
- (58) Kenik, E. A., Bayuzick, R. J., Kim, M. S., Koch, C. C. *Scr. Mater.* **1987**, *21*, 1137–1142.
- (59) Fortini, A., Mendeleev, M. I., Buldyrev, S., Srolovitz, D. *J. Appl. Phys.* **2008**, *104*, 74320.
- (60) Song, J., Srolovitz, D. J. *Acta Mater.* **2006**, *54*, 5305–5312.
- (61) Mimiran, Y. *Sedimentology* **1977**, *24*, 333–360.
- (62) Lakshminarayanan, R., Loh, X. J., Gayathri, S., Sindhu, S., Banerjee, Y., Kini, R. M., Valiyaveetil, S. *Biomacromolecules* **2006**, *7*, 3202–3209.
- (63) Gattuso, J. *Glob. Planet. Change* **1998**, *18*, 37–46.
- (64) Goreau, T. F. *Ann. N.Y. Acad. Sci.* **1963**, *109*, 127–167.
- (65) Hild, S., Marti, O., Ziegler, A. *J. Struct. Biol.* **2008**, *163*, 100–108.
- (66) Cartwright, J. H. E., Checa, A. G., Gale, J. D., Gebauer, D., Sainz-Díaz, C. I. *Angew. Chem. Int. Ed.* **2012**, *51*, 11960–11970.
- (67) Levi-Kalisman, Y., Raz, S., Weiner, S., Addadi, L., Sagi, I. *Adv. Funct. Mater.* **2002**, *12*, 43–48.
- (68) Politi, Y., Arad, T., Klein, E., Weiner, S., Addadi, L. *Science* **2004**, *306*, 1161–1164.
- (69) Gago-Duport, L., Briones, M. J. I., Rodríguez, J. B., Covelo, B. *J. Struct. Biol.* **2008**, *162*, 422–435.

- (70) Loste, E., Wilson, R. M., Seshadri, R., Meldrum, F. C. *J. Cryst. Growth* **2003**, *254*, 206–218.
- (71) Raz, S., Hamilton, P. C., Wilt, F. H., Weiner, S., Addadi, L. *Adv. Funct. Mater.* **2003**, *13*, 480–486.
- (72) Aizenberg, J., Addadi, L., Weiner, S., Lambert, G. *Adv. Mater.* **1996**, *8*, 222–226.
- (73) Weiner, S., Sagi, I., Addadi, L. *Science* **2005**, *309*, 1027–1029.
- (74) Tester, C. C., Brock, R. E., Wu, C.-H., Krejci, M. R., Weigand, S., Joester, D. *Cryst. Eng. Comm.* **2011**, *13*, 3975–3978.
- (75) Kim, Y.-Y., Ganesan, K., Yang, P., Kulak, A. N., Borukhin, S., Pechook, S., Ribeiro, L., Kröger, R., Eichhorn, S. J., Armes, S. P., Pokroy, B., Meldrum, F. C. *Nat. Mater.* **2011**, *10*, 890–896.
- (76) Brečević, L., Nielsen, A. E. *J. Cryst. Growth* **1989**, *98*, 504–510.
- (77) Gebauer, D., Gunawidjaja, P. N., Ko, J. Y. P., Bacsik, Z., Aziz, B., Liu, L., Hu, Y., Bergström, L., Tai, C.-W., Sham, T.-K., Edén, M., Hedin, N. *Angew. Chem. Int. Ed.* **2010**, *49*, 8889–8891.
- (78) Brooks, K. *Geol. Today* **2016**, *32*, 75–78.
- (79) T. C., C., P. C. Bennett. *Geology* **1993**, *21*, 971–974.
- (80) Nebel, H., Neumann, M., Mayer, C., Epple, M. *Inorg. Chem.* **2008**, *47*, 7874–7879.
- (81) Dickens, B., Brown, W. E. *Inorg. Chem.* **1970**, *9*, 480–486.
- (82) Hesse, K. F., Küppers, H. *Z. Kristallogr.* **1983**, *163*, 227–231.
- (83) Papadimitriou, S., Kennedy, H., Kennedy, P., Thomas, D. N. *Geochim. Cosmochim. Acta* **2013**, *109*, 241–253.
- (84) Swainson, I. P. *Am. Mineral.* **2008**, *93*, 1014–1018.
- (85) Carlström, D. *Biol. Bull.* **1963**, *125*, 441–463.
- (86) Señorale-Pose, M., Chalar, C., Dauphin, Y., Massard, P., Pradel, P., Marín, M. *Exp. Parasitol.* **2008**, *118*, 54–58.
- (87) Rodriguez-Blanco, J. D., Shaw, S., Bots, P., Roncal-Herrero, T., Benning, L. G. *Geochim. Cosmochim. Acta* **2014**, *127*, 204–220.
- (88) Effenberger, H. *Monatsh. Chem.* **1981**, *112*, 899–909.
- (89) Kralj, D., Brečević, L. *Colloids Surf., A* **1995**, *96*, 287–293.
- (90) Grasby, S. E. *Geochim. Cosmochim. Acta* **2003**, *67*, 1659–1666.
- (91) McConnel, J. D. C. *Mineral. Mag.* **1960**, *32*, 535–544.

- (92) Lowenstam, H. A., Abbott, D. P. *Science* **188**, 1975, 363–365.
- (93) Berland, S., Ma, Y., Marie, A., Andrieu, J. P., Bedouet, L., Feng, Q.
Protein Pept. Lett. **2013**, 20, 1170–1180.
- (94) K.M., W., N. Watabe. *Ann. N.Y. Acad. Sci.* **1963**, 109, 82–112.
- (95) Spann, N., Harper, E. M., Aldridge, D. C. *Naturwissenschaften* **2010**, 97, 743–751.
- (96) Schröder, R., Pohlit, H., Schüler, T., Panthöfer, M., Unger, R. E., Frey, H., Tremel, W. *J. Mater. Chem. B* **2015**, 3, 7079–7089.
- (97) Christy, A. G. *Cryst. Growth Des.* **2017**, 17, 3567–3578.
- (98) Mugnaioli, E., Andrusenko, I., Schüler, T., Loges, N., Dinnebier, R. E., Panthöfer, M., Tremel, W., Kolb, U. *Angew. Chem. Int. Ed.* **2012**, 51, 7041–7045.
- (99) Kabalah-Amitai, L., Mayzel, B., Kauffmann, Y., Fitch, A. N., Bloch, L., Gilbert, P. U. P. A., Pokroy, B. *Science* **2013**, 340, 454–457.
- (100) Plummer, L. N., Busenberg, E. *Geochim. Cosmochim. Acta* **1982**, 46, 1011–1040.
- (101) Kier, J. S., Pilkey, O. H. *Mar. Geol.* **1971**, 11, 189–200.
- (102) Macías-Sánchez, E., Willinger, M. G., Pina, C. M., Checa, A. G. *Sci. Rep.* **2017**, 7, 12728.
- (103) Wray, J. L., Daniels, F. *J. Am. Chem. Soc.* **1957**, 79, 2031–2034.
- (104) Berner, R. A. *Geochim. Cosmochim. Acta* **1975**, 39, 489–494.
- (105) Brown, W. H., Fyfe, W. S., Turner, F. J. *J. Petrol.* **1962**, 3, 566–582.
- (106) Oganov, A. R., Glass, C. W., Ono, S. *Earth. Planet. Sci. Lett.* **2006**, 241, 95–103.
- (107) Putten, E. V., Dehairs, F., Keppens, E., Baeyens, W. *Geochim. Cosmochim. Acta* **2000**, 64, 997–1011.
- (108) Baird, T., Solomon, S. E. *J. Exp. Mar. Biol. Ecol.* **1979**, 36, 295–303.
- (109) Takano, H., Furu-une, H., Burgess, J. G., Manabe, E., Hirano, M., Okazaki, M., Matsunaga, T. *Appl. Biochem. Biotechnol.* **1993**, 39-40, 159–167.
- (110) Weinbauer, M. G., Brandstätter, F., Velimirov, B. *Mar. Biol.* **2000**, 137, 801–809.
- (111) Towe, K. M. *Science* **1973**, 179, 1007–1009.
- (112) Sitepu, H., O'Connor, B. H., Li, D. *J. Appl. Crystallogr.* **2005**, 38, 158–167.
- (113) Ahmad Bany Yaseen, I., Al-Amoush, H., Al-Farajat, M., Mayyas, A.
Constr. Build. Mater. **2013**, 38, 465–471.
- (114) Moussa, A. B., Kantiranis, N., Voudouris, K. S., Stratis, J. A., Ali, M. F., Christaras, V. *J. Cult. Herit.* **2009**, 10, 152–157.

- (115) Vai, G. B., Lucchi, F. R. *Sedimentology* **1977**, *24*, 211–244.
- (116) Galdenzi, S., Maruoka, T. *J. Caves Karst Stud.* **2003**, *65*, 111–125.
- (117) Kasprzyk, A. *Sediment. Geol.* **2003**, *158*, 167–194.
- (118) Mees, F., Dapper, M. de. *Sediment. Geol.* **2005**, *181*, 225–229.
- (119) Wray, J. J., Squyres, S. W., Roach, L. H., Bishop, J. L., Mustard, J. F., Noe Dobrea, E. Z. *Icarus* **2010**, *209*, 416–421.
- (120) Dogan, A. U., Dogan, M., Chan, D. C. N., Wurster, D. E. *Carbonates Evaporites* **2005**, *20*, 2–7.
- (121) Becker, A., Sötje, I., Paulmann, C., Beckmann, F., Donath, T., Boese, R., Prymak, O., Tiemann, H., Epple, M. *Dalton Trans.* **2005**, 1545–1550.
- (122) Freyer, D., Voigt, W. *Monatsh. Chem.* **2003**, *134*, 693–719.
- (123) Hill, A. E. *J. Am. Chem. Soc.* **1937**, *59*, 2242–2244.
- (124) Hardie, L. A. *Am. Mineral.* **1967**, *32*, 171–200.
- (125) Kirfel, A., Will, G. *Acta Crystallogr., Sect. B: Struct. Sci* **1980**, *36*, 2881–2890.
- (126) Bock, E. *Can. J. Chem.* **1961**, *39*, 1746–1751.
- (127) Wang, Y. W., Meldrum, F. C. *J. Mater. Chem.* **2012**, *22*, 22055–22062.
- (128) VanDriessche, A. E. S., Benning, L. G., Rodriguez-Blanco, J. D., Ossorio, M., Bots, P., García-Ruiz, J. M. *Science* **2012**, *336*, 69–72.
- (129) Stawski, T. M., van Driessche, A. E. S., Ossorio, M., Diego Rodriguez-Blanco, J., Besselink, R., Benning, L. G. *Nat. Commun.* **2016**, *7*, 11177.
- (130) Abriel, W., Nesper, R. *Z. Kristallogr. Cryst. Mater.* **1993**, *205*, 99–113.
- (131) Singh, N. B., Middendorf, B. *Prog. Cryst. Growth Charact. Mater.* **2007**, *53*, 57–77.
- (132) Lewry, A. J., Williamson, J. *J. Mater. Sci.* **1994**, *29*, 5524–5528.
- (133) Badens, E., Veessler, S., Boistelle, R., Chatain, D. *Colloids Surf., A* **1999**, *156*, 373–379.
- (134) Ballirano, P., Caminiti, R. *J. Appl. Crystallogr.* **2001**, *34*, 757–762.

TRAPPING AMORPHOUS CARBONATES



Amorphous intermediates during the crystallization process received increasing interest in recent years due to the desire to gain more control over crystallization pathways and products. Yet, their fast transformation to a crystalline modification poses a severe problem to a detailed characterization. We circumvented this problem and developed a new reaction system that allows the stabilization and isolation of amorphous intermediates of various carbonates (calcium, strontium, barium, manganese, and cadmium). The long-term stabilization of these transient species enabled detailed investigation of their morphology, composition, and structure. Our study shows that a multi-step crystallization pathway *via* amorphous intermediates is open to a great number of carbonates.

This chapter contains an adapted manuscript submitted to the *Journal of the American Chemical Society*.

Authorship Contribution

Study conception and design	S. Leukel W. Tremel
Acquisition of data	S. Leukel M. Panthöfer M. Mondeshki G. Kieslich Y. Wu N. Krautwurst
Analysis and interpretation of data	S. Leukel M. Panthöfer M. Mondeshki G. Kieslich Y. Wu
Drafting of manuscript	S. Leukel
Critical revision	M. Panthöfer M. Mondeshki G. Kieslich Y. Wu W. Tremel

2.1 INTRODUCTION

Crystallization processes play a fundamental role in the synthesis and development of new materials, especially when specific polymorphs or distinct morphologies are desired. Many organisms solve this problem in biomineralization,¹⁻³ where proteins⁴ or templates⁵ are involved in the nucleation and crystal growth of inorganic compounds. In this way, bones⁶ or teeth⁷ are formed as hybrid materials with unusual morphologies and extraordinary mechanical properties.

Calcium carbonate is the most common and widespread biomineral.⁸ It is found mostly in marine organisms, forming the shells of mussels⁹ or the exoskeletons of algae¹⁰ and corals.^{11,12} Many organisms have developed strategies to stabilize an amorphous form of calcium carbonate (ACC), which serves as reservoir for subsequent crystallization and molding into the desired shape.^{13,14} Proteins and organic templates direct the morphology and phase during the crystallization,^{15,16} e.g. aragonite, the high pressure modification of calcium carbonate, is formed at ambient conditions for the nacre of clams.¹⁷ To interfere selectively in the nucleation and growth of crystals for synthetic applications,¹⁸ a detailed understanding of the crystallization process is necessary. Therefore, early crystallization stages and amorphous intermediates have received increasing attention. For metals,^{19,20} metal chalcogenides,^{21,22} molybdenum oxides,²³ calcium sulfate,^{24,25} clathrate hydrates,²⁶ or iron oxide,²⁷ crystallization *via* clusters (partially stabilized by “capping agents”), amorphous, and partially crystalline intermediates were reported, with CaCO₃ being a prominent system.²⁸⁻³¹ The ability of ACC to crystallize in different morphologies and modifications makes it an interesting model system for materials science.³² Phase selection can be influenced by temperature,³³ pressure,³⁴ or additives (e.g. magnesium ions and amino acids).^{32,35} Even chirality can be induced by chiral amino acids.³⁶⁻³⁸ In addition, calcium carbonate finds widespread use in industrial³⁹ and medical applications, i.e. as drug carrier.⁴⁰

Still, the characterization of these intermediates is a difficult task due to their metastability and the fast transformation of these short-lived species.^{41,42} Moreover, ACC can vary in water content,⁴³ particle size,⁴⁴ and amount of foreign ions.⁴⁵ In particular, the properties of ACC depend on the pH during synthesis.⁴⁶ ACC has been made in different ways: Faatz et al. used the hydrolysis of carbonic esters,⁴⁷ Han embedded ACC in a self-assembled

monolayer,⁴⁸ and Meldrum and co-workers employed freeze-drying.⁴⁹ A variety of inorganic^{50,51} and organic additives^{31,52–55} were used to stabilize the amorphous modification. However, these methods are restricted to the isolation of calcium carbonate and often require the addition of additives like Mg^{2+} cations, which are incorporated into ACC, thereby changing its composition.^{56,57} This restricts the generalization of the observed phenomena. Although several synthetic routes to ACC and studies on its structure have been reported,^{3,58,59} other amorphous carbonates (besides MnCO_3) could be isolated only with large amounts of additives^{60,61} and without structural characterization.⁶² Amorphous MnCO_3 was synthesized by mixing cooled MnSO_4 and Na_2CO_3 solutions.⁶³ Still, there is evidence that amorphous SrCO_3 and BaCO_3 are present in some bacteria.⁶⁴ Also, traces of amorphous SrCO_3 were observed in tribological experiments inside the micelles of strontium soaps.⁶⁵

Here, we describe a new reaction system that allows the stabilization and isolation of amorphous intermediates of metal carbonates. Immediately after their formation, the amorphous intermediates are trapped by encapsulating them with surface ligands and extracted from the reaction. This stops any further phase transformation abruptly. The system allows trapping highly reactive transient amorphous species of CaCO_3 , SrCO_3 , BaCO_3 , MnCO_3 , and CdCO_3 . Except for BaCO_3 , which crystallizes within hours, we were able to stabilize these intermediates for several weeks or months. This allowed a detailed investigation of their composition and structure by transmission electron microscopy (TEM), solid state nuclear magnetic resonance (NMR), Fourier transform infrared (FTIR) spectroscopy, thermogravimetric and differential thermal analysis (TGA-DTA), and high-energy synchrotron total scattering experiments. In this way, we could derive a structural model for ACC that allowed for the analysis of the Ca^{2+} coordination sphere. Our results show that crystallization *via* amorphous intermediates is a possible pathway for many carbonates of divalent metals and not restricted to calcium carbonate. The detailed structural characterization of a variety of amorphous carbonates represents a conceptual advance for our understanding of stepwise crystallization *via* amorphous intermediates.^{66–68}

2.2 RESULTS AND DISCUSSION

Stabilization of Amorphous Carbonates

The amorphous intermediates of the carbonates were isolated with a two-phase reaction system consisting of a water/methanol mixture and a cyclohexane phase. Sodium carbonate and sodium oleate were dissolved in the aqueous phase. Methanol prevented oleate from forming micelles in aqueous solution, thereby increasing the number of “free” oleate anions.⁶⁹ Cyclohexane was used as organic phase, because it is immiscible with methanol. A white emulsion forms upon stirring, as sodium oleate acts as a surfactant. A solution of the respective metal chloride in water/methanol was added, and the stirring was stopped immediately afterwards. The emulsion separated into two phases within seconds. The turbid cyclohexane phase contained the ligand-stabilized amorphous intermediates. This organic phase was decanted carefully, the product was isolated by centrifugation, washed with acetone, and subsequently stored in a desiccator. The surface-bound oleate ligand interrupts the crystallization of the amorphous particles. The solubility of carbonates in the cyclohexane phase is so low that no phase transformation *via* dissolution and recrystallization can occur. In air, the products remained amorphous for days to several months. No crystallization was observed *in vacuo*. Only amorphous BaCO_3 crystallized within several hours, which prevented to collect synchrotron data of this compound. However, its non-crystallinity could be confirmed by laboratory powder X-ray diffraction (Figure S1, Supporting Information).

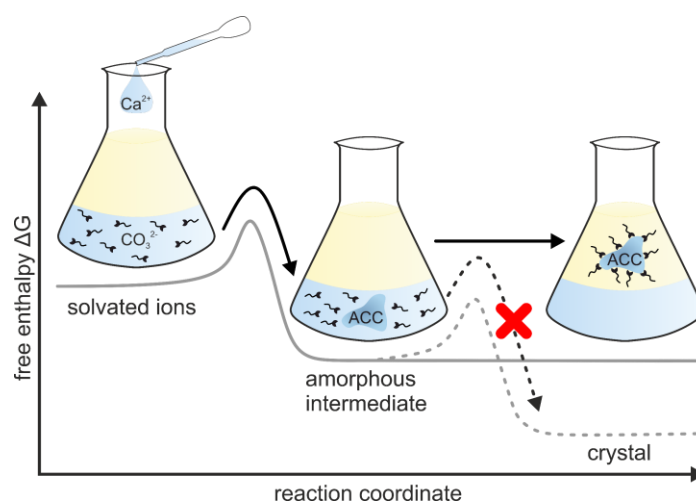


Figure 2.1 Reaction scheme of the stabilization of ACC: A calcium chloride solution is added to a two-phase system, consisting of cyclohexane and a solution of sodium carbonate and oleate in water/methanol. After the formation of ACC, the particles are capped immediately by the oleate ligand, which stops further transformation to a crystalline modification. The functionalization with oleate makes the particles hydrophobic, and they are extracted into the cyclohexane layer.

In the following, the amorphous carbonates of the respective elements are referred to as ACC (amorphous calcium carbonate), ASC (amorphous strontium carbonate), ABC (barium), AMnC (amorphous manganese carbonate), and ACdC (amorphous cadmium carbonate).

Morphology and Composition

TEM images (Figure 2.2) show comparable morphologies for all samples. The amorphous intermediates form drop-like nanoparticles with diameters of ~20 nm. The particles are polydisperse and fused to larger aggregates.

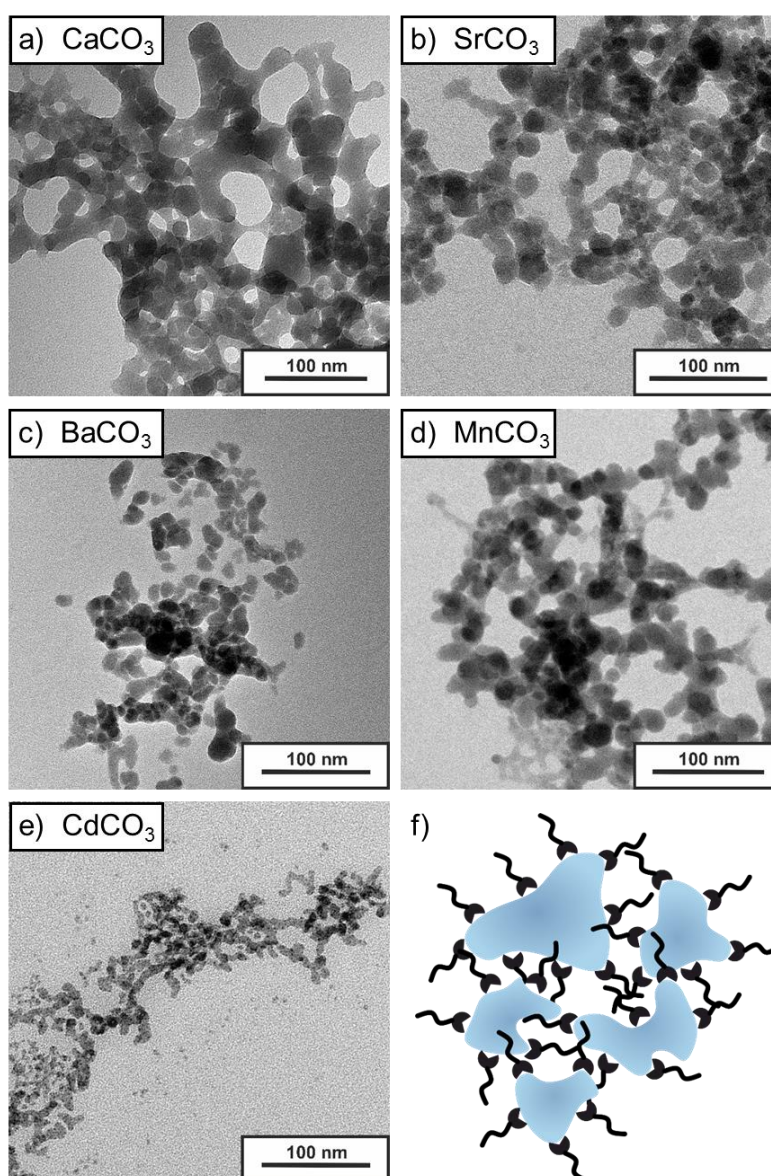


Figure 2.2 TEM image of a) ACC, b) ASC, c) ABC, d) AMnC, and e) ACdC. All carbonates form drop-like, fused nanoparticles with a size of ~20 nm. ACdC particles are significantly smaller. f) Schematic sketch of amorphous carbonate particles with oleate layer.

Whereas all alkaline earth carbonates and AMnC have a comparable particle size, ACdC particles are significantly smaller (~10 nm). We assume that the lower solubility of CdCO_3 ⁷¹ leads to a higher supersaturation on mixing, which results in the formation of a higher number of smaller nuclei according to classical nucleation theory.⁷² The drop-shaped morphology of all amorphous intermediates is in accordance with previous studies that suggest carbonate minerals to have liquid-like precursors.^{47,55,62} Despite their liquid-like appearance, the amorphous carbonates presented here are solids.

The composition of the amorphous intermediates was probed by thermogravimetric and differential thermal analysis (TGA-DTA). The results for ACC are shown in Figure 2.3. The TGA curve (red) exhibits two mass losses at 50–200 °C and at 350–500 °C. We attribute the first step (-11 wt%) to the loss of structural water. The second step (-19 wt%) is associated with the thermal decomposition of the oleate ligand. The respective temperature range is in agreement with reports for the decomposition of calcium soaps.⁷³ From the mass loss, we determined the composition of ACC as $\text{CaCO}_3 \times 0.9 \text{H}_2\text{O}$. Comparable values were found in previous studies.^{43,58,74} The sample contained ~0.1 mol of oleate per formula unit. Assuming a particle radius of ca. 10 nm from TEM, the amount of oleate corresponds to a layer thickness of ca. 2 nm (mathematical derivation, Supporting Information). This value is generally assumed for a monolayer of oleic acid.⁷⁵ Such a monolayer of oleic acid, coordinated with the carboxylate group to the ACC particle, is in agreement with the observed dispersibility properties in non-polar solvents.

For ASC, ABC, AMnC, and ACdA (Figure S2, Supporting Information), the approximate compositions were calculated: $\text{SrCO}_3 \times 0.8 \text{H}_2\text{O}$, $\text{BaCO}_3 \times 0.4 \text{H}_2\text{O}$ (water content was presumably reduced during the treatment in the vacuum oven), $\text{MnCO}_3 \times 0.9 \text{H}_2\text{O}$, and $\text{CdCO}_3 \times 0.7 \text{H}_2\text{O}$. All samples contained ca. 0.1 mol oleate. Except in ACdC, a higher content of ca. 0.2 mol was found. This corresponds to the smaller size of the ACdC particles (Figure 2e) and the respective higher ratio of surface to volume.

The DTA curve (blue) of ACC displays two endothermic effects, which correspond to the two steps of mass loss. The exothermic effect at 340 °C is caused by the crystallization of ACC to calcite. This temperature is in agreement with previous reports^{50,74} and indicates that the oleate coating does not exert an effect on the crystallization of the amorphous carbonates. The crystallization process proceeds *via* a solid state reaction, as ACC is already dehydrated at this temperature and no solvent-mediated mechanism is possible. Thermally induced

crystallization of ASC occurs at a lower temperature of 310 °C. ABC crystallizes at 250 °C. We assume that the weaker coordination of the carbonate on the larger (Pearson soft)⁷⁶ cation, e.g. Ba²⁺, results in higher mobility of the carbonate group and facilitates the structural rearrangement during the thermal crystallization process. The carbonates of the transition metals, AMnC and ACdC, show no thermally induced crystallization, as they decompose already at ca. 250 °C.

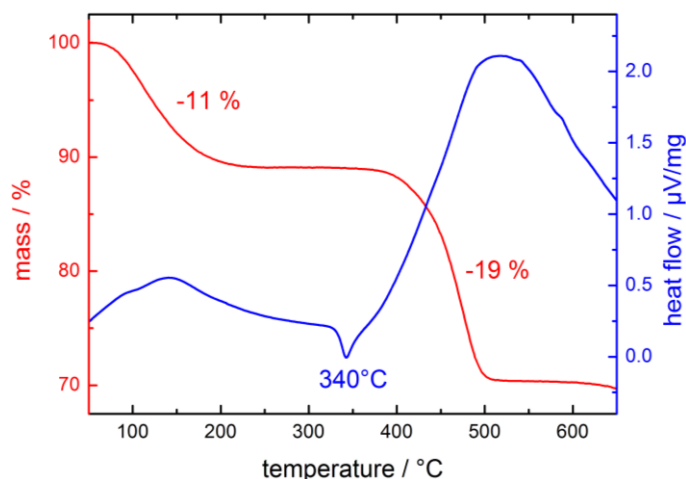


Figure 2.3 TGA-DTA of ACC capped with oleate. In the TGA curve (red), two mass loss steps occur. The first between 50 °C and 200 °C is attributed to the loss of structural water. The second mass loss around 450 °C originates from the decomposition of the oleate ligand. In the DTA curve (blue), we observe an exothermic effect at 340 °C, which indicates the thermally induced crystallization of ACC to calcite.

Oleate Capping

Nuclear magnetic resonance (NMR) is a powerful tool to probe the local structure of amorphous materials. Using ¹³C-enriched samples synthesized with Na₂¹³CO₃, we performed magic angle spinning ¹H-¹³C cross polarization experiments (¹³C{¹H} CP MAS-NMR) and recorded heteronuclear correlation spectra (HETCOR) of all amorphous intermediates (except for paramagnetic AMnC). The ¹³C{¹H} CP MAS-NMR spectrum of the ACC sample is displayed in Figure 2.4a. The presence of the oleate ligand is indicated by the signals of the methylene groups around 30 ppm and the ethenyl group at 130 ppm. The carboxylate group is not observed due to its negligibly small intensity, compared to the overlying carbonate signal of the ¹³C-enriched ACC centered around 168.5 ppm. The chemical shift of the carbonate is in accordance with previous reports of Nebel et al.⁷⁷ Compared to crystalline calcite (Figure 2.4a, inset), the carbonate signal of ACC is significantly broadened with a FWHM of 288 Hz. As broadening due to a lower mobility in the amorphous state is

highly unlikely, we attribute the broad signal to a variety of slightly different chemical environments of the carbonate group in ACC (*vide infra*, PDF).

HETCOR experiments were performed to probe the contact between the respective nuclei in the sample (Figure 2.4b). The ^{13}C spectrum on the x-axis displays the carbonate signal at 168.5 ppm and the methylene groups of the oleate chain around 30 ppm. On the y-axis, the ^1H spectrum shows the oleate signals around 0.9 ppm (ethenyl protons at 5.0 ppm). The water signal is too broad to be resolved (Figure S3, Supporting Information). Previous studies give values between 5.0 ppm⁷⁷ and 5.3 ppm⁴³ for the water signal of ACC. The HETCOR experiment shows a strong correlation between carbonate and the assumed water signal around 5 ppm, as ACC contains ~ 0.9 mol structural water (Figure 2.3). We also observe the contact of the hydrogen and carbon atoms in the oleate chain. Yet, the oleate carbon atoms show no correlation to the water protons, and we do not observe a correlation between oleate protons and the carbonate group. Therefore, we conclude that carbonate and water molecules are not connected to the oleate chains. The oleate chains are solely on the surface of the particles and are not incorporated into the amorphous material. Hence, the oleate-stabilized particles are a valid system to study the amorphous intermediates during the crystallization of the respective carbonates.

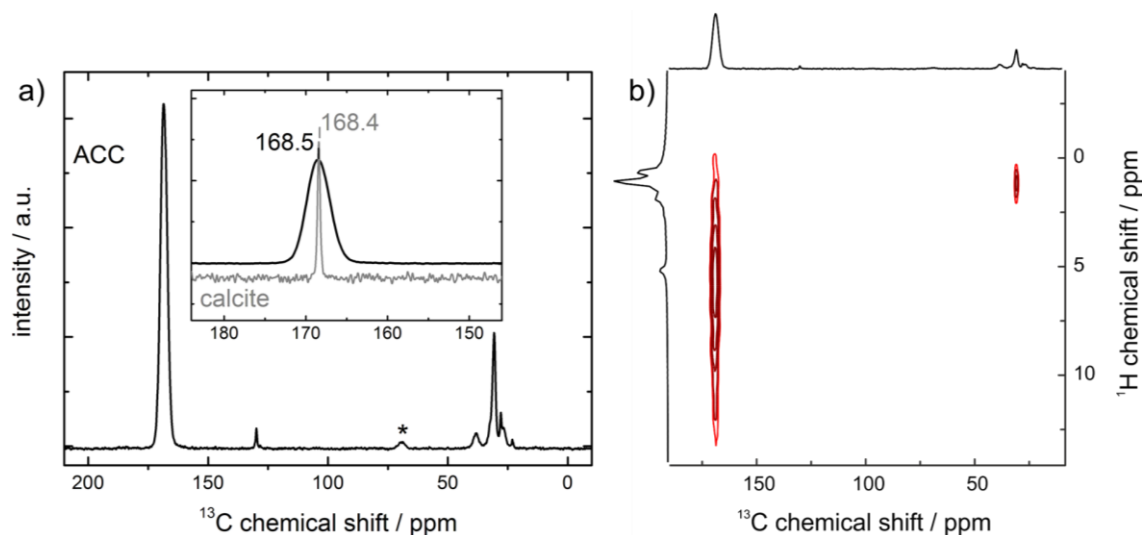


Figure 2.4 a) $^{13}\text{C}\{^1\text{H}\}$ CP MAS-NMR of ^{13}C -enriched ACC with oleate. Spectrum displays the methylene groups of the oleate chain around 30 ppm and the ethenyl group at 130 ppm. The carbonate signal centered at 168.5 ppm is broadened and slightly shifted, compared to calcite (inset). Spinning side band is marked with an asterisk. b) HETCOR spectrum of ^{13}C -enriched ACC with oleate. Contact between carbonate and water at ca. 5 ppm is indicated, as well as the evident correlation between the respective hydrogen atoms and carbon atoms of the oleate chain. The oleate signals shows no correlation with neither water nor carbonate. Therefore, we conclude that oleate is on the surface of the particles and not inside the amorphous material.

We observe comparable spectra for all amorphous carbonates (Figure S4, Supporting Information). Interestingly, ABC and – to a smaller degree – ASC display an additional small signal at ca. 162 ppm in the ^{13}C spectrum. For ABC, we observe a correlation between this signal and strongly deshielded protons at ~ 12 ppm. Both the coupling and the respective chemical shift⁷⁷ are strong evidence that hydrogencarbonate species are present in the amorphous intermediates of barium and strontium carbonate. For the other carbonates, these species are not observed and were also excluded in previous studies on ACC.⁷⁷ We assume that the weak coordination of the larger Pearson⁷⁶ soft cations (Ba^{2+} and Sr^{2+}) increases the basicity of the carbonate group, which results in the partial protonation of the former. Chemical shift and FWHM of the carbonate signal of the amorphous and respective crystalline carbonates are compiled in Table 2.1.

Table 2.1 ^{13}C chemical shift δ and linewidth of the carbonate signal of the amorphous carbonates and their respective crystalline modifications (in brackets).

Sample	$\delta(^{13}\text{C}) / \text{ppm}$	FWHM / Hz
ACC (calcite)	168.5 (168.4)	288 (33)
ASC (strontianite)	169.4 (170.3)	261 (38)
ABC (witherite)	168.5 (169.7)	261 (25)
ACdC (otavite)	168.4 (169.5)	343 (56)

Carbonate Environment

Infrared spectra were recorded of the amorphous intermediates and their respective crystalline modifications (Figure S5, Supporting Information). Figure 2.5a displays the FTIR spectrum of ACC. The sample exhibits the characteristic vibrational modes of the carbonate anion:⁷⁸ the symmetric stretching (ν_1), the out-of-plane deformation (ν_2), and the asymmetric stretching (ν_3) mode. Compared to calcite, the bands of ACC are broadened and slightly shifted. The ν_4 mode around 700 cm^{-1} is extremely broadened and therefore not detectable, which is expected for ACC.⁷⁷ In contrast, the ν_1 mode, which is symmetry-forbidden in calcite, has a pronounced band. This underlines the symmetry loss in the amorphous state. All amorphous carbonates show an intense, broad band at around 3300 cm^{-1} . This band originates from the O-H stretching vibration of structural water, quantified by thermogravimetric analysis (Figure 2.3, *vide supra*). The O-H bending vibration is manifested by the weak band at 1650 cm^{-1} . Additionally, we observe the C-H vibrations of the surface-bound oleate ligands at $2850\text{--}3000 \text{ cm}^{-1}$. For ACdC, these bands are more intense, which is consistent

with a smaller particle size and a resulting larger surface area that is coated with oleate (Figure S6, Supporting Information). The vibrational mode wavenumbers of the carbonate group are clearly shifted in a linear fashion with the ionic radius⁷⁹ r of the alkaline earth metals (Figure 2.5b). Whereas the stretching vibrations (ν_1 and ν_3) appear at lower energies with increasing radius, the out-of-plane vibrational mode ν_2 shows opposite behavior.

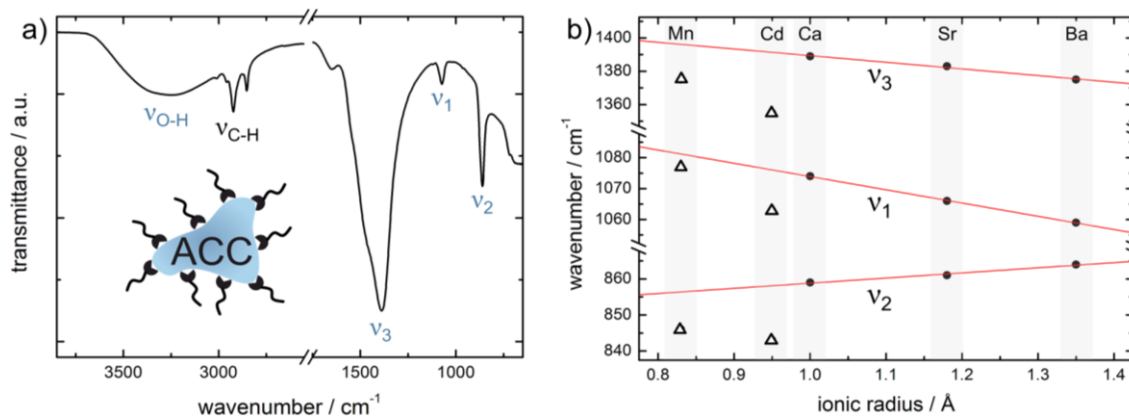


Figure 2.5 a) FTIR spectra of ACC with oleate ligand. Vibrational modes of the carbonate anions are assigned (ν_1 : symmetric stretching, ν_2 out-of-plane, ν_3 : asymmetric stretching). Moreover, the spectrum of ACC shows the C-H stretching vibrational modes of the oleate ligand and a pronounced water band around 3300 cm^{-1} . b) Vibrational mode wavenumbers of the amorphous carbonates plotted against the ionic radii of the metal cations. The carbonates of the alkaline earth elements show a linear dependence on the ionic radius (red line). The carbonates of the transition metals, AMnC and ACdC, do not follow this trend and their vibrational modes appear at lower wavenumbers.

Free CO_3^{2-} anions have D_{3h} symmetry with the ν_2 vibration at 879 cm^{-1} .⁸⁰ Interaction with cations in the solid decreases their symmetry and leads to a shift of the band position. Therefore, the ν_2 bands in the amorphous modifications appear clearly below this value. The wavenumbers show a clear trend with increasing ionic radius from Ca^{2+} to Ba^{2+} , which indicates a stronger interaction for calcium. As the metal-oxygen interaction becomes stronger, the C-O bond is weakened, which shifts the ν_2 band to lower wavenumbers. For both stretching vibrations ν_1 and ν_3 , a decrease of the wavenumber is found when going from Ca^{2+} to Ba^{2+} . As the oxygen atoms are required to move in these vibrational modes, a stronger metal-oxygen interaction shifts the bands to higher energies, i.e. to higher wavenumbers. The distinct deviation of the transition metals manganese and cadmium can be explained by a more covalent bonding character, in contrast to the mainly ionic interaction in the alkaline earth carbonates. In all cases, the vibrational modes are lower in energy than expected from the r - ν correlation. This indicates a significantly stronger interaction of the metal with the

oxygen, which is also indicated by the low decarboxylation temperatures of AMnC and ACdC (Figure S2, Supporting Information). Gatehous et al.⁸¹ reported a shift of ν_2 to lower wavenumbers in more covalent carbonates and nitrates. This is in accordance with our findings that the deviation is smaller for manganese than for cadmium, which forms more covalent bonds. The respective wavenumbers for the vibrational modes of the amorphous carbonates and their crystalline modifications are compiled in Table 2.2.

Table 2.2 Vibrational mode wavenumbers of the amorphous carbonates and their respective thermodynamic crystalline modification (in brackets).

Sample	ν_3 / cm^{-1}	ν_1 / cm^{-1}	ν_2 / cm^{-1}	ν_4 / cm^{-1}
ACC (calcite)	1389 (1388)	1074 (1089)	860 (872)	– (711)
ASC (strontianite)	1383 (1483)	1066 (1072)	861 (855)	– (706, 699)
ABC (witherite)	1375 (1411)	1059 (1059)	864 (855)	– (693)
AMC (rhodochrosite)	1383 (1395)	1077 (1075)	846 (861)	– (725)
ACdC (otavite)	1355 (1383)	1063 (1074)	843 (858)	– (722)

Structure

Total X-ray scattering experiments were performed at the Diamond Light Source, beamline I15, to determine the local structure of the amorphous intermediates. From these data, the pair distribution function (PDF) of each compound was calculated with the program GUDRUNX.⁸² The PDF is a distribution of the interatomic distances of the sample in real space. It has proved to be a powerful technique to probe the local structural environment in structurally disordered⁸³ and amorphous systems.⁸⁴ Figure 2.6a displays the experimental PDF of the ACC sample (black). Four peaks can be clearly distinguished.^{8,59} The first peak at 1.28 Å originates from the carbon-oxygen (C-O) distance in the carbonate group.⁸⁵ The metal-oxygen (M-O) distances in the first coordination sphere of the cation cause to the most intense peak at 2.40 Å, and the intramolecular O-O distance in the carbonate group also contributes. The peaks around 4.08 Å and 6.21 Å originate from a multitude of different interatomic distances. We modeled the PDF data using Topas Academic V6.⁸⁶ 100 runs starting from random configurations all converged in a small range of residuals from $R_{\text{wp}} = 9.7$ to $R_{\text{wp}} = 13.1$. A typical model is plotted in Figure 2.6a. We considered the contribution of the ACC core of the particles (red) as well as the oleate layer (turquoise). The oleate shell was modeled as a separate phase using rigid bodies with no internal degrees of freedom. The rigid bodies were allowed to translate and rotate in such a way that carbon

atoms 1 and 9 resided in spherical shells around $r = 13 \text{ \AA}$ and $r = 21 \text{ \AA}$, respectively. The shell was modeled with a total of 58 oleate molecules. For ease of computation, inversion symmetry (P-1) was applied. The main contribution of the oleate is the peak at 1.53 \AA originating from the C-C bond within the alkyl chain, which is observed as a shoulder on the C-O peak. Also, we evaluated the coordination number (interatomic distance $< 2.8 \text{ \AA}$) of the calcium atom, taking into account the ten best models (Figure 2.6b). The distribution of the coordination numbers (CN) is broad and exhibits a maximum slightly above $\text{CN} = 5$.

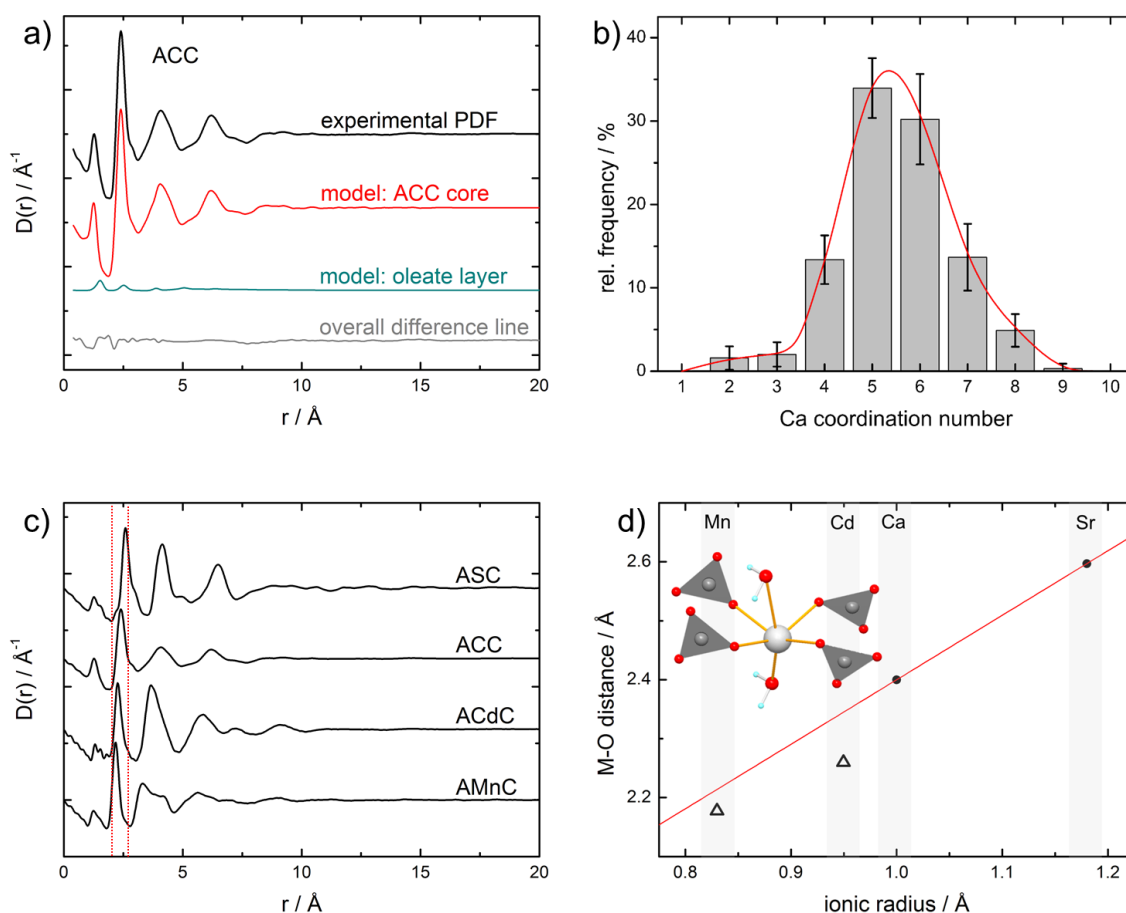


Figure 2.6 a) Experimental pair distribution function of the ACC sample (black) exhibits no ordering beyond 10 \AA . The ACC core (red) and the oleate layer (turquoise) of the particles were modeled. Difference line is shown in gray. b) Distribution of the Ca CN in the structural model of ACC. The maximum of the distribution is closer to $\text{CN} = 5$, in contrast to calcite, where Ca is coordinated by six oxygen atoms. c) Experimental PDFs of ASC, ACC, ACdC, and AMnC all exhibit a comparable lack of long-range order; cut-off is around 10 \AA in all cases. The second, most intense peak (highlighted) shifts significantly between samples. This peak originates primarily from the metal-oxygen (M-O) distance in the first coordination sphere of the cation. Intramolecular O-O distances of the carbonate also contribute. d) The M-O distance scales with the ionic radius of the respective cation in the amorphous carbonate. For the transition metals, manganese and cadmium, the distance is shorter than expected from the ionic radius (red line). This indicates the more covalent character of the metal-oxygen bond.

Compared to calcite with its distorted octahedral coordination by six oxygen atoms, calcium in ACC exhibits a lower mean coordination number. The reduced coordination number can be understood as a result of the fast, kinetically controlled precipitation of ACC, which prevents the saturation of the coordination sphere of calcium. The PDFs of ASC, ACdC, and AMnC strongly resemble that of ACC (Figure 2.6c). They slightly differ in the number of discernable peaks, but none of them shows significant ordering beyond 10 Å. Despite capping with oleate, ABC proved to be labile and crystallized before total scattering experiments could be performed. In a comparison of the different carbonates, the peak positions increase with the ionic radius of the respective metal cation. A plot of the M-O distance in the first coordination sphere against the ionic radius (Figure 2.6d) shows a monotonic correlation. Yet, for the amorphous transition metal carbonates, AMnC and ACdC, the M-O distance is shorter than estimated from the radius of the cation. The shortening of this distance is related to the more covalent character of the M-O bond, which is also indicated by the FTIR spectra (Figure 2.5b) and the low decomposition temperature of AMnC and ACdC (Figure S2, Supporting Information).

Conclusion

We devised a new reaction system that allows the synthesis of amorphous metal carbonates. Intermediates that appear during the crystallization process were trapped by capping them with oleate ligands immediately after their formation. This induced long-term stability to these transient species and allowed their detailed structural and spectroscopic characterization. Two-dimensional NMR experiments revealed that the ligand was not integrated into the amorphous carbonate. The amorphous intermediates form drop-like nanoparticles and contain structural water (less than one molecule per formula unit). Their PDFs show short-range order on the scale of several Å. By modelling the PDF data of ACC, we found a reduced coordination number of the cation compared to the crystalline modification. This study shows that crystallization pathways *via* amorphous intermediates are accessible not only to calcium, but to a broad group of carbonates. Our reaction system allowed to observe these still unknown first steps of their crystallization process. The multitude of amorphous intermediates that we observed in this mineral class of carbonates suggests that such a crystallization pathway is considerably more common than generally assumed. Moreover, our approach can be generalized for transient intermediates in systems other than carbonates.

During the precipitation experiments, the appearance of an amorphous intermediate phase changes the supersaturation with regard to the crystalline (and thermodynamically stable) product. Supersaturation is a key parameter affecting crystallization. Therefore, a decrease of the supersaturation due to the formation of an intermediate phase has strong implications on our view of the crystallization process and the possibilities to direct it with additives. This study broadens our understanding of complex pathways during crystallization and may aid ultimately in the synthesis of tailor-made materials.

2.3 EXPERIMENTAL SECTION

Materials

CaCl₂ (98 %, Merck), SrCl₂ (99.5 %, Alfa Aesar), MnCl₂ (97 %, ABCR), CdCl₂ (99 %, Sigma-Aldrich), BaCl₂ (99.5 %, Merck), Na₂CO₃ (99.5 %, Sigma-Aldrich), Na₂¹³CO₃ (99 %, Sigma-Aldrich), sodium oleate (82 %, Sigma-Aldrich), methanol (HPLC grade, Fisher Chemicals), cyclohexane (Analytical reagent grade, Fisher Chemicals), milli Q deionized water.

Synthesis

CaCl₂ (0.5 mmol) was dissolved in a mixture of water (5 mL) and methanol (5 mL) to yield a 0.05 M solution. Na₂CO₃ (0.5 mmol) and sodium oleate (0.06 mmol) were dissolved in a mixture of water (10 mL) and methanol (10 mL). The carbonate/oleate solution was transferred to a 200 mL Erlenmeyer flask, and 20 mL of cyclohexane was added. The mixture was stirred vigorously with a magnetic stirrer resulting in a milky white emulsion. Under continuous stirring, the CaCl₂ solution was added. Immediately after addition, the stirring was stopped and the emulsion separated into two phases. The upper turbid organic phase was separated by decantation and centrifuged to isolate the oleate-capped ACC particles. The product was washed with acetone and dried *in vacuo*.

The synthesis of ASC, AMnC, and ACdC was performed analogously with the respective metal chlorides. After the synthesis of ABC, the product was immediately dried in a vacuum oven at 40 °C. For NMR experiments, ¹³C-enriched samples were prepared using Na₂¹³CO₃.

Characterization

X-ray powder diffraction. X-ray diffraction patterns were recorded with a Bruker AXS D8 Discover diffractometer equipped with a HiStar detector using graphite monochromatized CuK α radiation. Samples were attached to a glass substrate without using an adhesive. Individual frames were typically recorded at $2\theta = 24^\circ, 34^\circ, 44^\circ, 54^\circ, 64^\circ, 74^\circ, 84^\circ$ (detector distance 150 mm, detector range $\Delta(2\theta) = 35^\circ$) in 0.02° steps covering a 2θ range from 5° to 85° . X-ray diffraction patterns were integrated from individual frames using the Bruker AXS GADDS software package⁸⁷ and merged using Bruker AXS EVA.⁸⁸

FTIR spectroscopy. ATR-FTIR spectroscopy was performed using a Nicolet iS10 Spectrometer manufactured by Thermo Scientific. The spectra were recorded in a frequency range from 650 cm^{-1} to 4000 cm^{-1} with a resolution of 1.4 cm^{-1} per data point.

Solid state NMR spectroscopy. All experiments were recorded on a Bruker Avance 400 DSX NMR spectrometer at a ^1H frequency of 399.87 MHz and ^{13}C frequency of 100.55 MHz. A commercial three-channel 4 mm Bruker probe head was used at 10 kHz magic angle spinning (MAS) for the solid samples. At this moderate spinning frequency, the additional heating effects caused by bearing gas friction are insignificant. Thus, the sample temperature was not further corrected. The ^{13}C single pulse (SP) direct excitation experiment was carried out for the reference calcite sample by a 90° pulse with a length of $4\ \mu\text{s}$ and repetition time of 2200 s averaging 32 transients. The ^1H - ^{13}C cross polarization (CP) experiments were recorded with a duration of the variable amplitude (64–100 %) CP contact time of $200\ \mu\text{s}$ collecting 5 k transients with 6 s recycle delay. The HETCOR experiment was recorded using 128 increments in the indirect dimension with 256 scans per increment in the States mode using 3 s recycle delay. To ensure that only the closest through space contacts are visible in the spectrum, a variable amplitude (64–100 %) cross polarization time of $20\ \mu\text{s}$ was applied. For all ^{13}C NMR experiments, a two pulse phase modulation (TPPM) heteronuclear decoupling scheme was used. The ^{13}C chemical shifts were referenced to external adamantane as a secondary standard at 38.48 ppm.

Thermal analysis. Coupled thermogravimetric and differential thermal analysis (TGA-DTA) was carried using a Netzsch STA 449 F3 Jupiter device. The sample ($\sim 10\text{ mg}$) was heated in an alumina cup in argon atmosphere from 50°C to 600°C at a heating rate of 10 K/min .

Transmission electron microscopy. TEM samples were prepared by drop-casting $20\ \mu\text{L}$ of the respective sample dispersion on 400 mesh carbon copper grids (Plano GmbH, Wetzlar,

Germany) and measured with a Technai Spirit G2 at 120 kV acceleration voltage, equipped with a standard 4K CCD camera.

Total scattering. Experiments were conducted at beamline I15 at the Diamond Light Source Inc. using a wavelength of 0.1707 Å (72.7 keV) and a 2D MAR 345 detector. CeO₂ was used to calibrate the experimental setup. Data were processed using DAWN.⁸⁹ The pair distribution function was calculated with GUDRUNX.⁸² Structural models were derived for a set of 73 Calcium ions, 73 carbonate ions and 67 water molecules inside a cubic box of space group symmetry P1. The volume of the box was derived from volume increments⁹⁰ and accords to a phase density of 2.351 g/cm³. Carbonate ions and water molecules were treated as rigid bodies. The C-O distance was made a free variable in the later steps of refinement while O-H distances were fixed. The repulsive interatomic/-molecular interactions were modeled by applying anti-bumping restraints for all element pairs according to values determined from the corresponding carbonates. Attractive interactions were modeled according to bond valences for Ca-O_{carb} and Ca-O_{water}, respectively. The starting models were generated by random expansion of all constituents from the origin using simulated annealing upon periodic boundary conditions. All modelling and refinement was performed using Topas Academic V6.

2.4 REFERENCES

- (1) Weiner, S., Addadi, L. *J. Mater. Chem.* **1997**, *7*, 689–702.
- (2) Carvalho, R. T. de, Salgado, L. T., Amado Filho, G. M., Leal, R. N., Werckmann, J., Rossi, A. L., Campos, A. P. C., Karez, C. S., Farina, M. *J. Phycol.* **2017**, *53*, 642–651.
- (3) Reeder, R. J., Tang, Y., Schmidt, M. P., Kubista, L. M., Cowan, D. F., Phillips, B. L. *Cryst. Growth Des.* **2013**, *13*, 1905–1914.
- (4) Cha, J. N., Shimizu, K., Zhou, Y., Christiansen, S. C., Chmelka, B. F., Stucky, G. D., Morse, D. E. *Proc. Natl. Acad. Sci. U.S.A.* **1999**, *96*, 361–365.
- (5) Wheeler, A. P., George, J. W., Evans, C. A. *Science* **1981**, *212*, 1397–1398.
- (6) Modlin, R. L., Sieling, P. A. *Science* **2005**, *309*, 252–253.

References

- (7) Weaver, J. C., Wang, Q., Miserez, A., Tantuccio, A., Stromberg, R., Bozhilov, K. N., Maxwell, P., Nay, R., Heier, S. T., DiMasi, E., Kisailus, D. *Mater. Today* **2010**, *13*, 42–52.
- (8) Addadi, L., Raz, S., Weiner, S. *Adv. Mater.* **2003**, *15*, 959–970.
- (9) Nehrke, G., Poigner, H., Wilhelms-Dick, D., Brey, T., Abele, D. *Geochem. Geophys. Geosyst.* **2012**, *13*, 75.
- (10) Dudley, W. C., Goodney, D. E. *Deep Sea Res. A* **1979**, *26*, 495–503.
- (11) Mass, T., Giuffre, A. J., Sun, C.-Y., Stifler, C. A., Frazier, M. J., Neder, M., Tamura, N., Stan, C. V., Marcus, M. A., Gilbert, P. U. P. A. *Proc. Natl. Acad. Sci. U.S.A.* **2017**, *114*, E7670-E7678.
- (12) Gattuso, J. *Glob. Planet. Change* **1998**, *18*, 37–46.
- (13) Olszta, M. J., Odom, D. J., Douglas, E. P., Gower, L. B. *Connect. Tissue Res.* **2009**, *44*, 326–334.
- (14) Weiss, I. M., Tuross, N., Addadi, L., Weiner, S. *J. Exp. Zool.* **2002**, *293*, 478–491.
- (15) Gong, Y. U. T., Killian, C. E., Olson, I. C., Appathurai, N. P., Amasino, A. L., Martin, M. C., Holt, L. J., Wilt, F. H., Gilbert, P. U. P. A. *Proc. Natl. Acad. Sci. U.S.A.* **2012**, *109*, 6088–6093.
- (16) Thompson, J. B., Paloczi, G. T., Kindt, J. H., Michenfelder, M., Smith, B. L., Stucky, G., Morse, D. E., Hansma, P. K. *Biophys. J.* **2000**, *79*, 3307–3312.
- (17) Belcher, A. M., Wu, X. H., Christensen, R. J., Hansma, P. K., Stucky, G. D., Morse, D. E. *Nature* **1996**, *381*, 56–58.
- (18) Gao, H.-L., Chen, S.-M., Mao, L.-B., Song, Z.-Q., Yao, H.-B., Cölfen, H., Luo, X.-S., Zhang, F., Pan, Z., Meng, Y.-F., Ni, Y., Yu, S.-H. *Nat. Commun.* **2017**, *8*, 287.
- (19) Ecker, A., Weckert, E., Schnöckel, H. *Nature* **1997**, *387*, 379–381.
- (20) Desireddy, A., Conn, B. E., Guo, J., Yoon, B., Barnett, R. N., Monahan, B. M., Kirschbaum, K., Griffith, W. P., Whetten, R. L., Landman, U., Bigioni, T. P. *Nature* **2013**, *501*, 399–402.
- (21) Corrigan, J. F., Fuhr, O., Fenske, D. *Adv. Mater.* **2009**, *21*, 1867–1871.
- (22) Xu, X., Wang, W., Liu, D., Hu, D., Wu, T., Bu, X., Feng, P. *J. Am. Chem. Soc.* **2018**, *140*, 888–891.
- (23) Liu, T., Diemann, E., Li, H., Dress, A. W. M., Müller, A. *Nature* **2003**, *426*, 59–62.

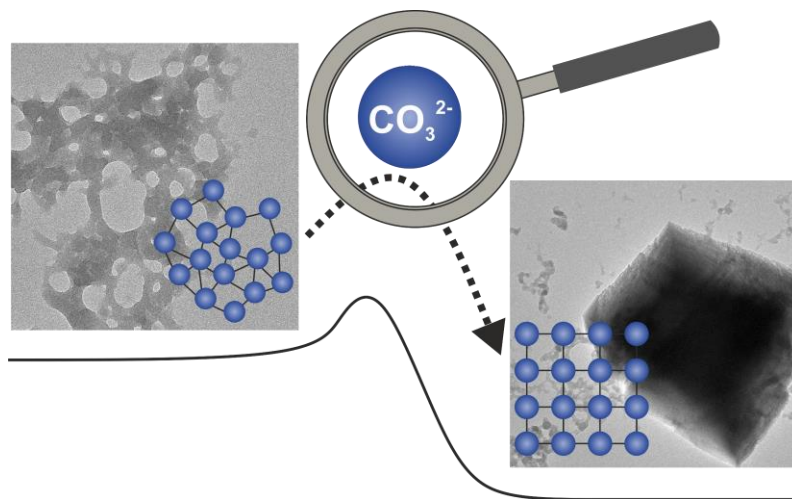
- (24) Stawski, T. M., van Driessche, A. E. S., Ossorio, M., Diego Rodriguez-Blanco, J., Besselink, R., Benning, L. G. *Nat. Commun.* **2016**, *7*, 11177.
- (25) Leukel, S., Panthöfer, M., Mondeshki, M., Schärftl, W., Plana-Ruiz, S., Tremel, W. *Langmuir* **2018**, *34*, 7096–7105.
- (26) Jacobson, L. C., Hujo, W., Molinero, V. *J. Am. Chem. Soc.* **2010**, *132*, 11806–11811.
- (27) Jillian F. Banfield, Susan A. Welch, Hengzhong Zhang, Tamara Thomsen Ebert, R. Lee Penn. *Science* **2000**, 751–754.
- (28) Gebauer, D., Cölfen, H. *Nano Today* **2011**, *6*, 564–584.
- (29) Ihli, J., Bots, P., Kulak, A., Benning, L. G., Meldrum, F. C. *Adv. Funct. Mater.* **2013**, *23*, 1965–1973.
- (30) Rodriguez-Navarro, C., Kudłacz, K., Cizer, Ö., Ruiz-Agudo, E. *Cryst. Eng. Comm.* **2015**, *17*, 58–72.
- (31) Dietzsch, M., Andrusenko, I., Branscheid, R., Emmerling, F., Kolb, U., Tremel, W. *Z. Kristallog. – Cryst. Mater.* **2017**, *232*, 8364.
- (32) Blue, C. R., Giuffre, A., Mergelsberg, S., Han, N., Yoreo, J. J. de, Dove, P. M. *Geochim. Cosmochim. Acta* **2017**, *196*, 179–196.
- (33) Ogino, T., Suzuki, T., Sawada, K. *Geochim. Cosmochim. Acta* **1987**, *51*, 2757–2767.
- (34) Fernandez-Martinez, A., Kalkan, B., Clark, S. M., Waychunas, G. A. *Angew. Chem. Int. Ed.* **2013**, *52*, 8354–8357.
- (35) Wolf, S. E., Loges, N., Mathiasch, B., Panthöfer, M., Mey, I., Janshoff, A., Tremel, W. *Angew. Chem. Int. Ed.* **2007**, *46*, 5618–5623.
- (36) Hazen, R. M., Filley, T. R., Goodfriend, G. A. *Proc. Natl. Acad. Sci. U.S.A.* **2001**, *98*, 5487–5490.
- (37) Orme, C. A., Noy, A., Wierzbicki, A., McBride, M. T., Grantham, M., Teng, H. H., Dove, P. M., DeYoreo, J. J. *Nature* **2001**, *411*, 775–779.
- (38) Jiang, W., Pacella, M. S., Athanasiadou, D., Nelea, V., Vali, H., Hazen, R. M., Gray, J. J., McKee, M. D. *Nat. Commun.* **2017**, *8*, 15066.
- (39) Choi, S. G., Chu, J., Brown, R. C., Wang, K., Wen, Z. *ACS Sustainable Chem. Eng.* **2017**, *5*, 5183–5190.
- (40) Zhao, Y., Luo, Z., Li, M., Qu, Q., Ma, X., Yu, S.-H., Zhao, Y. *Angew. Chem. Int. Ed.* **2015**, *54*, 919–922.

- (41) Shen, Q., Wei, H., Zhou, Y., Huang, Y., Yang, H., Wang, D., Xu, D. *J. Phys. Chem. B* **2006**, *110*, 2994–3000.
- (42) Levi-Kalisman, Y., Raz, S., Weiner, S., Addadi, L., Sagi, I. *Adv. Funct. Mater.* **2002**, *12*, 43.
- (43) Schmidt, M. P., Ilott, A. J., Phillips, B. L., Reeder, R. J. *Cryst. Growth Des.* **2014**, *14*, 938–951.
- (44) Zou, Z., Habraken, W. J. E. M., Bertinetti, L., Politi, Y., Gal, A., Weiner, S., Addadi, L., Fratzl, P. *Adv. Mater. Interfaces* **2017**, *4*, 1600076.
- (45) Littlewood, J. L., Shaw, S., Peacock, C. L., Bots, P., Trivedi, D., Burke, I. T. *Cryst. Growth Des.* **2017**, *17*, 1214–1223.
- (46) Tobler, D. J., Rodriguez Blanco, J. D., Sørensen, H. O., Stipp, S. L. S., Dideriksen, K. *Cryst. Growth Des.* **2016**, *16*, 4500–4508.
- (47) Faatz, M., Gröhn, F., Wegner, G. *Adv. Mater.* **2004**, *16*, 996–1000.
- (48) Han, T. Y.-J., Aizenberg, J. *Chem. Mater.* **2008**, *20*, 1064–1068.
- (49) Ihli, J., Kulak, A. N., Meldrum, F. C. *Chem. Commun.* **2013**, *49*, 3134–3136.
- (50) Ihli, J., Wong, W. C., Noel, E. H., Kim, Y.-Y., Kulak, A. N., Christenson, H. K., Duer, M. J., Meldrum, F. C. *Nat. Commun.* **2014**, *5*, 3169.
- (51) Loste, E., Wilson, R. M., Seshadri, R., Meldrum, F. C. *J. Cryst. Growth* **2003**, *254*, 206–218.
- (52) Sun, S., Chevrier, D. M., Zhang, P., Gebauer, D., Cölfen, H. *Angew. Chem. Int. Ed.* **2016**, *55*, 12206–12209.
- (53) Oaki, Y., Kajiyama, S., Nishimura, T., Imai, H., Kato, T. *Adv. Mater.* **2008**, *20*, 3633–3637.
- (54) Huang, S.-C., Naka, K., Chujo, Y. *Langmuir* **2007**, *23*, 12086–12095.
- (55) Wolf, S. E., Leiterer, J., Pipich, V., Barrea, R., Emmerling, F., Tremel, W. *J. Am. Chem. Soc.* **2011**, *133*, 12642–12649.
- (56) Albéric, M., Bertinetti, L., Zou, Z., Fratzl, P., Habraken, W., Politi, Y. *Adv. Sci.* **2018**, *264*, 1701000.
- (57) Raymond S. K. Lam, John M. Charnock, Alistair Lenniec, Fiona C. Meldrum. *Cryst. Eng. Comm.* **2007**, *9*, 1226–1236.
- (58) Michel, F. M., MacDonald, J., Feng, J., Phillips, B. L., Ehm, L., Tarabrella, C., Parise, J. B., Reeder, R. J. *Chem. Mater.* **2008**, *20*, 4720–4728.

- (59) Goodwin, A. L., Michel, F. M., Phillips, B. L., Keen, D. A., Dove, M. T., Reeder, R. J. *Chem. Mater.* **2010**, *22*, 3197–3205.
- (60) Homeijer, S. J., Barrett, R. A., Gower, L. B. *Cryst. Growth Des.* **2010**, *10*, 1040–1052.
- (61) Chen, L., Shen, Y., Xie, A., Huang, B., Jia, R., Guo, R., Tang, W. *Cryst. Growth Des.* **2009**, *9*, 743–754.
- (62) Wolf, S. E., Müller, L., Barrea, R., Kampf, C. J., Leiterer, J., Panne, U., Hoffmann, T., Emmerling, F., Tremel, W. *Nanoscale* **2011**, *3*, 1158–1165.
- (63) Radha, A. V., Navrotsky, A. *Am. Mineral.* **2014**, *99*, 1063–1070.
- (64) Martignier, A., Pacton, M., Filella, M., Jaquet, J.-M., Barja, F., Pollok, K., Langenhorst, F., Lavigne, S., Guagliardo, P., Kilburn, M. R., Thomas, C., Martini, R., Ariztegui, D. *Geobiology* **2017**, *15*, 240–253.
- (65) Mansot, J. L., Golabkan, V., Romana, L., Césaire, T. *J. Microsc.*, *203*, 110–118.
- (66) Jacobson, L. C., Matsumoto, M., Molinero, V. *J. Chem. Phys.* **2011**, *135*, 74501.
- (67) Xu, G., Yao, N., Aksay, I. A., Groves, J. T. *J. Am. Chem. Soc.* **1998**, *120*, 11977–11985.
- (68) Zhang, T. H., Liu, X. Y. *J. Phys. Chem. B* **2007**, *111*, 14001–14005.
- (69) Akhter, M.S., Alawi, S. M. *Colloids Surf., A* **2000**, *175*, 311–320.
- (70) Gludovatz, B., Hohenwarter, A., Catoor, D., Chang, E. H., George, E. P., Ritchie, R. O. *Science* **2014**, *345*, 1153–1158.
- (71) Stipp, S. L.S., Parks, G. A., Nordstrom, D.K., Leckie, J. O. *Geochim. Cosmochim. Acta* **1993**, *57*, 2699–2713.
- (72) Dubrovskii, V. Fundamentals of Nucleation Theory. In *Nucleation Theory and Growth of Nanostructures*; Dubrovskii, V. G., Ed.; Springer Berlin Heidelberg: Berlin, Heidelberg, 2014, pp. 1–73.
- (73) Valor, A., Reguera, E., Torres-García, E., Mendoza, S., Sanchez-Sinencio, F. *Thermochim. Acta* **2002**, *389*, 133–139.
- (74) Koga, N., Nakagoe, Y., Tanaka, H. *Thermochim. Acta* **1998**, *318*, 239–244.
- (75) Puentes, V. P., Krishnan, K. M., Alivisatos, A. P. *Science* **2001**, *291*, 2115–2117.
- (76) Pearson, R. G. *J. Am. Chem. Soc.* **1963**, *85*, 3533–3539.
- (77) Nebel, H., Neumann, M., Mayer, C., Epple, M. *Inorg. Chem.* **2008**, *47*, 7874–7879.
- (78) Flemming A. Andersen, Ljereka Brecevic. *Acta Chem. Scand.* **1991**, 1018–1024.

- (79) Shannon, R. D. *Acta Cryst A* **1976**, *32*, 751–767.
- (80) Busca, G., Lorenzelli, V. *Mater. Chem.* **1982**, *7*, 89–126.
- (81) M. Gatehouse, S. E. Livingstone, R. S. Nyhol. *J. Chem. Soc.* **1958**, 3137–3142.
- (82) Soper, A. K., Barney, E. R. *J. Appl. Crystallogr.* **2011**, *44*, 714–726.
- (83) Hiley, C. I., Playford, H. Y., Fisher, J. M., Felix, N. C., Thompsett, D., Kashtiban, R. J., Walton, R. I. *J. Am. Chem. Soc.* **2018**, *140*, 1588–1591.
- (84) Huang, J., Blakemore, J. D., Fazi, D., Kokhan, O., Schley, N. D., Crabtree, R. H., Brudvig, G. W., Tiede, D. M. *Phys. Chem. Chem. Phys.* **2014**, *16*, 1814–1819.
- (85) Pauling L. *The Nature of the Chemical Bond and the Structure of Molecules and Crystals: An Introduction to Modern Structural Chemistry*, 3rd ed.; Cornell University Press: Ithaca, 1960.
- (86) Coelho, A. A. *J. Appl. Crystallogr.* **2018**, *51*, 210–218.
- (87) GADDS V 4.1.19, Bruker AXS, Madison (WI) US (2003).
- (88) EVA 10.0 Rev. 1, Bruker AXS, Madison (WI) US (2003).
- (89) Basham, M., Filik, J., Wharmby, M. T., Chang, P. C. Y., El Kassaby, B., Gerring, M., Aishima, J., Levik, K., Pulford, B. C. A., Sikharulidze, I., Sneddon, D., Webber, M., Dhesi, S. S., Maccherozzi, F., Svensson, O., Brockhauser, S., Náráy, G., Ashton, A. W. *J. Synchrotron Radiat.* **2015**, *22*, 853–858.
- (90) Biltz W. *Raumchemie der festen Stoffe*; Voss: Leipzig, 1934.

CRYSTALLIZATION MECHANISM OF AMORPHOUS CARBONATES



To study the crystallization mechanism of amorphous carbonates, we synthesized non-stabilized amorphous modifications of CaCO_3 (ACC), SrCO_3 (ASC), and MnCO_3 (AMnC) as dispersions in an organic solvent. Just the absence of water prevents their crystallization. By the controlled addition of water, the crystallization was initiated. The kinetics and mechanism in the presence of water were examined by Fourier transform infrared spectroscopy (FTIR) and transmission electron microscopy (TEM). The evolution of the carbonate concentration during the crystallization process was monitored potentiometrically with a pH electrode. The kinetic data were interpreted by a mathematical model based on a dissolution-recrystallization reaction. Comparison with the Pearson hardness of the cations indicates that the hydration energy and the binding strength of the hydration shell pose the main kinetic barrier for recrystallization.

This chapter contains an adapted reproduction of *Crystal Growth & Design* **2018**, DOI: 10.1021/acs.cgd.8b00627, reprinted with permission of the American Chemical Society (© 2018).

Authorship Contribution

Study conception and design	S. Leukel W. Tremel
Acquisition of data	S. Leukel
Analysis and interpretation of data	S. Leukel
Drafting of manuscript	S. Leukel
Critical revision	W. Tremel

3.1 INTRODUCTION

Crystallization is a key step in the synthesis, purification, and separation of solids, both in nature and chemical production. Understanding the underlying mechanisms is crucial for controlling particle size, polymorph selection, product morphology, and properties. In recent years, crystallization *via* amorphous intermediates was demonstrated for calcium carbonate,¹ and later for calcium phosphate,² iron oxides,³ calcium silicate,⁴ clathrates,⁵ and proteins.⁶ Calcium carbonate is the most prominent example because of its role in regulating the carbon dioxide balance in the earth's atmosphere,^{7,8} in industrial processes,⁹⁻¹² and its widespread occurrence as biomineral in molluscs, brachiopods, and some tube-building polychaete worms.¹³⁻¹⁵ A precise control of the crystallization of calcium carbonate – as it is perfected in living organisms *via* proteins¹⁶ and organic matrices^{17,18} – opens the way to new materials with tailored structures and properties.¹⁹ The morphology, polymorph selection, and properties of calcium carbonate crystals can be modified by the addition of both small^{20,21} and macromolecules.^{22,23} This was demonstrated by the formation of hierarchical structures with elastic properties *via* amorphous calcium carbonate (ACC) in the presence of sponge proteins,²⁴ or by the formation of chiral hierarchical structures that were formed by adding chiral amino acids during the crystallization.²⁵ The pH-sensitive solubility of ACC nanoparticles was used to establish drug carrier systems for cancer therapy.²⁶

Many studies show that, during crystallization, calcium carbonate precipitates initially as amorphous liquid-like droplets, which subsequently transform to one of the crystalline modifications.²⁷⁻³⁰ Under ambient conditions, ACC crystallizes to calcite *via* vaterite,^{31,32} whereas aragonite is formed at elevated temperatures.³³ Fernandez-Martinez et al.³⁴ reported an aragonite-like protostructuring in ACC under pressure. The presence of magnesium ions in ACC retards crystallization³⁵ and alters the resulting crystalline modification depending on the magnesium concentration.³⁶ ACC has no fixed composition because of its variable water content,^{37,38} and it can easily incorporate foreign ions.³⁹ All of its hydrated forms have a higher enthalpy than the crystalline modifications,⁴⁰ which allows ACC to act as precursor to different crystalline modifications of calcium carbonate. Therefore, marine organisms use ACC, stabilized by proteins and impurities (Mg^{2+} PO_4^{3-}),¹⁵ as a reservoir for the crystallization of elaborate exoskeletons, spiculae, and shells.⁴¹⁻⁴⁴

The focus of current research has been on calcium carbonate, because its amorphous form is easily accessible. We tried to generalize the crystallization *via* amorphous intermediates with other carbonates like MnCO_3 and SrCO_3 . Radha and Navrotsky described the synthesis of amorphous MnCO_3 (AMnC) by mixing cooled MnSO_4 and Na_2CO_3 solutions,⁴⁵ but the crystallization pathway remained unclear. Amorphous SrCO_3 (ASC) was found in tribological experiments,⁴⁶ as transient species in liposomes,⁴⁷ and it was synthesized by using large amounts of additives.⁴⁸ Liquid-like amorphous precursor species of MnCO_3 and SrCO_3 were observed in an ultrasonic levitator by electron microscopy, but could not be isolated.⁴⁹

We present an additive-free synthesis to yield “pure” ASC that is applicable for ACC and amorphous AMnC as well. The amorphous samples were used to study their water-dependent crystallization kinetics by Fourier transform infrared (FTIR) spectroscopy, transmission electron microscopy (TEM), and potentiometric measurements. Large discrepancies in the crystallization rate and general crystallization behavior were observed for ACC, ASC, and AMnC. Potentiometric measurements were used to monitor the crystallization for different water concentrations. First evidence of “prenucleation clusters” of calcium carbonate were found in a potentiometric study of the ion concentrations.⁵⁰ We studied the crystallization of ACC, ASC, and AMnC by tracing the carbonate concentration in water/acetonitrile mixtures with time. The carbonate concentration was monitored with a pH electrode, calibrated with defined amounts of K_2CO_3 , and the voltage signal was used as readout. The use of a carbonate-selective electrode was prevented due to its instability in organic solvents.⁵¹ The evolution of the carbonate concentration with time was analyzed with a mathematical model, which allowed to probe the effect of water on the rate constants of dissolution and crystallization. This provides new insights into the crystallization of carbonates and presents itself as tool to tune crystallization processes.

3.2 RESULTS AND DISCUSSION

Synthesis of Amorphous Carbonates

Amorphous carbonates were precipitated without any external stabilization by additives or ligands. As water is crucial for the crystallization of carbonates, their precipitation was carried out in anhydrous methanol. Whereas CaCl_2 readily dissolved in pure methanol, a suitable carbonate source is more difficult to find. Cs_2CO_3 turned out to be a good choice

because of its solubility in organic solvents.⁵² It is important not to dissolve the Cs_2CO_3 in methanol, as it deprotonates methanol in the absence of water and yields cesium methanolate. Amorphous CaCO_3 (ACC), SrCO_3 (ASC), and MnCO_3 (AMnC) were obtained by sonicating methanolic solutions of the respective cations after adding solid Cs_2CO_3 . After washing with methanol, the amorphous precipitates were dispersed in acetonitrile (Figure S7, Supporting Information). They remained amorphous for several weeks. The dispersions were used for the crystallization experiments. Isolation of ASC without stabilizing polymers or additives⁴⁸ has not been reported so far.

The absence of any Bragg reflections in the powder X-ray diffractograms (PXRDs) shows the non-crystallinity of the products (Figure 3.1a). The samples were prepared on polyvinyl acetate films with perfluorinated ether to ensure minimum background for the measurements (Figure 3.1a, black line).

Figure 3.1b shows the FTIR spectra of ACC, ASC, and AMnC with the typical broadened bands associated with the disordered structure. The three amorphous compounds show the characteristic vibrational modes of carbonates.⁵³ The symmetric stretching (ν_1), the out-of-plane deformation (ν_2), and the asymmetric stretching (ν_3) modes. The in-plane-deformation mode (ν_4) around 700 cm^{-1} is not visible (or extremely broadened), as observed for ACC in previous studies.⁵⁴ The band positions of these modes in ASC ($\nu_3 = 1383\text{ cm}^{-1}$, $\nu_1 = 1066\text{ cm}^{-1}$, $\nu_2 = 861\text{ cm}^{-1}$), ACC ($\nu_3 = 1388\text{ cm}^{-1}$, $\nu_1 = 1074\text{ cm}^{-1}$, $\nu_2 = 859\text{ cm}^{-1}$), and AMnC ($\nu_3 = 1370\text{ cm}^{-1}$, $\nu_1 = 1076\text{ cm}^{-1}$, $\nu_2 = 848\text{ cm}^{-1}$) deviate from those of the respective crystalline polymorphs and indicate the amorphous structure.

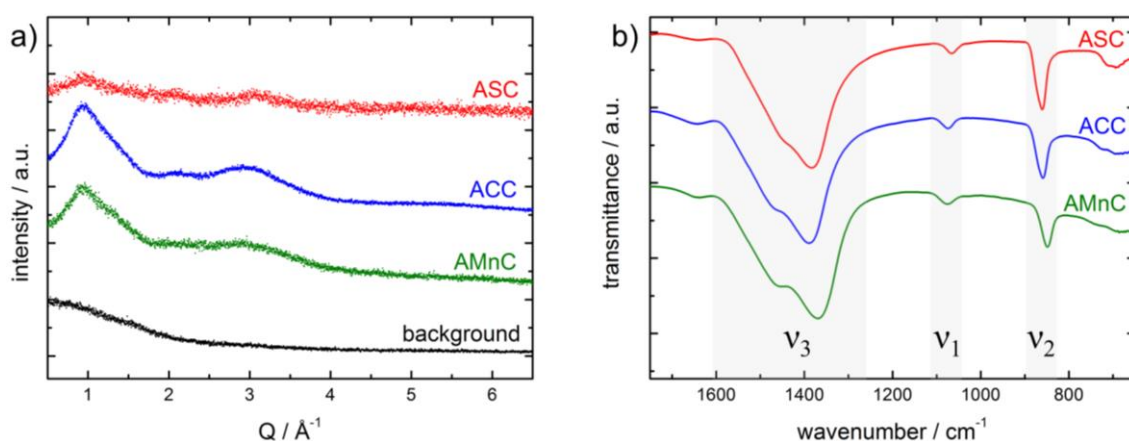


Figure 3.1. a) PXRDs of ASC, ACC, and AMnC without Bragg reflections indicate the non-crystallinity. Polyvinyl acetate film (black) was used to minimize the background. b) FTIR spectra of ASC, ACC, and AMnC exhibit the characteristic vibrational modes of the carbonate group.

Crystallization in Water/Acetonitrile Mixtures

Dispersions of ACC, ASC, and AMnC in acetonitrile were used to study the effect of water on the crystallization kinetics. The water concentrations of 10 vol% and 20 vol% in acetonitrile were used to have sufficient time for taking samples. Acetonitrile is readily miscible with water and – different from alcohols^{55,56} – known not to induce polymorph changes of CaCO₃ during crystallization. Aliquots of reaction mixtures of the respective carbonates in water/acetonitrile were taken in time intervals between 5 and 30 min, depending on the reaction rate. Subsequently, the reaction was stopped by adding an excess of acetone, followed by separating the sample by centrifugation and drying *in vacuo*.

FTIR spectra were recorded for each sample. The out-of-plane deformation (ν_2) mode was used to monitor the progress of the crystallization (Figure 3.2, inset). The shift of this band makes the amorphous and crystalline phases easy to distinguish. For CaCO₃ and MnCO₃, the band appears at higher wavenumbers in the crystalline modification. For SrCO₃, the band is shifted in the opposite direction. This shift is related to the crystal structures of CaCO₃, MnCO₃, and SrCO₃ due to the resulting differences in the coordination and bond lengths of the carbonate group. Rhodochrosite (MnCO₃) crystallizes in the calcite structure, strontianite (SrCO₃) in the aragonite structure. In aragonite, the C-O bond is longer than in calcite, which shifts ν_2 to lower wavenumbers.

The transmittance T of the ν_2 band was converted to the absorbance A ($A = -\log(T)$), which is proportional to the concentration of the respective species according to Lambert-Beer's law.⁵⁷ The ν_2 band was fitted with a bimodal Gaussian function to extract the relative amounts of the amorphous and the crystalline phases. We monitored the absorbance of the ν_2 band of the crystalline phase relating to $t = 0$, the initial absorbance was set as “0 %”. One carbonate sample was incubated overnight to achieve complete crystallization, the respective absorbance was defined as “100 %”. In this way, the crystallization of the amorphous phase could be monitored with time for ACC, ASC, and AMnC with two different water concentrations in acetonitrile (dotted line: 10 vol% water, solid line: 20 vol% water).

Figure 3.2 displays a clear difference in the crystallization rates. ASC crystallized almost instantly upon contact with water, the crystallization of ACC required approximately 30 min, the crystallization of AMnC several hours. The crystallization for ASC proceeded even in the dry state. This explains, why only crystalline SrCO₃ is found after contact with water, even after short reactions times (few minutes) and low water concentrations.

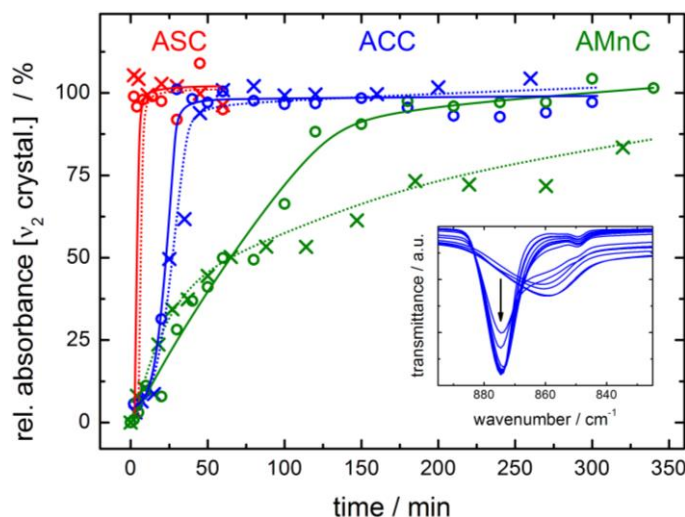


Figure 3.2. Crystallization kinetics of ASC, ACC, and AMnC in water/acetonitrile mixtures was monitored *via* FTIR for different water concentrations (dotted line: 10 vol% water; solid line: 20 vol% water) by evaluating the ν_2 band of the crystalline modification. Absorbance was derived from the transmittance of the out-of-plane-deformation mode (inset: FTIR spectra of ACC in 10 vol% water).

Besides the cation specific differences in the crystallization rate of ACC, ASC, and AMnC, the kinetics also depends on the water concentration. A higher water concentrations increases the transformation speed from the amorphous to the crystalline modification significantly, indicating the crucial effect of water on the crystallization process. Our findings correspond to the dependence of the crystallization rate of ACC on its degree of hydration.⁵⁸ The paths of the curves, in particular the sigmoidal path of ACC at a water concentration of 10 vol%, are qualitative indicators of the crystallization reaction. The crystallinity increases only slowly during the first minutes, but quite fast after 20 min. As ACC crystallizes initially as vaterite (*vide infra*), which exhibits a relatively high solubility ($K_{sp} = 1.22 \times 10^{-8} \text{ mol}^2/\text{L}^2$),⁵⁹ more time is needed to generate the necessary supersaturation by the dissolution of ACC. In contrast, the solubility product of rhodochrosite ($2.60 \times 10^{-11} \text{ mol}^2/\text{L}^2$)⁶⁰ is reached at much lower concentrations leading to the immediate formation of crystalline MnCO_3 .

Characterization of Crystallization Products

Figure 3.3 shows TEM images of SrCO_3 (a-c), CaCO_3 (d-f), and MnCO_3 (g-i). The first image of each series shows the amorphous carbonate prior to contact with water, the second image is a snapshot taken during crystallization, and the last image shows the crystalline product. A water concentration of 10 vol% was used (except for SrCO_3 , here only 2 vol% water were used because of the extremely fast crystallization. Compare Figure 3.2).

FTIR spectroscopy served as ensemble method to monitor the progress of crystallization. The out-of-plane deformation (ν_2) band is displayed as inset in each subfigure (wavenumbers are given in cm^{-1}). All amorphous carbonates appear as agglomerated nanoparticles with diameters of 10–20 nm and droplet-shaped morphology. During crystallization, the amorphous and crystalline phases coexist as indicated by the splitting of the ν_2 band.

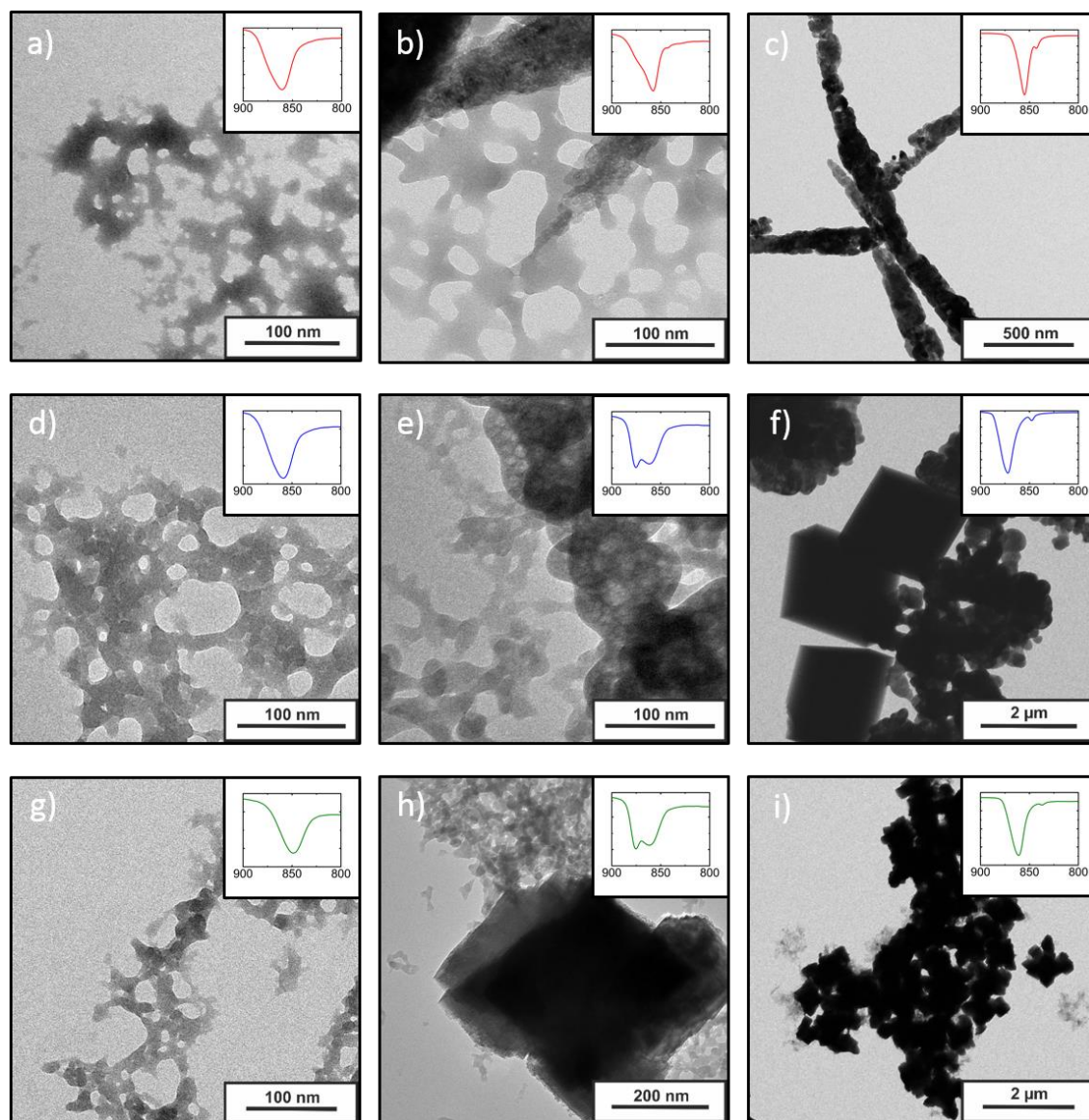


Figure 3.3 TEM snapshots during the crystallization of SrCO_3 a)-c), CaCO_3 d)-f), MnCO_3 g)-i). FTIR insets of the out-of-plane deformation mode show the progress of crystallization (wavenumbers are given in cm^{-1}). The first image of a series shows the pure amorphous carbonate (a, d, g), the second demonstrates the coexistence of amorphous and crystalline phase (b, e, g), the third shows the crystalline product (c, f, i).

Only one crystalline modification exists at ambient conditions for SrCO_3 and MnCO_3 . The particles have the typical morphologies of strontianite⁶¹ and rhodochrosite.⁶² A spherical morphology, characteristic for vaterite,^{63,64} was observed for CaCO_3 . The formation of metastable vaterite as first crystallization product was reported in other studies as well.^{23,28,32} The coexistence of the amorphous and crystalline phases and their apparent morphological difference support a dissolution-recrystallization mechanism and exclude a gradual solid-state transformation. The amorphous polymorph partially dissolves on contact with water. Due to the higher solubility of the amorphous polymorphs compared to the crystalline ones, the solution becomes supersaturated with regard to the crystalline phase, which eventually leads to its precipitation. The crystalline products are displayed in the last image of each series. The appearance of only one ν_2 band (see Figure 3.2) shows that the reaction is complete. Calcite is the thermodynamically stable polymorph of the CaCO_3 system at ambient conditions. Rhombohedral calcite crystals were formed next to spherical vaterite crystals, i.e. vaterite slowly transformed to calcite. For low water concentrations, this process was so slow that it could not be resolved with our experimental setup.

Crystallization Mechanism and Reaction Modeling

The overall kinetics for a single crystallization process, which is controlled by nucleation and growth, is often described by the Avrami equation.⁶⁵ However, the Avrami exponent n is not constant over time, except for AMnC. Therefore, we used reaction modeling rather than the Avrami model to describe our results. One might expect an influence of the respective surface on the crystallization kinetics, but TEM images (*vide supra*) show a comparable size and morphology of the different amorphous carbonate particles. Therefore, we assume that differences in the crystallization kinetics of these samples are not predominantly determined by deviations of the surfaces of the amorphous carbonates.

The crystallization was monitored with a pH module (glass iUnitrode electrode). Dissolved carbonate ions are strongly basic and increase the pH of the solution. We performed the crystallization experiments in mixtures of 20 vol%, 30 vol%, and 50 vol% water in acetonitrile. In mixed or non-aqueous systems, the apparent pH value does not correspond to the pH value measured in water.⁶⁶ Therefore, we calibrated the pH module for each water concentration with exactly weighed-in amounts K_2CO_3 (Figure S8, Supporting Information). In this way, the carbonate concentration was directly calculated from the voltage signal of

the pH module. Studies on buffers in acetonitrile-water mixtures suggest that the protonated form is favored at lower water concentrations.⁶⁷ Yet, our experimental setup does not allow for the discrimination between CO_3^{2-} and HCO_3^- . Therefore, we refer to the measured values just as “carbonate concentration”. For the respective systems, the measured carbonate concentrations as a function of time are displayed in Figure 3.4a-c.

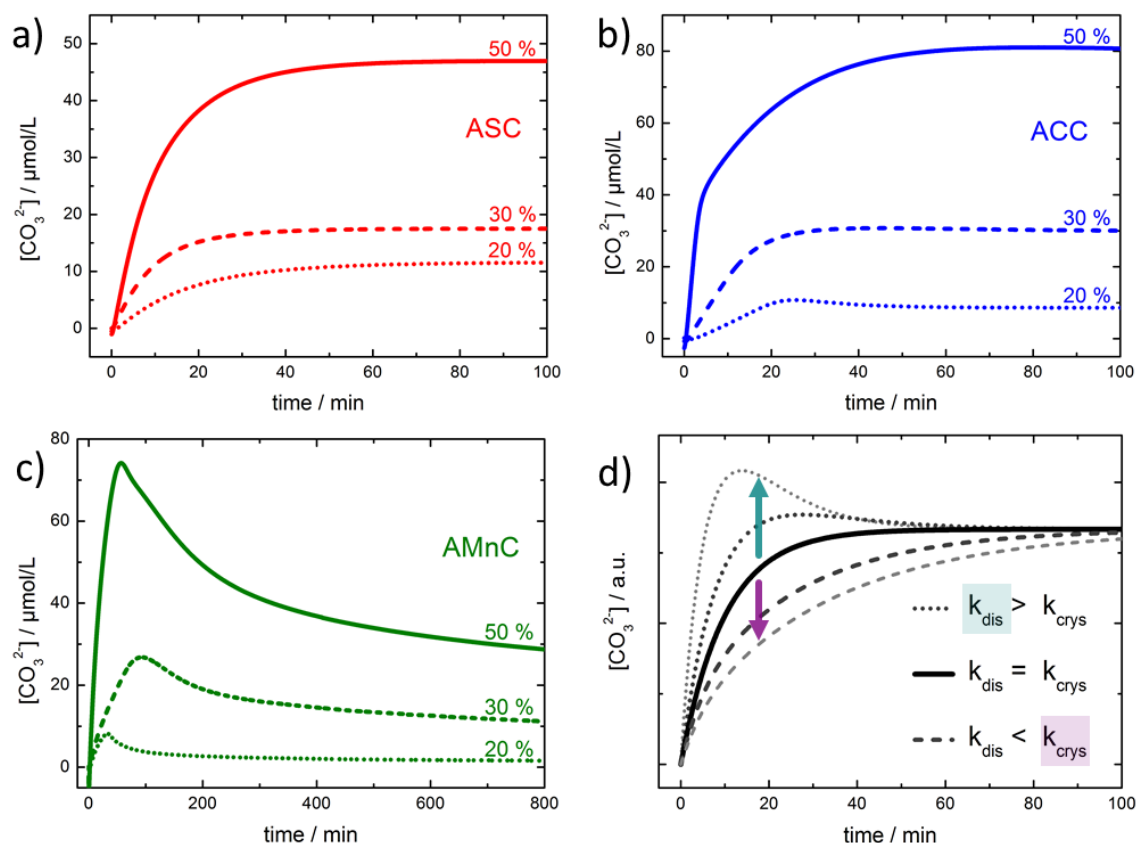
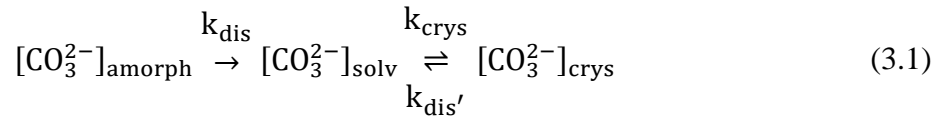


Figure 3.4 a-c) Carbonate concentration with time during crystallization of the amorphous phases at various water concentrations (20 vol%, 30 vol%, 50 vol%) in acetonitrile. d) Model for dissolution-recrystallization mechanism describing the experimental data based on the rate constants for dissolution (k_{dis}) and crystallization (k_{crys}). For AMnC, the crystallization is much slower than the dissolution. Contrary behavior is found for ASC; the fast crystallization prevails at every water concentration. ACC represents an intermediate case. For high water concentrations, the crystallization rate exceeds the dissolution rate, whereas, for low water concentrations, the crystallization rate drops under the dissolution rate.

The maximum carbonate concentration increases with increasing water content, which is related to the higher solubility of salts in water compared to organic solvents. Moreover, the equilibrium concentration at the end of the reaction scales with the solubility product of the respective crystalline carbonates in pure water (calcite:⁵⁹ $3.31 \times 10^{-9} \text{ mol}^2/\text{L}^2 >$ strontianite:⁶⁸ $5.42 \times 10^{-10} \text{ mol}^2/\text{L}^2 >$ rhodochrosite:⁶⁰ $2.60 \times 10^{-11} \text{ mol}^2/\text{L}^2$). All experiments showed an

initial increase of the carbonate concentration, after the dispersion of amorphous carbonates was added. For ACC, the graph at 50 vol% exhibits a kink after 3 min, where the increase of carbonate concentration attenuates significantly. This corresponds to the scenario described for ACC in Figure 3.2. The crystallization is slow at the start, but accelerates drastically after several minutes. This is accompanied by a sudden consumption of carbonate from solution, which leads to the leveling of the graph. For high water concentrations, the carbonate concentration for ASC and ACC reaches the equilibrium concentration after 30–60 min. AMnC and ACC at 20 vol% water show a different behavior. The carbonate concentration rises first to a maximum and drops subsequently to the equilibrium concentration. In addition, it takes considerably longer for AMnC to reach a constant carbonate concentration (compared to ACC and ASC), which is in agreement with the slow crystallization kinetics observed in Figure 3.2. These apparent differences between the carbonates can fully be explained with a qualitative model assuming a dissolution-recrystallization mechanism:



The amorphous carbonate $[\text{CO}_3^{2-}]_{\text{amorph}}$ dissolves with the rate constant k_{dis} . The carbonate in solution $[\text{CO}_3^{2-}]_{\text{solv}}$ crystallizes with a rate constant k_{crys} to the respective crystalline modification $[\text{CO}_3^{2-}]_{\text{crys}}$. The solubility product of the crystalline modification was considered by its dissolution with a rate constant $k_{\text{dis}'}$. This leads to three coupled differential equations (complete derivation given in the Supporting Information, p. VI). The evolution of the carbonate concentration in solution with time, which was accessible in our experimental setup, was calculated as:

$$[\text{CO}_3^{2-}]_{\text{solv}}(t) = A_0 \left(\left(\frac{k_{\text{dis}} - k_{\text{dis}'}}{k_{\text{crys}} + k_{\text{dis}'} - k_{\text{dis}}} \right) \left(e^{-k_{\text{dis}} t} - e^{-(k_{\text{crys}} + k_{\text{dis}'}) t} \right) + \left(\frac{k_{\text{dis}'}}{k_{\text{crys}} + k_{\text{dis}'}} \right) \left(1 - e^{-(k_{\text{crys}} + k_{\text{dis}'}) t} \right) \right) \quad (3.2)$$

This function is plotted in Figure 3.4d. We cannot fit the function directly to our data to extract values for the rate constants, but the evolution of the carbonate concentration is modeled reliably on a qualitative level. We varied the values of k_{dis} and k_{crys} starting from

equal rates of dissolution and recrystallization (bold black line). To facilitate the comparison, k_{dis} was chosen in a way to yield an identical end concentration of carbonate. When the crystallization rate k_{crys} excels the dissolution rate k_{dis} (purple arrow), the curve levels (dashed lines), because dissolving carbonate is incorporated instantly into the growing crystal. This behavior was observed for ASC at all water concentrations and for ACC at a concentration of 50 vol%.

The curve shape (dotted lines) changes significantly, when the dissolution rate k_{dis} is higher than the crystallization rate k_{crys} (green arrow). $[CO_3^{2-}]$ passes through a maximum, because the initial increase of the carbonate concentration is stronger due to its fast dissolution. At a high carbonate concentration, $[CO_3^{2-}]$ drops, because carbonate ions are consumed for nucleation and crystal growth. This behavior was observed for all AMnC samples and ACC (at a water concentration of 20 vol%). AMnC shows the lowest crystallization rate of the three carbonates, which is in agreement with its slow crystallization kinetics (Figure 3.2). At every water concentration, the transformation of ASC is kinetically determined by the dissolution of ASC due to the high recrystallization rate. This explains also, why ASC has never been isolated without stabilization by additives. According to the above model, ACC has comparable dissolution and crystallization rates. Higher water concentrations favor crystallization, whereas dissolution prevails at low water concentrations. As both processes accelerate at higher water concentrations (Figure 3.2), the crystallization rate is affected more by increasing water concentrations than the dissolution rate.

As the TEM images (Figure 3.3) suggest a comparable morphology for the different amorphous carbonates, we assume that the differences in the dissolution kinetics do not originate predominantly from deviating surface areas. The Pearson hardness⁶⁹ of the cations and the hydration energies dominate the different behavior of the three carbonates. The hydration enthalpy increases from Sr^{2+} ($\Delta H_{hyd} = -1445$ kJ/mol), via Ca^{2+} ($\Delta H_{hyd} = -1592$ kJ/mol), to Mn^{2+} ($\Delta H_{hyd} = -1845$ kJ/mol).⁷⁰ As the crystalline modifications of these carbonates are anhydrous, cation dehydration is crucial for the incorporation into the crystal.⁷¹ For Pearson soft Sr^{2+} , dehydration requires less energy and is thus faster than for Mn^{2+} with strongly bound water molecules in its hydration shell. ACC is an intermediate case between these extremes. By increasing the water concentration, the system changes from recrystallization-controlled to dissolution-controlled kinetics. At a low water concentration in acetonitrile, favorable water-water interactions via hydrogen bonds are reduced and water-acetonitrile

complexes are dominant.⁷² We assume that, for an excess of acetonitrile, the coordination of water molecules to Ca^{2+} is preferred and the binding of the hydration shell is stronger. This leads to a higher kinetic barrier for crystallization. Hence, by adjusting the water concentration, we can tune the phase transformation of amorphous carbonates to the crystalline polymorphs.

Conclusion

We synthesized three amorphous carbonates, ACC, ASC, and AMnC, in the absence of stabilizing additives and studied the mechanism and the kinetics of the transformation from the amorphous to the crystalline polymorphs as a function of the water concentration. The crystallization of ASC proceeds extremely fast, whereas the transformation of AMnC is relatively slow. ACC is an intermediate case between these extremes. For high water concentrations, the relatively lower dissolution rate kinetically dominates the reaction, whereas for lower concentrations, the crystallization is the rate-determining step. For all three carbonates, the crystallization speed increases with increasing water content. The crystallization processes were traced potentiometrically and in a step-by-step analysis by taking TEM snapshots during different stages of the crystallization process to identify different phases and product morphologies. The crystallization kinetics could be modeled based on a dissolution-recrystallization mechanism. A comparison with the Pearson hardness of the cations indicates that the hydration energy and the binding strength of the hydration shell pose the main kinetic barrier for the recrystallization. This allows tuning transformation from the amorphous to the crystalline phase by adjusting the water concentration.

3.3 EXPERIMENTAL SECTION

Materials

CaCl₂ (98 %, Merck), SrCl₂ (99.5 %, Alfa Aesar), MnCl₂ (97 %, ABCR), Cs₂CO₃ (99 %, Sigma-Aldrich), KCl (99.5 %, Carl Roth), K₂CO₃ (Analytical reagent grade, Fisher Chemicals), methanol (HPLC grade, Fisher Chemicals), acetonitrile (HPLC gradient grade, Fisher Chemicals), acetone (99.5 %, Riedel-de Haën), milli Q deionized water.

Synthesis

CaCl₂ (1 mmol) was dissolved in 20 mL of methanol. Then, Cs₂CO₃ (1 mmol) was added to the colorless solution and the reaction mixture was sonicated for 5 min. A cloudy colorless precipitate of ACC formed. It is important to note that Cs₂CO₃ has to be added directly as a solid. Dissolving in methanol leads to the formation of calcium methanolate. The obtained solid was washed with methanol and separated by centrifugation. Finally, 10 mL of acetonitrile were added, and the mixture was sonicated to give a milky dispersion of ACC in acetonitrile. ACC was stable in this dispersion with regard to crystallization for weeks. ASC and AMnC were synthesized analogously by using SrCl₂ or MnCl₂ instead of CaCl₂.

Crystallization Experiments

A dispersion of 0.5 mmol of the respective amorphous carbonate in 5 mL of acetonitrile was added to 15 mL of a water/acetonitrile mixture. The amount of water in this mixture was chosen in a way that the desired water concentration was reached after the addition of the carbonate dispersion. The reaction mixture was stirred (500 rpm) and samples were taken during the crystallization process. Therefore, 250 µL of the solution was collected with a pipette and diluted immediately with an excess of acetone to stop any further crystallization. These solutions were used for the preparation of samples for subsequent TEM studies. For monitoring the crystallization kinetics *via* FTIR, the solution was centrifuged, the precipitate dried *in vacuo*, and measured afterwards.

Potentiometric Experiments

The crystallization was monitored with a Metrohm pH electrode Titrande set-up at three different water concentrations in acetonitrile. The ionic strength of all solutions was adjusted

to 0.03 M by the addition of KCl. The volume was always set to 50 mL. To calculate the carbonate concentration from the voltage signal, the electrode was first calibrated with K_2CO_3 . Therefore, the desired carbonate concentration was adjusted by adding several microliters of 0.01–0.1 M $\text{K}_2\text{CO}_3/\text{KCl}$ solution. A 1:1 ratio of K_2CO_3 and KCl was used to model the ionic strength resulting from the dissolution of a salt with divalent ions (i.e. CaCO_3). An exemplary calibration curve can be found in the Supporting Information (Figure S8). For monitoring the crystallization, 1 mL of a 0.02 M dispersion of the respective amorphous carbonate in acetonitrile was added to the water/acetonitrile mixture. The solution was stirred constantly, and the voltage signal was recorded with a resolution of 1 s^{-1} .

Characterization

Powder X-ray diffraction. X-ray diffractograms were recorded on a STOE Stadi P equipped with a Mythen 1k detector using monochromatized $\text{MoK}\alpha$ radiation. The sample was attached to polyvinyl acetate films with perfluoroether (Fomblin Y, Aldrich). The sample was measured in transmission in 0.015° steps (continuous scan, 150 s°) covering a 2θ range from 1.5° to 47° .

FTIR spectroscopy. ATR-FTIR spectroscopy was performed using a Nicolet iS10 Spectrometer manufactured by Thermo Scientific. The spectra were recorded in a frequency range from 650 cm^{-1} to 4000 cm^{-1} with a resolution of 1.4 cm^{-1} per data point.

Transmission electron microscopy. TEM samples were prepared by drop-casting $20 \mu\text{L}$ of the respective sample dispersion on 400 mesh carbon copper grids (Plano GmbH, Wetzlar, Germany) and measured with a Technai Spirit G2 at 120 kV acceleration voltage, equipped with a standard 4K CCD camera.

Potentiometric pH sensing. Potentiometric measurements were performed using a computer-controlled system from Metrohm (Filderstadt, Germany), operated with the custom-designed software Tiamo (v2.4), and a supplementary pH module (Metrohm, pH module 867). The pH value in the sample was monitored in real time with a glass iUnitrode electrode (Metrohm, No. 6.0278.300). All experiments were carried out in a 90 mL titration vessel. The room temperature was controlled constantly at $T = 293 \text{ K}$.

3.4 REFERENCES

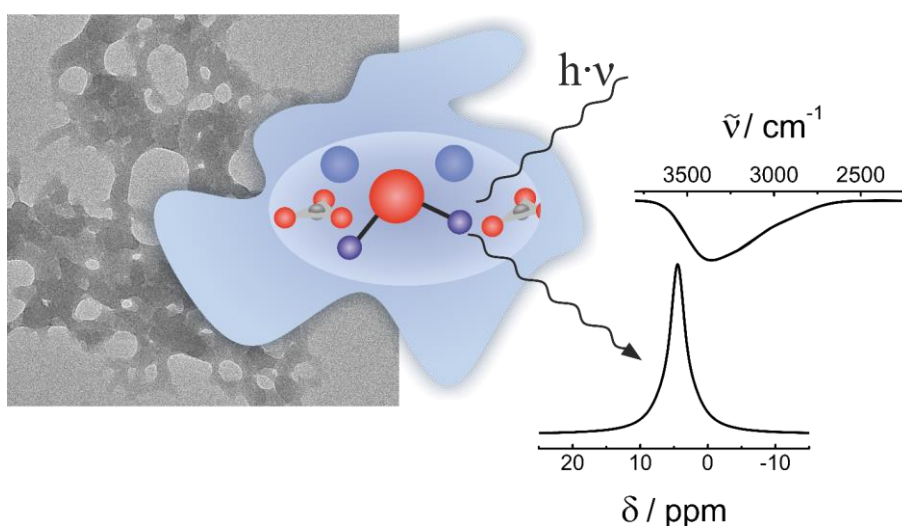
- (1) Beniash, E., Aizenberg, J., Addadi, L., Weiner, S. *Proc. R. Soc. B* **1997**, *264*, 461–465.
- (2) Beniash, E., Metzler, R. A., Lam, R. S. K., Gilbert, P. U. P. A. *J. Struct. Biol.* **2009**, *166*, 133–143.
- (3) Liang, X., Wang, X., Zhuang, J., Chen, Y., Wang, D., Li, Y. *Adv. Funct. Mater.* **2006**, *16*, 1805–1813.
- (4) Krautwurst, N., Nicoleau, L., Dietzsch, M., Fernandez-Martinez, A., Barton, B., Tremel, W. *Chem. Mater.* **2018**.
- (5) Jacobson, L. C., Hujo, W., Molinero, V. *J. Am. Chem. Soc.* **2010**, *132*, 11806–11811.
- (6) Gliko, O., Neumaier, N., Pan, W., Haase, I., Fischer, M., Bacher, A., Weinkauff, S., Vekilov, P. G. *J. Am. Chem. Soc.* **2005**, *127*, 3433–3438.
- (7) Richard E., Z., James C., Z., Ken, C., Toby, T. *Science* **2008**, *321*, 51–52.
- (8) Im Kim, G., Jo, B. H., Kang, D. G., Kim, C. S., Choi, Y. S., Cha, H. J. *Chemosphere* **2012**, *87*, 1091–1096.
- (9) Choi, S. G., Chu, J., Brown, R. C., Wang, K., Wen, Z. *ACS Sustain. Chem. Eng.* **2017**, *5*, 5183–5190.
- (10) Barhoum, A., Rahier, H., Abou-Zaied, R. E., Rehan, M., Dufour, T., Hill, G., Dufresne, A. *ACS Appl. Mater. Interfaces* **2014**, *6*, 2734–2744.
- (11) Zhang, Y., Shaw, H., Farquhar, R., Dawe, R. *J. Pet. Sci. Eng.* **2001**, *29*, 85–95.
- (12) Yang, Q., Liu, Y., Gu, A., Ding, J., Shen, Z. *J. Colloid Interface Sci.* **2001**, *240*, 608–621.
- (13) Marin, F., Bundeleva, I., Takeuchi, T., Immel, F., Medakovic, D. *J. Struct. Biol.* **2016**, *196*, 98–106.
- (14) Mass, T., Giuffre, A. J., Sun, C.-Y., Stifler, C. A., Frazier, M. J., Neder, M., Tamura, N., Stan, C. V., Marcus, M. A., Gilbert, P. U. P. A. *Proc. Natl. Acad. Sci. USA* **2017**, *114*, 7670–7678.
- (15) Addadi, L., Raz, S., Weiner, S. *Adv. Mater.* **2003**, *15*, 959–970.
- (16) Gong, Y. U. T., Killian, C. E., Olson, I. C., Appathurai, N. P., Amasino, A. L., Martin, M. C., Holt, L. J., Wilt, F. H., Gilbert, P. U. P. A. *Proc. Natl. Acad. Sci. USA* **2012**, *109*, 6088–6093.

- (17) Bentov, S., Weil, S., Glazer, L., Sagi, A., Berman, A. *J. Struct. Biol.* **2010**, *171*, 207–215.
- (18) Wheeler, A. P., George, J. W., Evans, C. A. *Science* **1981**, *212*, 1397–1398.
- (19) Gao, H.-L., Chen, S.-M., Mao, L.-B., Song, Z.-Q., Yao, H.-B., Cölfen, H., Luo, X.-S., Zhang, F., Pan, Z., Meng, Y.-F., Ni, Y., Yu, S.-H. *Nat. Commun.* **2017**, *8*, 287.
- (20) Didymus, J. M., Oliver, P., Mann, S., DeVries, A. L., Hauschka, P. V., Westbroek, P. *J. Chem. Soc., Faraday Trans.* **1993**, *89*, 2891–2900.
- (21) Wolf, S. E., Loges, N., Mathiasch, B., Panthöfer, M., Mey, I., Janshoff, A., Tremel, W. *Angew. Chem. Int. Ed.* **2007**, *46*, 5618–5623.
- (22) Yu, S.-H., Cölfen, H., Hartmann, J., Antonietti, M. *Adv. Funct. Mater.* **2002**, *12*, 541.
- (23) Balz, M., Therese, H. A., Li, J., Gutmann, J. S., Kappl, M., Nasdala, L., Hofmeister, W., Butt, H.-J., Tremel, W. *Adv. Funct. Mater.* **2005**, *15*, 683–688.
- (24) Natalio, F., Corrales, T. P., Panthöfer, M., Schollmeyer, D., Lieberwirth, I., Müller, W. E. G., Kappl, M., Butt, H., Tremel, W. *Science* **2013**, *339*, 1298–1302.
- (25) Jiang, W., Pacella, M. S., Athanasiadou, D., Nelea, V., Vali, H., Hazen, R. M., Gray, J. J., McKee, M. D. *Nat. Commun.* **2017**, *8*, 15066.
- (26) Zhao, Y., Luo, Z., Li, M., Qu, Q., Ma, X., Yu, S.-H., Zhao, Y. *Angew. Chem. Int. Ed.* **2015**, *54*, 919–922.
- (27) Rodriguez-Navarro, C., Kudłacz, K., Cizer, Ö., Ruiz-Agudo, E. *CrystEngComm* **2015**, *17*, 58–72.
- (28) Bots, P., Benning, L. G., Rodriguez-Blanco, J.-D., Roncal-Herrero, T., Shaw, S. *Cryst. Growth Des.* **2012**, *12*, 3806–3814.
- (29) Wolf, S. E., Leiterer, J., Kappl, M., Emmerling, F., Tremel, W. *J. Am. Chem. Soc.* **2008**, *130*, 12342–12347.
- (30) Pipich, V., Balz, M., Wolf, S. E., Tremel, W., Schwahn, D. *J. Am. Chem. Soc.* **2008**, *130*, 6879–6892.
- (31) Dietzsch, M., Andrusenko, I., Branscheid, R., Emmerling, F., Kolb, U., Tremel, W. *Z. Kristallog. – Cryst. Mater.* **2017**, *232*, 255–265.
- (32) Rodriguez-Blanco, J. D., Shaw, S., Benning, L. G. *Nanoscale* **2011**, *3*, 265–271.
- (33) Ogino, T., Suzuki, T., Sawada, K. *Geochim. Cosmochim. Acta* **1987**, *51*, 2757–2767.
- (34) Fernandez-Martinez, A., Kalkan, B., Clark, S. M., Waychunas, G. A. *Angew. Chem. Int. Ed.* **2013**, *52*, 8354–8357.

- (35) Loste, E., Wilson, R. M., Seshadri, R., Meldrum, F. C. *J. Cryst. Growth* **2003**, *254*, 206–218.
- (36) Blue, C. R., Giuffre, A., Mergelsberg, S., Han, N., Yoreo, J. J. de, Dove, P. M. *Geochim. Cosmochim. Acta* **2017**, *196*, 179–196.
- (37) Ihli, J., Wong, W. C., Noel, E. H., Kim, Y.-Y., Kulak, A. N., Christenson, H. K., Duer, M. J., Meldrum, F. C. *Nat. Commun.* **2014**, *5*, 3169.
- (38) Schmidt, M. P., Ilott, A. J., Phillips, B. L., Reeder, R. J. *Cryst. Growth Des.* **2014**, *14*, 938–951.
- (39) Littlewood, J. L., Shaw, S., Peacock, C. L., Bots, P., Trivedi, D., Burke, I. T. *Cryst. Growth Des.* **2017**, *17*, 1214–1223.
- (40) Radha, A. V., Forbes, T. Z., Killian, C. E., Gilbert, P. U. P. A., Navrotsky, A. *Proc. Natl. Acad. Sci. USA* **2010**, *107*, 16438–16443.
- (41) S. Weiner, I. Sagi, L. Addadi. *Science* **2005**, *309*, 1027–1028.
- (42) Yael, P., Talmon, A., Eugenia, K., Steve, W., Lia, A. *Science* **2004**, *306*, 1161–1164.
- (43) Weiss, I. M., Tuross, N., Addadi, L., Weiner, S. *J. Exp. Zool.* **2002**, *293*, 478–491.
- (44) Julia, C. M., Wilhelm, B., Doreen, F., Bernd, H., Matthias, E. *J. Molluscan Stud.* **2003**, *69*, 113–121.
- (45) Radha, A. V., Navrotsky, A. *Am. Mineral.* **2014**, *99*, 1063–1070.
- (46) J. L., M., V., G., L., R., T., C. *J. Microsc.* **2003**, *210*, 110–118.
- (47) Tester, C. C., Whittaker, M. L., Joester, D. *Chem. Commun.* **2014**, *50*, 5619–5622.
- (48) Homeijer, S. J., Barrett, R. A., Gower, L. B. *Cryst. Growth Des.* **2010**, *10*, 1040–1052.
- (49) Wolf, S. E., Müller, L., Barrea, R., Kampf, C. J., Leiterer, J., Panne, U., Hoffmann, T., Emmerling, F., Tremel, W. *Nanoscale* **2011**, *3*, 1158–1165.
- (50) Denis, G., Antje, V., Helmut, C. *Science* **2008**, *322*, 1819–1822.
- (51) Julie A., G., M. E., M. *Anal. Chim. Acta* **1982**, *141*, 57–64.
- (52) Xu, J., Yan, C., Zhang, F., Konishi, H., Xu, H., Teng, H. H. *Proc. Natl. Acad. Sci. USA* **2013**, *110*, 17750–17755.
- (53) Andersen, F. A., Brečević, L. *Acta Chem. Scand.* **1991**, 1018–1024.
- (54) Nebel, H., Neumann, M., Mayer, C., Epple, M. *Inorg. Chem.* **2008**, *47*, 7874–7879.
- (55) Manoli, F., Dalas, E. *J. Cryst. Growth* **2000**, *218*, 359–364.
- (56) Dickinson, S. R., McGrath, K. M. *J. Mater. Chem.* **2003**, *13*, 928–933.

- (57) Beer, A. *Ann. Phys.* **1852**, *162*, 78–88.
- (58) Albéric, M., Bertinetti, L., Zou, Z., Fratzl, P., Habraken, W., Politi, Y. *Adv. Sci.* **2018**, *264*, 1701000.
- (59) Plummer, L. N., Busenberg, E. *Geochim. Cosmochim. Acta* **1982**, *46*, 1011–1040.
- (60) Johnson, K. S. *Geochim. Cosmochim. Acta* **1982**, *46*, 1805–1809.
- (61) Rautaray, D., Sanyal, A., Adyanthaya, S. D., Ahmad, A., Sastry, M. *Langmuir* **2004**, *20*, 6827–6833.
- (62) John, S. *Geochim. Cosmochim. Acta* **1997**, *61*, 785–793.
- (63) Andreassen, J.-P. *J. Cryst. Growth* **2005**, *274*, 256–264.
- (64) Nehrke, G., van Cappellen, P. *J. Cryst. Growth* **2006**, *287*, 528–530.
- (65) Avrami, M. *J. Chem. Phys.* **1939**, *7*, 1103–1112.
- (66) Mussini, T., Mazza, F. *Electrochim. Acta* **1987**, *32*, 855–862.
- (67) Barbosa, J., Sanz-Nebot, V. *J. Pharm. Biomed. Anal.* **1992**, *10*, 1047–1051.
- (68) Plummer, L. N., Busenberg, E., Parker, V. B. *Geochim. Cosmochim. Acta* **1984**, *48*, 2021–2035.
- (69) Parr, P. G., Pearson, R. G. *J. Am. Chem. Soc.* **1983**, *105*.
- (70) Piana, S., Jones, F., Gale, J. D. *J. Am. Chem. Soc.* **2006**, *128*, 13568–13574.
- (71) Burgess J. *Metal Ions in Solution*; Ellis Horwood Ltd.: Chichester, England, 1978.
- (72) Bertie, J. E., Lan, Z. *J. Phys. Chem. B* **1997**, *101*, 4111–4119.

HYDROGEN BONDING IN AMORPHOUS CARBONATES



Anhydrous crystalline modifications of carbonates can form *via* hydrated amorphous intermediate species. We synthesized amorphous earth alkali carbonates and probed the structural water with Fourier transform infrared (FTIR) spectroscopy, ¹H nuclear magnetic resonance (¹H NMR) spectroscopy, and heteronuclear correlation (HETCOR) experiments. Temperature dependent determination of the spin-lattice relaxation time (T₁) provided information about the water motion in the amorphous compounds. Our findings show that the strength of the internal hydrogen bonding network is mainly determined by the Pearson hardness of the respective metal cation. Our study provides a coherent picture of the hydrogen bonding situation in these transient species and thereby contributes to a deeper understanding of the crystallization process of carbonates.

This chapter contains an adapted manuscript submitted to *Inorganic Chemistry*.

Authorship Contribution

Study conception and design	S. Leukel W. Tremel
Acquisition of data	S. Leukel M. Mondeshki
Analysis and interpretation of data	S. Leukel M. Mondeshki
Drafting of manuscript	S. Leukel
Critical revision	M. Mondeshki W. Tremel

4.1 INTRODUCTION

Calcium carbonate is the most widespread biomineral on earth.^{1,2} While biominerals that are purely based on other alkaline earth carbonates have not been reported so far, magnesium and – to a lower degree – strontium are incorporated into calcium carbonate biominerals and interfere significantly with the crystallization process. Magnesian calcite was found in the cuticles of crustaceans,³ in sea urchins,^{4,5} and echinoderms.⁶ Certain coccolithophores show a substantial bioaccumulation of strontium,^{7–9} which is high compared with values of precipitated “inorganic” calcite.¹⁰ The most prominent function of magnesium in calcium carbonate based biominerals is the stabilization amorphous calcium carbonate (ACC),¹¹ which serves as primary building material for all sorts of hard tissue.^{12,13} A change of the mechanical properties by incorporation of magnesium in biominerals has been discussed as well.¹⁴

The crystallization of calcium carbonate *via* amorphous intermediates has been studied intensely due to the importance of ACC for biomineralization. Its formation enables the accumulation and temporal storage of calcium and carbonate ions by organisms for subsequent crystallization of complex biomineral structures. By tailoring the physical and chemical conditions, polymorph control over the crystallization products of ACC could be achieved.¹⁵ ACC is typically the first phase to precipitate from solution.¹⁶ Since it is metastable,¹⁷ it transforms rapidly to one of the more stable crystalline calcium carbonate polymorphs.^{18,19} Several synthetic routes to ACC were developed, ranging from the addition of polymers²⁰ and proteins,²¹ to the confinement in silica shells,²² or freeze-drying.²³ Numerous studies appeared on the structure and composition of ACC, which exhibits short-range, but no long-range order.^{24,25} Tobler et al.²⁶ found gradual changes in local order of ACC on varying the pH during the synthesis, and “proto-structuring” of the amorphous phase with regard to the respective crystalline calcium carbonate polymorphs has been proposed.^{27,28} The poorly defined structure of ACC allows the incorporation of substantial amounts of foreign ions, which is documented for strontium²⁹ and magnesium.^{30–33} Therefore, amorphous magnesium carbonate (AMC) is mainly discussed in the context of a solid solution in ACC.³⁴ AMC is known to play a role in the crystallization of magnesium carbonates, but only one study appeared on the atomic structure of pure hydrated amorphous magnesium carbonate.³⁵ More often, amorphous magnesium carbonates are discussed as product of the

thermal decomposition of crystalline magnesium carbonates, e.g. nesquehonite.³⁶ Both AMC and ACC are tested for medical applications. While pH responsive drug carrier systems are being developed based on ACC,³⁷ amorphous magnesium carbonate with mesoporous structure³⁸ has been employed to improve the uptake of poorly soluble drugs.³⁹ Moreover, hydrated amorphous magnesium carbonate has been tested as carbon dioxide storage material.⁴⁰ Even fewer reports exist on amorphous strontium carbonate (ASC), which possibly originates from its extremely fast transformation to crystalline strontianite.⁴¹

Amorphous carbonates are generally hydrated materials. While most reports agree that ACC prepared from aqueous solution contains structural water, the amount of water depends on the synthesis conditions and the drying processes.^{42,43} Studies on amorphous zinc phosphate revealed that the water network stabilized the amorphous modification with regard to crystallization.⁴⁴ The water molecules form complex networks, connected through hydrogen bridges. In amorphous carbonates, either water molecules or carbonate groups serve as hydrogen bond acceptors. The importance of hydrogen bonds for the structure,⁴⁵ stability,⁴⁶ molecular conformation,⁴⁷ and dynamics^{48,49} in a vast number of chemical systems cannot be underestimated. The dissociation energies of hydrogen bonds cover more than two orders of magnitude (0.2–40 kcal/mol).⁵⁰

Fourier transform infrared (FTIR) spectroscopy and ¹H nuclear magnetic resonance (¹H NMR) spectroscopy are powerful tools to probe the strength of hydrogen bonding. In FTIR, a broadening of the band corresponding to the O-H stretching vibration indicates the presence of hydrogen bonds.⁵¹ The O-H bond is weakened and the band position shifts to lower wavenumbers, when a hydrogen acceptor is in its vicinity.^{52,53} Moreover, the interaction with a hydrogen bond acceptor decreases the electron density at the hydrogen atom,⁵⁴ resulting in a downfield shift in the ¹H NMR spectrum.⁵⁵ Solid state NMR is a particularly powerful technique to probe the local environment, especially in amorphous materials. ACC and magnesium bearing ACC were studied using ⁴³Ca NMR⁵⁶ and ²⁵Mg NMR spectroscopy.⁵⁷ A solid state NMR spectroscopy study of ACC, employing ¹H and ¹³C, was performed by Epple and co-workers.²⁴ The mobility of the nuclei can be determined from the correlation time τ_c , which is related to the spin-lattice relaxation time (T₁).^{58,59} This allowed to determine the molecular mobility of amorphous organic compounds,^{60,61} the mobility of proteins,⁶² and the molecular mobility of water adsorbed on polymers.⁶³

We probed the local water environment and the strength of the hydrogen bonding network in amorphous alkaline earth carbonates. To this end, we synthesized hydrated amorphous carbonates of magnesium, calcium, strontium, and barium. By careful drying, yet without completely removing the structural water, we could stabilize these transient species for sufficiently long periods of time. Amorphous barium carbonate still crystallized very rapidly, which prevented prolonged experiments. We probed the strength of the hydrogen bonds by FTIR spectroscopy. ^1H NMR and ^1H - ^{13}C HETCOR (heteronuclear correlation) magic angle spinning nuclear magnetic resonance (MAS-NMR) techniques were used to identify different proton species. Also, we probed the carbonate environment through $^{13}\text{C}\{^1\text{H}\}$ cross polarization (CP) MAS-NMR. Measuring the ^1H spin-lattice relaxation (T1) indicated a deviating mobility of the water molecules in the respective carbonates, especially experiments at variable temperature (VT) allowed to determine the respective activation energy for the water motion. Thus, this study provides a complete picture of the structural water in amorphous intermediate species and thereby expands our understanding of the crystallization process of the ubiquitous and eminently important mineral class of carbonates.

4.2 RESULTS AND DISCUSSION

Composition and Stability of Amorphous Earth Alkali Carbonates

Amorphous carbonates were precipitated without additional stabilization by additives or ligands from methanolic solution according to our recent study.⁶⁴ A drying step at 70 °C proved to be necessary in order to prevent fast crystallization, especially of ASC. The non-crystallinity of the products was confirmed by the absence of Bragg reflections in the powder X-ray diffractograms (PXRD, Figure 4.1a). To minimize the background, the samples were prepared on polyvinyl acetate films with perfluorinated ether (Figure 4.1a, gray line). The amorphous carbonates differ strongly in their stability with regard to crystallization (Figure S09, Supporting Information). In crystallization experiments employing a mixture of 20 vol% water in acetonitrile, AMC crystallized slowly within a day. ACC required several hours until crystallization was complete. ASC crystallized immediately upon contact with water. The amorphous modification of barium carbonate (ABC, *vide infra*) transformed to witherite already in air.

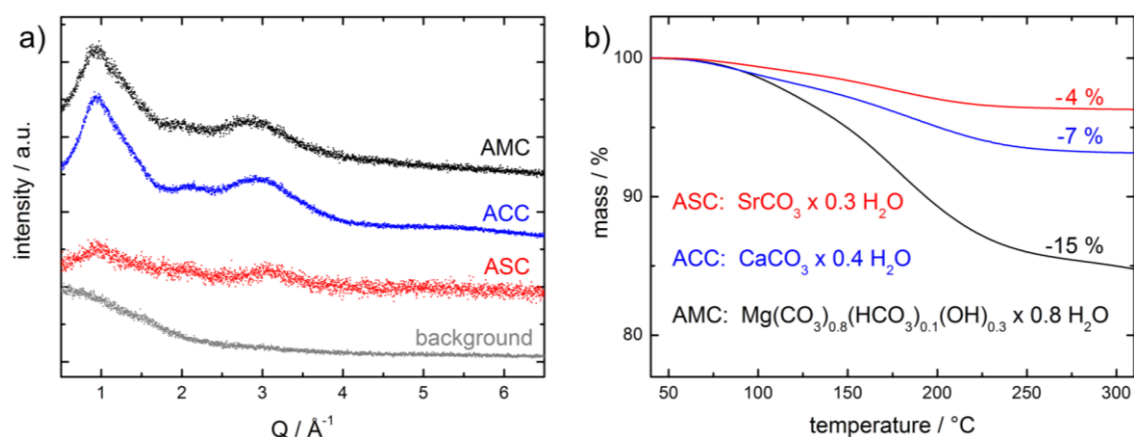


Figure 4.1 a) PXR D of the amorphous carbonates of magnesium (AMC: black), calcium (ACC: blue), strontium (ASC: red), and the sample background consisting of two polyvinyl acetate films and perfluorinated ether (gray). The amorphous structure is indicated by the absence of Bragg reflections. b) Thermogravimetric analysis (TGA) of the amorphous carbonates. All samples display a mass loss between room temperature and 250°C , which is attributed to a release of structural water. Approximate compositions of the respective samples are calculated based on the mass loss. For AMC, the hydroxide and hydrogencarbonate ions, which were found in ^1H NMR (*vide infra*), were considered.

The amount of water in the amorphous carbonates was determined by thermogravimetric analysis (Figure 4.1b). All samples showed a gradual mass loss between 50°C and 250°C (AMC: 15 %, ACC: 7 %, ASC: 4 %). Due to the incipient decomposition of AMC to MgO around 300°C ,^{36,65,66} we did not observe a constant mass after the loss of water. Based on the mass loss, the approximate composition of the amorphous carbonates was calculated. For AMC, we also considered the evidence of hydroxide and hydrogencarbonate ions, which were observed in ^1H NMR and HETCOR experiments (*vide infra*). This resulted in a composition of $\text{Mg}(\text{CO}_3)_{0.8}(\text{HCO}_3)_{0.1}(\text{OH})_{0.3} \times 0.8 \text{H}_2\text{O}$. The water content of the other samples, $\text{CaCO}_3 \times 0.4 \text{H}_2\text{O}$ and $\text{SrCO}_3 \times 0.3 \text{H}_2\text{O}$, was significantly lower. The amount of water is correlated with the Pearson hardness of the respective cation.⁶⁷ The small and Pearson hard Mg^{2+} cation binds water ligands stronger than the larger, softer Sr^{2+} cation. The observed water content is lower than in previous reports,^{22,43} which is due to the drying step at 70°C . Reeder and co-workers found a comparable water content for ACC, pretreated at 87°C .⁴² Yet, the similarity of the band shape in the FTIR spectra before and after drying suggests that the water environment is not significantly altered by the drying process (Figure S10, Supporting Information).

Strength of the Hydrogen Bonding

Figure 4.2a shows the FTIR spectra of AMC, ACC, and ASC. The hydration is confirmed by the broad band around 3300 cm^{-1} , which corresponds to the O-H stretching vibration of structural water in the compounds. The three samples show the characteristic vibrational modes of carbonates⁶⁸ (broadening due to the amorphous structure is observed), i.e. the symmetric stretching (ν_1), the out-of-plane deformation (ν_2), and the asymmetric stretching (ν_3) modes. The broadening of the in-plane-deformation mode (ν_4) around 700 cm^{-1} increases from strontium, *via* calcium, to magnesium carbonate, i.e. they cannot be resolved properly. The respective band positions in AMC ($\nu_3 = 1406\text{ cm}^{-1}$, $\nu_1 = 1090\text{ cm}^{-1}$, $\nu_2 = 854\text{ cm}^{-1}$), ACC ($\nu_3 = 1393\text{ cm}^{-1}$, $\nu_1 = 1074\text{ cm}^{-1}$, $\nu_2 = 858\text{ cm}^{-1}$), and ASC ($\nu_3 = 1382\text{ cm}^{-1}$, $\nu_1 = 1065\text{ cm}^{-1}$, $\nu_2 = 862\text{ cm}^{-1}$) agree with reported values^{38,64} and confirm the amorphous structure.

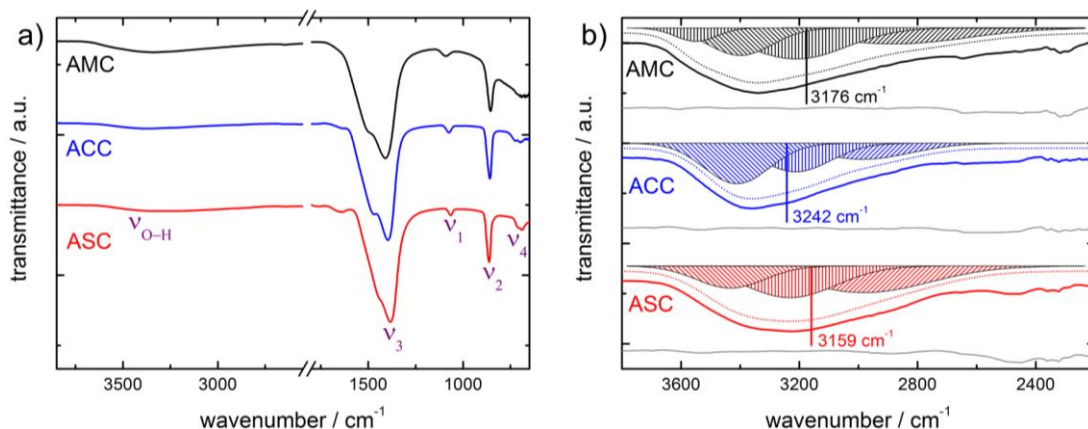


Figure 4.2 a) FTIR spectra display the characteristic carbonate vibrational modes ν_1 – ν_4 . The O-H stretching vibration around 3300 cm^{-1} suggests that all samples contain structural water. b) Normalized FTIR spectra of the O-H vibration of AMC, ACC, and ASC. The data are modeled by multi-modal Gaussian functions (difference lines shown in gray). Mean wavenumbers indicate an increase of the hydrogen bonding strength when going from ACC, *via* AMC, to ASC.

FTIR spectra of the amorphous carbonates in the region of the O-H stretching vibration are shown in Figure 4.2b. All samples exhibit a broad band, ranging from ca. 3700 cm^{-1} to 2300 cm^{-1} . This indicates that the water molecules form hydrogen bonds in the amorphous compounds.⁵⁰ Increasing strength of hydrogen bonding shifts the water band to smaller wavenumbers by weakening the O-H bond of the water molecule.^{52,53}

We evaluated the respective bands by a multimodal Gaussian fit. Three Gaussian functions were necessary for modelling the data reasonably.⁵¹ In case of AMC, a fourth function, centered around 3550 cm^{-1} , was employed to model the hump of the band at high wavenumbers.

We attribute this to the presence of hydroxide groups in AMC. The increased electron density strengthens the O-H bond and shifts the signal to higher wavenumbers. Fitting the bands with Gaussian functions allowed the extraction of a mean wavenumber for $\nu_{\text{O-H}}$. Thereby, the average hydrogen bonding strength in these compounds was compared. Water in ACC forms the weakest hydrogen bonds (3242 cm^{-1}), while stronger bonds occur in ASC (3159 cm^{-1}). AMC represents an intermediate case (3176 cm^{-1}). The mean wavenumber of $\nu_{\text{O-H}} = 3108\text{ cm}^{-1}$ suggests the strongest hydrogen bonds of all amorphous carbonates to occur in ABC (Figure S11, Supporting Information). Yet, it proved to be so unstable that no other experiments could be performed besides FTIR. According to the empirical formula found by Libowitzky,⁶⁹ the wavenumber of the O-H stretching vibration is related to the O-O distance in a hydrogen bond of the form O-H...O. In the case of the amorphous carbonates, the mean O-O distance is in the range from 2.67 \AA (for ABC) to 2.72 \AA (for ACC).

Aside from AMC, the hydrogen bonding strength increases with the ionic radius of the alkaline earth metals. We suggest that the hydrogen bond acceptor strength of the carbonate group is mainly determined by its coordination to the metal cation. Large (Pearson soft)⁷⁰ cations like Sr^{2+} and Ba^{2+} coordinate only weakly to the carbonate group. Thus, the electron density of the carbonate anion is higher, which leads to stronger hydrogen bonds. The opposite effect is found for small (Pearson hard) cations, which add a significant covalent character to the ionic metal oxygen bond. As a result, electron density is drawn from the carbonate group, and the hydrogen acceptor capacity decreases.

The decrease of metal-oxygen interaction is also indicated by the decreasing energy of the symmetric stretching vibration ν_1 of the carbonate ion when going from Mg^{2+} to Ba^{2+} (1090 cm^{-1} to 1058 cm^{-1}). Accordingly, alkaline earth hydroxides show a decreasing vibration frequency $\nu_{\text{O-H}}$ from Mg^{2+} to Sr^{2+} . The increased metal-oxygen interaction weakens the hydrogen acceptor strength of the hydroxide ion (Figure S12, Supporting Information). The stronger hydrogen bonds in AMC compared to ACC appear to contradict this model. However, AMC is not a pure carbonate. Hydroxide anions are present in the structure (*vide infra*) that serve as strong hydrogen bond acceptors.⁷¹ They contribute significantly to the strength of the internal hydrogen bond network.

Local Carbonate and Water Environment

To probe the chemical environment of the carbonate group, $^{13}\text{C}\{^1\text{H}\}$ CP MAS-NMR experiments with variable contact times were performed. The carbonyl region of the ^{13}C spectra of the amorphous carbonates is shown in Figure 4.3a (samples contained ^{13}C in natural abundance). It should be noted that the full width at half-maximum (FWHM) of the NMR signals in the spectra provides information about the homogeneity of the local field. Typically, amorphous compounds exhibit broadened carbonyl resonances due to the increased heterogeneity of the chemical environment.²⁴ The ^{13}C signal of AMC is characterized by a chemical shift of 165.8 ppm with a FWHM of 435 Hz. The resonance of ACC is detected at 168.0 ppm with a FWHM of 385 Hz; ASC exhibits the sharpest signal with a FWHM of 335 Hz at 167.3 ppm. The large FWHM in AMC corresponds to a higher local disorder due to the presence of hydroxide and hydrogencarbonate groups and a higher amount of water.

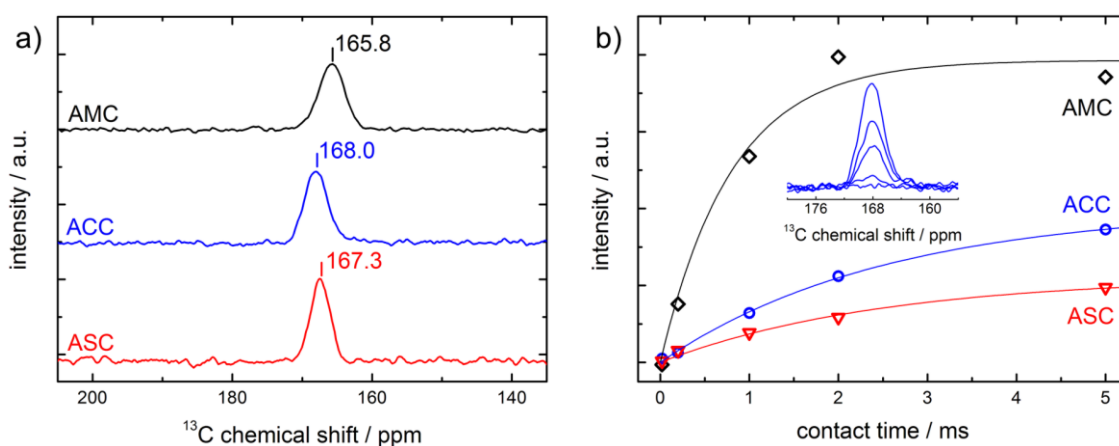


Figure 4.3 a) $^{13}\text{C}\{^1\text{H}\}$ CP MAS-NMR of the amorphous carbonates AMC, ACC, and ASC. The carbonate signals exhibit a broad FWHM (AMC: 440 Hz, ACC: 385 Hz, ASC: 335 Hz), which accounts for a variety of different local environments in the amorphous state. b) Build-up curve of the carbonate signal at different contact times for ^1H - ^{13}C cross polarization (fits shown). The efficiency of the cross polarization for the respective carbonates correlates with the water content, as determined by TGA.

The evolution of the ^{13}C intensities with increasing contact time t_c in cross polarization NMR experiments is displayed in Figure 4.3b. The build-up curves provide information about the efficiency of the cross polarization, which depends on the strength of the ^1H - ^{13}C dipole-dipole couplings, i.e. on the distance between the dipolar coupled ^1H and ^{13}C spin pairs, on the mobility of the molecule in general, or the local mobility of the functional groups containing the spin pair. For an isolated dipolar coupled pair, the CP build-up curve is oscillatory

in nature. For the alkaline earth carbonates in this work, a rather smooth exponential signal intensity increase was observed. It is due to a distribution of the orientations of the coupled pairs and the separations between ^1H and ^{13}C dipolar coupled spins. A distribution in the correlation times τ_c related with the water mobility may not be excluded as well.

Clearly, a higher water content would result in more protons to cross polarize and therefore a stronger ^{13}C signal (provided that the water molecules do not form large phase separated domains within the inorganic structure). As determined through TGA, the water content increases in the order $\text{ASC} < \text{ACC} < \text{AMC}$. Additionally, there are HCO_3^- and OH^- groups present in the structure for AMC. Thus, the CP build-up curve for the AMC is steeper compared to ASC and ACC, while the build-up curves for the latter two compounds are comparable (Figure 4.3b). Neglecting the relaxation of the ^{13}C and ^1H rotating frame, the build-up curves were fitted using equation 4.1:⁷²

$$I(t_{\text{cp}}) = I_0 \cdot \left(1 - e^{\left(-\frac{t_{\text{cp}}}{T_{\text{IS}}}\right)}\right) \quad (4.1)$$

$I(t_{\text{cp}})$ is the absolute intensity – which is correlated to the absolute water content in the amorphous carbonates – for the respective cross polarization (or contact) time t_{cp} . T_{IS} is the cross polarization time constant for the coupled ^1H - ^{13}C pairs. For ASC and ACC, we found comparable time constants of 2.48(47) ms and 2.52(19) ms. For AMC, the cross polarization time constant of 0.80(17) ms is much shorter.

In order to gain further insight into the water environment of the amorphous carbonates, we performed ^1H NMR and HETCOR experiments (Figure 4.4). The ^1H NMR spectra were approximated with pseudo-Voigt profiles.⁷³ All samples contain negligible (compared to the water signal) amounts of residual solvent from the synthesis with shifts of ~ 1 ppm.

The ^1H NMR spectrum of AMC exhibits three distinct proton signals detected in both experiments (Figure 4.4a,b). The most intense resonance at 5.18 ppm with a FWHM of 2890 Hz corresponds to structural water. The signal at 0.27 ppm (FWHM = 1140 Hz) is compatible with hydroxide ions, whose higher electron density causes a highfield shift.⁷⁴ The presence of hydroxide corresponds to the multitude of basic magnesium carbonates, e.g. dypingite ($\text{Mg}_5(\text{CO}_3)_4(\text{OH})_2 \times 5\text{H}_2\text{O}$)⁷⁵ and hydromagnesite ($\text{Mg}_5(\text{CO}_3)_4(\text{OH})_2 \times 4\text{H}_2\text{O}$).⁷⁶

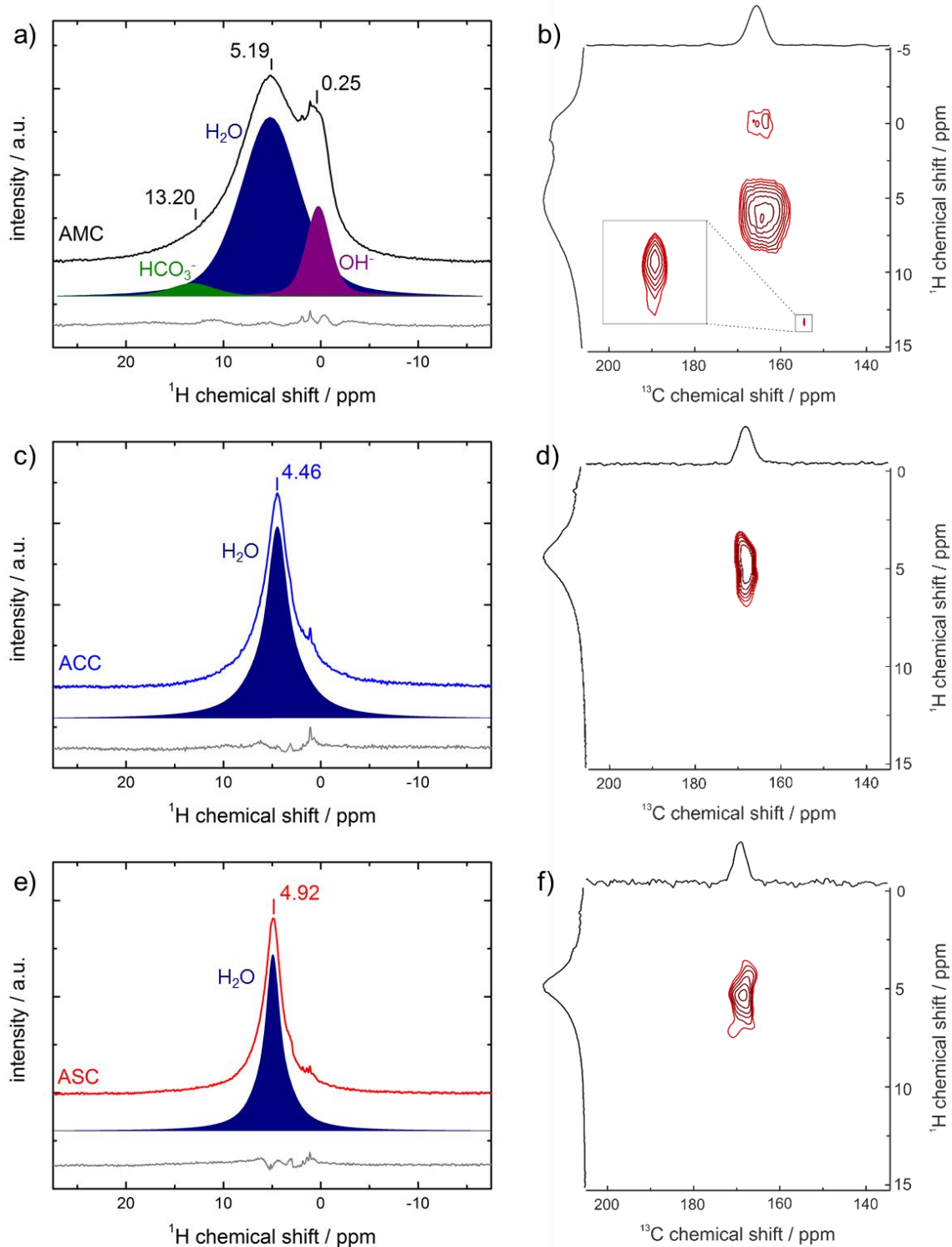


Figure 4.4 ^1H NMR and respective HETCOR spectra of the amorphous alkaline earth carbonates. The spectra are fitted with pseudo-Voigt profiles; difference lines are shown in gray. AMC (a,b) exhibits three different proton signals. The most intense signal at 5.19 ppm originates from water, while we attribute the weak signal at 0.25 ppm to more strongly shielded hydroxide groups. The coupling to a carbon shifted to higher field and the distinct deshielding of the signal at 13.20 ppm hint at the acidic proton of a hydrogencarbonate ion. ACC (c,d) and ASC (e,f) show only one signal at 4.46 ppm, respectively at 4.92 ppm. The ACC water signal has the smallest chemical shift, which corresponds to weaker hydrogen bonding.

The signal at 13.20 ppm (FWHM = 2160 Hz) appears as a shoulder in the ^1H NMR spectrum and is much better resolved in the HETCOR spectrum. It is clearly related with the presence of acidic protons in AMC. Furthermore, the coupling with a carbonate group shifted to higher field (154.8 ppm) in the HETCOR experiment suggests the presence of hydrogen-carbonate groups.²⁴ For nesquehonite ($\text{MgCO}_3 \times 3\text{H}_2\text{O}$), Moore and co-workers found that the description as hydrogencarbonate ($\text{Mg}(\text{OH})(\text{HCO}_3) \times 2\text{H}_2\text{O}$) is more accurate.⁷⁷ We assume to have a comparable situation in AMC, even though the intensity ratios of the three signals (80 % to 16 % to 4 %) show that hydrogen carbonate can only be a minority species (Figure 4.1b).

The ^1H NMR spectrum of ACC displays only one proton signal at 4.46 ppm with a FWHM of 1170 Hz (Figure 4.4c,d). This chemical shift corresponds to the weak hydrogen bonds that we already observed in the FTIR spectra (Figure 4.2b). In comparison, for monohydrocalcite (Figure S13, Supporting Information), the hydrated crystalline modification of calcium carbonate, both FTIR and ^1H NMR reveal better order and stronger hydrogen bonding than in ACC. Monohydrocalcite exhibits hydrogen bonds with a nearly optimal O-H-O angle of 180° (Figure S13a, inset, Supporting Information). In the amorphous state, it is unlikely that this angle occurs frequently (assuming a distribution of angles), which attributes to a weakening of the hydrogen bonding.

ASC exhibits one proton signal at 4.92 ppm with a FWHM of 810 Hz. This chemical shift corresponds to hydrogen bonding comparable in strength to AMC, which is in agreement with the FTIR results. ASC has the sharpest water signal of the amorphous carbonates, which may be associated with better local organization or higher water mobility.

Comparing the results of the ^1H NMR and the HETCOR experiments reveals that the water resonance in the amorphous carbonates changes from 4.46 ppm (ACC) to 5.18 ppm (AMC). The chemical shift of the protons is related to the local electron density, which is influenced by hydrogen bonding. Therefore, strong hydrogen bonds lead to a deshielding of the protons.^{50,54,78} We assume that the hydroxide ions in AMC act as strong hydrogen acceptors. Additionally, an increase of the signal broadening, when going from ASC, *via* ACC, to AMC, is clearly seen. The same trend appears in the ^{13}C NMR (Figure 4.3a) and the FTIR spectra (Figure 4.2a). Therefore, we assume that the variation in the local structure in the amorphous alkaline earth carbonates is highest in AMC and decreases for the heavier alka-

line earth homologues. In parallel, the stability of the amorphous state with regard to crystallization decreases (e.g. difficulty of stabilizing amorphous barium carbonate), which further suggests that the degree of disorder is highest in AMC.

Motional Behavior of Water

To evaluate the motional behavior of water in the amorphous carbonates, we recorded variable temperature (VT) ^1H NMR spectra of the amorphous carbonates (20 °C, 40 °C, and 60 °C). By increasing the temperature, the water signal shifts to higher field for all amorphous compounds. Such a shift is usually attributed to the weakening/breaking of hydrogen bonds due to the increase of interatomic distances.^{79,80}

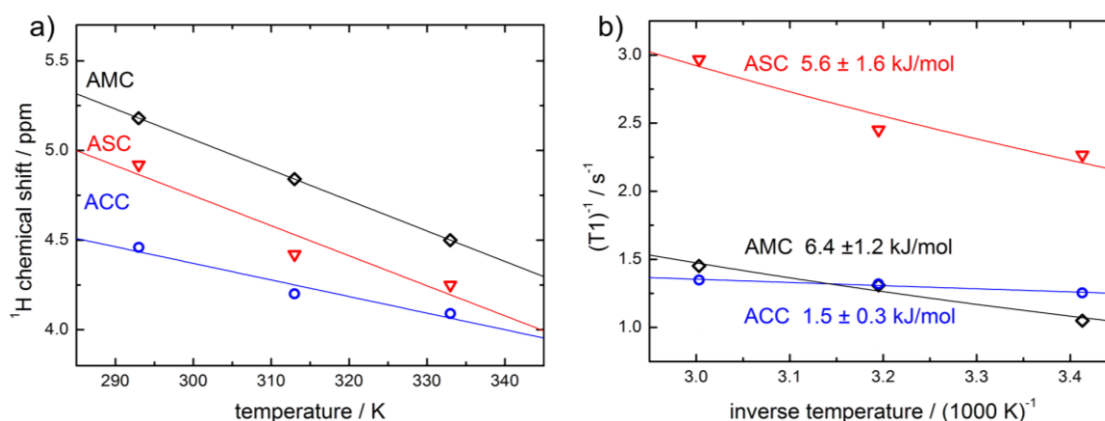


Figure 4.5 a) Temperature dependence of the ^1H chemical shift of the water signal in the amorphous carbonates. The signal in ACC is less sensitive to temperature, as it is primarily less affected by hydrogen bonding. b) Temperature dependence of the spin-lattice relaxation time (T_1) allows determination of the activation energy E_a for the water motion (values given in the figure). For AMC and ASC, these values are in a comparable range of 6 kJ/mol. The activation energy for the water motion in ACC is significantly lower due to the weaker hydrogen bonding.

We obtained the temperature coefficients $\Delta\delta/\Delta T$ for the respective carbonates by linearly fitting the chemical shift against the temperature (Figure 4.5a). We obtained similar values for AMC (0.0170 ppm/K) and ASC (0.0168 ppm/K), whereas the temperature coefficient for ACC is lower (0.0093 ppm/K). This further underlines the weakness of the hydrogen bonds of ACC. Temperature-induced weakening/breaking of the strong hydrogen bonds in AMC and ASC results in a distinct highfield shift of the water signal, whereas the influence of the temperature is less pronounced on the already weak hydrogen bonds in ACC.

We recorded VT inversion recovery spectra (Figure S14, Supporting Information) to determine the spin-lattice relaxation time T1 and related the results with the strength of the hydrogen bonding. The spectra were fitted using the equation 4.2.⁸¹

$$I(t) = I_{\infty} \cdot \left(1 - \exp\left(\frac{-t}{T1}\right) \right) + I_0 \quad (4.2)$$

We measured T1 for all amorphous carbonates as well as for monohydrocalcite as crystalline reference at three different temperatures (20 °C, 40 °C, and 60 °C). The results are displayed in Figure 4.5b. At ambient temperature, we find the following T1 relaxation times for the respective carbonates: AMC (T1 = 953 ms), ACC (T1 = 798 ms), and ASC (T1 = 441 ms). With increasing temperature, all T1 values decrease. The spin-lattice relaxation time T1 is well described by the Bloembergen-Purcell-Pound model,⁵⁸ which attributes for the tumbling motion of molecules on the local magnetic field disturbance (eq. 4.3).

$$\frac{1}{T1} = C \cdot \left[\frac{\tau_c}{1 + (\omega\tau_c)^2} + \frac{4\tau_c}{1 + (2\omega\tau_c)^2} \right] \quad (4.3)$$

This tumbling motion is characterized by the rotation correlation time τ_c . C is a constant, which is independent of the temperature and the frequency. If the tumbling rate is comparable to the Larmor ω frequency, relaxation is most effective. Faster or slower tumbling increase the relaxation time. The tumbling rate in solids is much smaller than the Larmor frequency. Thus, a faster motion, which can be caused by increased temperature, should lead to a decrease of the relaxation time T1. The temperature dependence of the tumbling motion can be approximated by an Arrhenius approach with the activation energy E_a (eq. 4.4).⁸²

$$\tau_c = \tau_{c0} \cdot \exp\left(\frac{E_a}{kT}\right) \quad (4.4)$$

Inserting eq. 4.4 in eq. 4.3 yields a dependence of the relaxation time T1 of the temperature T. Assuming $\omega\tau_c \gg 1$ in solids, we obtain:

$$\frac{1}{T1} \propto \exp\left(\frac{-E_a}{kT}\right) \quad (4.5)$$

We fitted our data with eq. 4.5 to obtain the activation energy E_a for the tumbling motion of the water molecules (Figure 4.5b). AMC and ASC show comparable activation energies of

6.4 ± 1.2 kJ/mol and 5.6 ± 1.6 kJ/mol. E_a is significantly lower for ACC (1.5 ± 0.3 kJ/mol). The activation energies for the water motion correspond to the strength of the hydrogen bonding that was deduced from FTIR and ^1H NMR. The activation energy for crystalline monohydrocalcite ($E_a = 5.4 \pm 0.1$ kJ/mol) is higher than in ACC (Figure S13d, Supporting Information). We attribute this difference to the strong directed hydrogen bonding in monohydrocalcite. This bonding situation also potentially causes the high absolute value for the T1 relaxation of 1376 ms at ambient conditions in monohydrocalcite. Shorter relaxation times in amorphous compounds, compared to the crystalline modification, were also reported for magnesium phosphates.⁸³

Conclusion

We examined the water content, local environment, and motional behavior in hydrated amorphous carbonates of magnesium, calcium, strontium, and barium with TGA, FTIR, and NMR techniques to gain information about the hydrogen bonding. The low stability of amorphous barium carbonate allowed only fast FTIR experiments. The Pearson hardness of the coordinating metal cations mainly determines the hydrogen acceptor strength of the carbonate group. On the first glance, AMC seems to contradict this trend. The solution is revealed in ^1H NMR and HETCOR experiments, which indicate that AMC is not a pure carbonate, but contains small amounts of hydrogencarbonate ions and additional proton species, which are identified as hydroxide ions. These hydroxide ions act as strong hydrogen acceptors and stabilize the water network in AMC. There is no experimental evidence for hydroxide ions in all other amorphous alkaline earth carbonates.

Table 4.1 Hydrogen bonding in amorphous earth alkali carbonates. Mean wavenumber of the O-H stretching vibration $\nu_{\text{O-H}}$, ^1H chemical shift δ , the respective linewidth, T1 relaxation time, and activation energy for the water motion E_a are given.

Sample	$\nu_{\text{O-H}} / \text{cm}^{-1}$	$\delta(^1\text{H}) / \text{ppm}$	FWHM / Hz	T1 / ms	$E_a / \text{kJ mol}^{-1}$
AMC	3176	5.18 (H_2O)	2890	953	6.4 ± 1.2
		0.27 (OH)	1140		
		13.20 (HCO_3^-)	2160		
ACC	3242	4.46 (H_2O)	1170	798	1.5 ± 0.3
ASC	3159	4.92 (H_2O)	810	441	5.6 ± 1.6

The results of various spectroscopic techniques (Table 4.1) allow for the classification of the hydrogen bonding strength in the amorphous carbonates: $AMC \approx ASC > ACC$. The FTIR spectrum of amorphous barium carbonate suggests that hydrogen bonding is even stronger in this compound, but the short lifetime prevented a more detailed analysis. The activation energy of the water motion E_a , determined by VT T1 measurements, scales with the strength of hydrogen bonding and has a minimum for amorphous calcium carbonate. A comparison with crystalline hydrated calcium carbonate (monohydrocalcite) suggests that the hydrogen bonds are not ideally oriented in the amorphous solid, which explains their softening. The minimum hydrogen bonding strength in ACC corresponds to the facile dehydration of biogenic ACC prior to crystallization.^{84–86}

This study provides a complete picture of hydrogen bonding and the water environment in amorphous earth alkali carbonates. Structural water is one of the most profound differences between amorphous intermediate species and the thermodynamic crystalline modifications in the carbonate system, which are predominately anhydrous (some crystalline hydrated modifications of basic magnesium carbonate exist). With this detailed characterization of their hydration, we contribute a key aspect to finally illuminating the crystallization process of carbonates as a whole.

4.3 EXPERIMENTAL SECTION

Materials

CaCl₂ (98 %, Merck) (99 %, Sigma-Aldrich), SrCl₂ (99.5 %, Alfa Aesar), MgCl₂×6H₂O (99 %, p.a., Carl Roth), BaCl₂ (99.5 %, Merck), Cs₂CO₃ (99 %, Sigma-Aldrich), K₂CO₃ (99 %, Merck), Ca(OH)₂ (96 %, puriss. p. a., Sigma-Aldrich), Sr(OH)₂×8H₂O (99 %, Alfa Aesar), Mg(OH)₂ (95 %, Sigma-Aldrich), acetone (99.5 %, Riedel-de Haën), methanol (HPLC grade, Fisher Chemicals), acetonitrile (HPLC gradient grade, Fisher Chemicals), milli Q deionized water.

Synthesis: Amorphous Carbonates

CaCl₂ (2 mmol) was dissolved in 20 mL of methanol. Subsequently, Cs₂CO₃ (2 mmol) was added, and the solution was sonicated for 1 min. After dissolution of the Cs₂CO₃, a colorless solid (ACC) precipitated, which was separated by centrifugation and washed twice with

10 mL of methanol to remove residual cesium chloride. Subsequently, the solid was dispersed in 20 mL of acetone under sonication and centrifuged again. The washing step with acetone was repeated. Finally, the solid was dried at 70 °C for several hours. The preparation of AMC and ASC proceeded analogously with the respective metal chlorides as reactants. The drying step at elevated temperatures was necessary, especially for ASC, as it crystallized during slow drying even *in vacuo*. Additionally, adsorbed surface water was removed, which increased the stability of the amorphous samples. To prevent spontaneous crystallization, the synthesis of amorphous barium carbonate required drying the product in a vacuum oven at 40 °C.

Synthesis: Monohydrocalcite

According to the optimized calcium magnesium ratio for the formation of monohydrocalcite,⁸⁷ CaCl₂ (2 mmol) and MgCl₂×6H₂O (0.5 mmol) were dissolved in 30 mL of deionized water. In the next step, K₂CO₃ (3.5 mmol) was dissolved in 15 mL of deionized water, and the solutions were combined, whereupon a colorless solid precipitated. The reaction solution was stirred for 8 h. Afterwards, the precipitate was separated by centrifugation and washed with methanol. The product, monohydrocalcite, was dried *in vacuo*.

Crystallization Experiments

The respective amorphous carbonates were prepared as described above. Instead of dispersing them in acetone and subsequently drying them for several hours, 20 mL of acetonitrile was added to yield 0.1 M dispersions of the amorphous carbonates. For a crystallization experiment, the respective carbonate dispersion was added to a water/acetone mixture to yield a final water concentration of 20 vol% (5 mL of the carbonate dispersion to a mixture of 11 mL of acetone and 4 mL of water). Samples were taken by transferring 250 µL of the reaction solution to a microcentrifuge tube and quenching further crystallization by the addition of 1.5 mL of acetone. The sample was centrifuged for 1 min at 14000 rpm. Then, the supernatant was decanted. The sample was washed again with 1.5 mL of acetone and dried afterwards *in vacuo*. Through FTIR, the progress of crystallization was monitored (Figure S9, Supporting Information).

Characterization

X-ray powder diffraction. X-ray diffractograms were recorded with a STOE Stadi P equipped with a Mythen 1k detector using monochromatized MoK α radiation. The sample was attached to polyvinyl acetate films with perfluoroether (Fomblin Y, Aldrich). The sample was measured in transmission in 0.015° steps (continuous scan, 150 s/°) covering a 2 θ range from 1.5° to 43°. Crystalline phases were identified according to the PDF-2 database⁸⁸ using Bruker AXS EVA.⁸⁹

FTIR spectroscopy. ATR-FTIR spectroscopy was performed using a Nicolet iS10 Spectrometer manufactured by Thermo Scientific. The spectra were recorded in a frequency range from 650 cm⁻¹ to 4000 cm⁻¹ with a resolution of 1.4 cm⁻¹ per data point.

Solid state NMR spectroscopy. All solid state NMR spectra were recorded on a Bruker Avance 400 DSX NMR spectrometer at a ¹H frequency of 399.87 MHz and ¹³C frequency of 100.55 MHz. A commercial three-channel 4 mm Bruker probe head at 10 kHz magic angle spinning (MAS) was used for all experiments. The ¹H NMR spectra were recorded averaging 32 transients with 8 s recycle delay. The ¹H T1 relaxation was determined using the inversion recovery method. The sample was heated using a Bruker BVT 3000 variable temperature unit and the temperature was controlled with an accuracy of ± 1 K. For all solid state ¹³C cross polarization MAS-NMR experiments, an initial 90° pulse with 4.0 μ s length and 5 s recycle delay were used. A ramped CP pulse (64–100 %) with duration of 20 μ s, 200 μ s, 1 ms, 2 ms, and 5 ms was used for recording the CP build-up curves. Two pulse phase modulation (TPPM) ¹H decoupling scheme was used while acquiring the ¹³C signal. Transients of 2 k were averaged for the CP experiments. The spectra were baseline-corrected and a broadening of 50 Hz was applied. The ¹H-¹³C heteronuclear correlation (HETCOR) 2D NMR spectra (pulse sequence according to van Rossum et al.⁹⁰) were acquired using ¹H-¹³C magnetization transfer with contact times of 2 ms and 256 transients/t1. The data points recorded were 2 k (t1) and 64 (t2) and zero-filled to 4 k (t1) and 128 (t2) before the 2D Fourier transformation. The other experimental parameters were identical to those for the 1D CP NMR experiments. The spectra were referenced to external adamantane at 1.63 ppm (¹H) and 38.5 ppm (¹³C).

Thermogravimetric analysis. TGA experiments were carried out using a Perkin Elmer TGA Pyris 6 device in the temperature range from 30 °C to 600 °C with a heating rate of 10 K/min in air.

4.4 REFERENCES

- (1) Addadi, L., Raz, S., Weiner, S. *Adv. Mater.* **2003**, *15*, 959–970.
- (2) Meldrum, F. C. *Int. Mater. Rev.* **2003**, *48*, 187–224.
- (3) Becker, A., Ziegler, A., Epple, M. *Dalton Trans.* **2005**, 1814–1820.
- (4) Raz, S., Hamilton, P. C., Wilt, F. H., Weiner, S., Addadi, L. *Adv. Funct. Mater.* **2003**, *13*, 480–486.
- (5) Borzęcka-Prokop, B., Weselucha-Birczyńska, A., Koszowska, E. *J. Mol. Struct.* **2007**, *828*, 80–90.
- (6) Duquette, A., Halanych, K. M., Angus, R. A., McClintock, J. B. *Antarct. Sci.* **2018**, *22*, 1–10.
- (7) Hermoso, M., Lefeuvre, B., Minoletti, F., Raféllis, M. de. *PLoS One* **2017**, *12*, e0185655.
- (8) Müller, M. N., Lebrato, M., Riebesell, U., Barcelos e Ramos, J., Schulz, K. G., Blanco-Ameijeiras, S., Sett, S., Eisenhauer, A., Stoll, H. M. *Biogeosciences* **2014**, *11*, 1065–1075.
- (9) Langer, G., Gussone, N., Nehrke, G., Riebesell, U., Eisenhauer, A., Kuhnert, H., Rost, B., Trimborn, S., Thoms, S. *Limnol. Oceanogr.* **2006**, *51*, 310–320.
- (10) Stoll, H. M., Rosenthal, Y., Falkowski, P. *Geochim. Cosmochim. Acta* **2002**, *66*, 927–936.
- (11) Politi, Y., Batchelor, D. R., Zaslansky, P., Chmelka, B. F., Weaver, J. C., Sagi, I., Weiner, S., Addadi, L. *Chem. Mater.* **2010**, *22*, 161–166.
- (12) Rodríguez-Navarro, A. B., Marie, P., Nys, Y., Hincke, M. T., Gautron, J. *J. Struct. Biol.* **2015**, *190*, 291–303.
- (13) Weiss, I. M., Tuross, N., Addadi, L., Weiner, S. *J. Exp. Zool.* **2002**, *293*, 478–491.
- (14) Robach, J. S., Stock, S. R., Veis, A. *J. Struct. Biol.* **2006**, *155*, 87–95.
- (15) Blue, C. R., Giuffrè, A., Mergelsberg, S., Han, N., Yoreo, J. J. de, Dove, P. M. *Geochim. Cosmochim. Acta* **2017**, *196*, 179–196.
- (16) Wolf, S. E., Leiterer, J., Kappl, M., Emmerling, F., Tremel, W. *J. Am. Chem. Soc.* **2008**, *130*, 12342–12347.
- (17) Radha, A. V., Forbes, T. Z., Killian, C. E., Gilbert, P. U. P. A., Navrotsky, A. *Proc. Natl. Acad. Sci. USA* **2010**, *107*, 16438–16443.

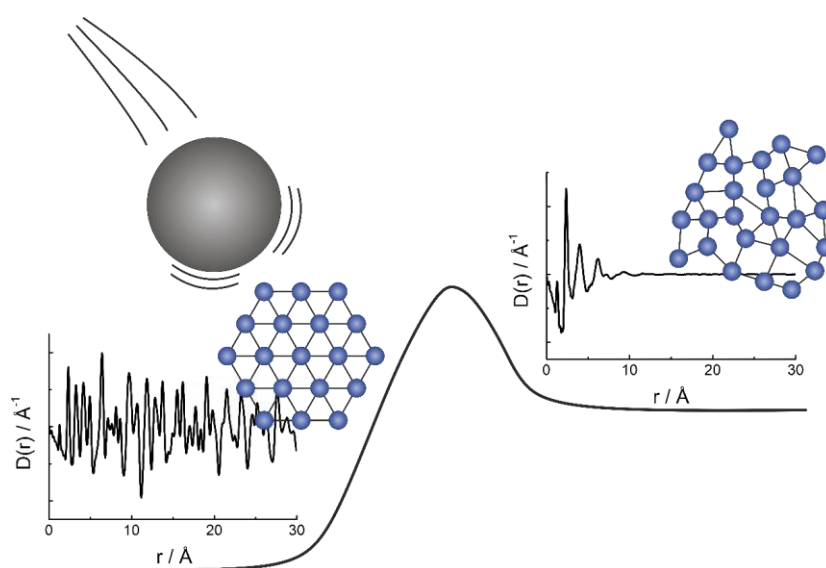
- (18) Rodriguez-Blanco, J. D., Shaw, S., Benning, L. G. *Nanoscale* **2011**, *3*, 265–271.
- (19) Rodriguez-Navarro, C., Kudłacz, K., Cizer, Ö., Ruiz-Agudo, E. *CrystEngComm* **2015**, *17*, 58–72.
- (20) Guillemet, B., Faatz, M., Gröhn, F., Wegner, G., Gnanou, Y. *Langmuir* **2006**, *22*, 1875–1879.
- (21) Wolf, S. E., Leiterer, J., Pipich, V., Barrea, R., Emmerling, F., Tremel, W. *J. Am. Chem. Soc.* **2011**, *133*, 12642–12649.
- (22) Ihli, J., Wong, W. C., Noel, E. H., Kim, Y.-Y., Kulak, A. N., Christenson, H. K., Duer, M. J., Meldrum, F. C. *Nat. Commun.* **2014**, *5*, 3169.
- (23) Ihli, J., Kulak, A. N., Meldrum, F. C. *Chem. Commun.* **2013**, *49*, 3134–3136.
- (24) Nebel, H., Neumann, M., Mayer, C., Epple, M. *Inorg. Chem.* **2008**, *47*, 7874–7879.
- (25) Goodwin, A. L., Michel, F. M., Phillips, B. L., Keen, D. A., Dove, M. T., Reeder, R. *J. Chem. Mater.* **2010**, *22*, 3197–3205.
- (26) Tobler, D. J., Rodriguez Blanco, J. D., Sørensen, H. O., Stipp, S. L. S., Dideriksen, K. *Cryst. Growth Des.* **2016**, *16*, 4500–4508.
- (27) Farhadi-Khouzani, M., Chevrier, D. M., Zhang, P., Hedin, N., Gebauer, D. *Angew. Chem. Int. Ed.* **2016**, *55*, 8117–8120.
- (28) Gebauer, D., Gunawidjaja, P. N., Ko, J. Y. P., Bacsik, Z., Aziz, B., Liu, L., Hu, Y., Bergström, L., Tai, C.-W., Sham, T.-K., Edén, M., Hedin, N. *Angew. Chem. Int. Ed.* **2010**, *122*, 9073–9075.
- (29) Littlewood, J. L., Shaw, S., Peacock, C. L., Bots, P., Trivedi, D., Burke, I. T. *Cryst. Growth Des.* **2017**, *17*, 1214–1223.
- (30) Yang, S.-Y., Chang, H.-H., Lin, C.-J., Huang, S.-J., Chan, J. C. C. *Chem. Commun.* **2016**, *52*, 11527–11530.
- (31) Wang, D., Hamm, L. M., Bodnar, R. J., Dove, P. M. *J. Raman Spectrosc.* **2012**, *43*, 543–548.
- (32) Wang, D., Wallace, A. F., Yoreo, J. J. de, Dove, P. M. *Proc. Natl. Acad. Sci. USA* **2009**, *106*, 21511–21516.
- (33) Loste, E., Wilson, R. M., Seshadri, R., Meldrum, F. C. *J. Cryst. Growth* **2003**, *254*, 206–218.
- (34) Radha, A. V., Fernandez-Martinez, A., Hu, Y., Jun, Y.-S., Waychunas, G. A., Navrotsky, A. *Geochim. Cosmochim. Acta* **2012**, *90*, 83–95.

- (35) White, C. E., Henson, N. J., Daemen, L. L., Hartl, M., Page, K. *Chem. Mater.* **2014**, *26*, 2693–2702.
- (36) Lanas, J., Alvarez, J. I. *Thermochim. Acta* **2004**, *421*, 123–132.
- (37) Zhao, Y., Luo, Z., Li, M., Qu, Q., Ma, X., Yu, S.-H., Zhao, Y. *Angew. Chem. Int. Ed.* **2015**, *54*, 919–922.
- (38) Frykstrand, S., Forsgren, J., Mihranyan, A., Strømme, M. *Microporous Mesoporous Mat.* **2014**, *190*, 99–104.
- (39) Zhang, P., Forsgren, J., Strømme, M. *Int. J. Pharm.* **2014**, *472*, 185–191.
- (40) Orlando, A., Lelli, M., Marini, L. *Appl. Geochem.* **2012**, *27*, 2500–2510.
- (41) Wolf, S. E., Müller, L., Barrea, R., Kampf, C. J., Leiterer, J., Panne, U., Hoffmann, T., Emmerling, F., Tremel, W. *Nanoscale* **2011**, *3*, 1158–1165.
- (42) Schmidt, M. P., Ilott, A. J., Phillips, B. L., Reeder, R. J. *Cryst. Growth Des.* **2014**, *14*, 938–951.
- (43) Koga, N., Nakagoe, Y., Tanaka, H. *Thermochim. Acta* **1998**, *318*, 239–244.
- (44) Bach, S., Celinski, V. R., Dietzsch, M., Panthöfer, M., Bienert, R., Emmerling, F., Schmedt auf der Günne, J., Tremel, W. *J. Am. Chem. Soc.* **2015**, *137*, 2285–2294.
- (45) Gilli, P., Bertolasi, V., Ferretti, V., Gilli, G. *J. Am. Chem. Soc.* **1994**, *116*, 909–915.
- (46) Cleland, W. W., Kreevoy, M. M. *Science* **1994**, *264*, 1887–1890.
- (47) Gellman, S. H., Dado, G. P., Liang, G. B., Adams, B. R. *J. Am. Chem. Soc.* **1991**, *113*, 1164–1173.
- (48) Cowan, M. L., Bruner, B. D., Huse, N., Dwyer, J. R., Chugh, B., Nibbering, E. T. J., Elsaesser, T., Miller, R. J. D. *Nature* **2005**, *434*, 199–202.
- (49) Smith, J. D., Cappa, C. D., Wilson, K. R., Messer, B. M., Cohen, R. C., Saykally, R. *J. Science* **2004**, *306*, 851–853.
- (50) Thomas Steiner. *Angew. Chem. Int. Ed.* **2002**, *41*, 48–76.
- (51) Brubach, J.-B., Mermet, A., Filabozzi, A., Gerschel, A., Roy, P. *J. Chem. Phys.* **2005**, *122*, 184509.
- (52) Gilli, G., Gilli, P. *J. Mol. Struct.* **2000**, *552*, 1–15.
- (53) Mikenda, W. *J. Mol. Struct.* **1986**, *147*, 1–15.
- (54) Alkorta, I., Elguero, J. *J. Phys. Chem. A* **1999**, *103*, 272–279.
- (55) Eckert, H., Yesinowski, J. P., Silver, L. A., Stolper, A. M. *J. Phys. Chem.* **1988**, *92*, 2055–2064.

- (56) Singer, J. W., Yazaydin, A. Ö., Kirkpatrick, R. J., Bowers, G. M. *Chem. Mater.* **2012**, *24*, 1828–1836.
- (57) Lin, C.-J., Yang, S.-Y., Huang, S.-J., Chan, J. C. C. *J. Phys. Chem. C* **2015**, *119*, 7225–7233.
- (58) Bloembergen, N., Purcell, E. M., Pound, R. V. *Phys. Rev.* **1948**, *73*, 679–715.
- (59) Woessner, D. E. *J. Chem. Phys.* **1962**, *36*, 1–4.
- (60) Masuda, K., Tabata, S., Sakata, Y., Hayase, T., Yonemochi, E., Terada, K. *Pharm. Res.* **2005**, *22*, 797–805.
- (61) Mehta, M., Kothari, K., Ragoonanan, V., Suryanarayanan, R. *Mol. Pharm.* **2016**, *13*, 1339–1346.
- (62) Separovic, F., Lam, Y. H., Ke, X., Chan, H. K. *Pharm. Res.* **1998**, *15*, 1816–1821.
- (63) Oksanen, C. A., Zografí, G. *Pharm. Res.* **1993**, *10*, 791–799.
- (64) Leukel, S., Tremel, W. *Crystal Growth & Design* **2018**,
DOI: 10.1021/acs.cgd.8b00627
- (65) Unluer, C., Al-Tabbaa, A. *J. Therm. Anal. Calorim.* **2014**, *115*, 595–607.
- (66) Anderson, P. J., Horlock, R. F. *Trans. Faraday Soc.* **1962**, *58*, 1993–2004.
- (67) Parr, R. G., Pearson, R. G. *J. Am. Chem. Soc.* **1983**, *105*, 7512–7516.
- (68) Andersen, F. A., Brečević, L. *Acta Chem. Scand.* **1991**, *45*, 1018–1024.
- (69) Libowitzky, E. *Monatsh. Chem.* **1999**, *130*, 1047–1059.
- (70) Pearson, R. G. *J. Am. Chem. Soc.* **1963**, *85*, 3533–3539.
- (71) Lutz, H. D., Beckenkamp, K., Möller, H. *J. Mol. Struct.* **1994**, *322*, 263–266.
- (72) Kolodziejcki, W., Klinowski, J. *Chem. Rev.* **2002**, *102*, 613–628.
- (73) Kielkopf, J. F. *J. Opt. Soc. Am.* **1973**, *63*, 987.
- (74) Jäger, C., Welzel, T., Meyer-Zaika, W., Epple, M. *Magn. Reson. Chem.* **2006**, *44*, 573–580.
- (75) Canterford, J. H. *Mineral. Mag.* **1984**, *48*, 437–442.
- (76) Fischbeck, R., Müller, G. *Contr. Mineral. and Petrol.* **1971**, *33*, 87–92.
- (77) Moore, J. K., Surface, J. A., Brenner, A., Wang, L. S., Skemer, P., Conradi, M. S., Hayes, S. E. *Environ. Sci. Technol.* **2015**, *49*, 657–664.
- (78) Brunner, E., Sternberg, U. *Prog. Nucl. Magn. Reson. Spectrosc.* **1998**, *32*, 21–57.
- (79) Muller, N., Reiter, R. C. *J. Chem. Phys.* **1965**, *42*, 3265–3269.
- (80) Baxter, N. J., Williamson, M. P. *J. Biomol. NMR* **1997**, *9*, 359–369.

- (81) Deichmann, R., Haase, A. *J. Magn. Reson.* **1992**, *96*, 608–612.
- (82) Han, J. H., Lee, K. W., Jeon, G. W., Lee, C. E., Park, W. K., Choi, E. H. *Appl. Phys. Lett.* **2015**, *106*, 23104.
- (83) Viani, A., Mali, G., Mácová, P. *Ceram. Int.* **2017**, *43*, 6571–6579.
- (84) Gong, Y. U. T., Killian, C. E., Olson, I. C., Appathurai, N. P., Amasino, A. L., Martin, M. C., Holt, L. J., Wilt, F. H., Gilbert, P. U. P. A. *Proc. Natl. Acad. Sci. USA* **2012**, *109*, 6088–6093.
- (85) Politi, Y., Metzler, R. A., Abrecht, M., Gilbert, B., Wilt, F. H., Sagi, I., Addadia, L., Weiner, S., Gilbert, P. U. P. A. *Proc. Natl. Acad. Sci. USA* **2008**, *105*, 17362–17366.
- (86) Cartwright, J. H. E., Checa, A. G., Gale, J. D., Gebauer, D., Sainz-Díaz, C. I. *Angew. Chem. Int. Ed.* **2012**, *51*, 11960–11970.
- (87) Nishiyama, R., Munemoto, T., Fukushi, K. *Geochim. Cosmochim. Acta* **2013**, *100*, 217–231.
- (88) PDF-2, Release 2004, JCPDS – International Center for Diffraction Data, Newton Square (PA) US (2004).
- (89) EVA 10.0 Rev. 1, Bruker AXS, Madison (WI) US (2003).
- (90) van Rossuma, B.-J., Förster, H., de Groot, H. J. M. *J. Magn. Reson.* **1997**, *124*, 516–519.

MECHANOCHEMICAL ACCESS TO AMORPHOUS CALCIUM CARBONATE



Amorphous calcium carbonate (ACC) is usually formed as an intermediate phase during crystallization of calcium carbonate in solution. We took a radically new approach and prepared a new form of amorphous calcium carbonate (BM-ACC) by high-energy ball milling from calcite. The addition of a small amount of foreign ions, in form of Na_2CO_3 , is crucial to achieve complete amorphization. We used the sodium cation as probe to study the degradation of the crystalline order by nuclear magnetic resonance (^{23}Na NMR) spectroscopy. A structural model revealing the partly unsaturated coordination sphere of the Ca^{2+} ions was derived from the analysis of total scattering data with high-energy synchrotron radiation. BM-ACC exhibits a distinctively different crystallization behavior from ACC prepared by wet chemical methods.

This chapter contains an adapted manuscript submitted to *Chemistry of Materials*.

Authorship Contribution

Study conception and design	S. Leukel W. Tremel
Acquisition of data	S. Leukel M. Panthöfer M. Mondeshki G. Kieslich Y. Wu N. Krautwurst
Analysis and interpretation of data	S. Leukel M. Panthöfer M. Mondeshki G. Kieslich Y. Wu
Drafting of manuscript	S. Leukel
Critical revision	M. Panthöfer M. Mondeshki G. Kieslich Y. Wu W. Tremel

5.1 INTRODUCTION

Calcium carbonate is widely used industrially for ceramics,¹ construction materials,² paper making,³ as filler material in pharmaceuticals,⁴ as phosphate binder,⁵ and as a drug carrier system.⁶ In addition, it is the most common biomineral in nature, forming eggshells,⁷ coral reefs,⁸ and hard tissue in marine organisms.^{9,10} The ability of calcium carbonate to crystallize *via* an amorphous intermediate (ACC) is of highest importance for its function as a biomineral, because this transient species can be molded into elaborate shapes by proteins and macromolecular templates.¹¹ The first industrial applications for ACC have been developed, e.g. hydrogels with ACC can be employed as an environmentally friendly composite material.^{12,13}

The local structure in ACC is still a subject of current research. Gebauer et al.¹⁴ observed a pH dependence of the short-range order in ACC, and Tobler et al. studied the OH⁻ incorporation into ACC.¹⁵ Protostructuring of ACC with regard to different crystalline modifications is discussed,¹⁴ as well as the concept of “polyamorphism” in biogenic ACC.¹⁶ Therefore, many approaches have been pursued to synthesize and stabilize ACC that range from freeze-drying,¹⁷ over the use of polymers¹⁸ and proteins,¹⁹ to the incorporation of foreign ions like magnesium.²⁰ Upscaling of ACC synthesis has been studied as well.²¹ These wet-chemical approaches start from Ca²⁺ and CO₃²⁻ ions in aqueous solution. The crystallization process is stopped at the ACC stage by stabilizing the product kinetically.

Ball milling is a well-known strategy to produce non-equilibrium structures. It is employed for breaking down bulk materials to nano-size.^{22–24} Ball milling can induce alloying of metals²⁵ or polymorph changes, e.g. a transformation from the anatase to the rutile modification of TiO₂.²⁶ Defect formation on a large scale leads ultimately to an amorphization of crystalline solids.²⁷ Elemental germanium²⁸ or zeolites^{29–31} show a loss of crystallinity during ball milling, and changes of the hydrate network have been reported for Co₃(PO₄)₂ × 8H₂O.³² This behavior is not restricted to inorganic materials. Organic compounds (e.g. sugars^{33–35}) and mixtures of organic and inorganic compounds^{36,37} undergo structural changes during mechanochemical treatment. This is highly relevant for pharmaceuticals because of the generally higher solubility of amorphous polymorphs, which enhances the uptake of drugs with poor water solubility.^{38,39} Mechanochemistry is of particular interest for large applications because of its scalability and the reduced use of solvents, which make it a “green chemistry”

technique.⁴⁰ Mechanochemical treatment of calcium carbonate has been the subject of intensive research for over 60 years. Burns and Bredig were the first to report the transformation of calcite to aragonite in a mechanically operated mortar.⁴¹ The reverse transformation from aragonite to calcite was described later.⁴² Also, vaterite can be transformed mechanochemically to calcite.^{43,44}

We applied mechanochemistry for the synthesis of ACC. Ball milled amorphous calcium carbonate (BM-ACC) particles were prepared by treating calcite, the thermodynamically stable crystalline CaCO_3 polymorph, in a planetary ball mill. Powder X-ray diffraction (PXRD) revealed a minimum concentration of 7.5 mol% Na_2CO_3 to be necessary for the complete amorphization of calcite. The process was monitored *ex situ* by quantitative Fourier transform infrared spectroscopy (FTIR) and ^{23}Na magic angle spinning nuclear magnetic resonance (^{23}Na MAS-NMR) spectroscopy, which provided information about the local atomic structure of the carbonate group and the sodium cations. The structural characterization of BM-ACC was performed by total scattering with high-energy synchrotron radiation. Analysis of the pair distribution function (PDF) revealed a lower coordination number of the Ca^{2+} cations (compared to calcite). Important differences between BM-ACC and wet-chemically prepared ACC (the properties of ACC obtained from solution can vary depending on the synthetic approach and the use of additives) are (i) the absence of structural water and the incorporation of foreign ions, which is not untypical for ACC.²⁰ (ii) BM-ACC is stable in air for several days. (iii) BM-ACC transforms to calcite *via* a surface-mediated dissolution-recrystallization mechanism without forming vaterite⁴⁵ as intermediate phase. (iv) Thermally induced crystallization to calcite occurs already at low (185 °C) temperature.

5.2 RESULTS AND DISCUSSION

Mechanochemical Synthesis BM-ACC

The new form of amorphous calcium carbonate was synthesized by mechanochemical treatment of calcite in a planetary ball mill by the addition of Na_2CO_3 . The phase purity of the calcite precursor was confirmed by PXRD (Figure 5.1a). Mixtures of calcite with variable amounts of Na_2CO_3 were ground in a planetary ball mill for 24 h with cyclohexane as dispersion medium. This long reaction time was chosen to complete the reaction and to reach mechanochemical equilibrium.⁴⁶ Milling of pure calcite led to a decrease of the crystallite

size, as indicated by reflection broadening, but full loss of long-range order was reached only in the presence of Na_2CO_3 . The typical modulation with two maxima of ACC appeared for 5 mol% Na_2CO_3 , while the characteristic (104) reflection of crystalline calcite at $Q = 2.1 \text{ \AA}^{-1}$ was still present. For 7.5 mol% Na_2CO_3 , all reflections vanished, and the sample was “X-ray amorphous”. This concentration sets the lower limit for amorphization, as the milling time of 24 h was unusually long. To reduce the milling time and to ensure complete amorphization, 10 mol% Na_2CO_3 was used for all further experiments. The resulting compound with the composition $\text{Ca}_{0.9}\text{Na}_{0.2}\text{CO}_3$ is referred to as BM-ACC.

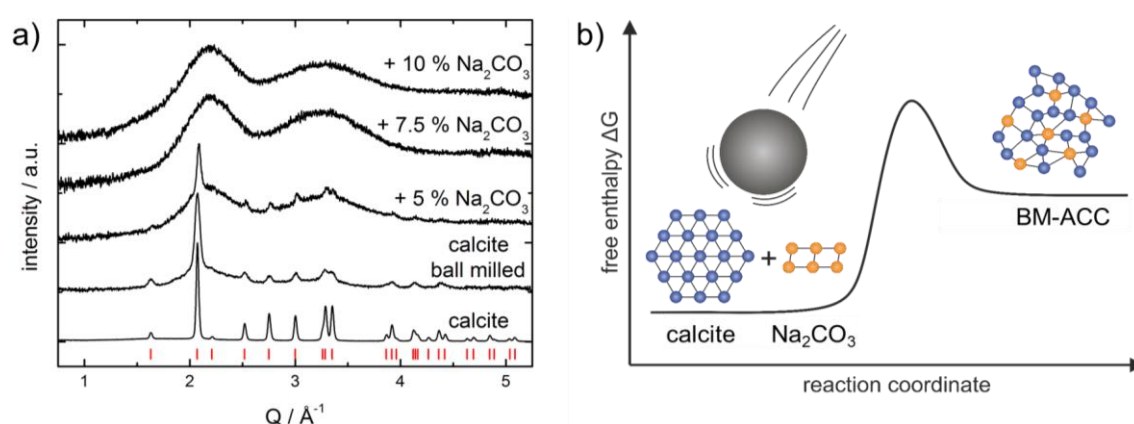


Figure 5.1 a) PXR D of mixtures of calcite and Na_2CO_3 after 24 h of mechanochemical treatment: Untreated pure calcite with reference pattern (red) is shown at the bottom. Milling pure calcite leads only to broadening of the reflections. After addition of 7.5 mol% Na_2CO_3 , complete amorphization was achieved. b) Schematic sketch of the reaction profile. Input of mechanical energy generates metastable BM-ACC from thermodynamically stable crystalline reactants.

Spectroscopic Characterization

Raman spectroscopy is sensitive to the crystallinity of a compound due to the ability to measure lattice vibrations at low wavenumbers.⁴⁷ Whereas the spectrum of calcite displays two lattice modes at 156 cm^{-1} and 283 cm^{-1} ,⁴⁸ these bands are absent for BM-ACC (Figure 5.2a). This is in agreement with the results of PXR D (Figure 5.1a) and supports the loss of long-range order. The relatively sharp band in the BM-ACC spectrum at 803 cm^{-1} derives from residual cyclohexane (Figure S15, Supporting Information), which was used as dispersion medium during milling. It could not be removed by storing the sample *in vacuo*, which suggest a physical incorporation in cavities in BM-ACC (*vide infra*). In the Raman spectrum, the symmetric stretching (1080 cm^{-1}) and the in-plane deformation (715 cm^{-1}) bands of the carbonate group in BM-ACC are significantly broadened, compared to the respective bands

in calcite and Na_2CO_3 . This implies a less defined coordination of the carbonate group in BM-ACC.

The same phenomenon is observed in the FTIR spectrum (Figure 5.2b). BM-ACC exhibits the four characteristic vibrational modes of carbonate (symmetric stretch $\nu_1 = 1071 \text{ cm}^{-1}$, out-of-plane deformation $\nu_2 = 857 \text{ cm}^{-1}$, asymmetric stretch $\nu_3 = 1377 \text{ cm}^{-1}$, in-plane-deformation $\nu_4 = 695 \text{ cm}^{-1}$ and 725 cm^{-1}).⁴⁸ Besides being broadened, the bands are slightly shifted for BM-ACC. The pronounced shift of the ν_2 mode to lower wavenumbers in BM-ACC was used to quantify the progress and kinetics of the amorphization/crystallization (*vide infra*). Unlike ACC obtained from the common wet chemistry routes,^{49,50} BM-ACC is anhydrous, as indicated by the absence of a O-H stretching vibration around 3500 cm^{-1} in the FTIR spectrum. The magnification of this region in the FTIR spectrum (Figure 5.2b, inset) and also the ^1H NMR spectrum of BM-ACC (Figure S15a, Supporting Information) show trace amounts of water, which is potentially physisorbed on the material.

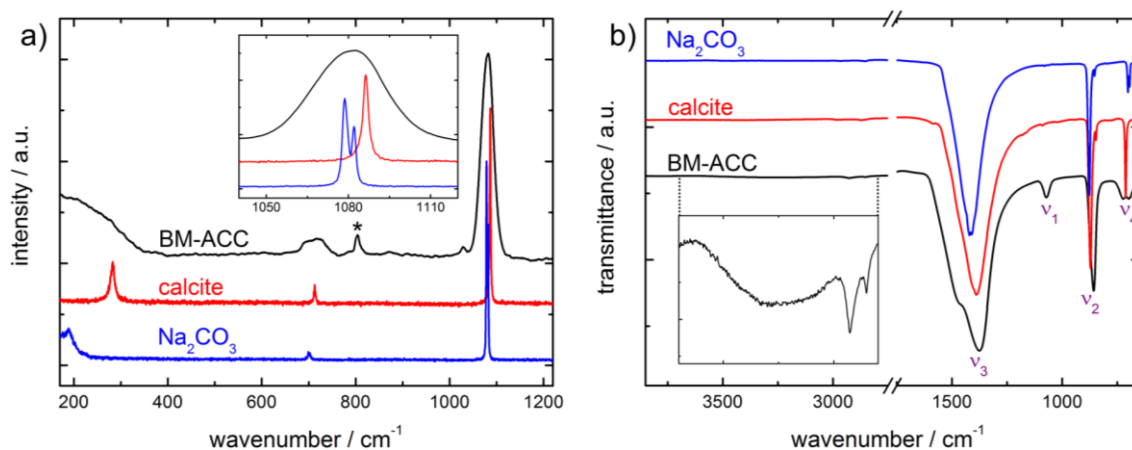


Figure 5.2 a) The Raman spectrum of BM-ACC displays the bands of the symmetric stretching (1080 cm^{-1}) and the in-plane deformation vibration (715 cm^{-1}). Both bands are significantly broadened compared to the respective vibrations of the reactants, calcite and Na_2CO_3 . The lattice vibration of calcite at 290 cm^{-1} is absent for BM-ACC, indicating the lack of long-range order. A band of the residual dispersion medium cyclohexane is marked with an asterisk. b) The FTIR spectrum of BM-ACC displays the characteristic vibrational modes of carbonate. They are shifted and broadened, compared to calcite and Na_2CO_3 . BM-ACC is anhydrous, shown by the absence of the OH-vibration at around 3500 cm^{-1} . Magnification of this region (200 x, inset) reveals the presence of cyclohexane (C-H stretching vibrations around 2900 cm^{-1}) and traces of water, which is possibly physisorbed on BM-ACC.

The implication of the hydration on the stability of ACC is heavily discussed in literature. In biogenic ACC samples, Addadi et. al reported that anhydrous ACC crystallizes rapidly, whereas the hydrated form is more stable.⁵¹ The crystallization enthalpies⁵² of the respective

species suggest a downhill sequence from hydrated ACC, *via* anhydrous ACC, to calcite. This was confirmed experimentally.⁵³ Besides energetic considerations, kinetic stabilization plays a major role in preventing crystallization of ACC. Konrad et al. synthesized ACC by freeze-drying, which resulted in a reduced water content of ACC (~0.4 mol H₂O per formula unit). Then, they probed the crystallization kinetics of this water-deficient ACC in various atmospheres.⁵⁴ In air, the crystallization was triggered by physisorption of a critical level of water, which enabled dissolution and recrystallization processes in a thin surface film. First evidence of crystallization was observed after four days. In contrast, ACC films prepared by wet chemistry, which were only dried in a stream of nitrogen, crystallized within one hour in air.⁵⁵ Therefore, careful dehydration can be regarded as a strategy to kinetically stabilize ACC, whereas hydration – and especially the formation of a surface water film – induces crystallization.

In air, BM-ACC is stable with regard to crystallization for several days. After four days, we observe the first hints of calcite in the sample (Figure S16, Supporting Information). Moreover, the amount of physisorbed water increases. Therefore, we assume a similar mechanism as for freeze-dried ACC: BM-ACC is a water-deficient species, which prevents fast crystallization, in contrast to wet-chemically prepared ACC. The formation of a surface water film is required to induce crystallization, and even then, crystallization proceeds slowly.

Solid-state NMR provides information about the local environment of the nuclei and thus about the short-range order in crystalline and amorphous systems. Crystalline materials are characterized by relatively sharp resonance signals in the NMR spectra in contrast to the broadened amorphous peaks. We studied the signal broadening of BM-ACC and the reactants, calcite and Na₂CO₃, with ¹³C and ²³Na MAS-NMR spectroscopy. ²³Na is a quadrupole nucleus (*I* = 3/2) and therefore sensitive to changes in the symmetry of its coordination sphere⁵⁶ and lattice defects.⁵⁷

¹³C-MAS-NMR experiments were performed to probe the chemical environment of the carbonate group. Figure 5.3a displays the carbonyl spectral region for Na₂CO₃, calcite, and BM-ACC. The ¹³C resonance signal of Na₂CO₃ is characterized by a chemical shift of 170.7 ppm with a full width at half maximum (FWHM) of 40 Hz, while the signal of calcite is detected at 168.5 ppm⁵⁸ with a FWHM of ca. 33 Hz. The shorter C-O distance of 1.18 Å in Na₂CO₃,⁵⁹ compared to 1.25 Å in calcite,⁶⁰ is related with a stronger deshielding and thus a downfield shift of the resonance of about 2.2 ppm. The FWHM of calcite is about 7 Hz

smaller compared to sodium carbonate. The FWHM of the NMR signals in the spectra of crystalline compounds provides information about the homogeneity of the local field and is a measure of the degree of crystallinity.⁶¹ The ^{13}C resonance of BM-ACC appeared at 168.4 ppm, in agreement with literature values for hydrated ACC.^{58,62} Yet, it should be noted that also amorphous carbonate species with deviating chemical shift were found.¹⁴ The broadening of the signal (FWHM = 370 Hz) implies increased heterogeneity in the chemical environment of the carbon atoms in BM-ACC and thus higher local variety and lack of long-range order.

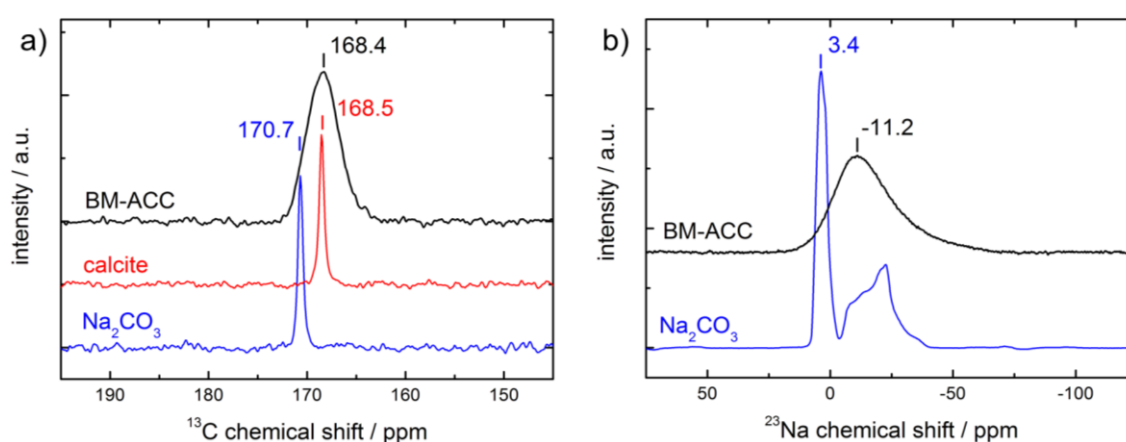


Figure 5.3 a) The ^{13}C MAS-NMR shows the respective carbonate signal of BM-ACC (black), calcite (red), and Na_2CO_3 (blue). The maxima of BM-ACC and calcite nearly coincide at 168.5 ppm, whereas the Na_2CO_3 signal is more strongly deshielded and shifted to 170.7 ppm. The FWHM of the BM-ACC signal is broadened due a higher variation of chemical environments of the carbonate group in the amorphous solid. b) ^{23}Na MAS-NMR of BM-ACC (black) and Na_2CO_3 (blue). The two signals in crystalline Na_2CO_3 arise from sodium coordination spheres with different symmetry. In BM-ACC, only one broad signal appears, indicating a less structured environment of the sodium cations.

The ^{23}Na MAS-NMR spectrum of crystalline Na_2CO_3 (Figure 5.3b) shows two distinct signals, corresponding to different symmetries of the sodium coordination in the lattice (Figure S17, Supporting Information). Two sodium positions (0, 0, 0; symmetry 2/m, Wyckoff site 2a, and 0, 0, $\frac{1}{2}$, symmetry 2/m, Wyckoff site 2c) exhibit octahedral coordination, and they are occupied by half of the sodium ions. This highly symmetric coordination sphere gives rise to the sharp signal at 3.4 ppm with a FWHM of 540 Hz. The remaining sodium ions are located in a position with lower symmetry (0.1760, $\frac{1}{2}$, 0.7478, site symmetry m, Wyckoff site 4i). Sodium is surrounded by six oxygen atoms in a distorted equatorial coordination with one oxygen atom above and two equidistant oxygen atoms below this plane (distorted capped bipyramid, CN = 9). The anisotropy of this coordination

polyhedron results in an electrical field gradient and thus signal broadening due to quadrupole interaction. This ^{23}Na resonance appears at approximately -15 ppm. The chemical shift of the ^{23}Na NMR signal is related to the Na-O distance and the coordination number of the sodium cation.⁶³ For high coordination numbers and larger Na-O distances, the signal is shifted to higher field. We can confirm this for Na_2CO_3 . The octahedrally coordinated sodium ions with a mean Na-O distance of 2.35 Å⁵⁹ appear at lower field, compared to the sodium ions in the distorted capped bipyramidal position with a mean Na-O distance of 2.70 Å.⁵⁹ BM-ACC exhibits one broad, not fully symmetric signal with a maximum around -11 ppm and a FWHM of 3250 Hz. No distinct sodium positions could be identified, which implies a low coordination symmetry and/or a large variation of the chemical environments. The chemical shift suggests an increased Na-O distance, which seems plausible for sodium ions in an amorphous matrix of calcium carbonate. The ^{23}Na MAS-NMR spectra suggest a very low degree of order around the respective nucleus. This confirms the absence of long-range order, which is in accordance with the X-ray powder diffractogram (Figure 5.1a) and the vibrational spectra (Figure 5.2).

Formation Kinetics of BM-ACC

As both FTIR and NMR spectroscopy can distinguish between amorphous and crystalline calcium carbonate, these techniques were deployed to probe the formation kinetics of BM-ACC. The evolution of the ν_2 mode was monitored by FTIR using the relatively clear separation of the respective bands of amorphous and crystalline calcium carbonate (Figure 5.2b). The spectra were normalized to the most intense ν_3 mode – the transmittance of this mode was usually in the range ~50 %. For this normalization, we assumed that the absorbance of the ν_3 mode remains constant during amorphization/crystallization, which allowed for good semi-quantitative image of the formation kinetics. The transmittance T of the ν_2 mode was converted to the absorbance A according to $A = -\log_{10}(T)$. Based on the Lambert-Beer law,⁶⁴ the absorbance is proportional to the concentration of the respective compounds. We monitored the change in absorbance of the ν_2 mode with time relating to $t = 0$. The relative amounts of crystalline calcite (873 cm^{-1}) and amorphous calcium carbonate (857 cm^{-1}) were determined by fitting the ν_2 band with a bimodal Gaussian function. The absorbance of calcite at $t = 0$ was set as “100 %”, the respective absorbance of completely X-ray amorphous BM-ACC as “0 %”. Thus, the relative absorbance of the ν_2 mode of calcite can be regarded

as a proxy for crystallinity. Pure calcite (red) and calcite with 10 mol% Na_2CO_3 (black) were processed in a planetary ball mill at 750 rpm. After distinct time intervals, samples were taken and analyzed by FTIR. The results are displayed in Figure 5.4a.

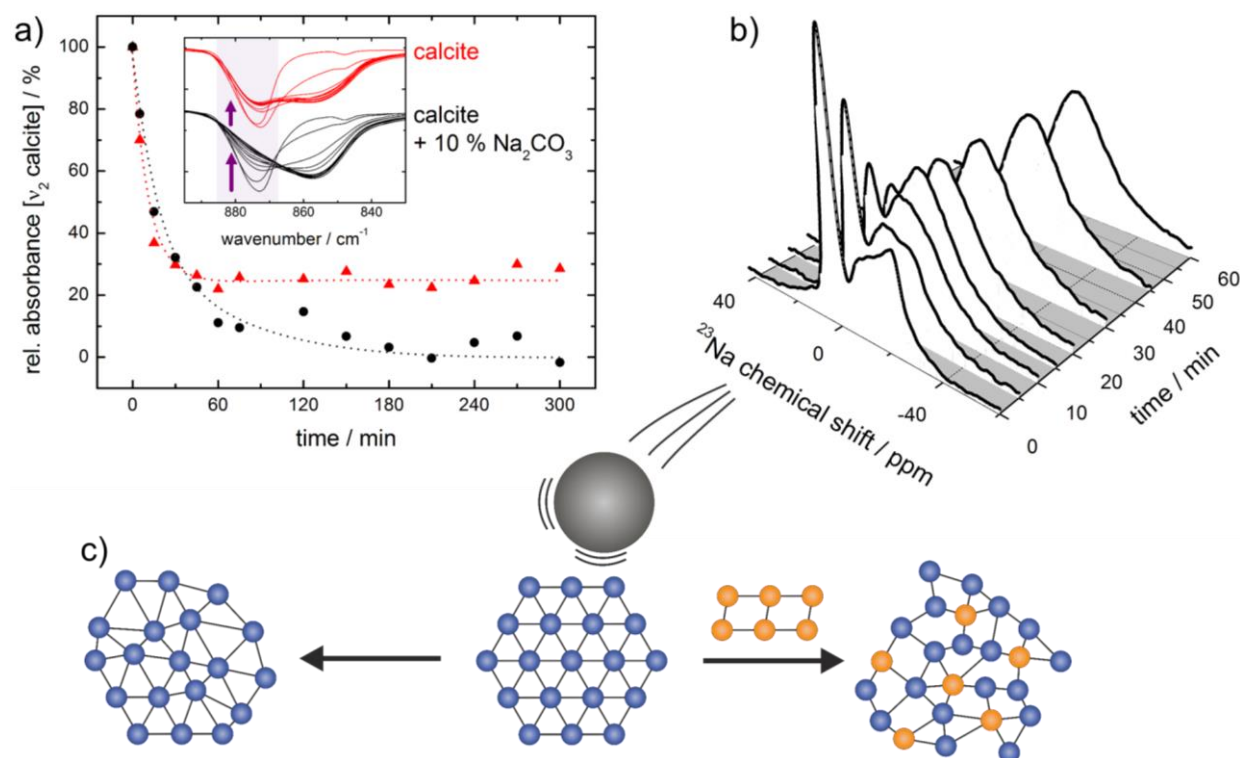


Figure 5.4 a) Decreasing crystallinity of pure calcite (red) and calcite mixed with 10 mol% Na_2CO_3 (black), as monitored by FTIR (inset). Absorbance is given in relative values regarding the absorbance of the ν_2 mode of calcite at $t = 0$. Addition of Na_2CO_3 is crucial to achieve complete amorphization. Dotted lines are shown to guide the eye. b) ^{23}Na MAS-NMR spectra at different ball milling times. The chemical environment of the Na^+ cations changes from distinct sites in the crystalline structure to a broad distribution of slightly different environments. c) Scheme displaying mechanochemical treatment of pure calcite (blue) and calcite with Na_2CO_3 (orange). The addition of foreign ions increases the number of defects and leads to amorphization, whereas the lattice in pure calcite is only partly damaged.

Both samples showed an exponential decay of the relative absorbance of the ν_2 mode of calcite. The amorphization of BM-ACC was completed after ca. 3 h, when no further drop of the calcite absorbance was observed. For pure calcite, the crystallinity remained constant after an initial decrease. The equilibrium concentration of crystalline calcite was ca. 30%, based on FTIR. The simultaneous presence of amorphous and crystalline calcium carbonate (Figure 5.4a, inset) is in accordance with the results of PXRD measurements (Figure 5.1a). The incorporation of sodium in the calcium carbonate structure was monitored by ^{23}Na MAS-NMR (Figure 5.4b). The quadrupole nucleus ^{23}Na is highly sensitive to changes

in the symmetry of its environment, making it a suitable probe for the process of amorphization. At the start, two signals from the different coordination sites in crystalline Na_2CO_3 were present. After ten minutes, a third signal appeared at an intermediate chemical shift of -11 ppm. This signal evolved to the final broad signal of BM-ACC (Figure 5.4b). The signals associated with crystalline Na_2CO_3 decreased to the same extent.

By ball milling Na_2CO_3 and calcite particles, sodium ions are transferred to the calcium carbonate phase and incorporated, thereby consuming the Na_2CO_3 crystals gradually. This formation process is illustrated in Figure 5.4c. Mechanochemical treatment of calcite crystals makes the calcite structure collapse by breaking down crystals to smaller particles and inducing defects. We assume that the amorphization is not complete, because the impact of the milling balls on the particles produces heat, which leads to recrystallization. Therefore, an equilibrium between amorphous and crystalline parts is reached. Addition of Na_2CO_3 during milling leads to an incorporation of sodium cations into the structure. This is facilitated by the similar ionic radii of Ca^{2+} (106 pm) and Na^+ (98 pm).⁶⁵ The lower charge of the Na^+ cations with a comparable ionic radius is a driving force for the generation of vacancies in the anionic sublattice. The Na^+ cations hinder recrystallization kinetically, because they are not incorporated easily into the calcite lattice (*vide infra*).

Structure

We performed high-energy total-scattering experiments to probe the structure of BM-ACC. From these data, the pair distribution function (PDF) was calculated using GUDRUNX.⁶⁶ The PDF exhibits four pronounced peaks at 1.29 Å, 2.38 Å, 3.98 Å, and 6.17 Å (Figure 5.5a). Beyond 8 Å, the PDF turns virtually into a flat line, which underlines the amorphous character of BM-ACC. In contrast, the PDF of calcite (Figure 5.5a, red) shows a multitude of distinct peaks, even at higher r . The long-range order of the reactant is degraded during milling. We modeled the PDF data using Topas Academic V6.⁶⁷ 100 runs starting from random configurations all converged with residuals ranging from $R_{\text{wp}} = 14.3$ to $R_{\text{wp}} = 16.3$. The calculated PDF of one model is plotted in Figure 5.5a (dotted line). The first peak of the experimental PDF originates from the intramolecular C-O distance within the carbonate ion. The distance of 1.29 Å in BM-ACC is slightly longer than the C-O distance in crystalline calcite (1.25 Å).⁶⁰ We assume that distortion and stress in BM-ACC causes the extension of the C-O bond. The lower average coordination number of calcium (*vide infra*) potentially

causes a stronger metal-oxygen interaction, which leads to a weakening of the C-O bond. The second peak is a superposition of the intramolecular O-O distance of the carbonate ion and the Ca-O distance of the first coordination sphere of calcium (contributions of interatomic distances, Figure S18, Supporting Information). The Ca-O distance of 2.40 Å is in good agreement with the respective value for crystalline calcite.⁶⁰ The Ca-Ca distance is the main contributor to the third peak of the experimental PDF. Yet, a variety of other interatomic distances also contribute to the peak. In calcite, these distances are clearly more distinguished, which indicates that ordering in BM-ACC is already reduced at that length scale (~4 Å). Farther Ca-O distances mainly cause the last clear peak around 6 Å.

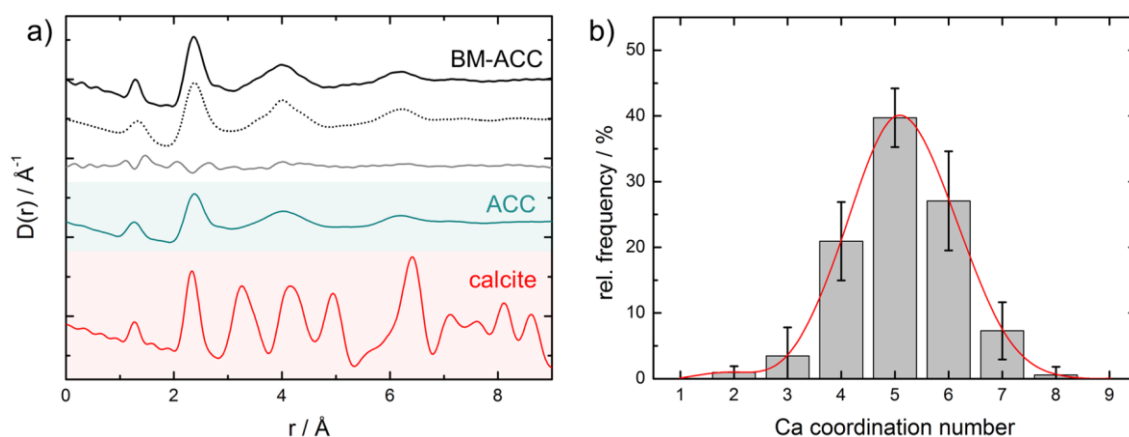


Figure 5.5 a) The experimental PDF (black) of BM-ACC shows no order beyond 8 Å. The PDF of the structural model (dotted line) and difference line (gray) are shown. The first peak of the PDF at 1.29 Å originates from the intramolecular C-O distance in the carbonate ion, the second peak arises mainly from the first oxygen coordination sphere of the cation. The other peaks are a combination of a multitude of interatomic distances. The PDF of BM-ACC strongly resembles the one of wet-chemically prepared ACC (green). Calcite (red) shows the typical long-range order of a crystalline compound. b) Distribution of the Ca-O coordination number in the structural models of BM-ACC is displayed. The mean coordination number of calcium is lowered to five, compared to six in crystalline calcite.

We compared the PDFs of BM-ACC (Figure 5.5a, black) and ACC (Figure 5.5a, green), which was synthesized wet-chemically from methanolic solution.⁶⁸ Both samples show the same degree of short-range order, only displaying four distinct peaks. Other methods to synthesize ACC as well as varying degrees of hydration⁶⁹ lead to comparable results.⁶² The position of the peaks agrees within several pm. As in calcite, the C-O distance in ACC synthesized from solution is slightly shorter than in BM-ACC. Additionally, the third peak in ACC is lightly shifted to larger r . As the Ca-Ca distance mainly contributes to this peak, the substitution of Ca^{2+} by Na^+ in BM-ACC reduces the Coulomb repulsion and decreases

the distance between the cations. Biogenic ACC exhibit the same degree of short-range order as synthetic ACC. In a comparative PFD study, Reeder et al. describe biogenic ACC in the gastroliths of lobsters as “nearly indistinguishable from [...] synthetic, hydrated ACC”.⁷⁰ As the degree of disorder in BM-ACC is of the same magnitude, we consider it a new form of ACC.

Furthermore, we evaluated the coordination number of the calcium atoms, taking into account the ten best models (Figure 5.5b). Whereas calcium in the calcite structure has a distorted octahedral coordination of six oxygen atoms, we find an average coordination number of only five in our models for BM-ACC. We assume that the mechanochemical energy is stored in defects and distortions of the material, which manifests itself in an unsaturated coordination sphere of calcium. Decreased coordination numbers of the metal in amorphous modifications were also observed in cobalt phosphate.³²

Crystallization of BM-ACC

Both the thermally and water-induced crystallization behavior of BM-ACC was examined. TEM images show that BM-ACC consists of fused nanoparticles, 10–20 nm in diameter. These nanoparticles form larger aggregates with diameters of several hundred nm (Figure 5.6a). No discrete nanoparticles were found by TEM, suggesting agglomeration/fusion occurs during milling to minimize the surface energy. Through selected area electron diffraction (SAED), we confirmed that BM-ACC is amorphous and not only nano-crystalline (Figure 5.6a, inset). After incubation in water, the aggregates are still present, but rhombohedral crystals appear on their surface (Figure 5.6b). The phase was identified as calcite by Rietveld refinement of the PXRD data (Figure 5.6c). We only observe large aggregates of calcite on the TEM grid, no single crystallites. Even though drying artifacts cannot be excluded completely, the pervasive aggregation of small calcite crystallites suggests heterogeneous nucleation of calcite on BM-ACC. AAS measurements confirmed the calculated composition of BM-ACC, based on the weighed-in reactants. During crystallization, the sample is depleted of sodium, which suggests a dissolution-recrystallization mechanism. To further investigate the crystallization process, we monitored the phase transformation by quantitative FTIR. As the crystallization proceeds too fast in pure water (BM-ACC crystallizes instantly), we deployed a mixture of 10 vol% water in acetonitrile to slow down the crystallization process.⁶⁸ We chose acetonitrile as a solvent for water, because no effects on

the crystallization process of calcium carbonate are reported for this solvent, in contrast to alcohols.^{71,72} Samples were taken after distinct time intervals, and FTIR spectra were recorded.

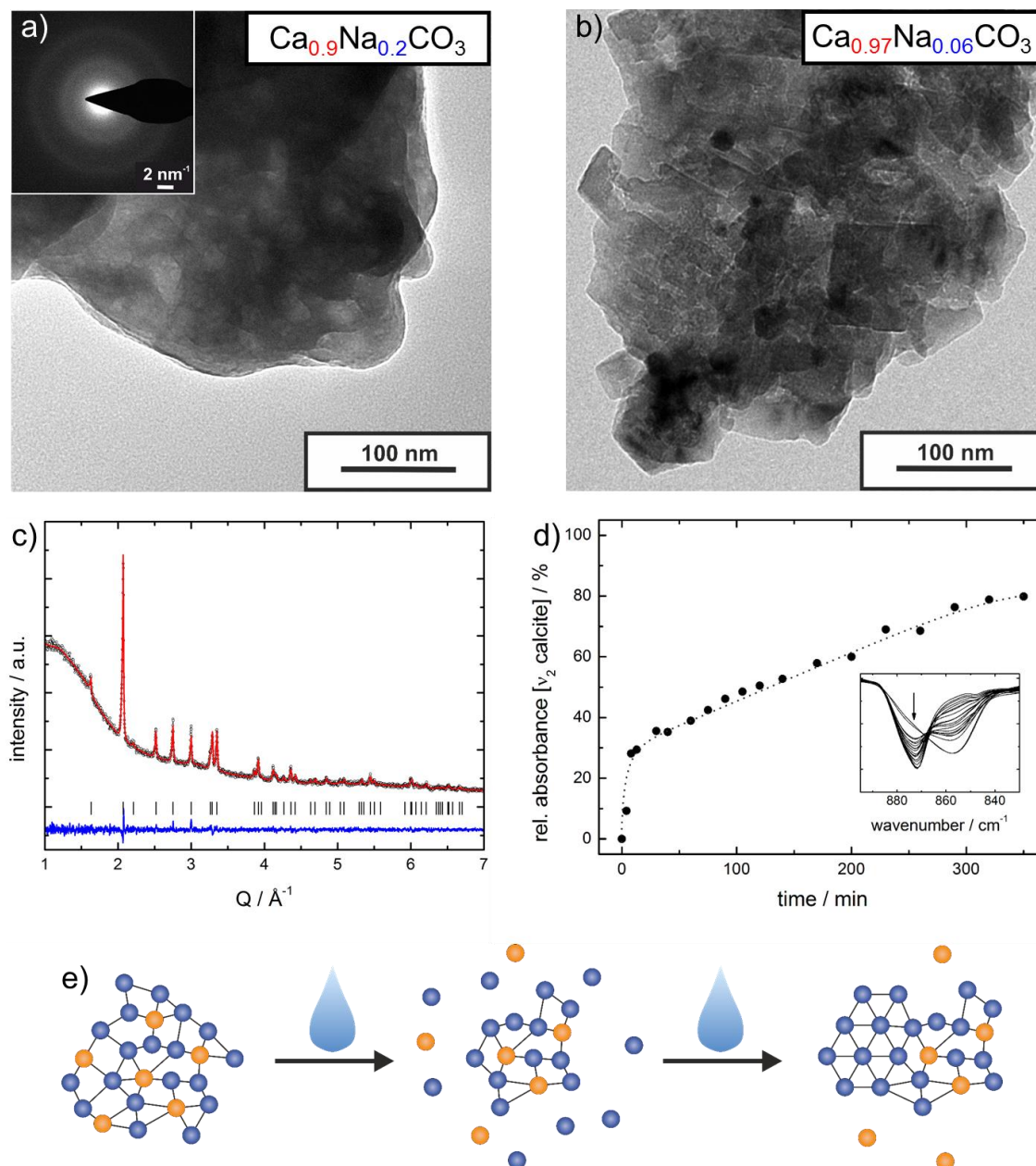


Figure 5.6 a) TEM image with SAED and composition of BM-ACC monitored by AAS. BM-ACC consists of fused nanoparticles. Electron diffraction confirms the amorphous character of BM-ACC. b) After incubation of BM-ACC in water for 1 h, rhombohedral crystals appear, while the material is depleted of sodium. c) Rietveld refinement identified the crystals as calcite. d) Time-resolved crystallization of BM-ACC in a mixture of 10 vol% water with acetonitrile, monitored by FTIR (inset). The dotted line is a guide for the eye. e) Scheme of the crystallization process: BM-ACC dissolves and calcite recrystallizes heterogeneously on the BM-ACC agglomerates, while sodium cations remain in solution.

We determined the progress of the crystallization by evaluating the absorbance of the ν_2 vibrational mode of calcite, analogously to the way we quantified the formation kinetics of BM-ACC (Figure 5.4a). After an initial fast rise, the absorbance of the ν_2 vibrational mode of calcite increases linearly for several hours. As calcite can nucleate heterogeneously on the BM-ACC aggregates, the nucleation barrier is lowered and the dissolution of BM-ACC is the rate-determining step of the crystallization kinetics. Therefore, we attribute the jump in the first 15 min to a quick dissolution of the nanostructured surface of the BM-ACC and the subsequent recrystallization of calcite. Afterwards, the crystallization slows down due to the reduced surface area of BM-ACC, which becomes partly overgrown with calcite crystals. In general, ACC from solution crystallizes *via* vaterite as intermediate,⁷³ also in the presence of acetonitrile.⁶⁸ Yet, BM-ACC crystallizes directly to calcite without such an intermediate (Figure S19, Supporting Information). In the presence of additives⁷⁴ and organic matrices,⁷⁵ direct transformation was also reported. Moreover, the nucleation on a template can induce direct crystallization to calcite.⁷⁶ A similar effect might also apply for BM-ACC, which potentially acts as nucleation site for calcite (Figure 5.6b). We propose the following crystallization mechanism for BM-ACC (Figure 5.6e): In the first rate-determining step, BM-ACC dissolves partially. While sodium remains in solution, calcite crystallizes rapidly on the surface of the BM-ACC aggregates. The heterogeneous nucleation on this template favors the formation of calcite.

On heating, ACC from solution crystallizes to calcite. Yet, the crystallization temperature depends strongly on the synthetic route to ACC,⁶⁹ reports range from 160 °C to 376 °C.^{69,74,77} Tobler et al. showed that the incorporation of hydroxide¹⁵ and citrate⁷⁴ ions significantly increases the thermal crystallization temperature. We performed TGA-DTA measurements to study thermally induced phase transformations of BM-ACC (Figure 5.7a). Around 185 °C, an exothermic effect occurred, which corresponds to the recrystallization to calcite. This value is at the lower end of reported crystallization temperatures of ACC, which attributes for a lower barrier for the crystallization process. At the crystallization temperature of BM-ACC, a mass loss of 1.5 % is observed, which arises from the release of the dispersion medium. Cyclohexane was identified in the Raman and FTIR spectra (Figure 5.2) and through ¹H and ¹³C NMR (Figure S15, Supporting Information). As the release coincides with the crystallization, we assume that cyclohexane is physically trapped in cavities that form during the mechanochemical treatment. Cyclohexane is released, only when the ions rearrange at

higher temperature during the crystallization process. On further heating, cyclohexane is gradually released, which is in agreement with the crystallization kinetics (*vide infra*).

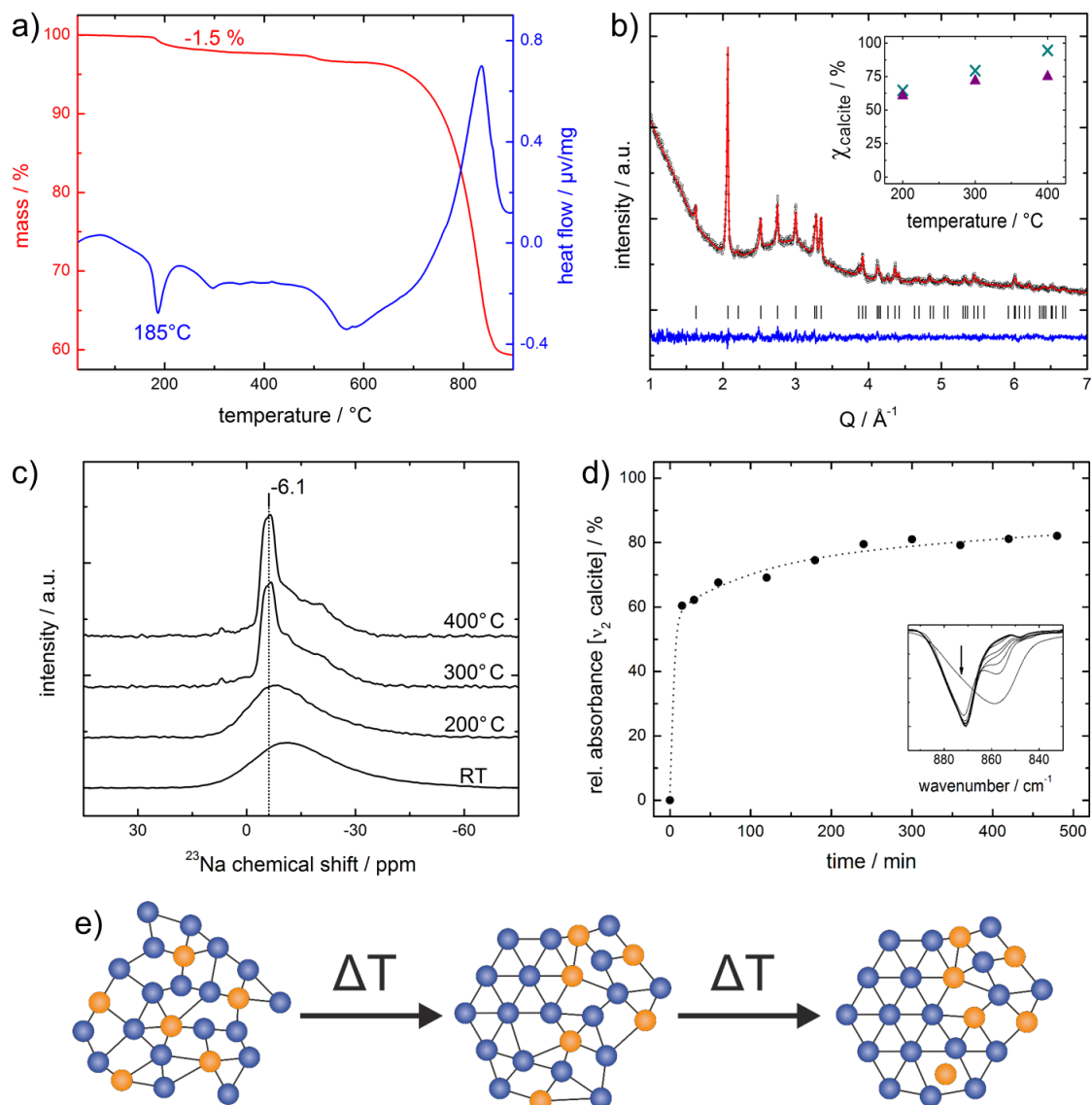


Figure 5.7 a) TGA-DTA of BM-ACC. The exothermic feature in the DTA curve (blue) indicates thermally induced crystallization to calcite at 185 °C. The TGA (red) depicts a mass loss at this temperature due to release of trapped cyclohexane. b) PXRD of BM-ACC after heating to 300 °C for 8 h. Rietveld refinement indicates 72 wt% crystalline calcite and 28 wt% amorphous material. The percentage of crystalline calcite after 8 h of thermal treatment increases with rising temperature (inset: %_{calcite} determined by FTIR (green) and Rietveld (purple)). c) ²³Na MAS-NMR of BM-ACC at room temperature (RT) and after heating to 200 °C, 300 °C, and 400 °C for 8 h. The sodium environment changes only slightly on heating to 200 °C. After heating to 300 °C/400 °C, a sharp signal around -6.1 ppm emerges, which indicates a more spherical symmetric coordination of sodium with decreased Na-O distance compared to BM-ACC. d) Time-resolved crystallization of BM-ACC at 300 °C, monitored by FTIR (inset). Initially, the sample crystallizes rapidly up to a conversion of ca. 60 %. Then, crystallization proceeds significantly more slowly and ca. 80 % calcite is obtained after 8 h. e) Scheme of the thermally induced crystallization process. Initially, BM-ACC crystallizes to “pure” calcite, while sodium is concentrated in the remaining amorphous material. Further heating leads to the incorporation of sodium into calcite.

PXRD with Rietveld refinement identified calcite as the only crystalline product of the thermally induced phase transformation around 185 °C. No phase separation occurred, as we did not observe any hint of crystalline Na₂CO₃ by PXRD, FTIR, or ²³Na NMR. Despite the exothermic effect in the DTA curve at 185 °C, BM-ACC does not crystallize completely at this temperature, as the amorphous background in the PXRD of BM-ACC, which was heated to 300 °C, indicates (Figure 5.7b). In order to monitor the temperature dependence, we heated three samples of BM-ACC for 8 h respectively to 200 °C, 300 °C, and 400 °C. The percentage of crystalline calcite was determined by PXRD with Rietveld refinement and FTIR (Figure 5.7b, inset). Both studies show the expected increase of crystalline material with increasing temperature from ca. 60 % at 200 °C to ca. 80 % at 400 °C. The methods show a slight discrepancy between the obtained values. FTIR overestimates the amount of amorphous carbonate. Still, the results agree on a qualitative level.

In general, the amount of sodium that can be incorporated into calcite is low. Kitano et al. found an upper limit of ca. 0.1 wt% for synthetic calcite.⁷⁸ In biogenic calcite, significantly higher sodium content is observed,⁷⁹ i.e. 0.3 wt% in *crassostrea virginica*⁸⁰ and 0.5 wt% in *balanus eburneus*.⁸¹ We performed ²³Na NMR experiments with the heated BM-ACC samples to probe the local environment of sodium during the crystallization process (Figure 5.7c). Interestingly, the ²³Na NMR spectrum of BM-ACC heated to 200 °C resembles – except for a slight downfield shift – the spectrum at room temperature (RT), although 60 % of the sample was already crystalline according to the Rietveld refinement. Only at 300 °C, the spectrum changes significantly. A sharp signal appears around -6.1 ppm. The smaller FWHM of 850 Hz suggests that sodium is situated in a more ordered environment, which is also closer to a spherical coordination symmetry (compare Figure 5.3b). The downfield shift of this signal, compared to BM-ACC at RT, indicates that the Na-O distance is decreased.⁶³ This implies that sodium is incorporated into a crystalline phase. Heating to 400 °C does not significantly change the spectrum. Additionally, the Rietveld refinement reveals that the c-axis of calcite in the heated BM-ACC samples increases with rising temperature from 17.051(2) Å at 200 °C, via 17.098(2) Å at 300 °C, to 17.114(1) Å at 400 °C. We observe a particularly strong increase between 200 °C and 300 °C, which corresponds to the strong change in the ²³Na NMR spectra. Therefore, we deduct that initially “pure” calcite crystallizes from BM-ACC on heating. At higher temperature, sodium-rich calcite forms; the incorporation of sodium elongates the c-axis of the calcite unit cell. Ishikawa et al. suggested

that the sodium ions preferably occupy interstitial sites in the calcite lattice.⁸² We cannot distinguish, if (i) sodium-rich and sodium-poor areas already pre-exist in BM-ACC and crystallize at different speed, or if (ii) the initial crystallization of “pure” calcite leads to an increase of the sodium concentration in the residual amorphous phase, which impedes further crystallization. Due to the generally high homogeneity of ball milled materials^{27,83,84} and the absence of distinct side phases, as suggested by NMR (Figure 5.3), we consider (ii) the more likely case though.

We monitored the kinetics of the thermally induced crystallization of BM-ACC by FTIR, exemplarily at 300 °C (Figure 5.7d). Immediately after exposing the sample to high temperature, the percentage of crystalline calcite increased to ca. 60 %. After 15 min, the crystallization proceeded more slowly. It took nearly 8 h to convert another 20% of the BM-ACC to calcite. We attribute the exothermic thermal effect in the DTA curve at 185 °C to the fast initial crystallization step, where predominantly “sodium-free” calcite forms. Subsequently, sodium is incorporated into the calcite phase, which significantly slows down the crystallization process. TEM images after heating (Figure S20, Supporting Information) show that the initial nanoparticulate structure of BM-ACC is lost.

Additionally, a second exothermic effect is observed at elevated temperature around 500 °C; again, a slight loss was visible in the TGA signal. PXRD indicated that the sodium-rich carbonate nyerereite,^{85,86} $\text{Na}_2\text{Ca}(\text{CO}_3)_2$, had formed (Figure S21, Supporting Information). This double Na-Ca carbonate, which occurs in magmatic rocks,⁸⁷ forms usually at elevated temperature above 400 °C.⁸⁸

We propose the following mechanism (Figure 5.7e): On heating of BM-ACC, two distinct crystallization processes with very different rates occur. In the first step, “pure” calcite crystallizes rapidly from BM-ACC, which increases the sodium concentration in the remaining amorphous material. In the second step, the sodium-rich amorphous material crystallizes – significantly more slowly – to calcite with sodium incorporation. Further temperature increase leads to the formation of the sodium-rich carbonate nyerereite. The delayed incorporation of sodium into the crystalline material shows that its presence poses barrier to prevent crystallization of BM-ACC. Tobler et al. observed a comparable effect on the thermally induced crystallization of ACC by the partial substitution of the carbonate anions by hydroxide¹⁵ and citrate.⁷⁴

Conclusion

A new form of amorphous calcium carbonate (BM-ACC) was synthesized by mechanochemical processing of CaCO_3 (calcite) and Na_2CO_3 in a planetary ball mill. The metastable product was stabilized by the incorporation of Na^+ cations. The minimum concentration of Na^+ impurities for the successful amorphization of calcite was determined by PXRD, and the structure of BM-ACC was studied by vibrational spectroscopy (FTIR and Raman), ^{13}C and ^{23}Na solid state MAS-NMR, and total scattering experiments with high-energy synchrotron radiation. ^{23}Na MAS-NMR proved highly useful to determine changes in the coordination and symmetry of the incorporated sodium ions. A structural model for BM-ACC was derived based on the synchrotron data, which revealed a partly unsaturated coordination sphere for the calcium cations. The kinetics of the amorphization process was monitored by quantitative FTIR spectroscopy and ^{23}Na MAS-NMR and showed an exponential decay of crystallinity during ball milling. Mechanochemical treatment of pure calcite was investigated in the same manner. Here, amorphization could not be achieved in the absence of Na^+ cations.

Whereas total scattering and ^{13}C NMR could reveal only little structural deviation between BM-ACC and “standard” ACC from solution, the absence of structural water in BM-ACC was the most striking difference. Both thermally and water-induced crystallization were examined. The crystallization behavior of BM-ACC deviates from wet-chemically prepared ACC. Upon contact with water, BM-ACC crystallizes directly to calcite without forming a vaterite intermediate. We found evidence that this phase transformation proceeds *via* dissolution of the nanoparticulate BM-ACC and subsequent crystallization of calcite, while Na^+ cations remained in solution. Agglomerates of BM-ACC particles serve as template for the heterogeneous nucleation of calcite. TGA-DTA revealed a phase transformation of BM-ACC to calcite at a low temperature of 185 °C. The sodium ions pose a barrier for the thermal crystallization of BM-ACC and are only gradually incorporated into the crystalline phase. First calcite forms, followed by sodium-rich calcite, and ultimately nyerereite.

Our findings unveil the amorphization mechanism of calcium carbonate during mechanochemical treatment. Impurities, in form of foreign ions, play a key role in the formation of amorphous calcium carbonate, because they represent a barrier to recrystallization during the milling process. The stabilization through impurities, in combination with mechanochemical processing, can be considered a general strategy for the synthesis of amorphous

phases, which is applicable to a variety of systems. Thereby, we could synthesize a yet unknown defect-variant of ACC with distinct reactive properties, characterize its structure, and probe its crystallization behavior. This opens the field to a variety of new amorphous modifications materials.

5.3 EXPERIMENTAL SECTION

Materials

Calcite (98%, Socal® 31, Solvay), Na₂CO₃ (99.95% extra pure, anhydrous, Acros), cyclohexane (Analytical reagent grade, Fisher Chemicals), acetone (99.5%, puriss. p.a., Riedel-de Haën), acetonitrile (HPLC gradient grade, Fisher Chemicals), milli Q deionized water.

Synthesis

For the mechanochemical synthesis, a planetary ball mill (Pulverisette 7 classic, Fritsch) was employed. Calcite (0.9 mmol) and Na₂CO₃ (0.1 mmol) were mixed and transferred to the grinding jar. 5 g of grinding balls (1 mm diameter, ZrO₂) and 10 mL of cyclohexane were added. The mixture was milled for 3 h at a speed of 750 rpm. Afterwards, the grinding balls were separated by decanting, the product was isolated by centrifugation from the resulting dispersion and dried *in vacuo*.

Amorphization Experiments

Calcite was processed with varying amounts of Na₂CO₃ in a planetary ball mill (Pulverisette 7 classic, Fritsch). Pure calcite (0.9 mmol) or mixtures with the respective amounts of Na₂CO₃ (5 mol%, 7.5 mol%, and 10 mol%) were transferred to the grinding jar. 5 g of grinding balls (1 mm diameter, ZrO₂) and 10 mL of cyclohexane were added. The mixture was milled at 750 rpm. For the PXRD study (Figure 5.1a), the milling was stopped after 24 h and the samples were isolated as described above. For the FTIR/²³Na NMR experiments (Figure 5.4a,b), the milling was paused after specific time intervals and several hundred μL of the cyclohexane dispersion were taken out with a pipette and transferred to a microcentrifuge tube. By centrifugation the solid was isolated and stored *in vacuo* for the subsequent measurements. Cyclohexane was added to the grinding jar to keep the volume constant and the milling was resumed.

Crystallization Experiments

A dispersion of BM-ACC (0.05 mmol) was prepared in 5 mL of acetonitrile and added to a mixture of water (2 mL) with acetonitrile (13 mL) to yield a final water concentration of 10 vol%. The reaction mixture was stirred (500 rpm) and samples were taken during the crystallization process. Therefore, 250 μ L of the solution was collected with a pipette, transferred to a centrifugation tube, and immediately diluted with an excess of acetone to stop any further crystallization. The solution was centrifuged and the precipitate dried *in vacuo*. Afterwards, FTIR spectra were recorded. For the TEM picture of crystallized BM-ACC, the sample was incubated in water for 1 h. Then, the solid was separated by centrifugation, washed with acetone, and redispersed in methanol. From the methanolic dispersion, the TEM specimen was prepared.

Characterization

X-ray powder diffraction. X-ray diffractograms of mechanochemically processed calcite- Na_2CO_3 mixtures (Figure 5.1a) were recorded with a Bruker AXS D8 Discover diffractometer equipped with a HiStar detector using graphite monochromatized $\text{CuK}\alpha$ radiation. Samples were attached to a glass substrate without using an adhesive. Individual frames were typically recorded at $2\theta = 24^\circ, 34^\circ, 44^\circ, 54^\circ, 64^\circ, 74^\circ, 84^\circ$ (detector distance 150 mm, detector range $\Delta(2\theta) = 35^\circ$) in 0.02° steps covering a 2θ range from 5° to 85° . X-ray diffraction patterns were integrated from individual frames using the Bruker AXS GADDS software package⁸⁹ and merged using Bruker AXS EVA.⁹⁰ Crystalline phases were identified according to the PDF-2 database⁹¹ using Bruker AXS.⁹⁰

X-ray diffractograms of crystallized BM-ACC (Figure 5.6c, 5.7b, and S21) were recorded with a STOE Stadi P equipped with a Mythen 1k detector using $\text{MoK}\alpha_1$ radiation. The sample was attached to polyvinyl acetate films with perfluoroether (Fomblin Y, Aldrich). The sample was measured in transmission in 0.015° steps (continuous scan, 150 s°) covering a 2θ range from 1.5° to 43° . Rietveld refinement⁹² was performed with Topas Academic V6 using the fundamental parameters approach,⁶⁷ based on a structural model for calcite⁹³ and nyerereite.⁹⁴ Crystalline phases were identified according to the PDF-2 database⁹¹ using Bruker AXS.⁹⁰ Quantification of amorphous content in partially crystallized samples was performed according to the PONCKS method⁹⁵ using a well weighted mixture of BM-ACC and calcite for calibration.

FTIR Spectroscopy. ATR-FTIR spectroscopy was performed using a Nicolet iS10 Spectrometer, manufactured by Thermo Scientific. The spectra were recorded in the frequency range from 650 cm^{-1} to 4000 cm^{-1} with a resolution of 1.4 cm^{-1} per data point.

Raman Spectroscopy. Raman spectra were recorded with a Horiba Yvon Lab RAM HR 800 spectrometer equipped with a microscope (Olympus BX41) and a CCD detector. The entrance slit was set to $100\text{ }\mu\text{m}$, the laser focal spot was $2\times 2\text{ }\mu\text{m}$. A Nd:YAG laser (532.12 nm) with a laser power 2 mW was used for excitation. The laser light was focused onto the fine powder sample using a $50\times$ long working distance objective. All Raman spectra were recorded in backscattering geometry at a resolution of 0.5 cm^{-1} in the range between 150 cm^{-1} and 1200 cm^{-1} , wherein at least five spectra for each sample were measured to improve the statistics.

Solid state NMR spectroscopy. All solid-state NMR experiments were recorded on a Bruker Avance 400 DSX spectrometer at ^1H frequency of 399.87 , ^{13}C frequency of 100.55 MHz and ^{23}Na frequency of 105.75 MHz . A three-channel commercial Bruker 4 mm probe head at spinning speeds of $8000 \pm 2\text{ Hz}$ was used for the ^1H , ^{13}C , and ^{23}Na direct excitation measurements. The ^1H NMR spectra were recorded averaging 32 transients with 8 s recycle delay. The ^{13}C direct excitation experiments were carried out for all samples by a 90° pulse with a length of $4\text{ }\mu\text{s}$ and repetition time of 2200 s acquiring 16 (for calcite) or 160 (for BM-ACC) transients. For all ^{13}C NMR experiments, a two-pulse phase modulation (TPPM) heteronuclear decoupling scheme was used. The ^{23}Na direct excitation experiments were carried out by a 90° pulse averaging 128 scans with a recycle delay of 5 s . The ^{23}Na kinetic measurements were performed using a Bruker 2.5 mm commercial probe head at a spinning speed of 20 kHz (500 transients) with a recycle delay of 1 s . The spectra were referenced to external adamantane at 1.63 ppm (^1H) and 38.5 ppm (^{13}C). The ^{23}Na spectra were referenced to external NaCl as a secondary standard at 7.2 ppm .

Thermal analysis. Coupled thermogravimetric and differential thermal analysis (TGA-DTA) was carried using a Netzsch STA 449 F3 Jupiter device. The sample ($\sim 10\text{ mg}$) was heated in an alumina cup in argon atmosphere from 50°C to 900°C at a heating rate of 10 K/min .

Transmission electron microscopy. TEM samples were prepared by drop-casting $20\text{ }\mu\text{L}$ of the respective sample dispersion on 400 mesh carbon copper grids (Plano GmbH, Wetzlar, Germany) and measured with a Technai Spirit G2 at 120 kV acceleration voltage, equipped with a standard 4K CCD camera.

Atom absorption spectroscopy. AAS measurements were conducted using Perkin Elmer 5100 ZL AA spectrometer with a Zeeman Furnace module, Na (at 589.0 nm) and Ca (at 422.7 nm) hollow cathode lamps, and air/acetylene mixture.

Total scattering. Total scattering experiments were conducted on beamline I15 at the Diamond Light Source Inc. using a wavelength of 0.1707 Å (72.7 keV) and a 2D MAR 345 detector. CeO₂ was used to calibrate the experimental setup. For the transport to the synchrotron facility, BM-ACC was stored under argon to prevent possible humidity-induced crystallization. Data were processed using DAWN.⁹⁶ The pair distribution function was calculated with GUDRUNX.⁶⁶ Structural models were derived for a set of 54 calcium, 12 sodium, and 60 carbonate ions inside a cubic box of space group symmetry P1. The volume of the box was derived from volume increments⁹⁷ and accords to a phase density of 2.51g/cm³. Carbonate ions were treated as rigid-bodies, the C-O distance was a free variable in later steps of refinement. Repulsive interatomic/-molecular interactions were modeled applying anti-bumping restraints for all element pairs according to values determined from the corresponding carbonates. Attractive interactions were modeled according to bond-valences for Ca-O and Na-O, respectively. The starting models were generated by random expansion of all constituents from the origin using simulated annealing upon periodic boundary conditions. All modelling and refinement was performed using Topas Academic V6.⁶⁷

5.4 REFERENCES

- (1) Montero, M. A., Jordán, M. M., Almendro-Candel, M. B., Sanfeliu, T., Hernández-Crespo, M. *Appl. Clay Sci.* **2009**, *43*, 186–189.
- (2) Matschei, T., Lothenbach, B., Glasser, F. P. *Cem. Concr. Res.* **2007**, *37*, 551–558.
- (3) Gamelas, J. A.F., Lourenço, A. F., Xavier, M., Ferreira, P. J. *Chem. Eng. Res. Des.* **2014**, *92*, 2425–2430.
- (4) Alvarez, V., Paulis, M. *Prog. Org. Coat.* **2017**, *112*, 210–218.
- (5) Sperschneider, H., Günther, K., Marzoll, I., Kirchner, E., Stein, G. *Nephrol. Dial. Transplant.* **1993**, *8*, 530–534.
- (6) Render, D., Samuel, T., King, H., Vig, M., Jeelani, S., Babu, R. J., Rangari, V. *J. Nanomater.* **2016**, *2016*, 1–8.

- (7) Wolf, S. E., Leiterer, J., Pipich, V., Barrea, R., Emmerling, F., Tremel, W. *J. Am. Chem. Soc.* **2011**, *133*, 12642–12649.
- (8) Gattuso, J., Frankignoulle, M., Bourge, I., Romaine, S., Buddemeier, R. W. *Glob. Planet. Change* **1998**, *18*, 37–46.
- (9) Politi, Y., Arad, T., Klein, E., Weiner, S., Addadi, L. *Science* **2004**, *306*, 1161–1164.
- (10) Raz, S., Hamilton, P. C., Wilt, F. H., Weiner, S., Addadi, L. *Adv. Funct. Mater.* **2003**, *13*, 480–486.
- (11) Belcher, A. M., Wu, X. H., Christensen, R. J., Hansma, P. K., Stucky, G. D., Morse, D. E. *Nature* **1996**, *381*, 56–58.
- (12) Sun, S., Mao, L.-B., Lei, Z., Yu, S.-H., Cölfen, H. *Angew. Chem. Int. Ed.* **2016**, *55*, 11765–11769.
- (13) Gorna, K., Hund, M., Vučak, M., Gröhn, F., Wegner, G. *Mater. Sci. Eng., A* **2008**, *477*, 217–225.
- (14) Gebauer, D., Gunawidjaja, P. N., Ko, J. Y. P., Bacsik, Z., Aziz, B., Liu, L., Hu, Y., Bergström, L., Tai, C.-W., Sham, T.-K., Edén, M., Hedin, N. *Angew. Chem. Int. Ed.* **2010**, *49*, 8889–8891.
- (15) Tobler, D. J., Rodriguez Blanco, J. D., Sørensen, H. O., Stipp, S. L. S., Dideriksen, K. *Cryst. Growth Des.* **2016**, *16*, 4500–4508.
- (16) Cartwright, J. H. E., Checa, A. G., Gale, J. D., Gebauer, D., Sainz-Díaz, C. I. *Angew. Chem. Int. Ed.* **2012**, *51*, 11960–11970.
- (17) Ihli, J., Kulak, A. N., Meldrum, F. C. *Chem. Commun.* **2013**, *49*, 3134–3136.
- (18) Gower, L. B., Odom, D. J. *J. Cryst. Growth* **2000**, *210*, 719–734.
- (19) Aizenberg, J., Addadi, L., Weiner, S., Lambert, G. *Adv. Mater.* **1996**, *8*, 222–226.
- (20) Politi, Y., Batchelor, D. R., Zaslansky, P., Chmelka, B. F., Weaver, J. C., Sagi, I., Weiner, S., Addadi, L. *Chem. Mater.* **2010**, *22*, 161–166.
- (21) Lei, Z., Sun, S., Wu, P. *ACS Sustainable Chem. Eng.* **2017**, *5*, 4499–4504.
- (22) Annenkov, M., Blank, V., Kulnitskiy, B., Larionov, K., Ovsyannikov, D., Perezhogin, I., Popov, M., Sorokin, P. *J. Eur. Ceram. Soc* **2017**, *37*, 1349–1353.
- (23) Fecht, H. J., Hellstern, E., Fu, Z., Johnson, W. L. *Metall. Trans. A* **1990**, *21*, 2333–2337.
- (24) Rubinstein, M. H., Gould, P. *Drug Dev. Ind. Pharm.* **2008**, *13*, 81–92.
- (25) Schwarz, R. B., Koch, C. C. *Appl. Phys. Lett.* **1986**, *49*, 146–148.

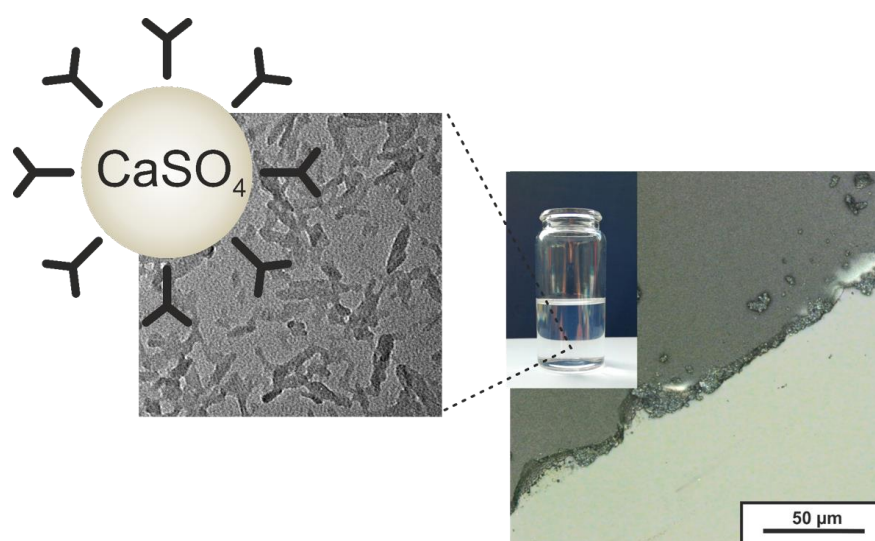
- (26) Šepelák, V., Bégin-Colin, S., Le Caër, G. *Dalton Trans.* **2012**, *41*, 11927–11948.
- (27) Weeber, A. W., Bakker, H. *Physica B* **1988**, *153*, 93–135.
- (28) Gaffet, E. *Mater. Sci. Eng., A* **1991**, *136*, 161–169.
- (29) Baxter, E. F., Bennett, T. D., Cairns, A. B., Brownbill, N. J., Goodwin, A. L., Keen, D. A., Chater, P. A., Blanc, F., Cheetham, A. K. *Dalton Trans.* **2016**, *45*, 4258–4268.
- (30) Bennett, T. D., Saines, P. J., Keen, D. A., Tan, J.-C., Cheetham, A. K. *Chemistry* **2013**, *19*, 7049–7055.
- (31) Cao, S., Bennett, T. D., Keen, D. A., Goodwin, A. L., Cheetham, A. K. *Chem. Commun.* **2012**, *48*, 7805–7807.
- (32) Bach, S., Visnow, E., Panthöfer, M., Gorelik, T., Buzanich, A. G., Gurlo, A., Kolb, U., Emmerling, F., Lind, C., Tremel, W. *Eur. J. Inorg. Chem.* **2016**, *2016*, 2072–2081.
- (33) Bordet, P., Bytchkov, A., Descamps, M., Dudognon, E., Elkaïm, E., Martinetto, P., Pagnoux, W., Poulain, A., Willart, J.-F. *Cryst. Growth Des.* **2016**, *16*, 4547–4558.
- (34) Steiner, D., Finke, J. H., Breitung-Faes, S., Kwade, A. *Adv. Powder Technol.* **2016**, *27*, 1700–1709.
- (35) Willart, J. F., Caron, V., Lefort, R., Danède, F., Prévost, D., Descamps, M. *Solid State Commun.* **2004**, *132*, 693–696.
- (36) Mallick, S., Pattnaik, S., Swain, K., De, P. K., Saha, A., Ghoshal, G., Mondal, A. *Eur. J. Pharm. Biopharm.* **2008**, *68*, 346–351.
- (37) Gupta, M. K., Vanwert, A., Bogner, R. H. *J. Pharm. Sci.* **2003**, *92*, 536–551.
- (38) Kobayashi, M., Hattori, Y., Sasaki, T., Otsuka, M. *J. Pharm. Pharmacol.* **2017**, *69*, 15–22.
- (39) Sonoda, R., Horibe, M., Oshima, T., Iwasaki, T., Watano, S. *Chem. Pharm. Bull.* **2008**, *56*, 1243–1247.
- (40) Krupa, A., Descamps, M., Willart, J.-F., Strach, B., Wyska, E., Jachowicz, R., Danède, F. *Mol. Pharm.* **2016**, *13*, 3891–3902.
- (41) Burns, J. H., Bredig, M. A. *J. Chem. Phys.* **1956**, *25*, 1281.
- (42) Criado, J. M., Trillo, J. M. *J. Chem. Soc., Faraday Trans.* **1975**, *71*, 961–966.
- (43) Northwood, D. O., Lewis, D. *Am. Mineral.* **1968**, *53*, 2089–2092.
- (44) Barriga, C., Morales, J., Tirado, J. L. *J. Mater. Sci.* **1985**, *20*, 941–946.

- (45) Mugnaioli, E., Andrusenko, I., Schüler, T., Loges, N., Dinnebier, R. E., Panthöfer, M., Tremel, W., Kolb, U. *Angew. Chem. Int. Ed.* **2012**, *51*, 7041–7045.
- (46) Schrader, R., Hoffmann, B. *Z. anorg. allg. Chem.* **1969**, 369.
- (47) Kosacki, I., Suzuki, T., Anderson, H. A., Colomban, P. *Solid State Ion.* **2002**, *149*, 99–105.
- (48) Gunasekaran, S., Anbalagan, G., Pandi, S. *J. Raman Spectrosc.* **2006**, *37*, 892–899.
- (49) Lam, R. S. K., Charnock, J. M., Lenniec, A., Meldrum, F. C. *CrystEngComm* **2007**, *9*, 1226–1236.
- (50) Faatz, M., Gröhn, F., Wegner, G. *Adv. Mater.* **2004**, *16*, 996–1000.
- (51) Addadi, L., Raz, S., Weiner, S. *Adv. Mater.* **2003**, *15*, 959–970.
- (52) Radha, A. V., Forbes, T. Z., Killian, C. E., Gilbert, P. U. P. A., Navrotsky, A. *Proc. Natl. Acad. Sci. USA* **2010**, *107*, 16438–16443.
- (53) Rodriguez-Navarro, C., Kudłacz, K., Cizer, Ö., Ruiz-Agudo, E. *CrystEngComm* **2015**, *17*, 58–72.
- (54) Konrad, F., Gallien, F., Gerard, D. E., Dietzel, M. *Cryst. Growth Des.* **2016**, *16*, 6310–6317.
- (55) Xu, X., Han, J. T., Cho, K. *Chem. Mater.* **2004**, *16*, 1740–1746.
- (56) Koller, H., Engelhardt, G., Kentgens, A. P. M., Sauer, J. *J. Phys. Chem.* **1994**, *98*, 1544–1551.
- (57) Jung, J. K., Han, O. H., Choh, S. H. *Solid State Nucl. Magn. Reson.* **1999**, *13*, 255–262.
- (58) Nebel, H., Neumann, M., Mayer, C., Epple, M. *Inorg. Chem.* **2008**, *47*, 7874–7879.
- (59) Čančarevič, Ž., Schön, J. C., Jansen, M. *Z. anorg. allg. Chem.* **2006**, *632*, 1437–1448.
- (60) Sitepu, H., O'Connor, B. H., Li, D. *J. Appl. Crystallogr.* **2005**, *38*, 158–167.
- (61) Wolf, S. E., Böhm, C., Harris, J., Hajir, M., Mondeshki, M., Marin, F. *KEM* **2016**, *672*, 47–59.
- (62) Michel, F. M., MacDonald, J., Feng, J., Phillips, B. L., Ehm, L., Tarabrella, C., Parise, J. B., Reeder, R. J. *Chem. Mater.* **2008**, *20*, 4720–4728.
- (63) Stebbins, J. F. *Solid State Ion.* **1998**, *122*, 137–141.
- (64) Beer, A. *Ann. Physik* **1852**, *162*, 78–88.
- (65) Goldschmidt, V. M. *Naturwissenschaften* **1926**, *14*, 477–485.
- (66) Soper, A. K., Barney, E. R. *J. Appl. Crystallogr.* **2011**, *44*, 714–726.

- (67) Coelho, A. A. *J. Appl. Crystallogr.* **2018**, *51*, 210–218.
- (68) Leukel, S., Tremel, W. *Crystal Growth & Design* **2018**, DOI: 10.1021/acs.cgd.8b00627
- (69) Schmidt, M. P., Ilott, A. J., Phillips, B. L., Reeder, R. J. *Cryst. Growth Des.* **2014**, *14*, 938–951.
- (70) Reeder, R. J., Tang, Y., Schmidt, M. P., Kubista, L. M., Cowan, D. F., Phillips, B. L. *Cryst. Growth Des.* **2013**, *13*, 1905–1914.
- (71) Seo, K.-S., Han, C., Wee, J.-H., Park, J.-K., Ahn, J.-W. *J. Cryst. Growth* **2005**, *276*, 680–687.
- (72) Manoli, F., Dalas, E. *J. Cryst. Growth* **2000**, *218*, 359–364.
- (73) Rodriguez-Blanco, J. D., Shaw, S., Benning, L. G. *Nanoscale* **2011**, *3*, 265–271.
- (74) Tobler, D. J., Rodriguez-Blanco, J. D., Dideriksen, K., Bovet, N., Sand, K. K., Stipp, S. L. S. *Adv. Funct. Mater.* **2015**, *25*, 3081–3090.
- (75) Politi, Y., Metzler, R. A., Abrecht, M., Gilbert, B., Wilt, F. H., Sagi, I., Addadi, L., Weiner S., Gilbert, P. U. P. A. *Proc. Natl. Acad. Sci. USA* **2008**, *105*, 17362–17366.
- (76) Aizenberg, J., Muller, D. A., Grazul, J. L., Hamann, D. R. *Science* **2003**, *299*, 1205–1208.
- (77) Koga, N., Nakagoe, Y., Tanaka, H. *Thermochim. Acta* **1998**, *318*, 239–244.
- (78) Kitano, Y., Okumura, M., Idogaki, M. *Geochem. J.* **1975**, *9*, 75–84.
- (79) Busenberg, E., Plummer, L. N. *Geochim. Cosmochim. Acta* **1985**, *49*, 713–725.
- (80) Rucker, J. B., Valentine, J. W. *Nature* **1961**, *190*, 1099–1100.
- (81) Pilkey, O. H., Harris, R. C. *Limnol. Oceanogr.* **1966**, *11*, 381–385.
- (82) Ishikawa, M., Ichikuni, M. *Chem. Geol.* **1984**, *42*, 137–146.
- (83) Benjamin, J. S. *Sci. Am.* **1976**, *234*, 40–49.
- (84) Nohara, S., Fujita, N., Zhang, S. G., Inoue, H., Iwakura, C. *J. Alloys Compd.* **1998**, *267*, 76–78.
- (85) McKie, D., Frankis, E. J. *Z. Kristallog.* **1977**, *145*, 73–95.
- (86) Bolotina, N. B., Gavryushkin, P. N., Korsakov, A. V., Rashchenko, S. V., Seryotkin, Y. V., Golovin, A. V., Moine, B. N., Zaitsev, A. N., Litasov, K. D. *Acta Crystallogr. B* **2017**, *73*, 276–284.
- (87) Dawson, J. B. *Nature* **1962**, *195*, 1075–1076.

- (88) Shatskiy, A., Gavryushkin, P. N., Litasov, K. D., Koroleva, O. N., Kupriyanov, I. N., Borzdov, Y. M., Sharygin, I. S., Funakoshi, K., Palyanov, Y. N., Ijiohtani, E. *Eur. J. Mineral.* **2015**, *27*, 175–184.
- (89) GADDS V 4.1.19, Bruker AXS, Madison (WI) US (2003).
- (90) EVA 10.0 Rev. 1, Bruker AXS, Madison (WI) US (2003).
- (91) PDF-2, Release 2004, JCPDS – International Center for Diffraction Data, Newton Square (PA) US (2004).
- (92) Rietveld, H. M. *J. Appl. Crystallogr.* **1969**, *2*, 65–71.
- (93) Chessin, H., Hamilton, W. C., Post, B. *Acta Cryst* **1965**, *18*, 689–693.
- (94) Gavryushkin, P. N., Thomas, V. G., Bolotina, N. B., Bakakin, V. V., Golovin, A. V., Seryotkin, Y. V., Fursenko, D. A., Litasov, K. D. *Cryst. Growth Des.* **2016**, *16*, 1893–1902.
- (95) Scarlett, N. V. Y., Madsen, I. C. *Powder Diffr.* **2006**, *21*, 278–284.
- (96) Basham, M., Filik, J., Wharmby, M. T., Chang, P. C. Y., El Kassaby, B., Gerring, M., Aishima, J., Levik, K., Pulford, B. C. A., Sikharulidze, I., Sneddon, D., Webber, M., Dhesi, S. S., Maccherozzi, F., Svensson, O., Brockhauser, S., Náráy, G., Ashton, A. *W. J. Synchrotron Radiat.* **2015**, *22*, 853–858.
- (97) Blitz W. *Raumchemie der festen Stoffe*; Voss: Leipzig, 1934.

CALCIUM SULFATE NANOPARTICLES WITH UNUSUAL DISPERSIBILITY



Calcium sulfate is one of the most important construction materials. Today, it is employed as high-performance compound in medical applications and cement mixtures. We report a synthesis for calcium sulfate nanoparticles with outstanding dispersibility properties in organic solvents without further functionalization. The nanoparticles (amorphous with small γ -anhydrite crystallites, 5–50 nm particle size) form long-term stable dispersions in acetone without any sign of precipitation. ^1H nuclear magnetic resonance (NMR) spectroscopic techniques and Fourier transform infrared (FTIR) spectroscopy reveal adsorbed 2-propanol on the particle surfaces that induce the unusual dispersibility. Adding water to the nanoparticle dispersion leads to immediate precipitation and phase transformation to gypsum *via* bassanite. The dispersibility in a volatile organic solvent and the crystallization upon contact with water open a broad field of applications for the CaSO_4 nanoparticles, e.g. as nanogypsum for coatings or the fabrication of hybrid composites.

This chapter contains an adapted reproduction of *Langmuir* **2018**, 34, 7096-7105, reprinted with permission of the American Chemical Society (© 2018).

Authorship Contribution

Study conception and design	S. Leukel W. Tremel
Acquisition of data	S. Leukel M. Mondeshki M. Panthöfer W. Schärtrl S. Plana Ruiz
Analysis and interpretation of data	S. Leukel M. Mondeshki M. Panthöfer W. Schärtrl S. Plana Ruiz
Drafting of manuscript	S. Leukel
Critical revision	M. Mondeshki M. Panthöfer W. Schärtrl S. Plana Ruiz W. Tremel

6.1 INTRODUCTION

Calcium sulfate is one of the most common evaporitic minerals on earth, and even on Mars deposits were found.¹ It occurs in several polymorphs that differ in structure and water content. Gypsum ($\text{CaSO}_4 \times 2\text{H}_2\text{O}$), the thermodynamically stable modification at ambient temperature and pressure, is found in large quantities in natural deposits. Bassanite ($\text{CaSO}_4 \times 0.5\text{H}_2\text{O}$), the hemihydrate, is metastable at all temperatures. It is found in some natural deposits as well,^{2,3} although in much smaller quantities than gypsum, and it was found recently as biomineral in medusae statoliths.⁴ The thermodynamically stable form at higher temperature is anhydrite (CaSO_4). The reported transition temperatures from gypsum to anhydrite vary between 42 °C and 60 °C,⁵⁻⁷ as the crystallization of anhydrite in water is kinetically hindered below 70 °C.^{8,9} Due to its stability at elevated temperatures, anhydrite is found in water-soluble mineral sediments that are formed by concentration/evaporation from aqueous solutions (evaporites).¹⁰

Both bassanite and anhydrite can be obtained by heating gypsum. This leads to a stepwise loss of structural water and results in the formation of bassanite in a first and of anhydrite in a second step.¹¹⁻¹⁴ In water, gypsum transforms upon heating to bassanite due to the low crystallization rate of anhydrite.⁸ Anhydrite forms only under hydrothermal conditions.¹⁵ Room temperature syntheses in organic solvents, reported by Tritschler et al., allowed the synthesis of well-defined bassanite nanorods¹⁶ and anhydrite.¹⁷

Its natural abundance and the broad variety of its industrial or medical applications make calcium sulfate a highly relevant material in technology. It is used widely in the construction industry, as a construction material (e.g. as plaster of Paris),^{18,19} or crucial component in cement mixtures.²⁰⁻²⁵ Calcium sulfate is deployed even in 3D printing.^{26,27} Its biocompatibility enables a variety of medical applications,²⁸ ranging from bone replacement²⁹⁻³² to drug carrier systems.^{33,34} With higher demands towards the material, the investigation of its nucleation and crystallization mechanism moved into focus. Bassanite was identified as a stable intermediate that transforms to gypsum by oriented attachment of nanocrystals.³⁵ Sub-3-nanometer particles were revealed by time-resolved small-angle X-ray scattering (SAXS) as primary species during the crystallization of calcium sulfate.³⁶ Transmission electron microscopy (TEM) studies suggest the presence of an amorphous form of calcium sulfate preceding bassanite.^{37,38} After hints for an amorphous phase were found in an infrared

spectroscopy study,³⁹ Meldrum and co-workers could stabilize amorphous calcium sulfate by confinement.⁴⁰

As the mechanical properties of calcium sulfate are grain size-dependent⁴¹ and the reactivity of materials in the nano-regime is mainly defined by their surface, calcium sulfate nanoparticles are of special interest for a variety of applications. Stark and co-workers⁴² used flame synthesis for the production of anhydrite nanoparticles, while Rees et al.⁴³ employed microemulsions of water in oil to produce calcium sulfate nanowires. Salvadori et al. synthesized water dispersible gypsum nanocrystals by subliming water after freeze-drying a saturated solution.⁴⁴ Cölfen and co-workers obtained well-defined bassanite nanorods by quenching aqueous calcium sulfate solutions with ethanol.¹⁶

We report a new facile synthesis for the preparation of calcium sulfate nanoparticles with unusual dispersibility properties. Without further functionalization, these nanoparticles form stable dispersions in acetone. Even at high concentrations, where the viscosity of the acetone dispersion increases significantly, there are no signs of precipitation. Size and morphology of the particles, determined by TEM in the dry state, are fully compatible with the properties in dispersion, as confirmed by dynamic light scattering (DLS). Polymorph identity and crystallite size were determined quantitatively by powder X-ray diffraction (PXRD) and subsequent Rietveld refinement⁴⁵ as well as selected area electron diffraction (SAED). The chemical composition was estimated by thermogravimetric analysis (TGA). In order to understand the unusual dispersibility properties, the attached solvent molecules were studied by Fourier transform infrared (FTIR) and ¹H nuclear magnetic resonance (¹H NMR) spectroscopy. Any contact of the nanoparticle dispersion with water leads to an immediate precipitation of calcium sulfate by agglomeration of the nanoparticles, followed by a phase transformation to gypsum on a longer time scale. This transformation was monitored by time-resolved FTIR spectroscopy, and bassanite was identified as intermediate. The findings of these experiments were confirmed by TEM snapshots and SAED taken at different points of time. Our results provide a coherent picture of the reaction mechanism of the nanoparticles upon contact with water. This knowledge is essential for possible applications and the processing of calcium sulfate particles. The volatility of acetone allowed fabricating transparent films and coatings from nanoparticle dispersions. The unusual dispersibility in an organic solvent enables the synthesis of polymer composites,⁴⁶ which is interesting not only for coatings and construction materials, but also for medical applications.

6.2 RESULTS AND DISCUSSION

Synthesis of CaSO₄ Nanoparticles

Calcium sulfate nanoparticles were synthesized by adding sulfuric acid to a solution of CaCl₂ in 2-propanol. Upon mixing, a colorless precipitate formed, which was separated from the solution by centrifugation. The precipitate dissolved instantly after addition of acetone to yield a clear and stable dispersion of calcium sulfate nanoparticles. Even after weeks, no solid precipitate was detected. The TEM micrograph in Figure 6.1a shows that the calcium sulfate nanoparticles from the dispersion have a liquid-like morphology. The sample was polydisperse with a size distribution ranging from 5 nm to 50 nm. As electron microscopy provides only a restricted overview of the sample and drying artifacts may obscure the state of the dispersion prior to drying, we used dynamic light scattering (DLS) as an ensemble method to characterize the average size of the calcium sulfate particles in dispersion (Figure 6.1b).^{47,48}

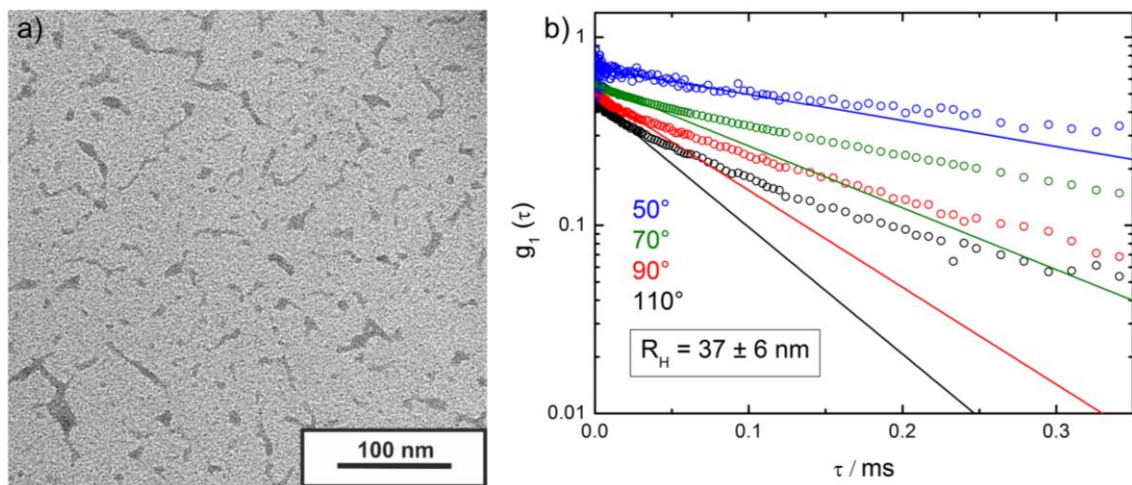


Figure 6.1 a) TEM shows polydisperse liquid-like nanoparticles of calcium sulfate with sizes ranging from 5 nm to 50 nm. b) DLS of a dispersion of calcium sulfate nanoparticles in acetone ($c = 1$ g/L). Data were recorded at four different angles and analyzed by the cumulant method (lines represent the linear fit through the first data points), yielding a z-averaged hydrodynamic radius of $R_H = 37 \pm 6$ nm.

Data were recorded for a dispersion with a particle concentration of 1 g/L at four different scattering angles (50°, 70°, 90°, and 110°). The measured intensity correlation $G_2(\tau)$ was normalized, and the amplitude correlation function $g_1(\tau)$ was derived using the Siegert relation. To determine the self-diffusion coefficient D_s , $g_1(\tau)$ is plotted logarithmically versus

the correlation time τ . By the cumulant fitting method, D_s was calculated from the initial slope of $\ln(g_1(\tau))$ for each angle. D_s is related to the hydrodynamic radius R_H by the Stokes-Einstein equation. For the respective angles, we obtained radii of 30.3 nm, 28.9 nm, 27.9 nm, and 37.2 nm. By plotting the respective diffusion coefficient against q^2 , we determined the apparent self-diffusion coefficient at $q^2 = 0$ by linear regression (Figure S22, Supporting Information). The obtained z-averaged hydrodynamic radius of $R_H = 37 \pm 6$ nm is in agreement with the picture derived from TEM (Figure 6.1a). It is important to note that the calculation of R_H assumes spherical particles and that light scattering data weigh larger particles disproportionately high. Still, both methods show the presence of discrete nanoparticles in acetone, and the particle size derived from two independent methods agree within experimental error.

Composition and phase determination

Thermogravimetric analysis showed an almost continuous mass loss of 20 % upon heating between room temperature and 250 °C (Figure 6.2a). Considering the ratio between the content of 2-propanol and water of about 1:7, extracted from the ^1H NMR spectra and confirmed by FTIR spectroscopy, the major part of the desorbed species is water (*vide infra*). A mass loss of 20 % corresponds to a composition of $\text{CaSO}_4 \times 1.3 \text{H}_2\text{O} \times 0.2$ -propanol. Structural characterization of the nanoparticles was performed by PXRD with subsequent Rietveld refinement (Figure 6.2b). The nanoparticles were identified as γ -anhydrite with cell parameters of $a = 6.272(2)$ Å, $b = 6.966(3)$ Å, and $c = 7.034(3)$ Å. The crystallite size was determined as 6.7(1) nm. Selected area electron diffraction (SAED) of the particles revealed a predominantly amorphous structure, though weak scattered reflections are visible (Figure 6.2c). The diffuse background in PXRD also hints at a considerable amount of amorphous material in the sample. High resolution transmission electron microscopy revealed some of the amorphous calcium sulfate particles to have a crystalline core (Figure 6.2d). The lattice planes show an interplanar spacing of 2.8 Å, which was determined by the spectrum image of the respective area (Figure 6.2d, inset) and corresponds to the (021) plane in γ -anhydrite.⁴⁹ The size of the crystallite observed in TEM is in good agreement with the crystallite size derived from the Rietveld refinement.

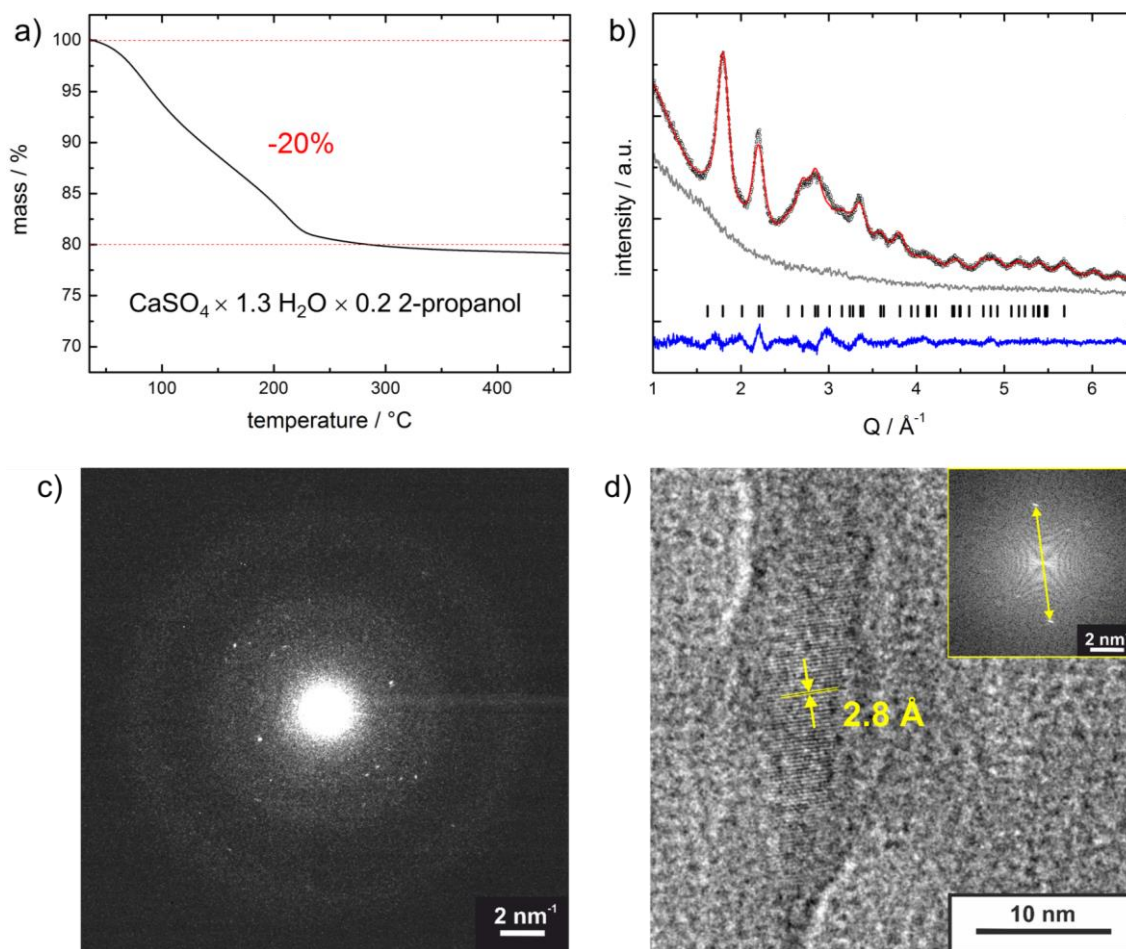


Figure 6.2 a) TGA of calcium sulfate nanoparticles. On heating, a mass loss of 20 % occurs. This corresponds (based on TGA and ^1H NMR) to a composition of $\text{CaSO}_4 \times 1.3 \text{H}_2\text{O} \times 0.2 \text{2-propanol}$. b) PXRD with Rietveld refinement (black circles: measured pattern, red line: calculated pattern, gray line: typical background of perfluoroether on polyvinyl acetate film, black dash: Bragg peak position, blue line: difference curve). The calcium sulfate nanoparticles adopt the γ -anhydrite structure with a crystallite size of $6.7(1) \text{ nm}$. c) SAED of calcium sulfate nanoparticles indicates mostly amorphous structure with some weak scattered reflections. d) HRTEM image shows small crystalline structure inside an amorphous calcium sulfate nanoparticle. Interplanar spacing of 2.8 \AA , derived from a spectrum image (inset), corresponds to the (021) plane in γ -anhydrite.⁴⁹

We assume that the structural water is situated predominantly in the amorphous regions of the particles, as the crystalline part, γ -anhydrite, is an anhydrous modification of calcium sulfate. The liquid-like morphology of the amorphous calcium sulfate particles further suggest their hydration, which is well described for amorphous carbonates^{50,51} and phosphates.⁵² Figure 6.3a displays the FTIR spectrum of the calcium sulfate nanoparticles. Four bands are assigned to the vibrational modes of the sulfate anion. The most intense band at 1085 cm^{-1} originates from the asymmetric stretching mode ν_3 . The band of the symmetric stretching mode ν_1 at 884 cm^{-1} is barely visible. This vibrational mode is not IR active. However, due to the non-isotropic environment of the sulfate ion in the solid, the transition is very weak,

but not forbidden anymore. The symmetric bending mode ν_4 is split into two bands at 667 cm^{-1} and 592 cm^{-1} , which has been observed for many sulfate minerals.⁵³ The asymmetric bending mode ν_2 of the sulfate ions in minerals is at lower energy ($\sim 450\text{ cm}^{-1}$) and lies outside the measuring range. The O-H stretching ($\sim 3300\text{ cm}^{-1}$) and the H-O-H bending mode (1634 cm^{-1}) indicate that the particles contain water. The water bands are broader and less structured than the corresponding bands of the hydrated calcium sulfate modifications bassanite and gypsum,⁵⁴ because the water molecules are not located at distinct positions of the structure, as in bassanite and gypsum. Although the sample was dried *in vacuo*, small amounts of 2-propanol were identified in the spectrum (red asterisks). The solvent also contributes partially to the O-H vibrational modes.

Solvent Surface Binding

The ^1H solid state NMR spectrum of the particles (Figure 6.3b) displays two distinct resonances at 1.0 ppm with a full width at half-maximum (FWHM) of 450 Hz and at 4.2 ppm (FWHM = 500 Hz) as well as a broad underlying signal with a maximum at ca. 1.7 ppm. The signals are assigned to 2-propanol, which was used during the synthesis. The deconvolution of the spectrum reveals additional intensity, considering the ratio of the areas of the 2-propanol resonance signals. We attribute this intensity to the presence of water in approximately sevenfold excess. This finding is consistent with the FTIR data (Figure 6.3a). The spectrum of pure 2-propanol is recorded at the same conditions for comparison and is presented in Figure S23 (Supporting Information).

In general, the broadening of the signals in the solid state can be related to fast relaxation due to quadrupolar nuclei or a paramagnetic contribution. As this does not apply here, we attribute the observed broadening to the reintroduction of the ^1H dipole-dipole couplings. This implies low mobility of water and 2-propanol. Thus, we suggest that 2-propanol and water are coordinated to the nanoparticles. Electron density redistribution would be the result of this coordination. Indeed, a downfield shift of the signals of bound 2-propanol is observed, compared to the solution signals. Furthermore, the deshielding and the respective downfield shift is larger for the hydrogen atom on the central (C2) carbon (3.9 ppm to 4.2 ppm), which is closer to the nanoparticle surface. The effect on the hydrogen atoms of the methyl groups is also clearly observed but less pronounced (1.0 ppm to 1.1 ppm).

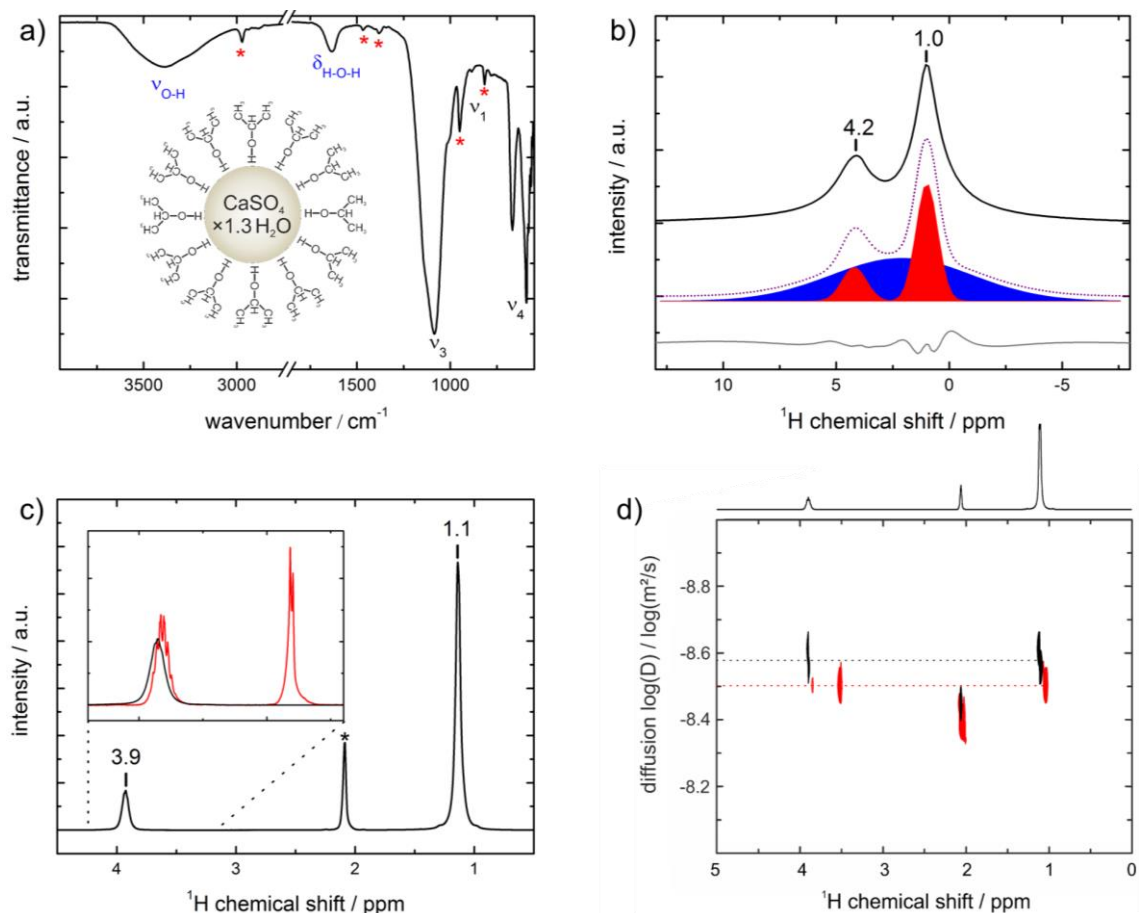


Figure 6.3 a) FTIR spectrum with schematic sketch of a particle. Three vibrational modes of the sulfate ion ($\nu_1 = 884 \text{ cm}^{-1}$, $\nu_3 = 1085 \text{ cm}^{-1}$, $\nu_4 = 667 \text{ cm}^{-1}$ and 592 cm^{-1}) are assigned. Water is identified by the characteristic broad O-H stretching vibration around 3300 cm^{-1} and the H-O-H bending vibration at 1634 cm^{-1} . 2-propanol is marked with red asterisks. b) Solid state ^1H NMR of calcium sulfate nanoparticles, dried *in vacuo* (black), with the deconvoluted spectrum (below): the two 2-propanol signals are depicted in red and a water/OH signal in blue. Due to the significant signal broadening and overlap, the resonances of the OH proton and the C2 proton can no longer be distinguished from one another in contrast to free 2-propanol (Figure S23, Supporting Information). The difference curve is shown in gray. c) Solution ^1H NMR spectrum of the nanoparticles in acetone- d_6 . The signals of 2-propanol are assigned (1.1 ppm and 3.9 ppm). The water and the OH group of the bound 2-propanol signals are too broad to be resolved. Inset shows free 2-propanol in acetone- d_6 (red) for comparison. Acetone is marked with an asterisk. d) ^1H diffusion-ordered NMR spectroscopy (DOSY) of the nanoparticles (black) and free 2-propanol (red) in acetone- d_6 . The slower diffusion of the coordinated 2-propanol (1.1 ppm and 3.9 ppm) indicates binding on the surface of the particles.

In order to further understand the solvent surface binding, we applied solution NMR techniques. Figure 6.3c displays the ^1H NMR spectrum of the nanoparticles dispersed in acetone- d_6 . Two signals of 2-propanol (1.1 ppm, 3.9 ppm) appear, which correspond to the respective methyl groups and the C2 proton. The resonance of the solvent is marked with an asterisk. The downfield shift of the 2-propanol signals is observed in solution as well. No resonances for the OH group of 2-propanol or water are detected. This signal broadening

beyond detection is related with the polar groups and confirms the coordination of the 2-propanol molecules to the particle *via* the OH group. In this case, however, the observed peaks of the CH and CH₃ moieties are significantly sharper, compared to the solid state. Both FWHM are in the range of 5–6 Hz. This difference is related with the fast rotation about the σ -bond between the coordinated OH group and the CH moiety. Thereby, the dipole-dipole couplings are averaged and resolution is enhanced. However, the FWHM for the coordinated 2-propanol remains almost two times larger than the one for free 2-propanol (2–3 Hz) in the same solvent coordination. Signal broadening caused by the reduced mobility of molecules attached to nanoparticles in solution, has been reported before.^{55,56}

In order to investigate if the coordination is stable or related with an exchange on the nanoparticle surface (desorption/adsorption), we applied ¹H diffusion-ordered NMR spectroscopy (DOSY) on both the solution of 2-propanol in acetone-d⁶ (0.5 vol%) and the dispersion of the nanoparticles in the same solvent (ca. 10 g/L). Both ¹H DOSY spectra are overlaid in Figure 6.3d. The diffusion coefficients extracted from the diffusion analysis were 2.75×10^{-9} m²/s for coordinated and 3.30×10^{-9} m²/s for free 2-propanol in acetone. No signals for free 2-propanol were observed in the nanoparticle suspensions, i.e. there is no evidence for ligand exchange.

FTIR and different ¹H-NMR experiments show the presence of 2-propanol, which is persistent *in vacuo*. The findings suggest a strong coordination of 2-propanol to the calcium sulfate nanoparticles, as illustrated in Figure 6.3a. Bassanite can incorporate small solvent molecules (like methanol) instead of water into its channel structure,⁸ which have a diameter of 4 Å. The channels in γ -anhydrite are significantly smaller; for amorphous calcium sulfate, no reports of such a structural element exist. Therefore, the larger 2-propanol molecule is forced to bind to the surface of the particles. We assume that surface binding of 2-propanol is crucial for dispersing the particles in acetone. Richardi et al.⁵⁷ showed by simulations of the structure of liquid acetone that the distribution of O-O distances have a maximum at 5.46 Å. This corresponds to an interaction of the carbon backbones with relative large O-O separations. The ¹H-NMR data suggest a binding of the OH-group of 2-propanol to the particle surface, i.e. the carbon backbone of 2-propanol is directed to the surrounding solvent. We assume that the surface-bound 2-propanol molecules preferably interact with the carbon backbones of the acetone. Experimentally, we were able to substitute the dispersion medium acetone, by 2-butanon, dimethylsulfoxide, and dimethylformamide. The dispersibility in

other organic solvents like ethanol, THF, or acetonitrile is low. As the particles are only dispersible in solvents with a similar carbon backbone structure as the surface-bound 2-propanol, the resemblance of these structural motives seems to be crucial for a favorable interaction. Still, a dispersion of the nanoparticles in acetone is miscible with a variety of organic solvents (e.g. methanol, THF, ethyl acetate, and chloroform) without any signs of precipitation. Mixing the dispersion with a highly non-polar solvent, like cyclohexane or toluene, results in the immediate precipitation of the particles.

Dispersion Properties

The calcium sulfate particles form a clear and stable dispersion in acetone (Figure 6.4a, inset). This allows to cast dense nanoparticle films on a glass slide, which dry to form transparent films (Figure 6.4c). Adding a few drops of water to the dispersion leads to immediate precipitation of a colorless solid and a strong increase of the viscosity of the dispersion (Figure 6.4b, inset). The precipitate consists of needle-shaped crystals, ca. 20 μm in size. This morphology is typical for hydrated calcium sulfate modifications, bassanite and gypsum. PXRD confirms the needles to consist of gypsum (Figure S24, Supporting Information).

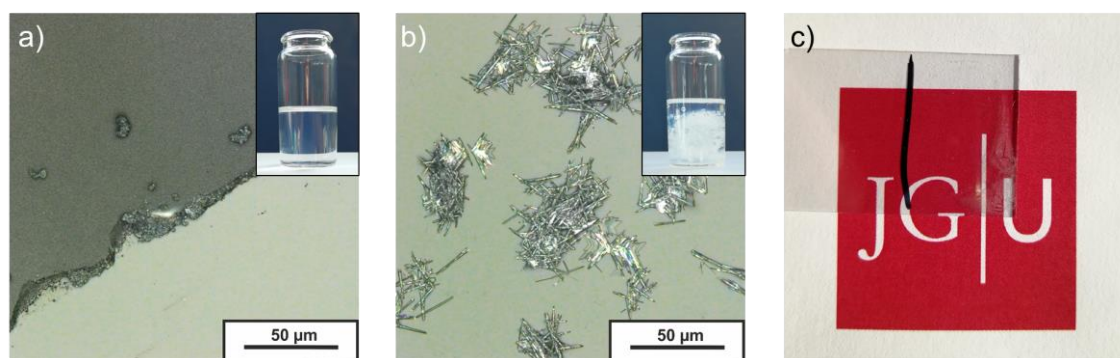


Figure 6.4 a) Laser microscopy image of a dense film of calcium sulfate nanoparticles on a glass slide, fabricated from the clear and stable dispersion in acetone (inset). b) Laser microscopy image of nanoparticles after contact with water; gypsum needles have formed (Figure S24, Supporting Information). Adding a few drops of water to the dispersion leads to immediate precipitation of the particles (inset). c) Transparent nanoparticle film on a glass slide (on the right of the black line). Drying cracks in the film appear at the edge of the slide.

Upon contact with water, two separate processes occurred on different time scales. Whereas particle agglomeration and precipitation occurred instantly, even at the smallest water concentrations of 0.5 vol%, the phase transformation of the nanoparticles to bassanite and

gypsum (the hydrated crystalline modifications) proceeded more slowly and required larger amounts of water. We assume that water molecules replace surface-bound 2-propanol in a first reaction step. The less favorable particle-acetone interactions after the loss of the 2-propanol surface layer led to agglomeration. The particles could not be redispersed in acetone/2-propanol, because water binding on the particle surface is too strong to permit exchange with 2-propanol. The precipitated particles could be dispersed to some extent in methanol. This was used to prepare the TEM samples shown in Figure 6.6 (*vide infra*), but a clear dispersion as in acetone could not be obtained again.

Phase Transformation

To analyze the phase transformation, a water/acetone mixture was added to the nanoparticle dispersion in acetone up to a final water concentration of 20 vol%. FTIR samples were taken after specific time intervals. The results are shown in Figure 6.5a.

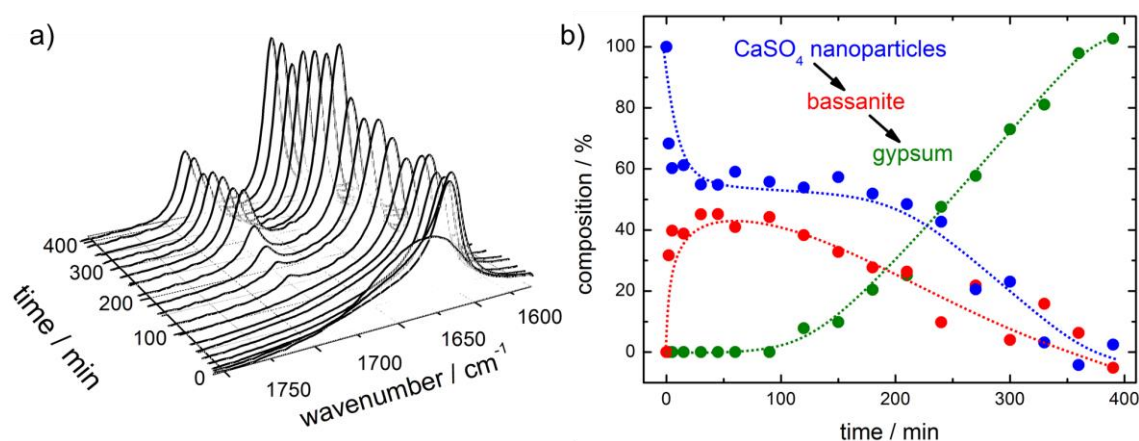


Figure 6.5 a) Evolution with time of the H-O-H bending vibration of calcium sulfate nanoparticles in a mixture of 20 vol% water with 80 vol% acetone. Upon contact with water, the intensity of the broad band at 1634 cm⁻¹ decreases and a sharper band at 1619 cm⁻¹ appears, which is attributed to bassanite. After 90 min, a third band at 1683 cm⁻¹ appears, while the intensity of the band at 1619 cm⁻¹ still increases due to the formation of gypsum. b) Phase composition (dotted guidelines shown) derived from a trimodal Gaussian fit of the bands, which allowed to calculate the contribution of calcium sulfate nanoparticles, bassanite, and gypsum phases at each point of the reaction.

We analyzed the H-O-H bending vibration of water between 1600 cm⁻¹ and 1750 cm⁻¹ to determine the phase composition. The calcium sulfate nanoparticles exhibit one broad water band with a maximum at 1634 cm⁻¹ (compare Figure 6.3a). Whereas bassanite has a single sharp band at 1619 cm⁻¹, the band of gypsum is split into a large band at 1620 cm⁻¹ and a

smaller one at 1684 cm^{-1} . We used a trimodal Gaussian fit to determine the area of each band and to calculate the composition of the sample at each point (Figure 6.5b). Almost half of the calcium sulfate nanoparticles transformed to bassanite during the first minutes upon contact with water. The ratio between both components remained nearly constant during the first 90 min. Gypsum started to form subsequently, while the amount of calcium sulfate nanoparticles and bassanite decreased to the same extent. After over 6 h, the transformation was complete and the sample consisted of gypsum only. These results, which are in accordance with other reports of bassanite as intermediate during the crystallization of gypsum,^{35,37} suggest that calcium sulfate nanoparticles transform to gypsum *via* bassanite. Although this seems obvious during the first 90 min of the reaction, it is not clear, whether the transformation proceeds only *via* bassanite or if a direct transformation to gypsum is possible after the first gypsum crystals have formed.

To further understand the crystallization mechanism, we took TEM snapshots at different points of time during the crystallization experiment in the water/acetone mixture (Figure 6.6). For the sample preparation, the reaction was stopped by centrifugation and washing with pure acetone to prevent any further phase transformation. Subsequently, the precipitate was dispersed in methanol and drop-casted on a TEM grid.

Before contact with water, we observed only drop-like calcium sulfate nanoparticles. The SAED indicates their predominantly amorphous structure with several weak reflections of γ -anhydrite (compare Figure 6.3c). Thin needles formed within 5 min, which were identified as bassanite (Figure 6.6b). The calcium sulfate nanoparticles are still present in larger quantity. After 150 min, additional crystals appeared, which were much bigger with a needle-like morphology. These needles consist of isotropically oriented gypsum crystallites (Figure 6.6c). At the end of the reaction (Figure 6.6d), we detect only gypsum, which is the stable calcium sulfate polymorph in aqueous environment (Figure 6.4b and Figure S24, Supporting Information).

The TEM snapshots of the phase transformation are in accordance with the FTIR kinetics. The nanoparticles partially transform to a second species (small bassanite needles). These species are present throughout the reaction, while large gypsum needles appear later as final product. The second image (Figure 6.6b) shows that the growth of the bassanite needles proceeds *via* nanoparticle attachment, as the rims of the needles still show the bumpy morphology of the nanoparticles. Crystal growth by oriented attachment^{58–60} is a possible

pathway that was reported for the growth of bassanite needles from bassanite nanorods, which self-assemble oriented along their *c*-axis.³⁵ *In situ* SAXS experiments revealed that self-assembly occurs already during the first stages of calcium sulfate crystallization.³⁶ Most studies agree on a dissolution-recrystallization mechanism for the transformation of bassanite to gypsum.^{61–65} Yet, the polycrystalline structure of the gypsum needles (Figure 6.6c) suggests that oriented attachment is also a potential pathway for their formation.

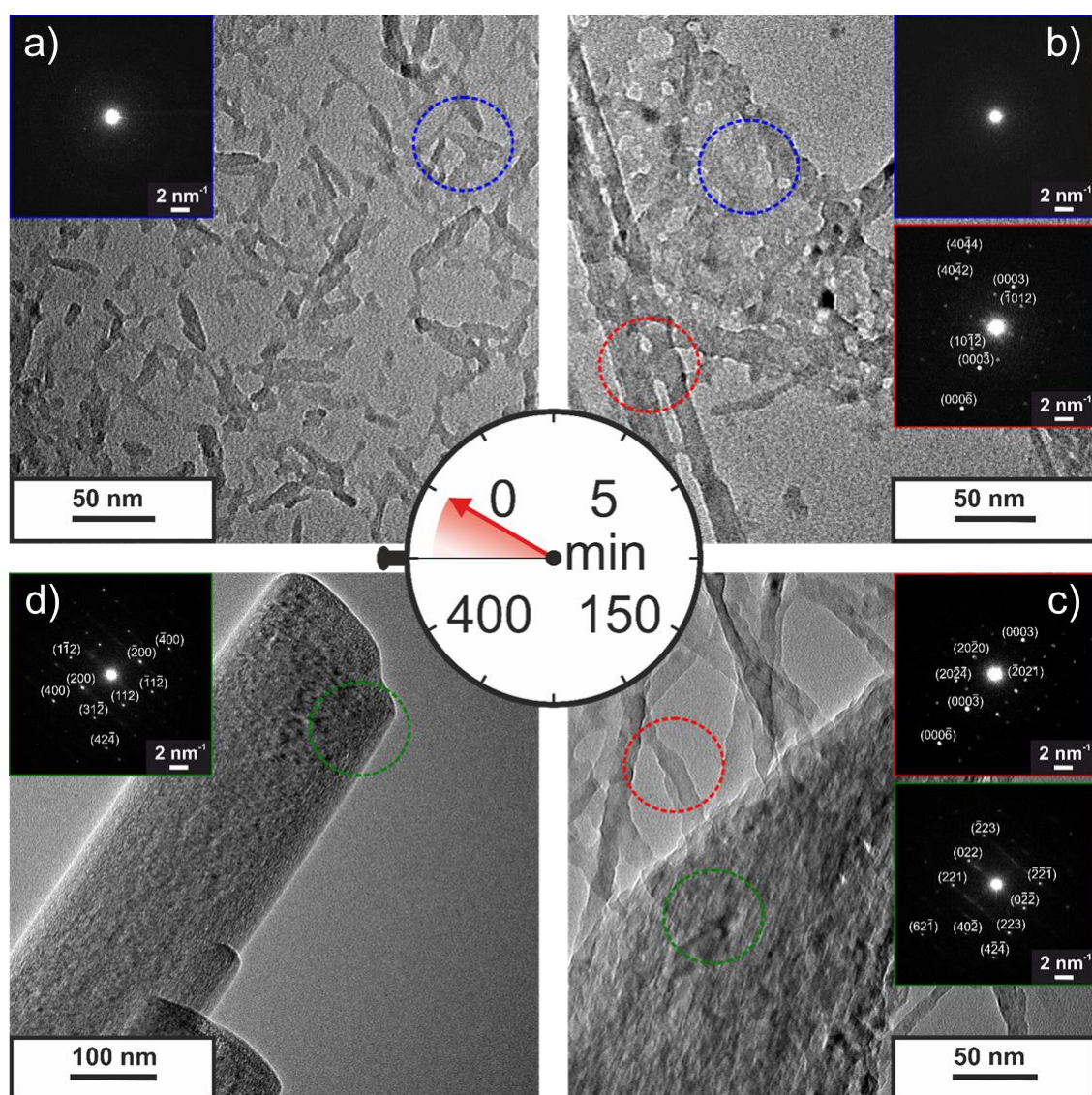


Figure 6.6 TEM study of the crystallization of calcium sulfate nanoparticles. Experiments were performed in a mixture of 20 vol% water with 80 vol% acetone. a) Calcium sulfate nanoparticles before contact with water. The particles are predominantly amorphous. b) Needle-shaped bassanite (reflections assigned in the red inset) form after 5 min from the calcium sulfate nanoparticles. c) Large gypsum needles (reflections assigned in the green inset) start to form after 150 min, while thin bassanite needles are still present. d) After 400 min, gypsum is the only crystalline modification in the sample.

Conclusion

We devised a new synthesis for calcium sulfate nanoparticles with unusual dispersibility in 2-propanol. These particles form long-term stable dispersions in acetone without additional functionalization and without any signs of precipitation. We demonstrated by ^1H NMR and FTIR spectroscopy that surface-bound 2-propanol gives rise to a favorable interaction with the solvent. The nanoparticles are polydisperse with a size distribution between 5 nm and 50 nm. They have a liquid-like morphology and contain significant amounts of structural water. PXRD and Rietveld refinement showed the presence of γ -anhydrite embedded in predominantly amorphous particles, as indicated by SAED. Adding water to the nanoparticle dispersion in acetone leads to instant agglomeration, followed by a phase transition to bassanite. Monitoring the kinetics of this process by FTIR revealed that the nanoparticles crystallize eventually to gypsum needles *via* a polycrystalline bassanite intermediate. The dispersibility in volatile organic solvents and the elucidation of the crystallization mechanism allow for applications of the calcium sulfate nanoparticles in hybrid materials, e.g. for transparent optical films.

6.3 EXPERIMENTAL SECTION

Materials

CaCl_2 (98 %, Merck), 2-propanol (99.8 %, puriss. p.a., Riedel-de Haën), sulfuric acid (95.0–97.0 %, puriss. p.a, Sigma-Aldrich), acetone (99.5 %, Riedel-de Haën), methanol (HPLC grade, Fisher Chemicals), cyclohexane (analytical reagent grade, Fisher Chemicals), acetone- d^6 (99.8 %, Deutero), 2-propanol- d^8 (98 %, Deutero), milli Q deionized water.

Synthesis

CaCl_2 (2 mmol) was dissolved in 20 mL of 2-propanol yielding a 0.1 M solution (I). Then, 106 μL of concentrated sulfuric acid (2 mmol) was added to 20 mL of 2-propanol yielding a 0.1 M solution (II). After mixing solutions (I) and (II), a colorless precipitate of calcium sulfate formed immediately. The precipitate was separated by centrifugation and washed with 2-propanol. Afterwards, 20 mL of acetone was added to the precipitate. Sonication for 1 min yielded a slightly cloudy dispersion of calcium sulfate. The dispersion was purified

by centrifugation for 10 min at 9000 rpm. A minor colorless residue was discarded. The clear colorless supernatant contained the calcium sulfate nanoparticles dispersed in acetone. The particles were precipitated by adding 20 mL of cyclohexane to perform FTIR, NMR, PXRD, and TGA experiments.

Crystallization Experiments

The nanoparticle dispersion in acetone was added to a water/acetone mixture to yield a final water concentration of 20 vol% (5 mL of the nanoparticle dispersion to a mixture of 11 mL of acetone and 4 mL of water). Samples were taken by transferring 250 μ L of the reaction solution to a microcentrifuge tube and quenching further crystallization by the addition of 1.5 mL of acetone. The sample was centrifuged for 1 min at 14000 rpm. Then, the supernatant was decanted. The sample was washed again with 1.5 mL of acetone and dried *in vacuo* afterwards. These samples were used for FTIR and TEM studies.

Film Fabrication

Transparent calcium sulfate films were prepared by depositing the nanoparticle dispersion on a glass slide and quickly evaporating the solvent in a drying chamber at 80 °C.

Characterization

X-ray powder diffraction. X-ray diffractograms were recorded with a STOE Stadi P equipped with a Mythen 1k detector using monochromatized MoK α radiation. The sample was attached to polyvinyl acetate films with perfluoroether (Fomblin Y, Aldrich). The sample was measured in transmission in 0.015° steps (continuous scan, 150 s/°) covering a 2 θ range from 1.5° to 43°. Rietveld refinement⁴⁵ was performed with Topas Academic v6 using the fundamental parameters approach,⁶⁶ based on a structural model for anhydrite by Kirfel et al.⁴⁹ Crystalline phases were identified according to the PDF-2 database⁶⁷ using Bruker AXS EVA.⁶⁸

FTIR spectroscopy. ATR-FTIR spectroscopy was performed using a Nicolet iS10 Spectrometer manufactured by Thermo Scientific. The spectra were recorded in a frequency range from 650 cm⁻¹ to 4000 cm⁻¹ with a resolution of 1.4 cm⁻¹ per data point.

Solid state NMR spectroscopy. The ¹H spectra were recorded on a Bruker Avance 400 DSX NMR spectrometer at a ¹H frequency of 399.87 MHz. A commercial three-channel 4 mm

Bruker probe head at 10 kHz magic angle spinning (MAS) averaging 32 scans was used. The spectra were referenced to external adamantane at 1.63 ppm as a secondary reference.

Solution NMR spectroscopy. For these NMR experiments, the samples were synthesized as described above, but 2-propanol- d^8 was used in the second washing step to remove free non-deuterated 2-propanol. Subsequently, the particles were dispersed in acetone- d^6 . All ^1H NMR experiments were conducted on a Bruker Avance DRX 400 NMR spectrometer operating at ^1H frequency of 400.31 MHz equipped with 5 mm inverse two channel probe head with z-gradients. The single pulse excitation experiments were recorded using a 30° pulse angle with a recycle delay of 1 s averaging 32 scans. Stimulated echo sequence with bipolar gradient pulses and a longitudinal eddy current delay was used for the ^1H diffusion-ordered spectroscopy (DOSY) experiments. The gradient strength was incremented in 16 steps from 2 % to 95 % of the maximum gradient strength. The diffusion time and the gradient pulse length were 100 ms and 2.0 ms with 2 s recycle delay, respectively. After Fourier transformation and baseline correction, the diffusion dimension of the 2D DOSY spectra was processed using the Bruker Topspin 1.3 software package. The diffusion analysis was performed using the Topspin T_1/T_2 relaxation package.

Thermogravimetric analysis. TGA experiments were carried out using a Perkin Elmer TGA Pyris 6 device in the temperature range from 30°C to 600°C with a heating rate of 10 K/min in air.

Dynamic light scattering. A four-angle light scattering instrument (50° , 70° , 90° , and 110°) equipped with a multi-tau digital correlator (laser diode: 532 nm, max. 100 mW) was employed. The instrument was custom-built by Wolfgang Schupp/HS GmbH/Oberhilbersheim according to the demands of Dr. Wolfgang Schärtl. Here, 10 mL of a dispersion (1 g/mL) of the calcium sulfate nanoparticles in acetone was filled in a cuvette and measured at four angles. The data were analyzed by the cumulant method.

Transmission electron microscopy. TEM samples were prepared by drop-casting 20 μL of the respective sample dispersion on 400 mesh carbon copper grids (Plano GmbH, Wetzlar, Germany). The samples were measured with a FEI Tecnai Spirit TWIN LaB₆ at 120 kV equipped with a Gatan US1000 CCD-camera (2048×2048 pixels) and a FEI Tecnai F30 S-TWIN at 300 kV equipped with a Gatan US4000 CCD-camera (4096×4096 pixels). A 70 μm condenser aperture and standard illumination settings were used for the TEM images acquisition and the selected area electron diffraction (SAED). A 20 μm selected area aperture

was used for the SAED acquisition. Diffraction patterns from Figure 6.6 were acquired with the Tecnai F30 microscope by means of a NanoBeam Diffraction (NBD) setting in order to have a beam of 50–150 nm. A 10 μm condenser aperture, spot size 6, and gun lens 8 were used for the NBD setting.

Laser microscopy. Laser microscopy images were taken using a Keyence VK 8710 with a wavelength of 658 nm.

6.4 REFERENCES

- (1) Langevin, Y., Poulet, F., Bibring, J.-P., Schmitt, B., Douté, S., Gondet, B. *Science* **2005**, *307*, 1581–1584.
- (2) Mees, F., Stoops, G. *Sedimentology* **2003**, *50*, 1139–1145.
- (3) Akpokodje, E. G. *Chem. Geol.* **1984**, *47*, 361–364.
- (4) Becker, A., Sötje, I., Paulmann, C., Beckmann, F., Donath, T., Boese, R., Prymak, O., Tiemann, H., Epple, M. *Dalton Trans.* **2005**, 1545–1550.
- (5) Hardie, L. A. *Am. Mineral.* **1967**, *52*, 171–201.
- (6) Hill, A. E. *J. Am. Chem. Soc.* **1937**, *59*, 2242–2244.
- (7) Innorta, G., Rabbi, E., Tomadin, L. *Geochim. Cosmochim. Acta* **1980**, *44*, 1931–1936.
- (8) Freyer, D., Voigt, W. *Monatsh. Chem.* **2003**, *134*, 693–719.
- (9) Ossorio, M., van Driessche, A.E.S., Pérez, P., García-Ruiz, J. M. *Chem. Geol.* **2014**, *386*, 16–21.
- (10) Testa, G., Lugli, S. *Sediment. Geol.* **2000**, *130*, 249–268.
- (11) Jacques, S. D. M., González-Saborido, A., Leynaud, O., Bensted, J., Tyrer, M., Greaves, R. I. W., Barnes, P. *Mineral. Mag.* **2009**, *73*, 421–432.
- (12) Seufert, S., Hesse, C., Goetz-Neunhoeffler, F., Neubauer, J. Z. *Kristallogr. Suppl.* **2009**, *2009*, 447–452.
- (13) Powell, D. A. *Nature* **1958**, *182*, 792.
- (14) Wiedemann, H. G. *Z. Anal. Chem.* **1975**, *276*, 21–31.
- (15) Meller, N., Kyritsis, K., Hall, C. *J. Solid State Chem.* **2009**, *182*, 2743–2747.
- (16) Tritschler, U., Kellermeier, M., Debus, C., Kempter, A., Cölfen, H. *CrystEngComm* **2015**, *17*, 3772–3776.

- (17) Tritschler, U., van Driessche, A. E. S., Kempster, A., Kellermeier, M., Cölfen, H. *Angew. Chem. Int. Ed.* **2015**, *54*, 4083–4086.
- (18) Charola, A. E., Pühringer, J., Steiger, M. *Environ. Geol.* **2007**, *52*, 339–352.
- (19) Karni, J., Karni, E. *Mater. Struct.* **1995**, *28*, 92–100.
- (20) Xu, L., Wu, K., Rößler, C., Wang, P., Ludwig, H. M. *Cement Concr. Compos.* **2017**, *80*, 298–306.
- (21) Serpell, R., Zunino, F. *Cem. Concr. Res.* **2017**, *100*, 398–412.
- (22) Bizzozero, J., Gosselin, C., Scrivener, K. L. *Cem. Concr. Res.* **2014**, *56*, 190–202.
- (23) Ioannou, S., Reig, L., Paine, K., Quillin, K. *Cem. Concr. Res.* **2014**, *56*, 75–83.
- (24) Poon, C. S., Kou, S. C., Lam, L., Lin, Z. S. *Cem. Concr. Res.* **2001**, *31*, 873–881.
- (25) Tzouvalas, G., Dermatas, N., Tsimas, S. *Cem. Concr. Res.* **2004**, *34*, 2113–2118.
- (26) Ledingham, A. D., English, J. D., Akyalcin, S., Cozad, B. E., Ontiveros, J. C., Kasper, F. K. *Am. J. Orthod. Dentofac.* **2016**, *150*, 1056–1062.
- (27) Zhou, Z., Buchanan, F., Mitchell, C., Dunne, N. *Mater. Sci. Eng., C* **2014**, *38*, 1–10.
- (28) Thomas, M. V., Puleo, D. A. *J. Biomed. Mater. Res. B* **2009**, *88*, 597–610.
- (29) Sindhura Reddy, N., Sowmya, S., Bumgardner, J. D., Chennazhi, K. P., Biswas, R., Jayakumar, R. *Biochim. Biophys. Acta* **2014**, *1840*, 2080–2090.
- (30) Guarnieri, R., Pecora, G., Fini, M., Aldini, N. N., Giardino, R., Orsini, G., Piattelli, A. *J. Periodontol.* **2004**, *75*, 902–908.
- (31) Crespi, R., Capparè, P., Gherlone, E. *J. Periodontol.* **2009**, *80*, 210–218.
- (32) Orsini, G., Ricci, J., Scarano, A., Pecora, G., Petrone, G., Iezzi, G., Piattelli, A. *J. Biomed. Mater. Res. B* **2004**, *68*, 199–208.
- (33) Doty, H. A., Leedy, M. R., Courtney, H. S., Haggard, W. O., Bumgardner, J. D. *J. Mater. Sci. Mater. Med.* **2014**, *25*, 1449–1459.
- (34) McConoughey, S. J., Howlin, R. P., Wiseman, J., Stoodley, P., Calhoun, J. H. *J. Biomed. Mater. Res. B* **2015**, *103*, 870–877.
- (35) Van Driessche, A. E. S., Benning, L. G., Rodriguez-Blanco, J. D., Ossorio M., Bots, P., García-Ruiz, J. M. *Science* **2012**, *336*, 69–72.
- (36) Stawski, T. M., van Driessche, A. E. S., Ossorio, M., Diego Rodriguez-Blanco, J., Besselink, R., Benning, L. G. *Nat. Commun.* **2016**, *7*, 11177.
- (37) Wang, Y.-W., Kim, Y.-Y., Christenson, H. K., Meldrum, F. C. *Chem. Commun.* **2012**, *48*, 504–506.

- (38) Saha, A., Lee, J., Pancera, S. M., Bräeu, M. F., Kempter, A., Tripathi, A., Bose, A. *Langmuir* **2012**, *28*, 11182–11187.
- (39) Jones, F. *CrystEngComm* **2012**, *14*, 8374–8381.
- (40) Wang, Y.-W., Christenson, H. K., Meldrum, F. C. *Adv. Funct. Mater.* **2013**, *23*, 5615–5623.
- (41) Coquard, P., Boistelle, R., Amathieu, L., Barriac, P. *J. Mater. Sci.* **1994**, *29*, 4611–4617.
- (42) Osterwalder, N., Loher, S., Grass, R. N., Brunner, T. J., Limbach, L. K., Halim, S. C., Stark, W. J. *J. Nanopart. Res.* **2007**, *9*, 275–281.
- (43) Rees, G. D., Evans-Gowing, R., Hammond, S. J., Robinson, B. H. *Langmuir* **1999**, *15*, 1993–2002.
- (44) Salvadori, B., Capitani, G., Mellini, M., Dei, L. *J. Colloid Interface Sci.* **2006**, *298*, 487–490.
- (45) Rietveld, H. M. *J. Appl. Crystallogr.* **1969**, *2*, 65–71.
- (46) Nissinen, T., Li, M., Davis, S. A., Mann, S. *CrystEngComm* **2014**, *16*, 3843–3847.
- (47) Stetefeld, J., McKenna, S. A., Patel, T. R. *Biophys. Rev.* **2016**, *8*, 409–427.
- (48) Schärfl W. *Light Scattering from Polymer Solutions and Nanoparticle Dispersions*, 1st ed.; Springer-Verlag: Heidelberg, 2007.
- (49) Kirfel, A., Will, G. *Acta Crystallogr., Sect. B: Struct. Sci* **1980**, *36*, 2881–2890.
- (50) Gebauer, D., Gunawidjaja, P. N., Ko, J. Y. P., Bacsik, Z., Aziz, B., Liu, L., Hu, Y., Bergström, L., Tai, C.-W., Sham, T.-K., Edén, M., Hedin, N. *Angew. Chem. Int. Ed.* **2010**, *122*, 9073–9075.
- (51) Wolf, S. E., Leiterer, J., Kappl, M., Emmerling, F., Tremel, W. *J. Am. Chem. Soc.* **2008**, *130*, 12342–12347.
- (52) Bach, S., Celinski, V. R., Dietzsch, M., Panthöfer, M., Bienert, R., Emmerling, F., Schmedt auf der Günne, J., Tremel, W. *J. Am. Chem. Soc.* **2015**, *137*, 2285–2294.
- (53) Lane, M. D. *Am. Mineral.* **2007**, *92*, 1–18.
- (54) Yan, C., Nishida, J., Yuan, R., Fayer, M. D. *J. Am. Chem. Soc.* **2016**, *138*, 9694–9703.
- (55) Klünker, M., Mondeshki, M., Nawaz Tahir, M., Tremel, W. *Langmuir* **2018**, *34*, 1700–1710.

- (56) Badia, A., Singh, S., Demers, L., Cuccia, L., Brown, G. R., Lennox, R. B. *Chem. Eur. J.* **1996**, *2*, 359–363.
- (57) Richardi, J., Fries, P. H., Fisher, R., Rast, S., Krienke, H. *Mol. Phys.* **1998**, *93*, 925–938.
- (58) Penn, R. L., Banfield, J. F. *Am. Mineral.* **1998**, *83*, 1077–1082.
- (59) Woehl, T. J., Park, C., Evans, J. E., Arslan, I., Ristenpart, W. D., Browning, N. D. *Nano Lett.* **2014**, *14*, 373–378.
- (60) Zhang, H., Banfield, J. F. *J. Phys. Chem. Lett.* **2012**, *3*, 2882–2886.
- (61) Singh, N. B., Middendorf, B. *Prog. Cryst. Growth Charact. Mater.* **2007**, *53*, 57–77.
- (62) Fujii, K., Kondo, W. *J. Chem. Soc., Dalton Trans.* **1986**, *4*, 729–731.
- (63) Schiller, K. *J. appl. Chem. Biotechnol.* **1974**, *24*, 379–385.
- (64) Ridge, M. J., King, G. A., Molony, B. *J. appl. Chem. Biotechnol.* **1972**, *22*, 1065–1075.
- (65) Mikhail, R. S., Malek, I. A. *J. Chem. Technol. Biotechnol.* **1971**, *21*, 277–282.
- (66) Coelho, A. A. *J. Appl. Crystallogr.* **2018**, *51*, 210–218.
- (67) PDF-2, Release 2004, JCPDS – International Center for Diffraction Data, Newton Square (PA) US (2004).
- (68) EVA 10.0 Rev. 1, Bruker AXS, Madison (WI) US (2003).

CONCLUSION

In this dissertation, the crystallization of various carbonates *via* amorphous intermediates was studied. Carbonates, particularly calcium carbonate, represent interesting model systems to investigate the fundamental processes of crystallization. The occurrence of transient amorphous intermediate species has received increased attention in the last years, as they represent an opportunity to influence and control the crystallization process. Therefore, composition, morphology, structure, and crystallization mechanisms of these amorphous intermediates were studied in detail. Due to the lability and transient nature of these intermediates, their stabilization and isolation represent a difficult challenge in regard to their chemical synthesis.

The different compounds, scopes, and questions required individual synthetic approaches to prepare the respective amorphous intermediates. Thus, three separate projects that focused on specific aspects of crystallization *via* amorphous intermediates were created.

Firstly, a reaction system was developed to capture the transient species immediately after their formation and to simultaneously induce long-term stability. These samples allowed for a detailed characterization of unknown amorphous intermediates. Additionally, dispersions of non-stabilized amorphous carbonates were synthesized to study the transformation mechanisms of these species to crystalline modifications. Finally, structural water in the amorphous carbonates and the strength of the hydrogen bonding network were examined. Furthermore, two sub-projects were addressed. Firstly, a new form of amorphous calcium carbonate was synthesized from crystalline calcite by a mechanochemical approach using a planetary ball mill. Secondly, a synthesis of partially amorphous calcium sulfate nanoparticles was devised. These particles exhibit unusual dispersibility properties in organic media and promise interesting applications as “nano-gypsum”.

In the first project, a new two-phase reaction system was developed that enabled the stabilization of amorphous carbonates of various metals (calcium, strontium, barium, manganese, and cadmium). In the aqueous phase of the system, metal carbonates were precipitated in the presence of a detergent, sodium oleate. Immediately after the formation of the nanoparticulate amorphous intermediates, these droplet-shaped particles were coated by an oleate layer and extracted into the organic phase. Thereby, long-term stability of several days to weeks, except only hours in barium carbonate, was induced in these normally extremely short-lived species. Heteronuclear correlation spectroscopy indicated the presence of oleate solely on the surface of the particles; no mixed carbonate/oleate phase was observed. Thus, we regarded the samples as actual intermediates during the crystallization process, which were stabilized by oleate capping *ex post*. Their composition was determined by thermogravimetric experiments; the amount of structural water in the hydrated amorphous carbonates was determined to be less than 1 mol H₂O per formula unit. Simultaneously, the thermally induced crystallization was monitored by differential thermal analysis. To characterize the local structure of the amorphous intermediates, total scattering experiments with high-energy synchrotron radiation were performed that allowed the derivation of the respective pair distribution function (PDF). On basis of the PDF, a structural model for amorphous calcium carbonate was developed. We observed a broad distribution of coordination numbers for calcium. The mean coordination number of calcium was reduced when compared to crystalline calcium carbonate. We showed that crystallization *via* amorphous intermediates is a possible pathway for a variety of carbonates, and we characterized these transient species in detail.

Through the precipitation of carbonates in anhydrous organic solvents, we obtained dispersions of amorphous carbonate nanoparticles of calcium, strontium, and manganese. No additional stabilization was necessary, since the absence of water prevented crystallization. The crystallization process was initiated through the addition of water. FTIR studies showed that there was an acceleration in the rate of crystallization with increasing water concentration. Additionally, this process was monitored by electron microscopy and potentiometric measurements. We developed a mathematical model that qualitatively describes our observations by a dissolution-recrystallization mechanism of the amorphous carbonates. The Pearson hardness of a metal cation determines the kinetics of crystallization – the harder the cation, the slower the rate of crystallization. This observation indicates that the desolvation

of the cation represents the rate-determining step during the transformation to a crystalline modification. Furthermore, we observed that the respective sub-processes, dissolution and recrystallization, are affected differently by water concentration. Thus, by working in a solvent mixture, the water concentration represents a way to manipulate the crystallization process.

All studied amorphous intermediates are hydrated species. The local water environment and the strength of the internal hydrogen bonding network in amorphous carbonates were investigated in detail by various NMR techniques and FTIR spectroscopy. Amorphous carbonates of magnesium, calcium, strontium, and barium were synthesized from methanolic solution. Analysis of the O-H stretching vibration in FTIR and the chemical shift of water in ^1H NMR indicated that the Pearson hardness of the respective cation mainly determines the hydrogen bonding strength in the amorphous carbonate. The bonding strength decreased going from Pearson soft barium, *via* strontium, to calcium. Yet, amorphous magnesium carbonate exhibited relatively strong hydrogen bonds, despite Mg^{2+} being the hardest cation of the above. In this compound, the hydrogen bonding network is stabilized by additional hydroxide ions that act as strong hydrogen bond acceptors. From the temperature dependence of the spin-lattice relaxation time (T_1), the activation energy for the motion of the water molecules was calculated. The results are in accordance with the strength of the internal hydrogen bonding; amorphous calcium carbonate had the weakest hydrogen bonds and had the lowest activation energy for water motion. By the detailed study of the structural water in amorphous carbonates, an essential step to the complete characterization of these transient intermediate species was taken.

In addition to the synthesis of amorphous carbonates from solution, a new mechanochemical approach was developed to prepare amorphous calcium carbonate. By processing crystalline calcium carbonate (calcite) in a planetary ball, a previously unknown amorphous modification of calcium carbonate was obtained, which was referred to as BM-ACC (ball milled amorphous calcium carbonate). However, amorphization of calcite was only possible by the addition of foreign ions, in form of 10 mol% Na_2CO_3 , during the milling process. The comparable ionic radii but deviating charge of Na^+ and Ca^{2+} represent a driving force for the creation of defects and disorder. Through ^{23}Na NMR, the sodium nucleus was used as a probe to monitor the degradation of the local structure during the milling process. Total scattering experiments showed the same degree of short-range order within 10 Å, as it was

observed in amorphous calcium carbonate precipitated from solution. We observed a decreased coordination number of the calcium cation in BM-ACC compared to crystalline calcium carbonate. Through heating or the addition of water, BM-ACC crystallizes to calcite. Upon contact with water, BM-ACC partially dissolves and recrystallizes as calcite, while the sodium cations remain in solution. The large aggregates of agglomerated BM-ACC nanoparticles, which are a result of the mechanochemical synthesis, act as template for the growth of calcite crystals. During the thermally induced crystallization, the sodium ions proved to stabilize the amorphous phase. Only at higher temperature and prolonged heating time, they are gradually incorporated into the crystalline material. Our findings reveal the amorphization mechanism of calcite in a planetary ball mill on the atomic scale and highlight the role of impurities for stabilizing the amorphous modification. Thereby, we present a general access to defect-stabilized amorphous materials by high-energy ball milling.

In the second sub-project, inspired by the precipitation of amorphous carbonates in organic solvents, calcium sulfate nanoparticles were synthesized in 2-propanol. These droplet-shaped particles, 30 nm in size, are predominantly amorphous with small crystalline areas of γ -anhydrite. Due to the attachment of 2-propanol molecules on their surface, as confirmed by FTIR and NMR, the particles exhibited a highly unusual dispersibility in acetone. The dispersion in acetone showed no sign of precipitation over weeks and was miscible with a variety of organic solvents. This allowed for the production of transparent calcium sulfate films by drop-casting the dispersion on glass slides and evaporating the solvent. By the addition of water to the dispersion in acetone, the nanoparticles precipitated immediately. Additionally, a phase transformation to crystalline gypsum occurred. We monitored this process by FTIR and electron microscopy. Thereby, we identified bassanite fibers as an intermediate phase, which are formed by the oriented attachment of the nanoparticles. The unusual dispersibility in organic solvents, combined with the formation of gypsum needles on contact with water, promises a variety of possible applications as “nano-gypsum”.

In conclusion, these studies illuminate the crystallization pathway *via* amorphous intermediates for a variety of carbonates. Different synthetic approaches were developed to isolate these transient species and to enable a detailed characterization of their morphology, composition, and structure. Water plays a key role in these systems, both as structural water inside the amorphous carbonates and as a solvent influencing the transformation to a

crystalline modification. The Pearson hardness of the respective cation in the amorphous carbonate mainly determines the strength of the internal hydrogen bonding network as well as stability with regard to crystallization *via* a dissolution-recrystallization mechanism. Moreover, a mechanochemical approach was developed to synthesize a new form of amorphous calcium carbonate from a crystalline starting material. The formation, structure, and crystallization behavior of this compound were examined, particularly focused on the implications of impurities in the amorphous carbonate. Finally, a synthesis of partially amorphous calcium sulfate nanoparticles was devised, based on the precipitation of amorphous carbonates in anhydrous media. Their unusual dispersibility in organic solvents as well as their phase transformation to gypsum needles on contact with water promise a variety of applications. This dissertation highlights the the role of amorphous intermediates during crystallization, which represents a pathway accessible to a variety of systems. The detailed characterization of these transient species deepens our understanding of this fundamental process and offers the potential to ultimately design and control crystallization.

APPENDIX

SUPPORTING INFORMATION

Calculation of Oleate Layer Thickness

The volume V_{ACC} of a spherical ACC nanoparticles with radius r_{ACC} is:

$$V_{ACC} = \frac{4\pi}{3} r_{ACC}^3 \quad (S1)$$

With the atomic mass of ACC M_{ACC} and its density ρ_{ACC} , the number of moles of amorphous calcium carbonate per particle n_{ACC} is calculated to be:

$$n_{ACC} = \frac{V_{ACC} \cdot \rho_{ACC}}{M_{ACC}} \quad (S2)$$

With the approximate composition of $\text{CaCO}_3 \times 0.9 \text{H}_2\text{O} \times 0.1$ oleate, we find for the number of moles oleic acid per particle n_{ol} :

$$n_{ol} = 0.1 n_{ACC} \quad (S3)$$

Assuming bulk density for the solvent layer, we get for the volume respectively:

$$V_{ol} = n_{ol} \cdot \frac{M_{ol}}{\rho_{ol}} \quad (S4)$$

The new volume of the particle with oleate layer and the respective radius r_{ACC+ol} is:

$$\frac{4\pi}{3} r_{ACC+ol}^3 = V_{ACC} + V_{ol} \quad (S5)$$

$$\frac{4\pi}{3} r_{ACC+ol}^3 = \frac{4\pi}{3} r_{ACC}^3 + \frac{n_{ol} \cdot M_{ol}}{\rho_{ol}} \quad (S6)$$

Inserting eq. S2 and eq. S3 into eq. S6 leads to:

$$\frac{4\pi}{3} r_{\text{ACC+ol}}^3 = \frac{4\pi}{3} r_{\text{ACC}}^3 + \frac{0.1 \rho_{\text{ACC}} \cdot M_{\text{ol}} \cdot 4\pi r_{\text{ACC}}^3}{3 \rho_{\text{ol}} \cdot M_{\text{ACC}}} \quad (\text{S7})$$

$$r_{\text{ACC+ol}} = \sqrt[3]{1 + \frac{0.1 \rho_{\text{ACC}} \cdot M_{\text{ol}}}{\rho_{\text{ol}} \cdot M_{\text{ACC}}} \cdot r_{\text{ACC}}} \quad (\text{S8})$$

As an approximation, we used the density of monohydrocalcite ($\text{CaCO}_3 \times 1 \text{H}_2\text{O}$) and, for the oleate ligand, the respective values of oleic acid.

M_{ACC}	$116.3 \frac{\text{g}}{\text{mol}}$	ρ_{ACC}	$2.43 \frac{\text{g}}{\text{cm}^3}$
M_{ol}	$282.4 \frac{\text{g}}{\text{mol}}$	ρ_{ol}	$0.89 \frac{\text{g}}{\text{cm}^3}$

$$r_{\text{ACC+ol}} = 1.18 \cdot r_{\text{ACC}} \quad (\text{S9})$$

The assumption of a mean particle radius of $\sim 10 \text{ nm}$ (according to TEM) results in an oleate layer thickness of $\sim 2 \text{ nm}$.

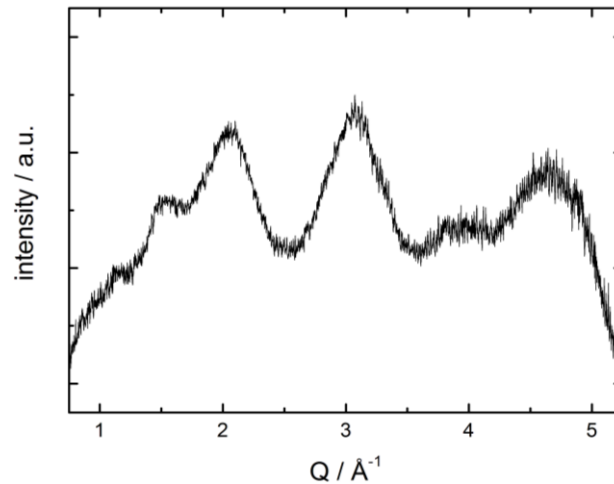


Figure S1. PXRD of amorphous BaCO_3 with oleate. The absence of Bragg reflections indicate the non-crystallinity of the sample.

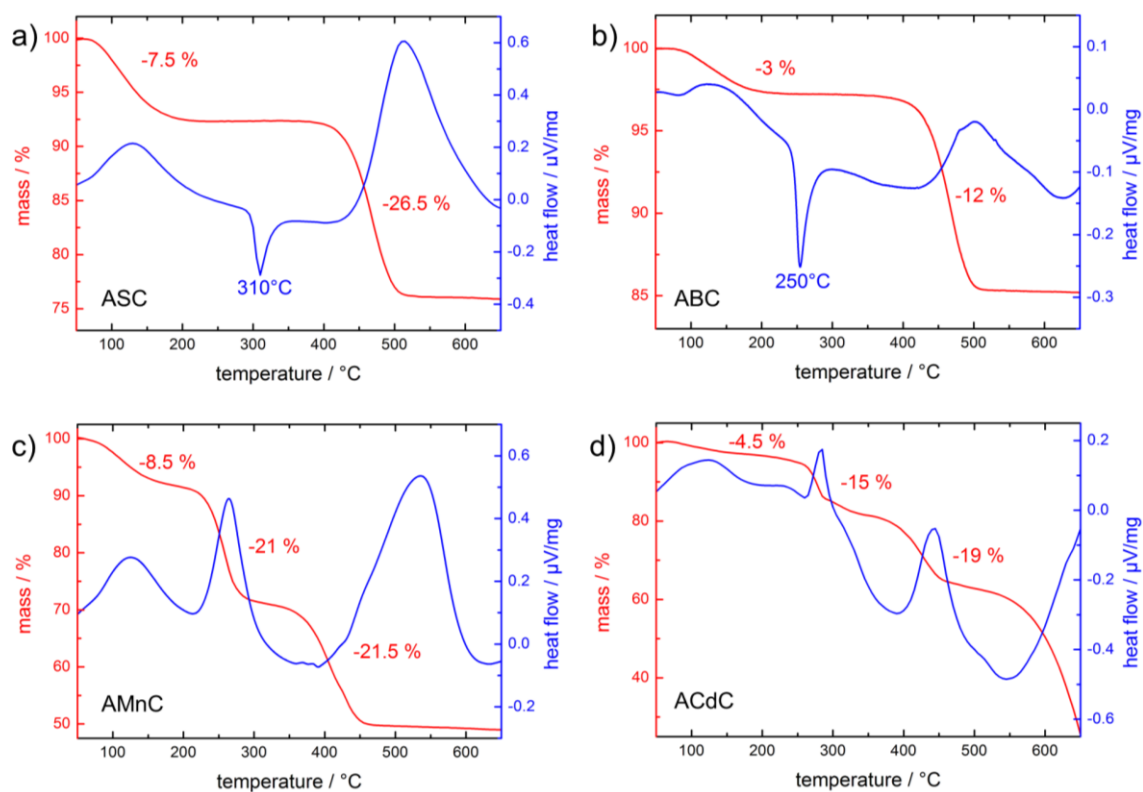


Figure S2. Thermogravimetric and differential thermal analysis (TGA-DTA) of amorphous a) SrCO_3 , b) BaCO_3 , c) MnCO_3 , and d) CdCO_3 . All samples show a mass loss step in the TGA curve (red) between 50 °C and 200 °C, which we attribute to structural water. AMnC and ACdC decompose around 250 °C. Therefore, no thermally induced crystallization is observed in the DTA curve (blue) of these samples. The earth alkali carbonates, ASC and ABC, exhibit an exothermic effect at 310 °C, respectively at 250 °C, which indicates the thermally induced crystallization.

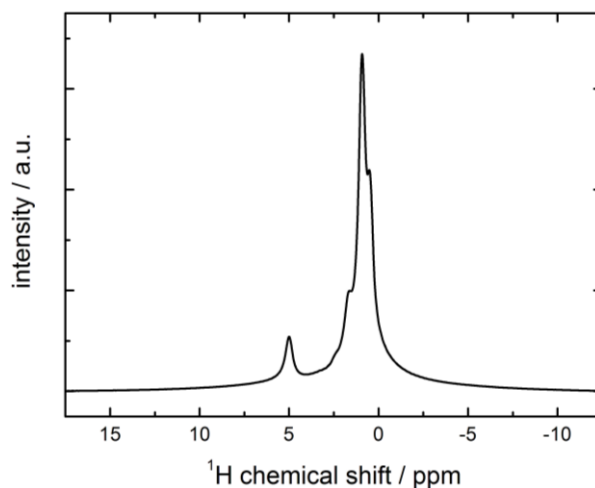


Figure S3. ^1H NMR spectrum of ACC with oleate capping. The proton signals of the oleate ligand (methylene protons around 1 ppm, ethenyl protons at 5 ppm) are clearly visible. The underlying signal of structural water is too broad to be resolved.

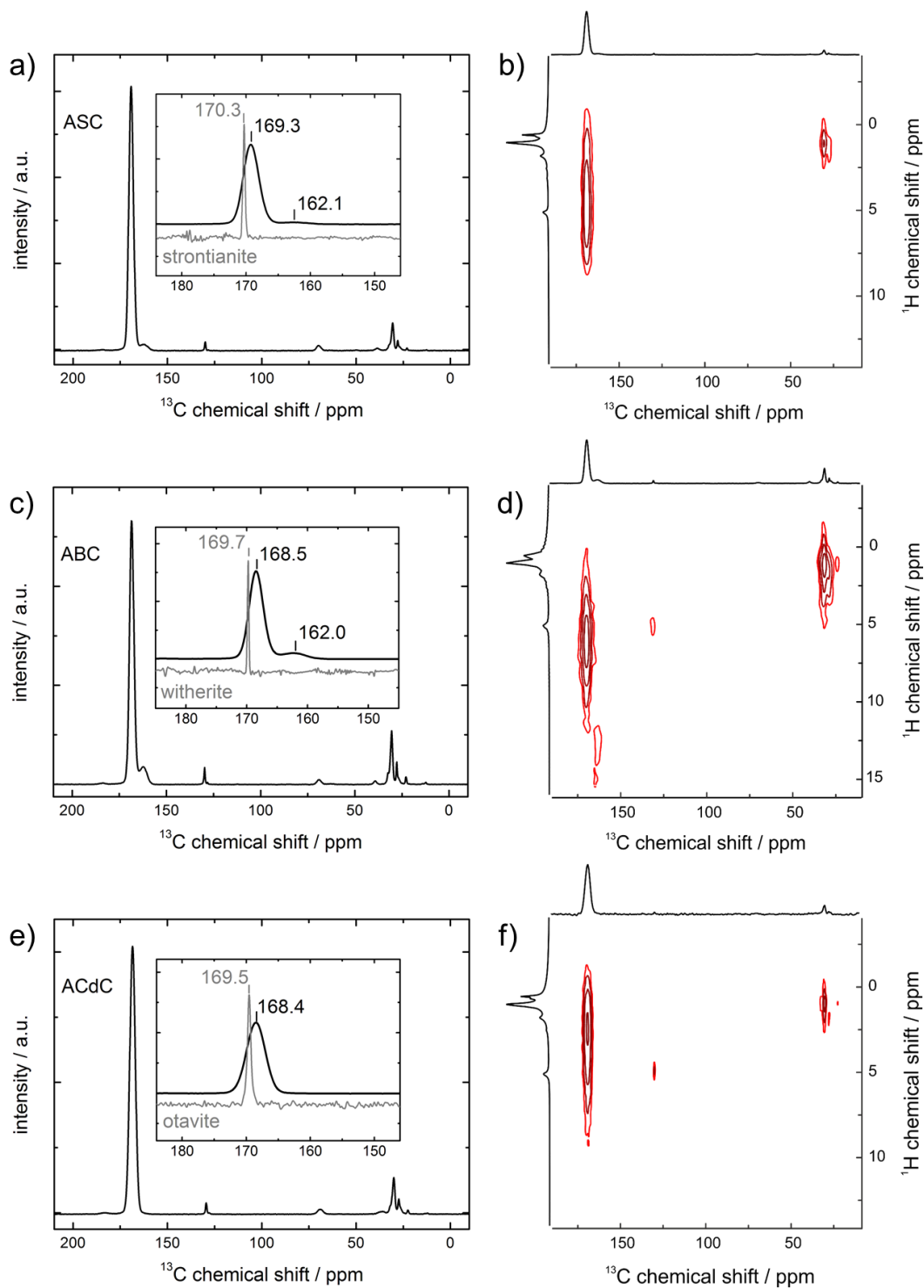


Figure S4. $^{13}\text{C}\{^1\text{H}\}$ CP MAS-NMR and HETCOR spectra of (a,b) ASC, (c,d) ABC, and (e,f) ACdC. Respective crystalline references are shown as inset (gray). Besides the carbonate and oleate signals, ASC and ABC display a further signal around 162 ppm. The HETCOR spectrum of ABC shows that this signal is correlated to strongly deshielded, i.e. acidic, protons. This is a strong evidence for the presence of hydrogencarbonate species in these samples.

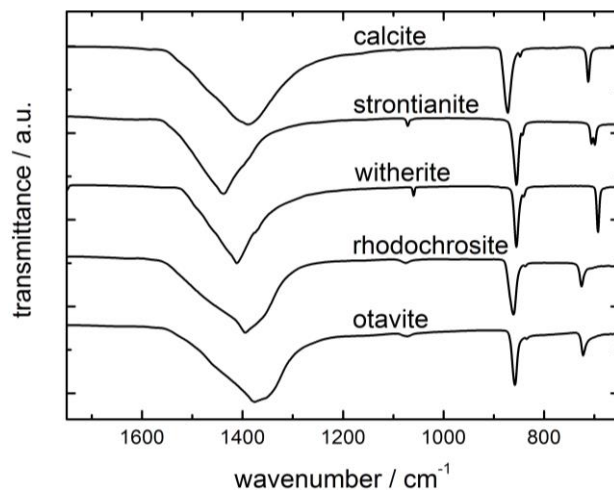


Figure S5. FTIR spectra of the thermodynamic crystalline modifications of CaCO_3 , SrCO_3 , BaCO_3 , MnCO_3 , and CdCO_3 .

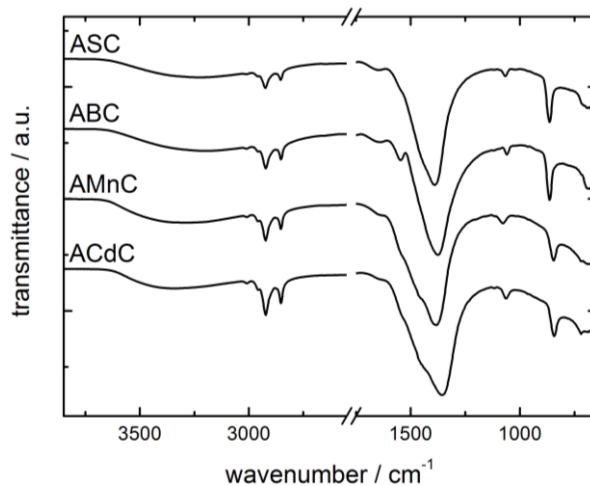


Figure S6. FTIR spectra of the amorphous modifications of SrCO_3 , BaCO_3 , MnCO_3 , and CdCO_3 with oleate and structural water.

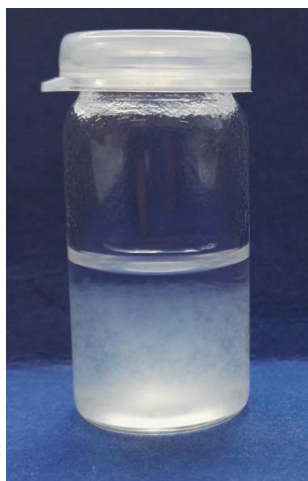


Figure S7. ACC dispersion in acetonitrile.

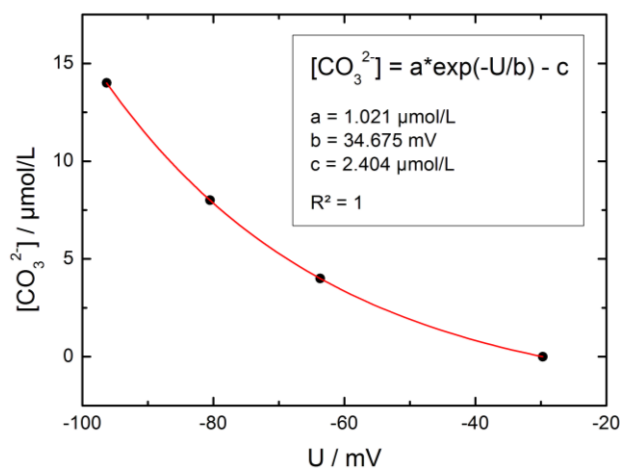
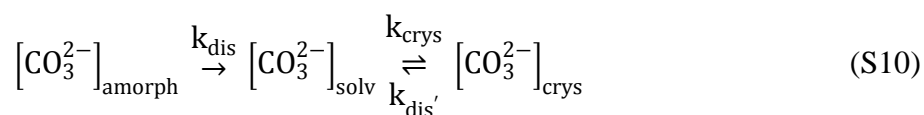


Figure S8. Exemplary calibration curve for the carbonate concentration in 20 vol% water in acetonitrile.

Mathematical Derivation of Carbonate Concentration with Time

The phase transformation of the amorphous carbonate to a crystalline modification was modeled based on dissolution (k_{dis}) of the amorphous carbonate and subsequent crystallization (k_{crys}). The solubility product of the crystalline carbonate was taken into account by $k_{\text{dis}'}$.



The concentration of carbonate in solution $[\text{CO}_3^{2-}]_{\text{solv}}$ with time t is monitored in our experiment. In the following, $[\text{CO}_3^{2-}]_{\text{amorph}} = A$, $[\text{CO}_3^{2-}]_{\text{solv}} = B$, and $[\text{CO}_3^{2-}]_{\text{crys}} = C$ are used.



This system is described by the three following coupled differential equations.

$$\frac{dA}{dt} = -k_{\text{dis}} A \quad (\text{S12})$$

$$\frac{dB}{dt} = k_{\text{dis}} A + k_{\text{dis}'} C - k_{\text{crys}} B \quad (\text{S13})$$

$$\frac{dC}{dt} = k_{\text{crys}} B - k_{\text{dis}'} C \quad (\text{S14})$$

The equations are solved under the following starting conditions, as at $t = 0$, only the amorphous carbonate (A) is present. The total amount of carbonate is constant.

$$A(0) = A_0 \quad (\text{S15})$$

$$B(0) = 0 \quad (\text{S16})$$

$$C(0) = 0 \quad (\text{S17})$$

$$A + B + C = \text{constant} = A_0 \quad (\text{S18})$$

Equation S12 is solved:

$$A(t) = A_0 e^{-k_{\text{dis}} t} \quad (\text{S19})$$

Inserting eq. S18 in eq. S13 yields the following expression.

$$\frac{dB}{dt} = k_{\text{dis}} A + k_{\text{dis}'} (A_0 - A - B) - k_{\text{crys}} B \quad (\text{S20})$$

$$\frac{dB}{dt} = (k_{\text{dis}} - k_{\text{dis}'}) A - (k_{\text{crys}} + k_{\text{dis}'}) B + k_{\text{dis}'} A_0 \quad (\text{S21})$$

For solving the non-homogeneous differential equation S21, its homogeneous form must be solved first.

$$\frac{dB}{dt} - (k_{\text{crys}} + k_{\text{dis}'}) B = 0 \quad (\text{S22})$$

$$B(t) = \Theta e^{-(k_{\text{crys}} + k_{\text{dis}'})t} \quad (\text{S23})$$

By inserting eq. S23 and eq. S19 in eq. S21, the non-homogeneous differential equation is solved by variation of the constant Θ .

$$\begin{aligned} & \frac{d\Theta}{dt} e^{-(k_{\text{crys}} + k_{\text{dis}'})t} - \Theta (k_{\text{crys}} + k_{\text{dis}'}) e^{-(k_{\text{crys}} + k_{\text{dis}'})t} \\ & = (k_{\text{dis}} - k_{\text{dis}'}) A_0 e^{-k_{\text{dis}} t} - \Theta (k_{\text{crys}} + k_{\text{dis}'}) e^{-(k_{\text{crys}} + k_{\text{dis}'})t} + k_{\text{dis}'} A_0 \end{aligned} \quad (\text{S24})$$

$$\frac{d\Theta}{dt} e^{-(k_{\text{crys}} + k_{\text{dis}'})t} = (k_{\text{dis}} - k_{\text{dis}'}) A_0 e^{-k_{\text{dis}} t} + k_{\text{dis}'} A_0 \quad (\text{S25})$$

$$\frac{d\Theta}{dt} = (k_{\text{dis}} - k_{\text{dis}'}) A_0 e^{(k_{\text{crys}} + k_{\text{dis}'} - k_{\text{dis}})t} + k_{\text{dis}'} A_0 e^{(k_{\text{crys}} + k_{\text{dis}'})t} \quad (\text{S26})$$

$$\begin{aligned} \Theta & = \left(\frac{k_{\text{dis}} - k_{\text{dis}'}}{k_{\text{crys}} + k_{\text{dis}'} - k_{\text{dis}}} \right) A_0 e^{(k_{\text{crys}} + k_{\text{dis}'} - k_{\text{dis}})t} \\ & \quad + \left(\frac{k_{\text{dis}'}}{k_{\text{crys}} + k_{\text{dis}'}} \right) A_0 e^{(k_{\text{crys}} + k_{\text{dis}'})t} + \Gamma \end{aligned} \quad (\text{S27})$$

$$\begin{aligned} B(t) & = \left(\frac{k_{\text{dis}} - k_{\text{dis}'}}{k_{\text{crys}} + k_{\text{dis}'} - k_{\text{dis}}} \right) A_0 e^{-k_{\text{dis}} t} + \left(\frac{k_{\text{dis}'}}{k_{\text{crys}} + k_{\text{dis}'}} \right) A_0 \\ & \quad + \Gamma e^{-(k_{\text{crys}} + k_{\text{dis}'})t} \end{aligned} \quad (\text{S28})$$

With the starting condition $B(0) = 0$, the constant Γ can be calculated.

$$B(0) = \left(\frac{k_{\text{dis}} - k_{\text{dis}'}}{k_{\text{crys}} + k_{\text{dis}'} - k_{\text{dis}}} \right) A_0 + \left(\frac{k_{\text{dis}'}}{k_{\text{crys}} + k_{\text{dis}'}} \right) A_0 + \Gamma = 0 \quad (\text{S29})$$

$$\Gamma = - \left(\frac{k_{\text{dis}} - k_{\text{dis}'}}{k_{\text{crys}} + k_{\text{dis}'} - k_{\text{dis}}} \right) A_0 - \left(\frac{k_{\text{dis}'}}{k_{\text{crys}} + k_{\text{dis}'}} \right) A_0 \quad (\text{S30})$$

Inserting eq. S30 in eq. S28 gives the behavior of the concentration of dissolved carbonate B with the time t.

$$B(t) = A_0 \left(\left(\frac{k_{\text{dis}} - k_{\text{dis}'}}{k_{\text{crys}} + k_{\text{dis}'} - k_{\text{dis}}} \right) \left(e^{-k_{\text{dis}} t} - e^{-(k_{\text{crys}} + k_{\text{dis}'}) t} \right) + \left(\frac{k_{\text{dis}'}}{k_{\text{crys}} + k_{\text{dis}'}} \right) \left(1 - e^{-(k_{\text{crys}} + k_{\text{dis}'}) t} \right) \right) \quad (\text{S31})$$

In equilibrium, the concentration B reaches the following value:

$$\lim_{t \rightarrow \infty} B(t) = \frac{k_{\text{dis}'}}{k_{\text{crys}} + k_{\text{dis}'}} \quad (\text{S32})$$

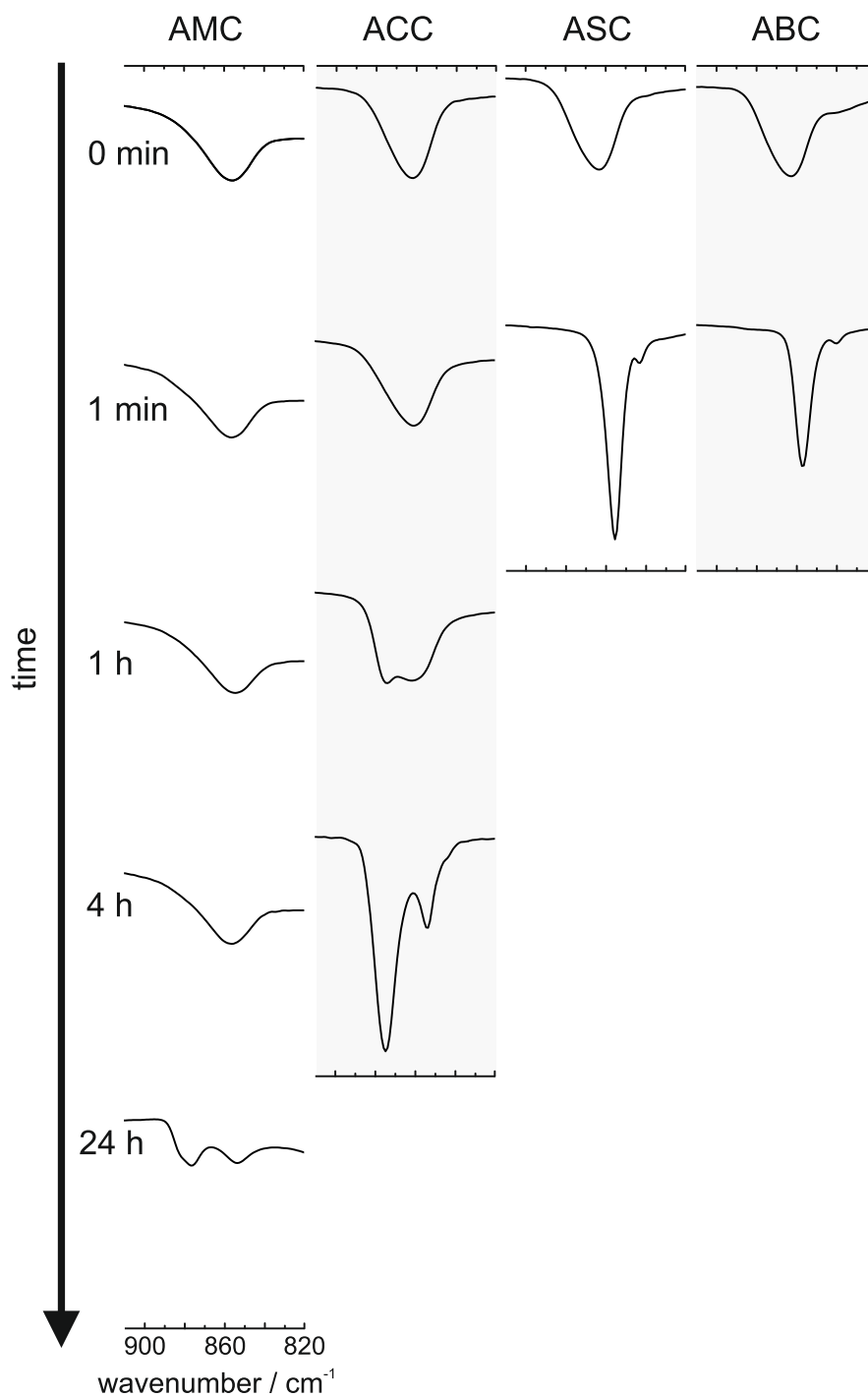


Figure S9. Stability of amorphous carbonates with regard to crystallization. AMC, ACC, ASC, and ABC were dispersed in a mixture of 20 vol% water and 80 vol% acetonitrile. At specific times, samples were taken and FTIR spectra were recorded. The displayed ν_2 mode is sensitive to the transformation amorphous-crystalline. Both ASC and ABC crystallize completely within one minute to strontianite, respectively witherite. After 1 h, ACC starts to crystallize; 3 h later, the sample is completely crystalline. AMC is the most stable of the amorphous carbonates. It takes one day to crystallize to hydromagnesite.

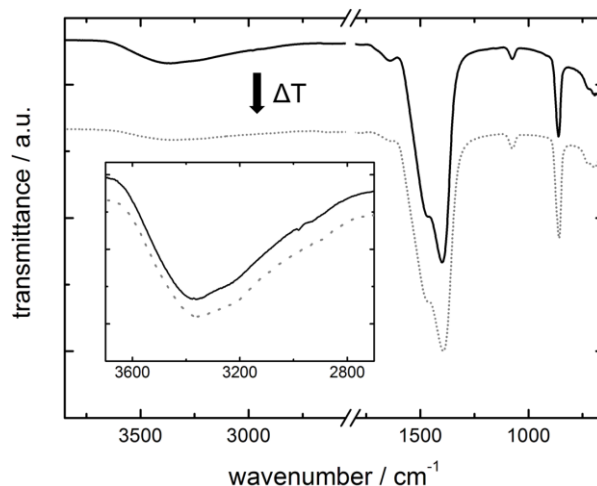


Figure S10. FTIR spectra of ACC before (black, straight) and after drying at 70 °C (gray, dotted). The shape of the $\nu_{\text{O-H}}$ band persists during drying, which indicates no significant changes in the water structure (inset: scaled $\nu_{\text{O-H}}$ bands).

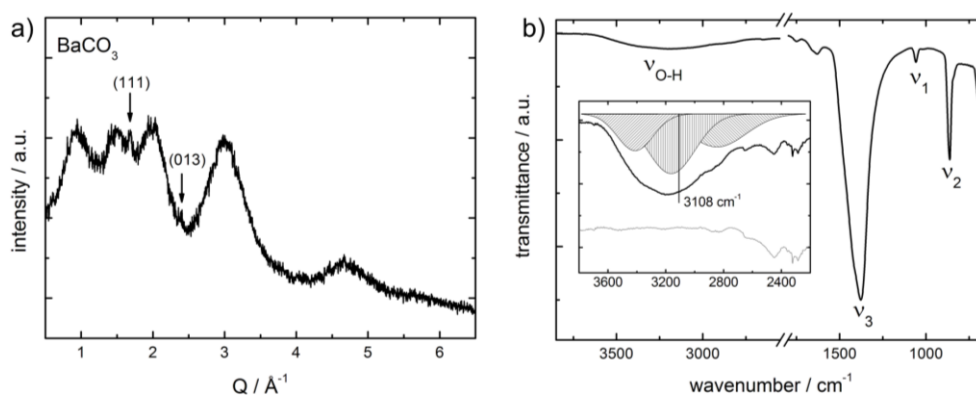


Figure S11. a) PXRD of amorphous barium carbonate. Two Bragg reflections emerge, which correspond to the (111) plane and the (013) plane in crystalline barium carbonate (witherite). The incipient crystallization of the sample during the measurement indicates the instability of the amorphous modification. b) FTIR of amorphous barium carbonate ($\nu_3 = 1376 \text{ cm}^{-1}$, $\nu_1 = 1058 \text{ cm}^{-1}$, $\nu_2 = 863 \text{ cm}^{-1}$). The O-H stretching region is fitted with a trimodal Gaussian function (inset), giving a mean wavenumber of $\nu_{\text{O-H}} = 3108 \text{ cm}^{-1}$.

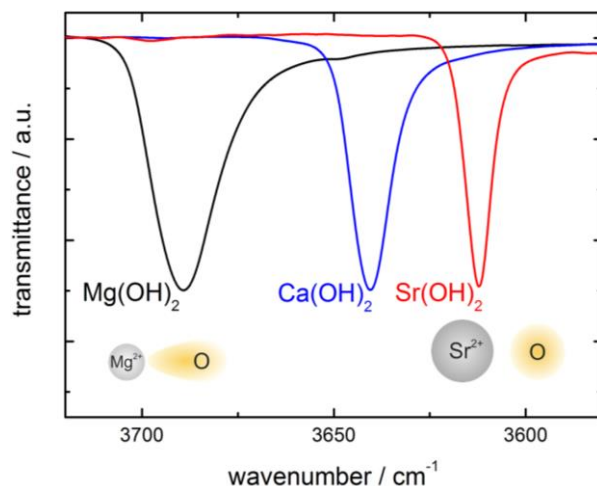


Figure S12. FTIR spectra of earth alkali hydroxides. Polarization of the oxygen by the metal cation diminishes the hydrogen bonding acceptor strength of the oxygen and shifts the O-H stretching band to higher wavenumbers.

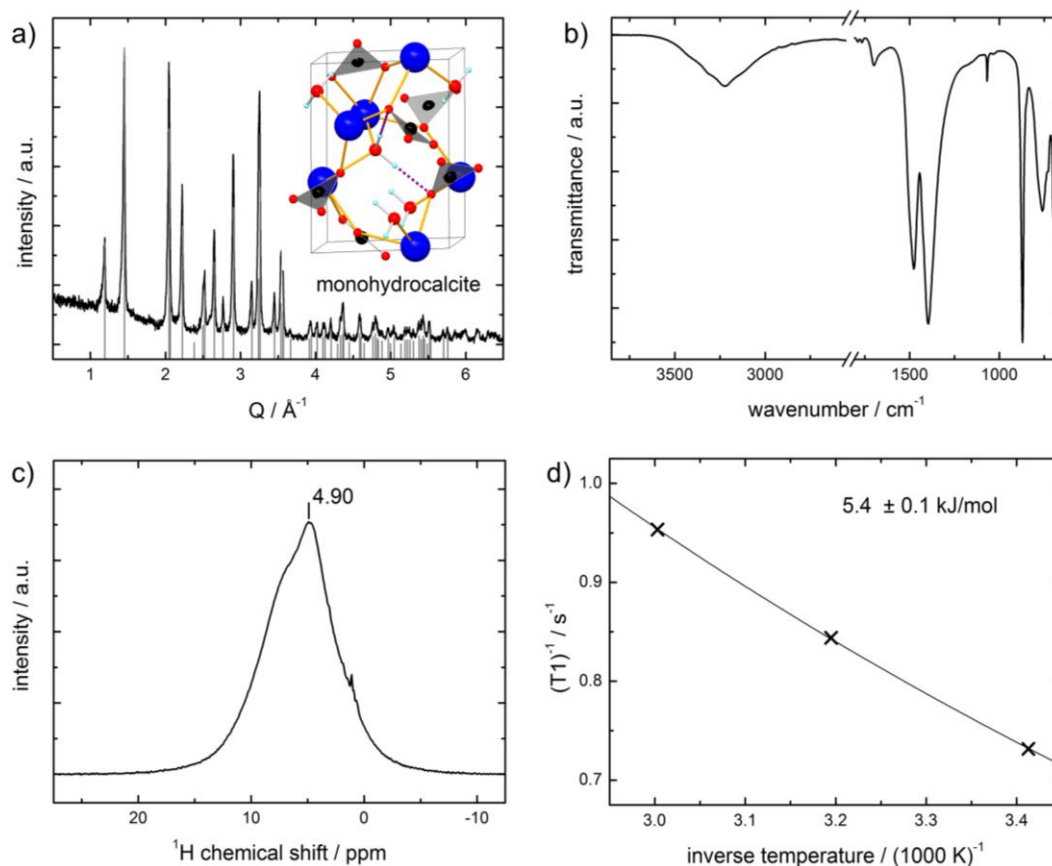


Figure S13. a) PXRD of monohydrocalcite with reference pattern (gray), the unit cell is shown as inset (calcium: blue, carbon: black, oxygen: red, hydrogen: light blue, hydrogen bonds: purple dotted lines) b) FTIR spectrum and c) ^1H NMR of monohydrocalcite. d) Evaluation of the temperature dependent T_1 relaxation times gives an activation energy for the water motion of $E_a = 5.4 \pm 0.1 \text{ kJ/mol}$.

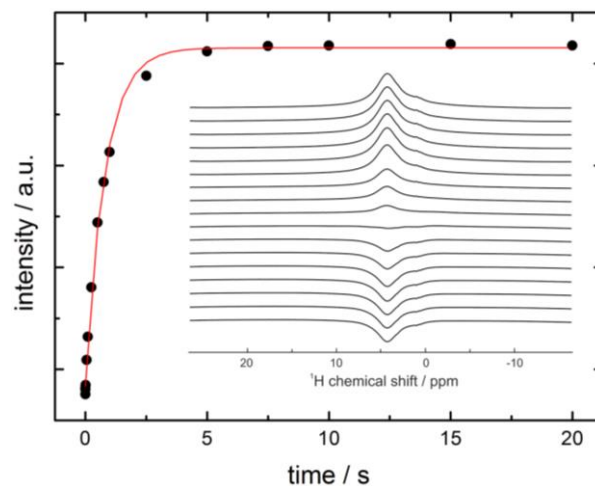


Figure S14. Determination of the T1 relaxation time by inversion recovery method. Exemplary data for ACC at 20°C are displayed. Data are fitted (red) with eq. 4.1 (Chapter 4, p. 90) to extract T1.

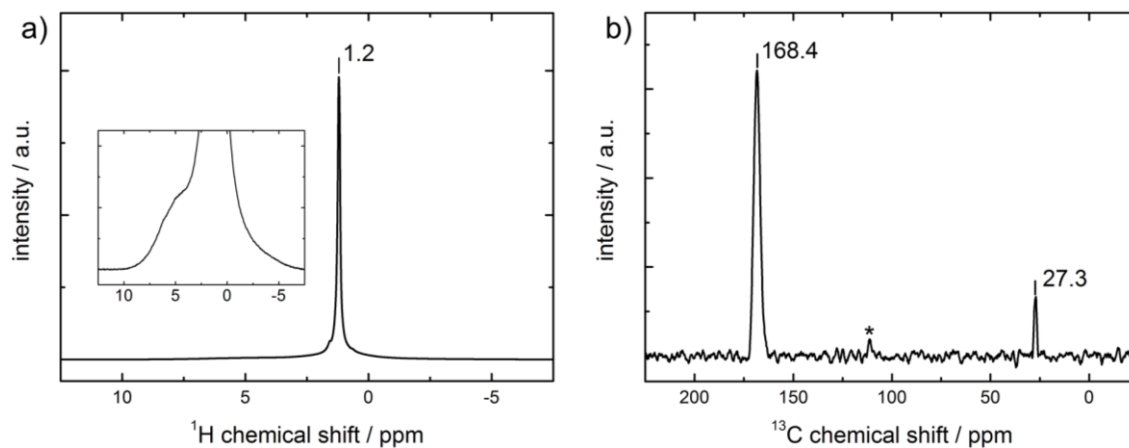


Figure S15. a) ^1H NMR of BM-ACC exhibits one sharp signal at 1.2 ppm originating from the dispersion medium cyclohexane. Magnification of this region (100 \times , inset) reveals a shoulder around 5 ppm, which we attribute to trace amounts of physisorbed water. b) ^{13}C NMR displays signals of the carbonate group (168.4 ppm) and cyclohexane (27.3 ppm). Polytetrafluoroethylene from sample preparation is marked with an asterisk. Integration of the signals suggests a composition of ca. 1.4 mol% cyclohexane per formula unit BM-ACC.

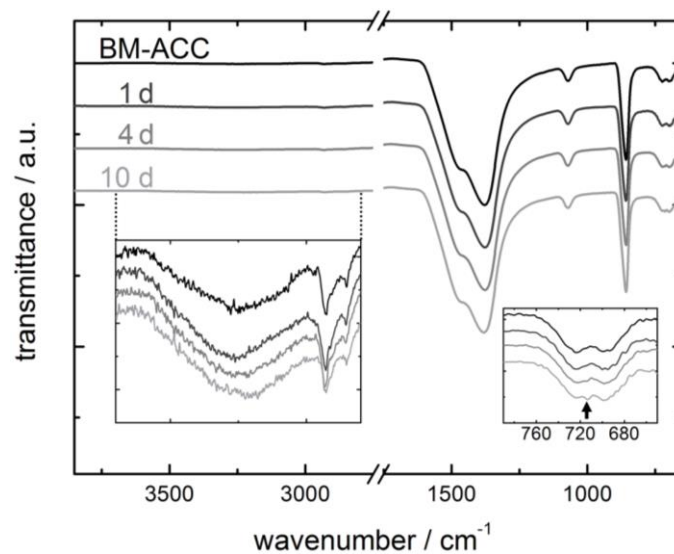


Figure S16. Crystallization of BM-ACC in air. BM-ACC was stored in air at ambient conditions for ten days. The FTIR spectra show no evident changes within that time. Yet, the incipient crystallization after four days is indicated by the emerging band of the ν_4 vibrational mode of calcite at 712 cm^{-1} (left inset). Magnification of the region between 3700 cm^{-1} and 2800 cm^{-1} (right inset) reveals an increase of the amount of physisorbed water after exposing the sample to air.

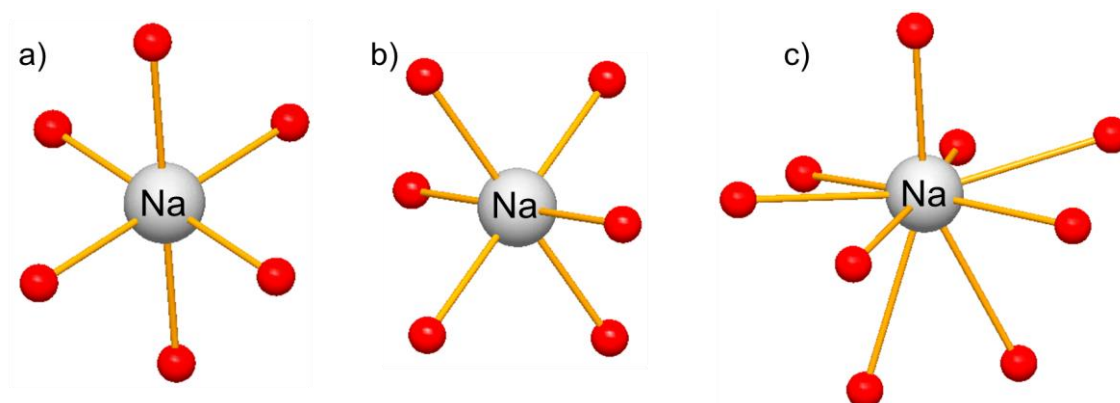


Figure S17. Three possible sodium coordinations in Na_2CO_3 . Half of the ions occupy proportionally the two octahedrally coordinated positions (a, b). The other half of sodium ions are situated in an anisotropic coordination sphere (c).

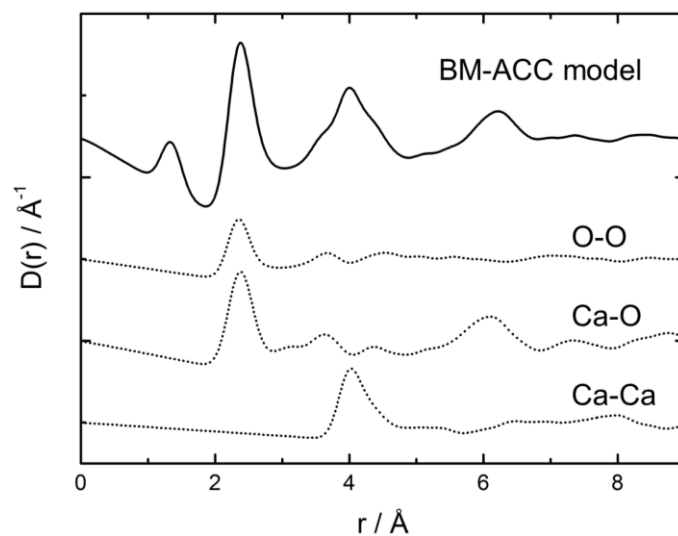


Figure S18. Partial PDFs of the pivotally contributing interatomic distances in the structural model of BM-ACC. The first signal at 1.29 Å originates from the C-O distance in the carbonate group. The second peak at 2.40 Å is mainly a superposition of the O-O distances within the carbonate group and the Ca-O distance in the first coordination sphere of calcium. The third peak around 4 Å originates mainly from the distance between the cations. Mostly farther Ca-O distances cause the last peak slightly above 6 Å.

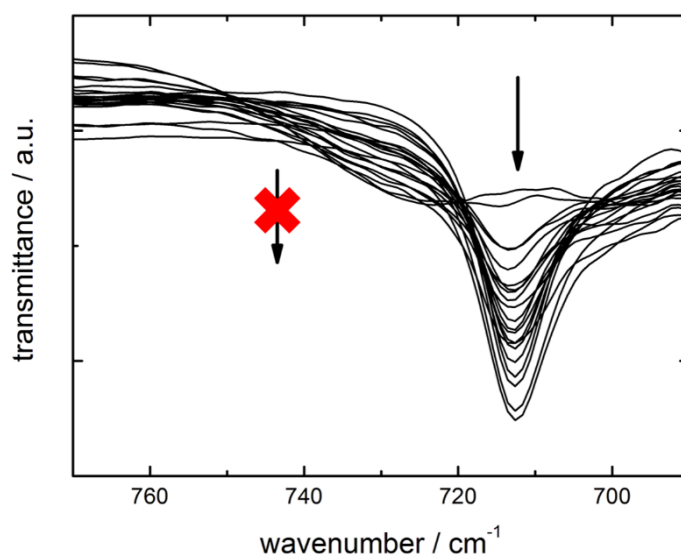


Figure S19. Crystallization of BM-ACC in a mixture of 10 vol% water with acetonitrile. Calcite, which is identified by the characteristic ν_4 vibrational mode at 712 cm^{-1} , is the only crystalline modification that occurs. The out-of-plane vibrational mode of vaterite at 745 cm^{-1} is not observed at any point.

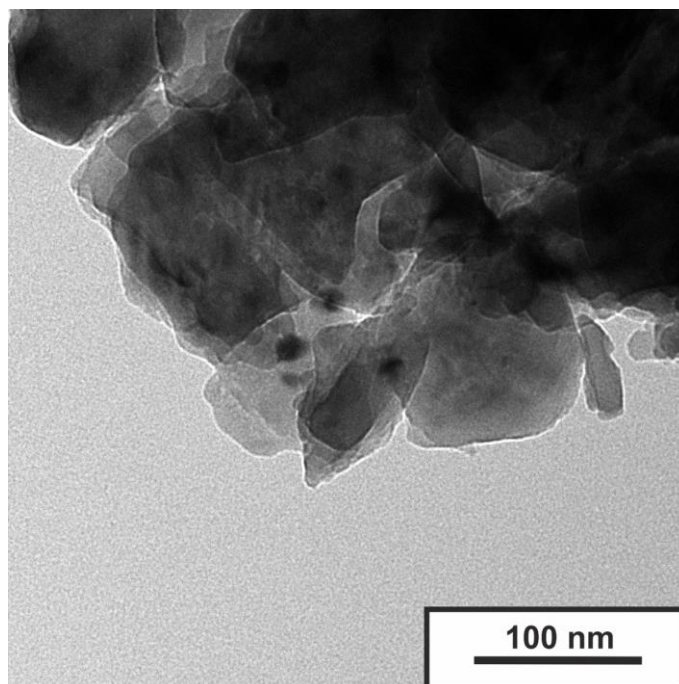


Figure S20. TEM image of BM-ACC heated to 300°C for 8 h. The nanoparticular surface structure is not observed anymore.

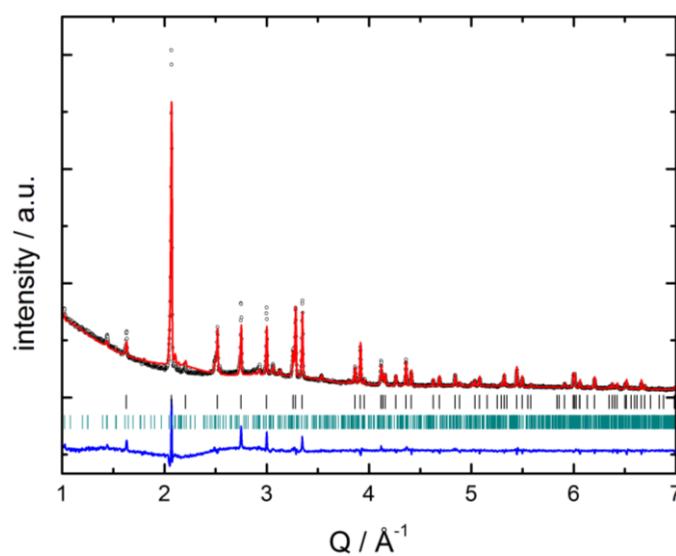


Figure S21. PXRD with Rietveld refinement of BM-ACC heated to 550°C for 1 h (black circles: measured pattern, red line: calculated pattern). Besides the amorphous phase (17.7 %), two crystalline phases were identified. The sample consisted mostly of calcite (67.5 %, black ticks), but also the sodium-rich carbonate nyerereite, $\text{Na}_2\text{Ca}(\text{CO}_3)_2$ (14.8 %, turquoise ticks), formed at elevated temperature. As can be seen from the difference curve (blue), the annealing process leads to significant changes in the amorphous phase.

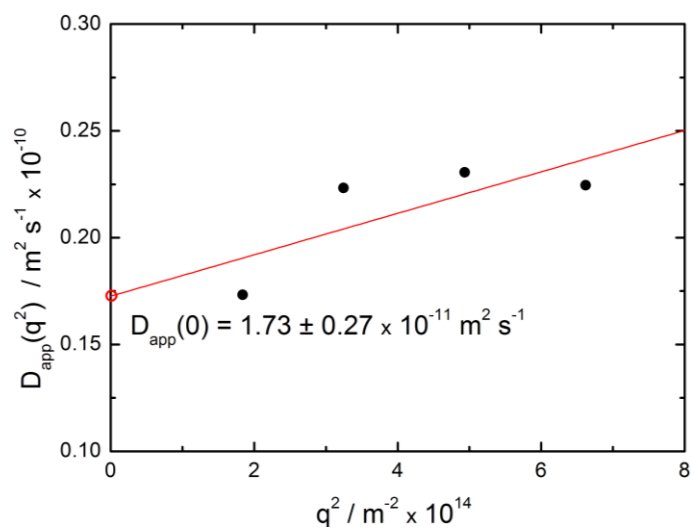


Figure S22. Determination of the apparent diffusion coefficient for $q^2 = 0$ by linear regression of the diffusion coefficients at the respective scattering vectors.

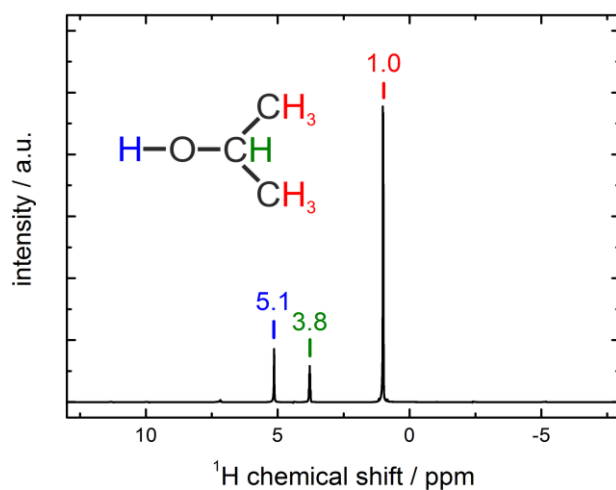


Figure S23. ^1H NMR spectrum of liquid 2-propanol, recorded using the solid state NMR spectrometer at low MAS.

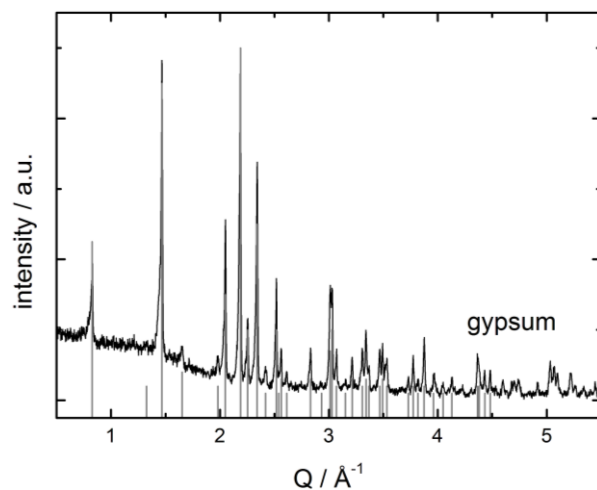


Figure S24. PXRD of the precipitate obtained by mixing the dispersion of the calcium sulfate nanoparticles in acetone with water. Phase analysis indicates solely gypsum (gray reference pattern).

CURRICULUM VITAE

[REDACTED]

[REDACTED]

[REDACTED]

[REDACTED]

[REDACTED]

[REDACTED]

[REDACTED]

[REDACTED]

[REDACTED]

[REDACTED]

[REDACTED]

[REDACTED]

[REDACTED]

[REDACTED]

[REDACTED]

[REDACTED]

[REDACTED]

[REDACTED]

[REDACTED]

[REDACTED]

[REDACTED]

[REDACTED]

[REDACTED]

[REDACTED]

[REDACTED]

[REDACTED]

[REDACTED]

[REDACTED]

[REDACTED]

[REDACTED]

[REDACTED]

[REDACTED]